Analyse par graphes de la connectivité fonctionnelle de repos par IRM : vers de nouveaux biomarqueurs de la récupération fonctionnelle dans l'AVC

Maite Termenon Conde

Communauté
UNIVERSITÉ Grenoble Alpes

THÈSE

Pour obtenir le grade de

DOCTEUR DE LA COMMUNAUTÉ UNIVERSITÉ GRENOBLE ALPES

Spécialité : **Biotechnologie, Instrumentation, Signal**
Arrêté ministériel : 7 août 2006

Présentée par

Maite TERMENÓN CONDE

Thèse dirigée par **Chantal DELON-MARTIN**
co-encadrée par **Assia JAILLARD**
et **Sophie ACHARD**

préparée au sein du **Grenoble Institut des Neurosciences (GIN)**
dans **L'École Doctorale Ingénierie pout la santé, la cognition, l'environnement (EDISCE)**

Analyse par graphe de la connectivité fonctionnelle de repos par IRM. Vers de nouveaux biomarqueurs de la récupération fonctionnelle

Thèse soutenue publiquement le **15 decembre 2016**,
devant le jury composé de:

M. Michel DESVIGNES
Professeur, Université de Grenoble-Alpes, Président
M. Bertrand THIRION
Directeur de Recherche, INRIA, Rapporteur
Mme. Isabelle LOUBINOUX
Directrice de Recherche, Toulouse Neuroimaging Center (TONIC), INSERM, Rapporteur
Mme. Charlotte ROSSO
MD, Maître de conférence, Hôpital Pitié-Salpétrière (Paris), Examinateur
Mme. Chantal DELON-MARTIN
CR, INSERM - Grenoble Institut des Neurosciences, Directrice de thèse
Mme. Assia JAILLARD
MD, CHU Grenoble, Encadrante de thèse
Mme. Sophie ACHARD
CR, CNRS - Université de Grenoble, Encadrante de thèse, Invité

Acknowledgements

First of all, I would like to express my gratitude to my thesis supervisors, Chantal DELON-MARTIN, for your dedication, your always useful explanations, your helpful advises and for being always available; Assia JAILLARD, your patience explaining several times the clinical point of view, for all your teas & coffees, your sense of humor, and your deep discussions; and Sophie ACHARD, for dedicating me so much of your precious time, for all your feedback, the skype meetings at night and your generosity. Thank you very much for giving me the opportunity of working with the three of you. It has been a great honor to be guided by you, I think we do a great women power team!

I am very grateful to the reviewers, Bertrand THIRION and Isabelle LOUBINOUX, brave enough to read this thesis till the end and for their insightful comments, as well as Michel DESVIGNES and Charlotte ROSSO for being part of my defense committee.

My greatest thanks goes to the Barbier team of the GIN, both present and past members. I apologize in advance to the people that I may forget. I feel so lucky of having spent these three important years of my life surrounded by people like you, always nice, always smiling, always eating croissants! Benjamin LEMASSON - I have no words, thank you for being such a great colleague, all your bureaucratic help, your jokes and your patience with this poor foreign student -, Emmanuel BARBIER - great team leader, always helpful, always available -, the team girls: Ligia SIMOES - all your visits and empathy -, Emmanuelle BELLOT - all your funny moments -, Lydiane HIRSCHLER - those amazing cakes and recipes -, Melina BOULDI - ma trés belle amie -, Ivy USZYNSKI - great sense of humor -, and Sandra MONTALESCOT - always sincere -, Marie Claude ZANONI - your paper work always with a laugh -, Claire ROME - your great advices as a recent mum -, Agnes JOB - always listening and motivating me -, Herve MATHIEU - for doing me speak in "French" all the time -, Jan WARNKING - your help with computers and our great wine taste sense -, Nora COLLOMB - always with a smile and nice words -, Michel DOJAT - for your scientific feedback - and Vasile STUPAR - all the coffee discussions. Big thanks as well to the remaining GIN colleagues!

Special thanks to the Région Rhône-Alpes, for giving me the opportunity (and the money) to do my PhD thesis.

I would also like to thank all my family and friends for their support and encouragement. To my parents, for supporting me whatever the decisions I take.

To Miguel, for introducing me to the realm of science and the world behind the wall. To Unai, you did everything more complicated but much more fun. To my brothers, for making me believe that I can achieve any goal, always revolution! To 'bola de paja', these three years in Grenoble were much more interesting thanks to you all. To my 'cuadrilla', unconditional support, always.

Contents

List of Figures

List of Tables

Abstract

In the recent years, there has been a great amount of work developing new investigation methods of the brain connectivity based on fMRI. The exploration of brain networks with resting-state fMRI (rs-fMRI) combined with graph theoretical approaches has become popular, with the perspective of finding network graph metrics as biomarkers in the context of clinical studies. A preliminary requirement for such findings is to assess the reliability of the graph based connectivity metrics in healthy subjects. In this thesis, taking advantage of a large test-retest database provided by the Human Connectome Project, we quantified the reliability of the graph metrics computed both at global and regional level depending, at optimal cost, on two key parameters, the sample size (number of subjects) and the number of time points (or scan duration). We also explored how other factors, such as the parcellation scheme, the connectivity measure or the filtering method may influence this reliability. In a clinical context, stroke is one of the leading causes of mortality and disability worldwide. Resulting in focal structural damage, it induces changes in brain function at both local and global levels. Following stroke, cerebral networks present structural and functional reorganization to compensate for the functional impairment provoked by the lesion itself and its remote effects. In this thesis, we studied the role of the contralesional hemisphere in the reorganization of brain function of stroke patients using resting state fMRI and graph theory. We explored this reorganization using the 'hub disruption index' (κ), a global index sensitive to the reorganization of nodes within the graph. We explored the relation between κ and behavioral clinical scores to assess whether κ could be used as a surrogate biomarker of stroke recovery.

Keywords: rs-fMRI, graph theory, stroke, hub disruption index (κ), reliability, contralesional, biomarkers, recovery, Human Connectome Project.

Résumé

Cette dernière décennie, un important travail de développement méthodologique a été mené pour explorer la connectivité fonctionnelle de repos par IRM. L'exploration des réseaux cérébraux par IRM fonctionnelle de repos combinée à une approche de graphes est devenue populaire dans la perspective de trouver des métriques de graphes qui puissent être des biomarqueurs dans différentes situations pathologiques. Un prérequis pour pouvoir identifier ces métriques est de s'assurer de leur fiabilité chez des sujets sains. Dans cette thèse, partant de la grande base de données de repos avec 2 examens du Projet de Connectome Humain, nous avons quantifié la fiabilité des métriques globales et régionales de graphe, pour un coût optimal, en fonction de deux paramètres clé : la taille de l'échantillon (nombre de sujets) et le nombre de points temporels (durée d'acquisition). Nous avons également exploré d'autres facteurs, comme la parcellisation, la mesure de connectivité et la méthode de filtrage fréquentielle, susceptibles d'impacter cette fiabilité. L'accident vasculaire cérébral (AVC) est une des causes principales de mortalité et d'handicap dans le monde. En créant des lésions focalisées, il entraine des modifications des fonctions cérébrales à la fois au niveau local mais aussi global. Après un AVC, les réseaux cérébraux présentent des réorganisations structurelles et fonctionnelles pour compenser les déficits fonctionnels provoqués par la lésion comme par ses effets à distance. Dans cette thèse, nous avons étudié le rôle de l'hémisphère contralésionel dans la réorganisation des fonctions cérébrales de patients ayant subi un AVC en utilisant l'analyse des données d'IRMf de repos par la théorie des graphes. Nous avons exploré cette réorganisation en utilisant un index global sensible à la réorganisation des noeuds d'un graphe, baptisé 'index de perturbation des noeuds' (κ). Nous avons enfin exploré la relation entre cet index et les scores cliniques pour évaluer son intérêt comme candidat-biomarqueur dans la récupération aprés un AVC.

Mots clés : IRM fonctionnelle de repos, théorie des graphes, AVC, index de perturbation des noeuds (κ), fiabilité, contralesionel, biomarqueurs, récupération, Projet du Connectome Humain.

Chapter 1

Introduction

Grenoble is a city known for advanced technologies where 1 person over 5 is employed in research and development. Clinicians are working since decades in close collaboration with scientific teams involved in advanced methods of image and signal processing and assissted guided surgery, among others. In neurology, long term research collaborations mainly in the fields of Parkinson disease, epilepsy, traumatic brain injury and stroke have been established, and the creation of the Grenoble Institut des Neuroscience (GIN) reinforced these collaborations. Neuroimaging has become an essential tool to investigate these pathologies using advanced mathematical methods.

Taking advantage of existing close collaborations with scientist from multiple disciplines, this thesis emerges in a multidisciplinary context, creating synergy from the fields of neuroimaging, signal processing, advanced mathematical methods and new stroke treatment based on stem cells therapy.

Stroke represents the ensemble of lesions of the central nervous system caused by an injury of the brain vascular system. It is one of the leading causes of mortality and disability worldwide, and the incidence of stroke is expected to increase due to aging of the population and the sharp rise in diabetes and obesity. These facts motivate the increasing investment in research studies with the aim of finding effective treatments to improve the outcome of stroke victims. One of these treatments is the use of stem cells therapy.

Magnetic resonance imaging (MRI) is a non-invasive technique that presents the opportunity to study the internal structure of the brain (structural MRI) and also, the activity of the brain when we perform particular tasks (task based functional MRI) or while we rest (resting state functional MRI). This brain activity relies on brain regions that are connected among them and there are different ways to study this connectivity.

One way is based on graph theory. It is a method that applies in multiple fields, to explain interactions between different objects (or individuals). It can be used to represent a roadmap, a social network, a molecule or a galaxy distribution, for example.

In this work, we used resting state functional MRI to study the brain connec-

tivity along the recovery of stroke victims applying an advanced mathematical model based on graph theory.

My background is in industrial electronics and automation engineering, with a postgrade in biomedical engineering and a master in computer science and artificial intelligence. This thesis has been a challenge for me due to the lack of knowledge in the field of clinical science, the advanced functional magnetic resonance imaging techniques and some of the mathematical methods applied that were unkwon for me.

This thesis is thus divided in three parts. First, I start with the state of the art presenting stroke (Chapter 2), functional magnetic resonance imaging methods (Chapter 3), the analysis of how the brain is connected (Chapter 4) and advanced mathematical methods to study this connectivity (Chapter 5). This first part is finished with the aim and motivation of this work (Chater 6). The second part of this thesis describes the methodological contributions achieved (Chapters 7 to 10), mainly focusing on the reliability of graph methods applied to study brain connectivity. In the last part of this thesis, I explain the methods (Chapter 11) and the results (Chapters 12 and 13) obtained applying graphs to study the recovery of stroke patients are presented. In a final chapter, Chapter 14, a general conclusions and future perspectives are discussed.

Contributions

Two publications are the main contributions of this thesis. The first one is the analysis of the reliability of the method used in this thesis, graph based analysis of brain functional connectivity. Part of this work (Chapters 8) was published in June 2016 in the journal Neuroimage and presented in the fifth bienal resting state conference in Vienna. The second main contribution (Chapters 9 and 12) was to study the reorganization of the contralesional hemisphere of stroke patients, using the same method validated previously. This work was published in August 2016 in Frontiers in Computational Neuroscience and also presented in the fifth bienal resting state conference in Vienna.

The posters presented during this thesis in different conferences are listed in the Appendix B.

Journals:

M. Termenon, A. Jaillard, C. Delon-Martin, S. Achard, **Reliability of graph analysis of resting state fMRI using test-retest dataset from the Human Connectome Project**, NeuroImage, Available online 6 June 2016, ISSN 1053-8119, `http://dx.doi.org/10.1016/j.neuroimage.2016.05.062`

M. Termenon, S. Achard, A. Jaillard, C. Delon-Martin, **The "Hub Disruption Index", a Reliable Index Sensitive to the Brain Networks Reorganization. A Study of the Contralesional Hemisphere in Stroke**, Frontiers in Computational Neuroscience, 2016, 10:84, `http://dx.doi.org/10.3389/fncom.2016.00084`

Oral presentations

2016:
Reliability of graph analysis of resting state fMRI using test-retest dataset from the Human Connectome Project, Atlas workshop, Grenoble, May 2016.

2015:
Brain graph connectivity computation: Theory and training. Second Brain connectivity course, Grenoble, September 2015.

Spécialisation hémisphérique chez les hommes et les femmes : Représentation de la connectivité cérébrale par la méthode des graphes en IRM fonctionnelle de repos., Société Française de Résonance Magnétique en Biologie et Médecine (SFRMBM), Grenoble, 2015.

Posters

2016:
M. Termenon, A. Jaillard, C. Delon-Martin, S. Achard, **Reliability of graph analysis of rs-fMRI using test-retest dataset from the Human Connectome Project**, Fifth Biennial Conference on Resting State / Brain Connectivity.

M. Termenon, S. Achard, A. Jaillard, C. Delon-Martin, **Hub disruption index (kappa), an index that measures alterations of node connectivity and captures brain networks reorganization**, Fifth Biennial Conference on Resting State / Brain Connectivity.

2014:
M. Termenon, A. Jaillard, S. Achard, C. Delon-Martin, **Hemispheric specialization in men and women using graph theory: a resting-state functional connectivity MRI study in highly educated healthy adults**, Fourth Biennial Conference on Resting State / Brain Connectivity.

M. Termenon, A. Jaillard, S. Achard, F. Renard, C. Delon-Martin **Is homotopic intramural connectivity related to cytoarchitectonic cortical classification?**, 20th Annual Meeting of the Organization for Human Brain Mapping.

Part I

State of the art

Chapter 2

Stroke in the human brain

2.1 The human brain

The nervous system is a multiprocessor that receives information from the somatosensory, visual and auditory systems to control voluntary movement and regulate automatic activities such as breathing, heartbeat or digestion. In humans, the brain gives us the capacity for speech reflective thoughts, fine movement coordination, attention, judgment, emotion and social behavior. It keeps our memories, enables us to feel emotions and pain, and gives us our identity.

The human brain consists of three subdivisions: brainstem, cerebellum, and the telencephale cerebral subdivided into two hemispheres. The cerebral cortex is the outer covering of gray matter over the hemispheres covered by the cortex.

Each hemisphere is composed of five lobes: the frontal lobe, the parietal lobe, the temporal lobe, the occipital lobe and the limbic lobe, see Fig. 2.1. Each lobe contains several cortical areas, each associated with a particular function, such us vision, audition, motor control, and language. The shape of both hemispheres is very similar, and most cortical areas are replicated on both sides. However, some areas are deeply lateralized; specifically brain areas engaged in language are associated to the left hemisphere in most people. Other functions, such as visual-spatial skills, are usually linked to the right hemisphere.

The neocortex represents the great majority of the cerebral cortex. It has six layers and contains between 10 and 14 billion neurons (20 billion in the whole cerebral cortex) [Armstrong, 1990]. Neurons are connected via synapses to several thousand other neurons. These neurons communicate with one another by means of long fibers called axons, which carry signal pulses called action potentials to distant parts of the brain or body targeting specific recipient cells. The structure of a typical neuron is shown in Fig. 2.2.

The brainstem consists of four parts: the diencephalon, the midbrain, the pons and the medulla. The brainstem is a mixture of deep nuclei and white matter tracts through which sensorimotor information circulates between the cortex, the cerebellum and the spinal cord, see Fig. 2.3. The brainstem nuclei

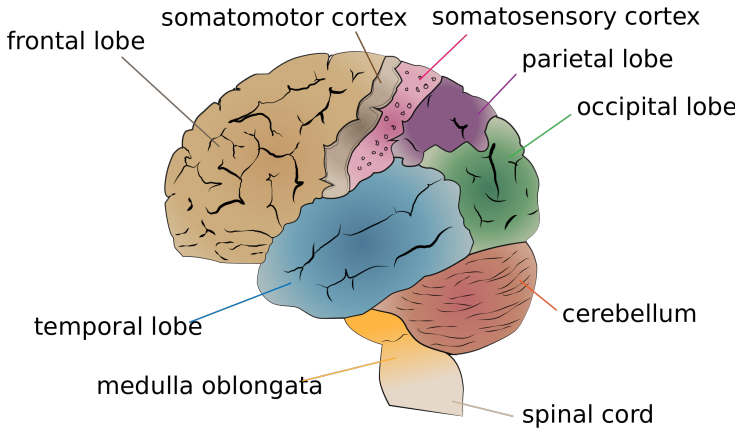

Figure 2.1: Left hemisphere of the brain showing the four lobes (frontal, parietal, temporal and occipital lobes), the somatomotor and somatosensory cortex, the cerebellum and brainstem.

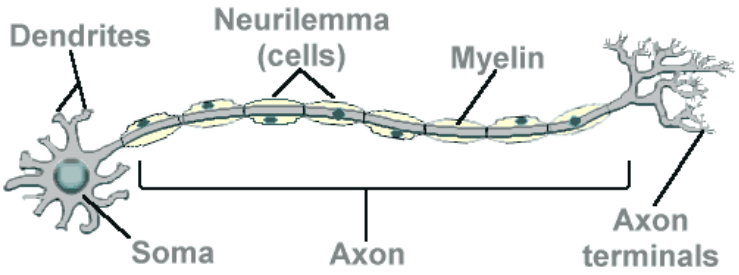

Figure 2.2: The structure of a typical neuron includes four main components: dendrites, cell body (or soma), axon, and axon terminals. The soma contains the nucleus; the dendrites receive signals from the axon terminals of other neurons; the axon conducts electric pulses (known as action potentials) and the axon terminals transmit signals to other cells.

play an important role in the control of cardiac, respiratory, oculomotor and vestibular functions, as well as the level of consciousness [Boundless, 2016].

The cerebellum, is located caudally to the pons. Both structures constitute the metencephalon round the fourth ventricle. The cerebellum is connected to the brainstem via the cerebellar peduncles. It plays an important role in the control of equilibrium, tonus and motor adaptation contributing to coordination, precision, and accurate timing [Fine et al., 2002].

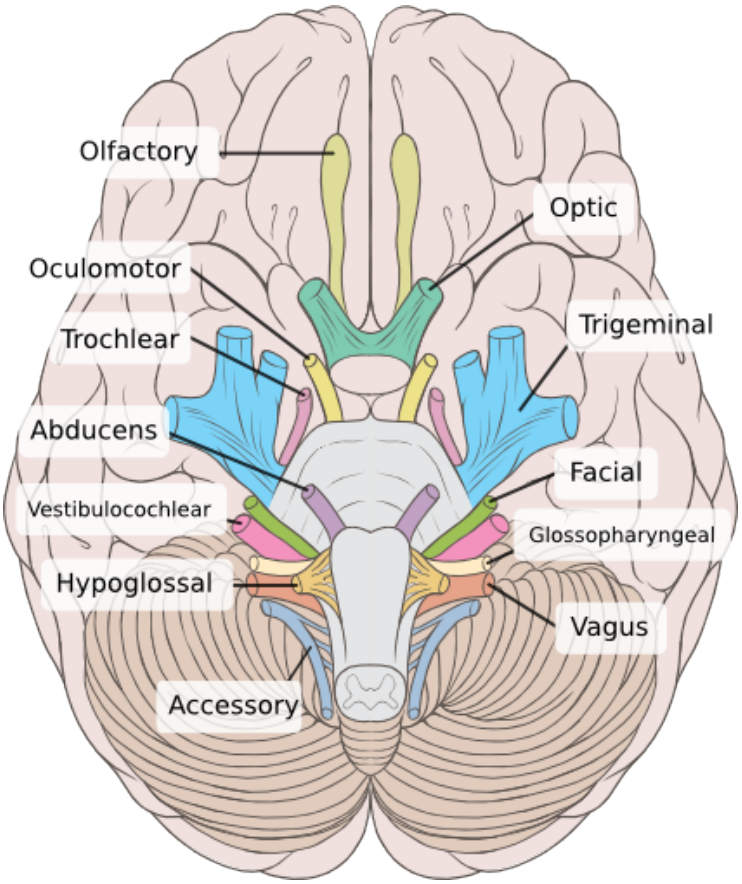

Figure 2.3: Mid-line incision of the human brain. Courtesy of Dr. Johannes Sobotta - Atlas and Text-book of Human Anatomy Volume III Vascular System, Lymphatic system, Nervous system and Sense Organs.

The brain is mainly composed of three different tissues: gray matter (GM), white matter (WM) and cerebrospinal fluid (CSF). The gray matter is constituted of mostly unmyelinated neurons and it contains areas of nerve connections and processing. In the brain, GM is distributed at the surface of the cerebral and cerebellar cortex, the basal ganglia (caudate, putamen, pallidum) and the thalamus, embedded in the white matter of the cerebral hemispheres, the deep cerebellar nuclei (dentate, fastigial, globulus nuclei) and the numerous nuclei of the brainstem. The WM is composed of myelinated nerve cells (axons) that form tracts to connect GM areas to each other and to the spinal cord, carrying nerve impulses from the neuron. The myelin that is composed of segments separated by nodes of Ranvier, has a crucial function in facilitating conduction in axons.

The CSF is a fluid produced in the ventricles that flows over the ventricular and pial surface of the brain and spinal cord. It contains glucose, oxygen, and ions, but no cellular component. The CSF serves to support and cushion the CNS against trauma, removes waste products of metabolism, drugs and other substances which diffuse into the brain from the blood, and carries away solutes, drugs and neurotransmitters which pass into venous blood via the arachnoid villi [Hall, 2010].

Along this thesis, we study how the brain is affected by stroke (introduced in the following section) focusing on the cerebral cortex and cerebellum. Specifically, we study the GM of the brain in the cerebral cortex, the depths of the cerebrum and the GM of the cerebellum.

2.1.1 Functional cerebral organization

The brain can also be divided into areas depending on the function they perform. We can distinguish two functional areas: the sensory areas and the motor areas, that allow you to react upon a sensation. See Fig. 2.4 for a map of the distribution of those areas.

Sensory areas

Somatosensory cortex The primary somatosensory cortex is located in the postcentral gyrus, which is a prominent structure in the parietal lobe of the human brain. It is the main sensory receptive area for the sense of touch and proprioception.

The sensory homunculus (Fig. 2.5) includes cortical representation of the body based on the degree of sensory innervation.

Lesions affecting the primary somatosensory cortex can produce symptoms including: agraphesthesia (disorientation of the skin's sensation across its space), astereognosia (inability to identify an object by active touch of the hands without other sensory input), hemihypesthesia (reduction in sensitivity on one side of the body), and loss of vibration, proprioception (sense of the relative position of neighbouring parts of the body and strength of effort being employed in movement) and fine touch. It can also produce hemineglect (inability of a person to process and perceive stimuli on one side of the body or environment).

The secondary somatosensory cortex receives connections from the primary sensory cortex and also less specific thalamic nuclei. It contributes to many somatosensory processing tasks including pain perception, tactile attention, and somatosensory working memory. This responds to sensory stimuli bilaterally, although with much less precision than the primary cortex. Nonetheless, lesions to this area may impair some elements of sensory discrimination [Swenson, 2006].

Visual cortex The visual cortex of the brain is the part responsible for processing visual information. It is located in the occipital lobe. The primary visual cortex is highly specialized for processing information about static and

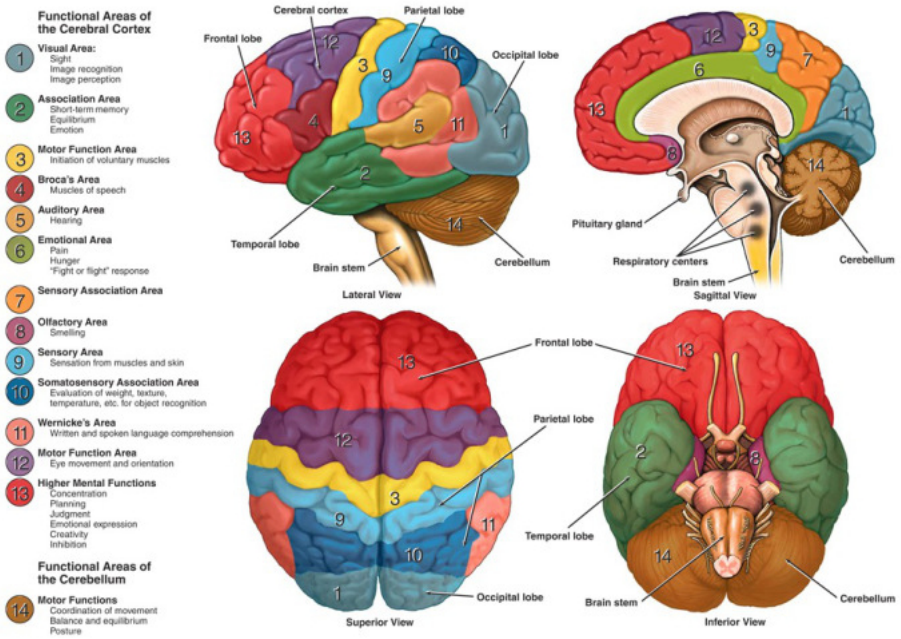

Figure 2.4: Brain functional areas for vision, association, motor function, Broca's speech, hearing, emotions, sensation, smell, written language, cognition and base motor functions like balance, equilibrium and posture. Nucleus Medical Media (2015). Anatomy and Functional Areas of the Brain. Nmal. Retrieved Oct 1, 2016, from `http://www.sciencemedicalart.com/anatomy-and-functional-areas-of-the-brain/view-item?ItemID=1868`

moving objects and is excellent in pattern recognition. The primary visual cortex projects to cortical areas surrounding it, called the visual association areas, where signals are interpreted and form is recognized. Selective lesions of these association areas will produce an inability to recognize objects even when they may be seen [Swenson, 2006]. There are additional aspects of visual function, such as color recognition or recognizing movement that are represented in other regions of adjacent cortex.

Auditory cortex The primary auditory cortex, located in the temporal lobe, processes auditory information. It is a part of the auditory system, performing basic and higher functions in hearing. Thaks to bilateral sound representation, unilateral cortical lesions do not affect hearing [Swenson, 2006].

There are auditory association areas surrounding the primary auditory cortex that are involved in the interpretation of sound. In the dominant hemisphere, for understanding language, the cortex surrounding the auditory cortex is required. This is called Wernicke's area. Damage to Wernicke's area can produce

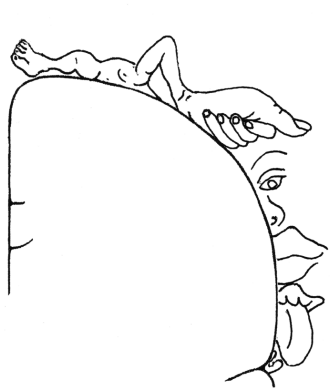

Figure 2.5: Sensory homunculus of the human brain shows the somatosensory representation of the body on the cerebral cortex. For example, very sensitive areas such as the lips and the fingertips have a larger representation than other parts of the body.

disability to understand language, even written language. In the nondominant hemisphere, it may be involved in understanding the tone of the voice [Swenson, 2006].

Motor areas

Primary motor cortex The primary motor cortex is located in the dorsal portion of the frontal lobe. Motor representation at the primary motor cortex is orderly arranged from the toe (at the top of the cerebral hemisphere) to mouth (at the lowest part). Some body parts may be controlled by partially overlapping regions of cortex.

Premotor cortex The premotor cortex (PMC) is an area of motor cortex lying within the frontal lobe of the brain just anterior to the primary motor cortex. The premotor cortex plays a role in planning movement, in the spatial and temporal control of movement, in understanding the actions of others, and in monitoring planned behavior. These functions are supported by distinct subregions of the premotor cortex that have different cytoarchitectonics properties. The PMC projects directly to the spinal cord via the corticospinal tract to control motor functions.

In Fig. 2.6, we show the location of the motor area, with its corresponding homunculus of the human brain.

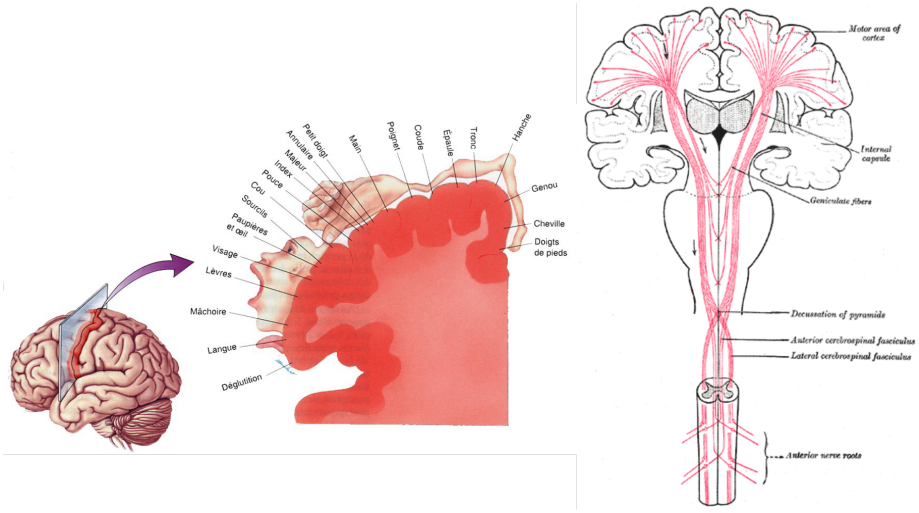

Figure 2.6: Location of the motor area, with its corresponding homunculus of the human brain.

2.2 Stroke

Stroke represents the ensemble of lesions of the central nervous system caused by a disease of the blood vessels (arteries and veins).

2.2.1 Epidemiology

Stroke is one of the leading causes of mortality and disability worldwide. In the EU, stroke affects approximately 6 million people, with around 1.1 million new cases every year. In France, there are between 130 to 150 000 new cases of stroke per year (a stroke every four minutes), a quarter of patients under 65 years old. More than 50% of stroke patients have residual impairment with neurological and/or cognitive sequelae (sometimes severe), causing a huge burden on the patients, their relatives, and society. In developed countries, given the aging population, projections predict an increase in the prevalence of stroke by 180% for 2030. Thus, effective interventions to attenuate residual impairment are urgently needed.

There are several risk factors that increase the probability of a stroke. The main modifiable risk factors are hypertension, physical inactivity, hypercholesterolemia (abnormally elevated levels of lipids and/or lipoproteins in the blood, obesity, smooking, food diet, heart disease, diabetes or excess of alcohol. Other risk factors, non modifiable, are age, sex (higher risk in men), inheritance, migraine, race and ethnicity (higher risk in Asians, blacks and Hispanics). See Fig. 2.7 for the distribution of stroke mortality worlwide.

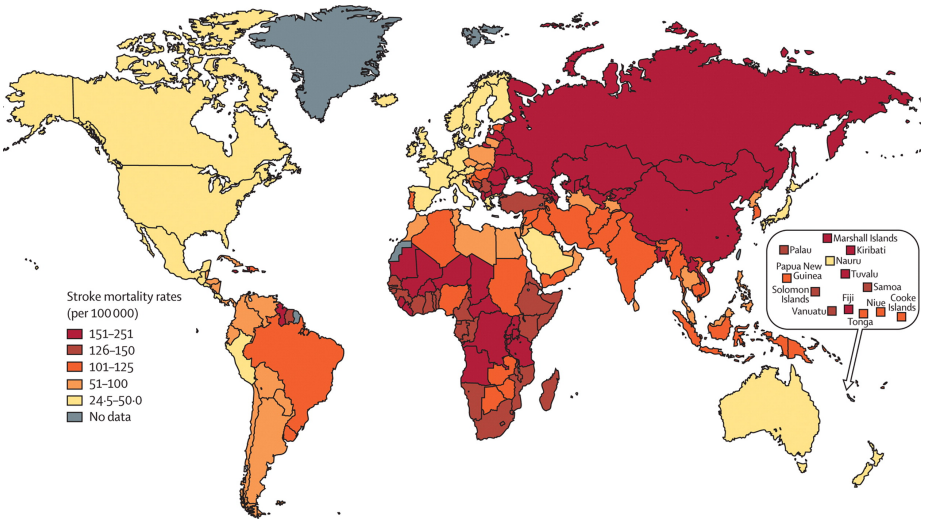

Figure 2.7: Age-adjusted and sex-adjusted stroke mortality rates worldwide. The highest rates are in eastern Europe, north Asia, central Africa, and south Pacific. [Johnston et al., 2009].

2.2.2 Physiopathology of ischemic stroke

Stroke is divided into two types: infarct or ischemic stroke and cerebral hemorrhage. Ischemic strokes, which we will discuss along this thesis, represent about 85% of stroke cases. They are caused by a decrease in cerebral blood flow (CBF) usually confined to a specific region of the brain. In the infarction core, CBF is almost nil. This region evolves towards cell death in minutes. Around this infarction core, the CBF may be less than the threshold of normal neuronal function, but remains above the threshold for cell death. This area is called *penumbra*. It is a metastable zone, which permits cell survival during a certain duration, at most a few hours (see Fig. 2.8). The penumbra is the main therapeutic target during the acute phase, especially recanalization using thrombolysis or arterial thrombectomy, which aims at restoring cerebral blood flow.

Mechanism of recovery

The term recovery has been used to refer to describe clinical improvements after stroke. Recovery after stroke can be classified into three types [Hommel et al., 2016]:

1. Restitution of damaged structures or functions. Example: recovery after recanalization resulting in penumbra reperfusion.

2. Recovery of impaired functions based on neuroplasticity and perilesional

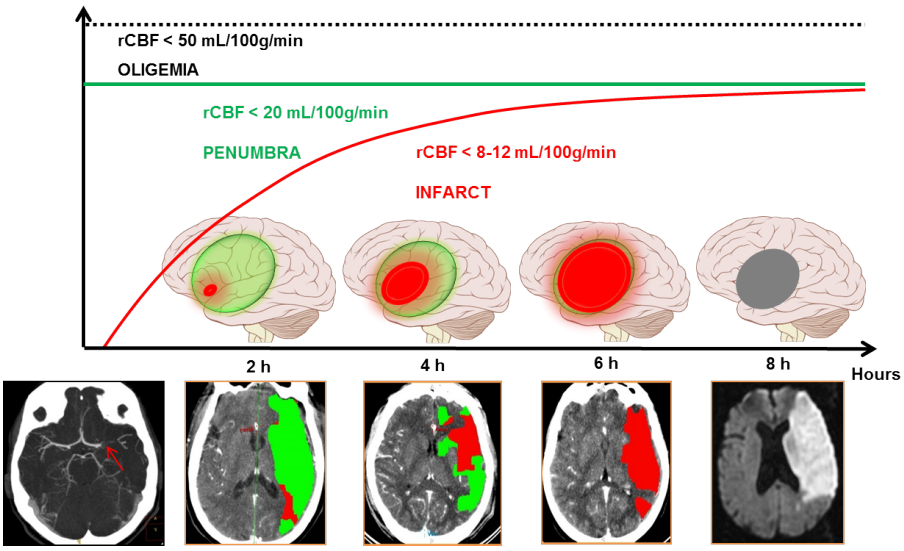

Figure 2.8: Immediately after an ischemic stroke, a core of irreversibly damaged brain tissue (red) is surrounded by an area of viable but at-risk tissue called the penumbra (green). Unless blood flow is restored quickly, the tissue within the penumbra will be also lost (right).

neural reorganization resulting in a normal pattern of activation or network and to good to complete recovery. Example: recovery after capsular infarction or primary motor cortex infarction.

3. Compensatory recovery based on beneficial and maladaptive plasticity and contralesional and perilesional neural reorganization resulting in incomplete recovery, associated to epilepsia and spasticity that may worsen neurological deficits.

Post Stroke plasticity and Brain repair

The adult brain has a striking capacity for self-repair 2.9 often resulting in re-emergence of developmental organizational patterns. During stroke recovery, beyond phenomena related to adaptive functional compensation, there is "structural" brain plasticity based on the surviving tissue participating in reorganization of damaged networks and exhibiting neuro-synaptogenesis with axonal sprouting that can persist for several months [Arvidsson et al., 2002]. This form of post-stroke plasticity notably occurs in elderly human brains [Minger et al., 2007]. Stroke also increases neurogenesis from neural stem cells (NSC) of the subventricular zone (SVZ) and hippocampal dentate gyrus, generating neuroblasts that migrate to the lesion and differentiate into mature neurons. This

post-stroke neurogenesis is closely linked to angio-vasculogenesis and glial function leading to the concept of a "glio-neurovascular niche" as a favorable "stem cell niche". Endothelial cells, but not vascular smooth muscle cells, release factors that both stimulate the self-renewal of NSC and also enhance neuron production. Microvessels size and density changes stimulate the neuronal plasticity after stroke. For several months following stroke, neuroblasts from the SVZ migrate close to vessels through an area exhibiting early vascular remodeling stimulated by the release of neurotrophic factors. Neuroblasts also enhance angiogenesis, a relationship underlining the bidirectional link between microvascular and neuronal remodeling. Ischemia promotes the formation of new blood vessels (angiogenesis) in the regions that were ischemic. A recent discovery, the neurogenesis, consists of multiplication and migration of neuroblasts from the periventricular region toward the infarcted area where these neuroblasts can turn into nerve cells (neurons and glial cells) and promote the production of growth factors. Synaptogenesis which characterizes the development of new dendrites participate in the structural and functional changes that characterize brain plasticity [Detante et al., 2014].

2.2.3 Clinical manifestation

2.2.3.1 The stroke syndrome

The diagnosis of stroke, which is usually not debatable, is characterized by the sudden occurrence of a nonconvulsive focal neurological deficit [Ropper et al., 2014].

The mode of occurrence The onset is usually abrupt, and it is expressed in seconds or minutes. This is especially the case in emboli. When the mechanism is atherothrombosis, the deficit can be installed in a few hours, rarely few days. Its installation is often more fluctuating than progressive. Intracerebral hematomas can be installed in seconds and then abruptly continue to gradually get worse over a few hours.

The focal syndrome The focal syndrome is characterized by focal deficit which defines the topography of the infarct or hematoma. It locates the lesion very precisely.

The 'silent' stroke Not all strokes have clinical manifestation and some occur without the patient or his family noticing. In these cases, the accumulation of accidents and especially brain imaging can make the diagnosis.

2.2.3.2 Topographic hemispheric syndromes

An understanding of cerebral vascular territories is important in understanding stroke. All hemispheric arteries have branches that divide a cortical territory from a deep territory. The territories that are at the junction of deep and

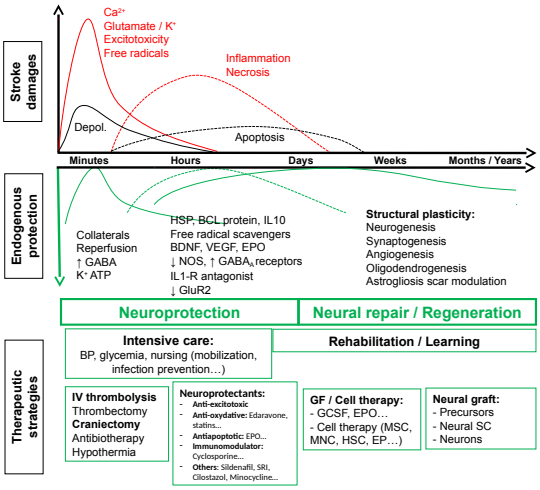

Figure 2.9: Time course of stroke and associated therapeutic time-windows. BCL: B-cell lymphoma protein; BDNF: brain derived neurotrophic factor; BP: blood pressure; Depol.: peri-infarct depolarisation; EP: endothelial progenitors (CD34+); EPO: erythropoietin; GCSF: granulocyte-colony stimulating factor; GF: growth factors; GluR2: glutamate receptor (subunit 2); HSC: hematopoietic stem cells (CD34+); HSP: heat-shock protein; IL: interleukin; IP3: inositol tri-phosphate; IV: intravenous; MNC: mononuclear cells; MSC: mesenchymal stromal/stem cells; NOS: NO synthase; SRI: serotonin reuptake inhibitors; VEGF: vascular endothelial growth factor. Image reproduced from [Detante et al., 2014].

superficial territories as well as those at the junction between the superficial arterial territories are very sensitive to overall decreases in perfusion pressure. Arterial territories are represented in Fig. 2.10.

The clinical picture that results from an occlusion of any one artery differs in minor ways from one patient to another, but there is sufficient uniformity to justify the assignment of a typical syndrome to each of the major cerebral arteries and their branches and their identification by neurological examination. Thus, the clinical picture depends on the site of arterial occlusion and extent of brain damage.

Anterior cerebral artery (ACA)

This artery, through its cortical branches, supplies the anterior three-quarters of the medial surface of the frontal lobe.This artery covers 3/4 of the anterior frontal pole (cortical territory) and the greater part of the inner face of the hemispheres. Deep branches supply the anterior limb of the internal capsule,

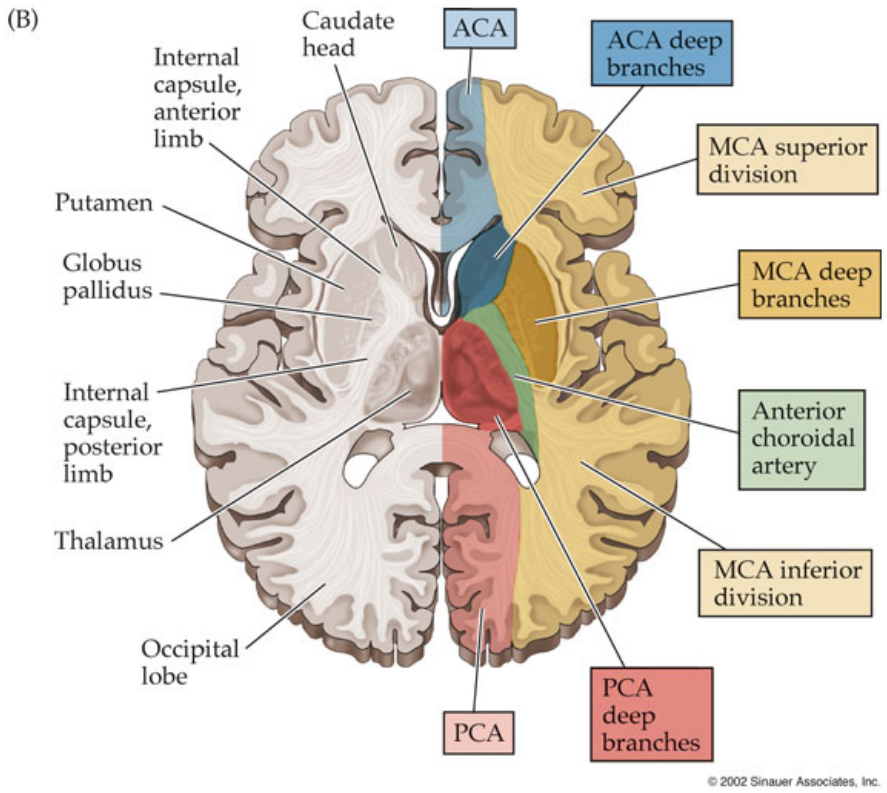

Figure 2.10: Cerebral Arterial Territories: Anterior Cerebral Artery (ACA), Middle Cerebral Artery (MCA), Posterior Cerebral Artery (PCA) and Anterior choroidal Artery (AchA) [Blumenfeld, 2010].

the inferior part of the head of the caudate nucleus, and the anterior part of the globus pallidus.

Infarctions in the ACA's territory are manifested mainly by cognitive deficits. The more severe are observed when the two anterior cerebral arteries are occluded. Clinical picture presents paraplegia, sphincter incontinence, often a very important slowness of intellectual, lack of initiative, aphasia, reasoning disorders, inability to anticipate, troubles making choices, personality disorders, unstable emotions, mood disorders (depression). The head and eyes can be deviated on the lesion's side.

Middle cerebral artery (MCA)

The middle cerebral artery (MCA) artery has superficial and deep hemispheral branches that supply the largest portion of the cerebral hemisphere. Through

its cortical branches, it supplies the lateral (convexity) part of the cerebral hemisphere (see Fig. 2.10) encompassing: (1) the cortex and white matter of the lateral and inferior parts of the frontal lobe - including motor areas 4 and 6, contraversive centers for lateral gaze and the motor speech area of Broca (dominant hemisphere); (2) the cortex and white matter of the parietal lobe, including the primary and secondary sensory cortices and the angular and supramarginal gyri; and (3) the superior parts of the temporal lobe and insula, including the receptive language area of Wernicke. The deep penetrating or lenticulostriate branches of the MCA supply the putamen, a large part of the head and body of the caudate nucleus, the outer globus pallidus, the posterior limb of the internal capsule, and the corona radiata. The MCA may be occluded in its proximal longitudinal portion, or the stem that is proximal to its bifurcation (the term M1 is used by radiologists to denote this portion of the vessel). An occlusion at this site blocks the flow in the small deep penetrating vessels as well as in superficial cortical branches. An occlusion at the distal end of the stem blocks only the orifices of the divisions of the artery in the sylvian sulcus but leaves unaffected the deep penetrating vessels.

MCA stem occlusion syndrome The clinical picture is particularly severe: contralateral hemiplegia (face, upper limb, lower limb), hemianaesthesia contralateral (same topography as motor weakness), homonymous lateral hemianopia, head and eyes deviation on the side of the lesion, cognitive impairment (global aphasia, multimodal neglect syndrome). The prognosis is poor in the absence of early unblocking, with up to 40% of deaths due to the severity of the neurological impairment, and very disabling sequelae for survivors.

Striato capsular infarction Patients have a degree of hemiparesis and, depending on the extent of the lesion within basal ganglia, may have moderate aphasia or hemineglect.

superficial MCA infarction This type of cerebral infarction includes a degree of sensorimotor impairment often associated with cognitive impairment, aphasia or multimodal neglect of moderate to severe intensity. There is usually a superior quadrantanopia or hemianopia. Frequently, regardless of the side of the obstruction, other cognitive deficits are observed. In particular, impairment of executive functions and especially the working memory. With right-sided ones, a left visual neglect is common. With left-sided lesions there is initially a global aphasia, which changes to a predominantly nonfluent (Broca) aphasia, with the emergence of an effortful, hesitant, grammatically simplified, and dysmelodic speech. When the infarction occurs in the lower branch of the MCA, the Wernicke's aphasia is the characteristic damage of the dominant hemisphere. Partial language deficits are observed in lesions of smaller size.

Anterior choroidal artery (AchA)

The anterior choroidal artery (AchA) originates from the internal carotid artery. It supplies the internal segment of the globus pallidus and posterior limb of the internal capsule and several contiguous structures including (in most patients) the optic tract (deep territory) and the hippocampus (superficial territory). The typical clinical picture is hemiplegia, hemi-hypoesthesia, homonymous hemianopia, and neglect, with well-preserved language and cognition. With right-sided lesions, there may be a left spatial neglect and constructional apraxia; slight disorders of speech and language may accompany left-sided lesions. However, there is no uniform syndrome attributable to occlusion of the AchA and in most cases its territory of supply is overlapped by small surrounding vessels, leading to pure motor hemiplegia and sometimes, to ataxic hemiparesis.

Posterior cerebral artery (PCA)

Both posterior cerebral arteries are formed by the bifurcation of the basilar artery and thin posterior communicating arteries join this system to the internal carotid arteries. The superficial PCA territory includes the inferomedial part of the temporal lobe and the medial occipital lobe, including the lingula, cuneus, precuneus, and visual Brodmann areas 17, 18, and 19. The deep branches supply the inferior, medial, and anterior parts of the thalamus (thalamoperforate branches), the geniculate body and the central and posterior parts of the thalamus (thalamogeniculate branches), lateral part of the cerebral peduncle, lateral tegmentum and corpora quadrigemina, and pineal gland (medial branches), and the posterosuperior thalamus, choroid plexus, posterior parts of the hippocampus, and decussation of deep white matter fornices (posterior choroidal branches) [Ropper et al., 2014].

Depending upon the location and severity of the occlusion, signs and symptoms may vary within the population affected by an occlusion of PCA. Lesions in the superficial territory can result in complications such as visual deficits, dyslexia, color naming and discrimination problems, memory defect, topographic disorientation.

Occlusions of the branches of the PCA that supply the thalamus can result, among others, in spontaneous pain, somatosensory impairments, and involuntary movements.

The brainstem and cerebellum are supplied by the basilar artery formed by the convergence of the two vertebral arteries, and their branches including the three cerebellar arteries. Vertebrobasilar infarcts often have very diverse clinical manifestations, because the lesions can be arranged on different levels of the brain stem.

2.2.4 Treatment for stroke rehabilitation

While preventive approaches are effective in reducing stroke mortality and incidence, current treatment of ischemic stroke is effective but limited to the acute

period. Improved subacute stroke care is essentially due to stroke units effect, physiotherapy and rehabilitation. Most hemiplegic patients regain the ability to walk to some extent, usually within a 3- to 6-month period, and this should be a primary aim in rehabilitation. The presence of deep sensory loss or anosognosia in addition to hemiplegia are the main limiting factors. Some degree of cognitive dysfunctioning is almost constant at the subacute stage of stroke [Jaillard et al., 2009], and remains frequently observed at the chronic stage in association with social dysfunctioning [Hommel et al., 2009] and depression [Hommel et al., 2015]. In total, more than half of the patients are left with sensorimotor and cognitive disabilities, resulting in additional burden to health care, in terms of social, handicap and financial costs [Gustavsson et al., 2010].

Non invasive brain stimulation including transcranial magnetic stimulation (TMS) and transcranial direct current stimulation (tDCS), has been used to investigate brain plasticity changes resulting from stroke as well as language [Dammekens et al., 2014] and motor function improvement [Hoyer and Celnik, 2011], but its safety and efficacy remains to be demonstrated.

Stem cells based therapy

Recent progress in the field of stem cell research offers attractive strategies to enhance functional outcome after stroke. In particular, mesenchymal stem cells are shown to be beneficial in experimental stroke models by acting through brain own repair mechanisms such as neurogenesis, synaptogenesis, angiogenesis and immunomodulation. The major advantage of such regenerative therapies is the extended therapeutic time window up to several weeks or months after the initial insult. This makes the treatment available to a much larger number of stroke patients.

It is well-known that stroke effects are not limited to neurons but involve glial and endothelial cells and the surrounding extracellular matrix in a "glio-neurovascular niche" that interacts with the peripheral immune system. Stem cells have the potential to develop into many different cell types in the body during early life and growth. In many tissues, they serve as an internal repair system, dividing without limit to replenish other cells as long as the person (or animal) is still alive. When a stem cell divides, each new cell has the potential either to remain a stem cell or become another type of cell with a more specialized function, such as a muscle cell, red blood cell, or brain cell [Gutiérrez-Fernández et al., 2013].

The functional benefits of cell therapy on stroke recovery are well established in animal [Lees et al., 2012, Gutiérrez-Fernández et al., 2013], but are still under evaluation in humans.

Clinical Trials in CHU Grenoble

The CHU Grenoble leads two clinical trials related to stem cells treatment of stroke. The first one, "Intravenous Stem Cells After Ischemic Stroke" (ISIS,

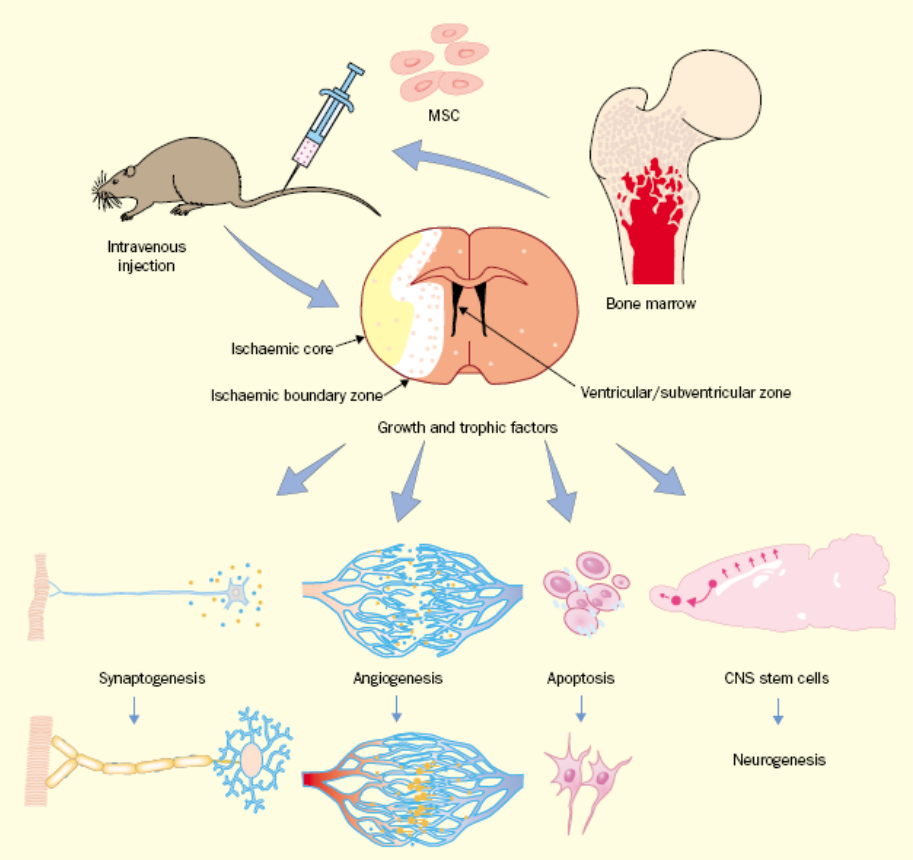

Figure 2.11: Illustration of the experimental work supporting the potential application of MSC to the treatment of stroke. Bone marrow is extracted from the animal or human being and the MSC are separated and cultured for three to five passages. They are then injected intravenously into the animal with neural injury and migrate selectively to injured tissue and localise to the boundary zone of the lesion. Image reproduced from [Chopp and Li, 2002].

PHRC 2007)[1] tried to evaluate the feasibility and tolerance of the intravenous injection of autologous mesenchymal stem cells for patients presenting an ischemic stroke (less than 6 weeks). The randomized trial included 31 patients with a 2-year follow-up period. An ancillary MRI study, HERMES (HEuristic value of multimodal MRI to assess MEsenchymal stem cell therapy in Stroke, PHRC 2010), explored the mechanisms of recovery associated to multimodal MRI changes. The patients data used in this PhD thesis were collected in this

[1] https://clinicaltrials.gov/ct2/show/NCT00875654?term=ISIS+stroke+stem+cells&rank=1

project.

A new multicentre clinical trial, "REgenerative Stem cell therapy for STroke in Europe" (RESSTORE)[2], is sponsored by CHU Grenoble in the context of an european multisite project HORIZON 2020.

Its clinical objective is to provide essential information on the therapeutic efficacy of intravenous delivery of allogenic adipose tissue derived mesenchymal stem/stromal cells in 400 stroke patients.

[2] http://www.resstore.eu/

Chapter 3

Magnetic resonance imaging (MRI): from acquisition to preprocessing

3.1 Introduction

Magnetic resonance imaging (MRI) is a non-invasive medical imaging technique extensively used in radiology for the diagnosis of several diseases. MRI scanners use magnetic fields and radio waves to excite and register the relaxation of hydrogen nuclei (single protons) mainly contained in water molecules (Fig. 3.1). This way, it is possible to explore the internal body without exposure to ionizing radiation.

All MR images are produced using pulse sequences that contains radiofrequency (RF) pulses (for excitation) and gradients of magnetic field (for image formation) of carefully controlled durations and timings [McRobbie et al., 2007]. These images show high resolution anatomic details and allows to separate different soft tissues based on their different relaxation properties [Gore, 2003].

The spatial resolution of the MRI images is defined by the size of the imaging voxels. The size of the voxel and therefore the resolution depends on the matrix size, the field-of-view (FOV), and the slice thickness, that depend on the gradients strength. Nowadays, in structural MRI, the voxel size is usually around 1 mm^3. A single voxel in a MRI scan typically contains on the order of one million neurons and tens of billions of synapses [Huettel et al., 2014] (the actual number depending on voxel size and the area of the brain being imaged). MRI scans are acquired in slices.

There are two main types of information provided by brain MRI and used in this work: structural MRI and functional MRI.

Figure 3.1: The Philips Achieva 3.0T TX scanner of the MRI research facility at Grenoble University Hospital (IRMaGe CHU Grenoble).

3.2 Structural MRI

Structural MRI is used to study the anatomy and pathology of the brain describing the shape, size and integrity of its inner structures. There are multiple techniques to map the structures of the brain. Depending on the imaging technique used, specific features of anatomical structures will be emphasized, allowing to differentiate brain tissues or determine which structures are abnormal.

In MRI, some important intrinsic properties are the proton density and two characteristic times called spin-lattice relaxation time and spin-spin relaxation time, T_1 and T_2 respectively. Proton density is related to the number of hydrogen atoms in a particular volume, and relaxation times describe how long the protons of each tissue takes to get back to equilibrium after a RF pulse [McRobbie et al., 2007].

It is all a matter of contrast. Image contrast is a function of differences in tissue properties. By modifying MRI sequence parameters such as TR and TE, for example, structural MRI can emphasize the contrast between gray matter (GM) and white matter (WM) (such as in T_1-weighted inversion-recovery sequence) or between brain tissue and cerebrospinal fluid (CSF) (e.g., T_2-weighted spin-echo sequence).Fluid-attenuated inversion recovery (FLAIR) is a technique that uses a 180° inversion pulse to suppress the CSF signal from the image. As the CSF signal is completely suppressed for cortical or periventricular areas, lesions that are adjacent to spinal fluid become much more hyperintense compared with conventional T_2 imaging [Brant-Zawadzki et al., 1996]. This type of image is of particular interest in acute stroke patients. See Fig. 3.2 for an example of these techniques in a stroke patient.

There are many other structural MRI techniques depending on the particular properties or structures in study, such as angiography, diffusion imaging and susceptibility imaging among others. See McRobbie et al. [2007] for a description.

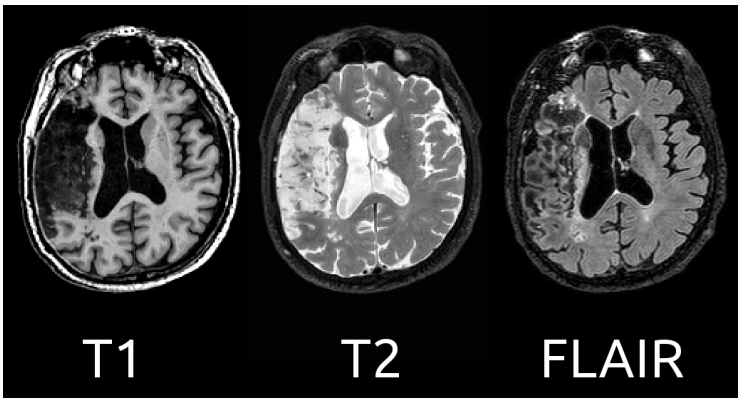

Figure 3.2: Illustration of different structural MRI images of a stroke patient. On the left, T_1-weighted acquisition provides good contrast between gray matter (dark gray) and white matter (lighter gray) tissues, while CSF is void of signal (black). On the middle, T_2-weighted acquisition provides good contrast between CSF (bright) and brain tissue (dark). On the right, FLAIR acquisition offers a more detailed view of the stroke lesion. Courtesy of Dr. Jaillard (CHU Grenoble).

3.3 Functional magnetic resonance imaging (fMRI)

Over a century ago, Roy and Sherrington [1890] observed that cerebral blood flow and neural activity were coupled, so when an area of the brain is active, the blood flow that reaches that area is also increased. This is based on the principle that local fluctuations in neural activity are linked to changes in oxygenated and deoxygenated concentrations of hemoglobin. When neural activity in a brain region increases, more oxygen and glucose are required. These resources are provided by an increased oxygen availability in the arterial component of the vascular system, resulting in a higher concentration of oxygenated hemoglobin in the venus component of that particular brain area soon after its activation. This phenomenon is known as the haemodynamic response (see Fig. 3.3).

Due to the fact that oxygenated and deoxygenated hemoglobin present different magnetic properties, MRI can detect activity related fluctuations in the oxygen proportion between oxygenated and deoxygenated hemoglobin. In the case of fMRI, the MRI signal is measured using sequences sensitive to T_2* (gradient echo)[1]. An increased neuronal activity in a brain region, will increase the blood oxygen concentration in the adjacent capillaries and locally reduce the

[1] T_2* relaxation refers to decay of transverse magnetization caused by a combination of spin-spin relaxation and magnetic field inhomogeneity. T_2* can be considered as the observed T_2, whereas T_2 can be considered as the true T_2 of the tissue being imaged. T_2* is always less than or equal to T_2. Their relation can be written as: $1/T_{2*} = 1/T_2 + 1/T_{2i}$, where $1/T_{2i}$ is the relaxation rate contribution attributable to field inhomogeneities across a voxel i.

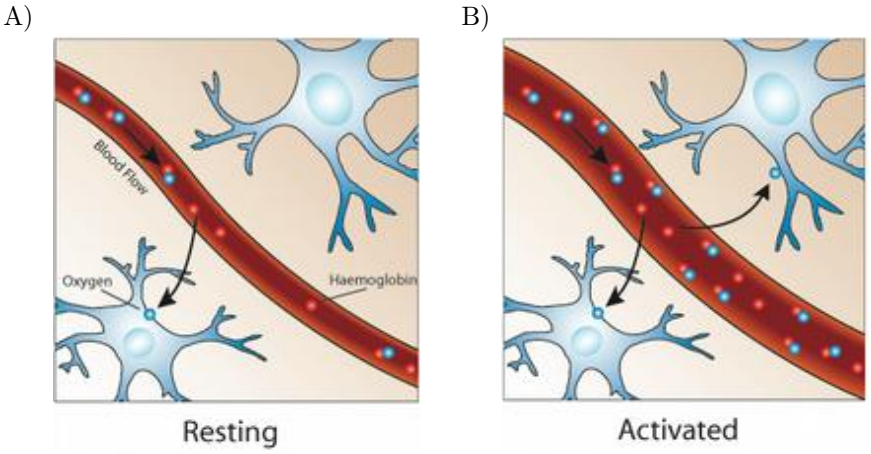

Figure 3.3: Illustration of the haemodynamic response. A) When a neuron is activated, it consumes oxygen from the blood stream, leading to an increase in the concentration of deoxy-hemoglobin in the blood. After the onset of neuron activity, the active neurons consume the oxygen available in the local blood stream and thus the relative level of deoxy-hemoglobin increases more.B) After this initial increase in deoxy-hemoglobin concentration, local blood flow increases in response to neuronal activity, providing a large amount of oxygen-rich blood, more than the required amount to preserve oxygen consumption due to neural activity. This results in local decrease in the concentration of deoxy-hemoglobin in the vessel with respect to A).

magnetic field inhomogeneities. Less inhomogeneities leads to increased T_2*-weighted signal. This is refered to as **the blood oxygen level-dependent (BOLD)** signal, discovered by Ogawa et al. [1990].

By using fast-acquiring MRI methods such as EPI (EchoPlanar Imaging) sequence, gradient-echo images of the brain can be acquired in few seconds (2 or 3 s) with reasonable spatial resolution (around 2 mm). By capturing multiple brain images during several minutes, it is possible to display BOLD signal fluctuations over time. In order to control the changes in brain state, different stimuli or tasks are used, such as images, sounds or finger movements, for example. By controlling the exact moment that the stimulus/task is applied, it is possible to study the brain regions associated with that particular stimulus/task [Huettel et al., 2014, Ferreira and Busatto, 2013]. In Fig. 3.4 an example of BOLD signal is shown. Fox et al. [2005] studied the primary visual cortex during a simple task paradigm that requires subjects to open and close their eyes.

Even if fMRI does not provide a direct measure of neural activity, it is a non invasive technique that can be applied over the whole brain (including cerebellum). It is highly used in research but also with clinical purposes.

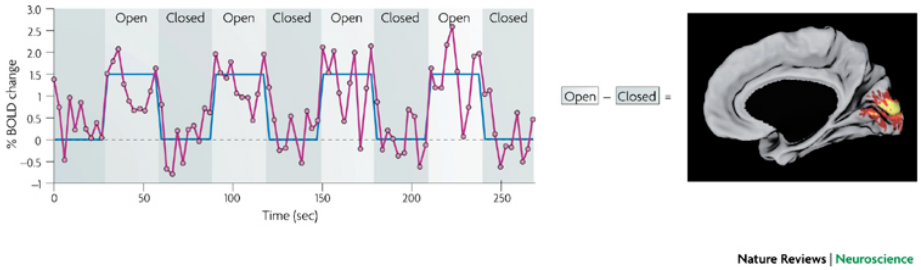

Figure 3.4: Unaveraged blood oxygen level dependent (BOLD) time course (magenta) from a region in the primary visual cortex during a simple task paradigm that requires subjects to open and close their eyes. The paradigm is shown in blue (delayed to account for the haemodynamic response). Traditional functional magnetic resonance imaging (fMRI) analysis involves correlating BOLD data with a stimulation time-course across multiple blocks. Statistical tests are performed to test at voxel level if there is an effect related to stimulus, highlighting regions that are modulated by the task paradigm. In this case, contrasting the eyes-closed condition from the eyes-open condition identifies a BOLD signal intensity difference in the primary visual cortex (shown on the right). Reproduced with permission from Fox et al. [2005].

3.4 Resting state fMRI

A particular case of fMRI is the so-called resting state fMRI (rs-fMRI). It uses the same technique of fMRI but measuring the changes of BOLD signal without applying any controlled stimuli neither task. It is based on the principle that the brain at rest is not idle, quite the contrary it presents strong and persistent functional activity [Buckner et al., 2008]. Such activity presents a particular property: it is composed of spontaneous low-frequency fluctuations (< 0.1 Hz) of BOLD signal [Van Dijk et al., 2010]. An example of such a time course during rs-fMRI of a region in the brain is shown in Fig. 3.5 with its typical frequency content.

If two brain regions have a similar activation pattern, they are highly correlated. They are considered to have a common functional role. The correlation across different voxel/regions is a manifestation of functional connectivity of the brain [Biswal et al., 1995]. The investigation of these spontaneous functional connectivity is the field of research of rs-fMRI. A detailed explanation of the methods to investigate functional connectivity is given in the next section.

3.4.1 Acquisition of rs-fMRI data

There are several parameters that need to be fixed before acquiring the functional images. The resolution of functional images is lower than the structural ones, usually voxel size is between 2 and 4 mm^3. Typical values for a 3D volume of 36 slices of 3.5 mm thick are TE = 30 ms and TR = 2 s for a 3 Tesla scan-

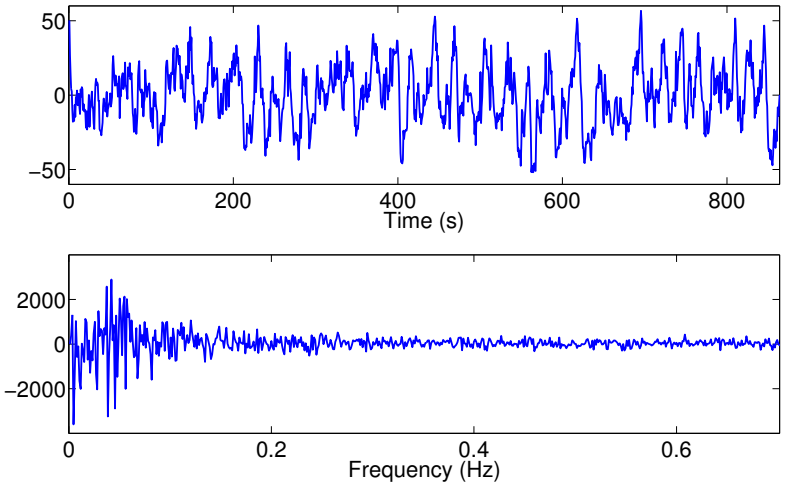

Figure 3.5: Example of spontaneous blood oxygen level dependent (BOLD) activity recorded during resting fixation and extracted from the left precentral gyrus of a healthy volunteer (TR=0.72s and 1200 EPI volumes acquired). Above, time course in the temporal domain. Below, real part of the same area in the frequency domain after Fourier discrete transformation.

ner. A typical duration for a whole brain volume is about 2s. Nowadays, there exist multiband acquisition systems that permit to lower the image acquistion duration to 0.72s, as it is performed in the human Connectome Project.

When introduced in the scanner for a rs-fMRI, subjects are required to let their mind wandering and not to fall asleep. Sometimes, they are required to close their eyes or to fix them on a projected white cross-hair on a dark gray background. This fact can influence the results, as shown in Xu et al. [2014b], where they found a different pattern of reorganization of the functional network in the eye-opened state compared to the eye-closed state with decreased or increased efficiency at the brain regions related to the visual network (among others).

3.4.2 Preprocessing of structural and rs-fMRI data

There are several factors that make complex the analysis of rs-fMRI data [Poldrack et al., 2011]. Among them, the major factor are related to i) the dimensionality of the data, which is very large; ii) the acquisition of the images, that is vulnerable to artifacts such as head movements or distortions due to inhomogeneities in the magnetic field; iii) the acquired data vary among different subjects and across time within subjects. This is the reason why, before analyzing rs-fMRI connectivity, multiple considerations and preprocessing steps have to be followed to "clean" the data.

The brain is an organ always functioning. These functions are based on

neuronal activity located in the GM. In order to further explore these functions, the analysis needs to be within the GM and the GM need to be isolated. This is done through preprocessing of structural images.

Bias field correction

Structural MRI acquisitions often present slow variations of intensity across the image due to magnetic field heterogeneities rather than anatomical differences. These variations also can be produced by inhomogeneities in the field coils used in the scanner or by magnetic susceptibility changes at the boundaries between anatomical tissue and air [Sled and Pike, 1998]. This can result in WM in one part of the image having the same intensity as GM measurements elsewhere. This effect is usually not noticeable in functional MRI, but in structural MRI, if this artifact is not corrected, it can cause problems with tissue segmentation, which often assumes that the image intensities of a given type of tissue are relatively uniform throughout the image.

There are several methods to perform bias field correction, but they can be divided into two different approaches. The first one consists in removing low spatial frequency signal from the image by filtering out low pass frequencies. The second approach combines bias field correction with tissue segmentation. It is a more complex method that models the different classes of tissue and attempts to equalize the distributions of intensities of the tissue classes across different subparts of the brain, considering local information contained in the image. This latter approach outperforms methods based on global filtering [Poldrack et al., 2011].

Tissue segmentation

Depending on the analysis, it is often required to segment the brain in different tissues as GM, WM and CSF. It is challenging to obtain an accurate brain segmentation because images are noisy, there are many voxels that contain a mixture of different tissues in varying proportions and as mentioned before, there could be some intensity variations [Poldrack et al., 2011]. See Fig. 3.6 for an example of segmentation of a T_1-weighted image into 6 different classes.

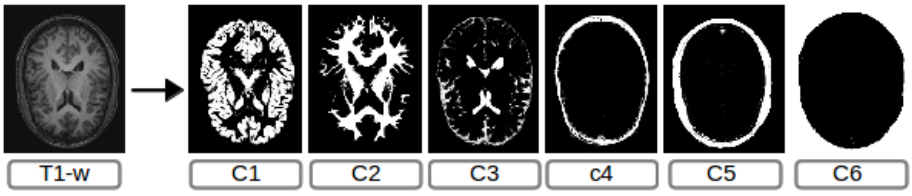

Figure 3.6: T_1-weighted segmentation into 6 different classes. In order, gray matter (C1), white matter (C2), cerebrospinal fluid (C3), skull (C4), non brain (C5) and air (C6). This segmentation was performed using the unified segmentation algorithm developed by Ashburner and Friston [2005].

There are multiple methods to segment brain MRI. They can be grouped as: manual segmentation, intensity based methods, atlas based methods, surface based methods and hybrid segmentation methods. See Despotović et al. [2015], for a review. In this work we used a hybrid segmentation method, named "Unified segmentation" [Ashburner and Friston, 2005], that combines image registration, tissue classification with priors, and bias correction within the same generative model.

Image registration

When registering images, we are determining a geometric transformation which aligns one image to fit another (for instance, a reference template). These geometric transformations can be linear (affine) or non-linear. Affine transformation usually include translation, rotation, scaling steps (among others), that is global transformations that cannot model local geometric differences between the images. Contrary, non linear registration allow elastic or nonrigid transformations, to locally warp the target image to align with the reference.

There are multiple functions already available to perform these linear and non-linear image registration, such freely available softwares bing included in SPM or FSL, among others.

Quality control

It is important to be sure that the data are not corrupted by artifacts. It is recommended to keep a close eye on both the raw and the processed data at each step to ensure their quality [Poldrack et al., 2011]. In this thesis, we controlled the quality of the data by visual inspection (using FSLview[2] movie mode). We also used ART toolbox[3] to detect large signal variations and large motion in the images.

Motion correction

The acquisition of rs-fMRI data last during several minutes and some head movements, even if they are minimal, are expected. These movements have a big impact in the data if they are not corrected [Murphy et al., 2013, Power et al., 2015]. Multiple steps at different stages of the data preprocessing can be applied in order to reduce the influence of these head movements. The first one is known as realignment or motion correction, where successive image volumes in the time series are co-registered to a reference volume. It uses a rigid body transformation that assumes that the size and shape of the volumes that will be co-registered are identical. This way, one volume can be realigned to other volume by combining rotation and translation transformation, without change of scale. This step provides time series with translation and rotation movements.

[2] http://fsl.fmrib.ox.ac.uk/fsl/fslview/

[3] https://www.nitrc.org/projects/artifact_detect/

Slice time correction

Functional MRI data are collected using 2D MRI acquisition sequences so that volumes are acquired one slice at a time. This means that data in different parts of the brain are acquired at different times, with these differences ranging from 0 to TRs. Slices can be acquired in ascending or descending order, or using an interleaved acquisition method (e.g. first the odd slices and second the even slices). The most common approach to resolve this problem is to choose a reference slice (often the first or the middle one) and interpolate the signal of each slice to match the timing of the reference slice [Poldrack et al., 2011].

Spatial normalization

In order to be able to compare brain activation patterns across several individuals, all the brains in the study must be aligned with one another. However, each individual brain has its own size and shape, with a large variability among them. The usual way to deal with this problem is to register them to a common template, i.e. Montreal Neurological Institute (MNI152) reference template [Fonov et al., 2009] or a specific template built from the data in the study. There are multiple ways to perform it. In this work, we first coregister the anatomical data to the fMRI data. Then, the anatomical data are registered to the reference template. The transformation matrix obtained is applied to the fMRI data to normalize the fMRI data to the same reference template.

Spatial smoothing

It consists on blurring the data intentionally, by applying a spatial filter to remove high frequency information, with the aim at reducing the noise and increasing the signal to noise ratio (SNR) [Poldrack et al., 2011]. It is a controversial step because it creates spatial correlations even between regions which are different, and depending on the analysis that will be performed, it is recommended or not. An alternative way to increase the SNR without blurring the images is to average the voxels that belong to the same region. This is what is done in this work.

Voxel- or region-based analysis

Analysis can be performed in two ways, voxel-based or region-based analysis. The former studies the correlation between each pair of voxels, implying a high computational cost and also difficult to face from the statistical point of view [Abraham, 2015]. The latter, region-based analysis implies the parcellation of the brain into regions. In the next subsection, "time series extraction", I detail the particular issues of this approach.

In Fig.3.7, we show the pipeline we applied to preprocess the healthy subjects database.

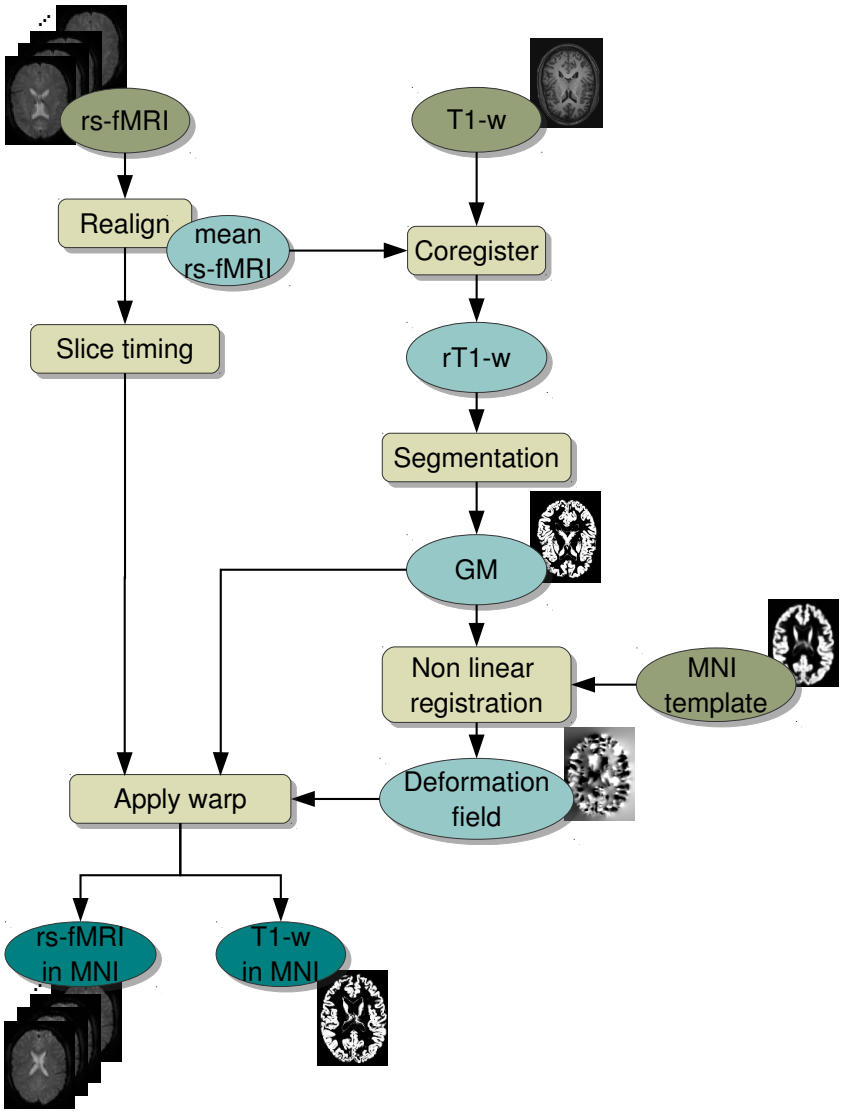

Figure 3.7: Preprocessing steps followed to obtain the GM and the rs-fMRI data of one subject registered to MNI152 standard space.

3.4.3 Time series extraction

The time series obtained from the rs-fMRI data indicate the evolution along time of each voxel/region of the brain. In order to obtain 'clean-up' time series,

several confounding factors need to be removed.

Confound removal

Rs-fMRI signal relies on the temporal correlation of signal changes between different parts of the brain. Any non-neural activity related process that affects this signal may impact the measure of functional connectivity, yielding to spurious results [Murphy et al., 2013].

Potential confounds arise from head motion during the acquistion and physiological signals such as cardiac and respiratory cycles, arterial CO_2 concentration or blood pressure autoregulation.

There are two main techniques to remove confounds from resting-state BOLD time series: 1) those utilising external recordings of physiology and 2) data-based cleanup methods using the rs-fMRI data. In the former, if physiological data (e.g., heart beats and respiration) are recorded during the MRI acquisition, these data can be used to remove the physiological fluctuations from the rs-fMRI time series. This approach can considerably improve the time series, but the physiological monitoring is not always feasible. In the latter, the simplest strategy is to bandpass filter the data. This way, fluctuations outside the frequency range of interest do not affect functional connectivity measures. But there are confounds that are not removed just by filtering the data.

The motion of the participant in the scanner may bias correlations between voxels/regions in rs-fMRI. Motion correction usually consists of six motion regressors (3 translations, 3 rotations) estimated from the data by determining the amount of movement required to optimally register each brain volume to the previous volume. The motion parameters are obtained in the realignment step during the preprocessing of the rs-fMRI data. Variance related to these motion regressors can be removed from the time series using a multiple linear regression model. There are tools, such as ART toolbox[4] in Matlab or FSL motion outliers[5], that detect timepoints corrupted by large motion in an fMRI dataset. Their output is a confound matrix that can be used to completely remove the effects of these timepoints on the analysis.

Global signal regression (GSReg) removes the global mean BOLD signal computed across all voxels in the brain, assuming that any process that globally affects BOLD signals must be unrelated to neural activity and, therefore, must be a confound. Even if this GSReg was widely used in early rs-fMRI studies because it revealed a more consistent and focal pattern of functional connectivity across the brain, it has been called into question over recent years [Murphy et al., 2013]. Modelling group comparisons, Saad et al. [2012] showed that GSReg could alter local and long-range correlations, potentially extending group differences that exist only in one region to regions that show no true functional connectivity differences. Interpretation of functional connectivity results after GSReg is difficult and, therefore, this rs-fMRI cleanup method should be avoided [Murphy et al., 2013].

[4] `https://www.nitrc.org/projects/artifact_detect/`
[5] `http://fsl.fmrib.ox.ac.uk/fsl/fslwiki/FSLMotionOutliers`

As BOLD signals related to neural activity fluctuations should be predominantly present in GM, nuisance regressors derived from other areas such as CSF, WM, the sagittal sinus or the edges of the brain have also been employed.

As it will be shown in the experimental section of this thesis, we have not applied any GSReg. Instead, fMRI voxel values were weighted by the GM probability of these voxels. This weighting limits the contamination of the time series by white matter signals and cerebrospinal fluids. Doing that, we reduce the influence of the partial volume effect related to voxels that contains both GM and WM or GM and CSF. The problem of regressing out WM and CSF in the functional data is that it may remove also some GM signal. Thus, in this thesis, the mean WM and CSF signals were not regressed.

Parcellation

When doing region based functional connectivity analysis, we need to parcellate the brain into different regions. There are several options to perform this parcellation. The most common approach is to use an available atlas of the brain and use it as a mask to divide all the brains in the study into predefined regions. These predefined regions can be obtained from structural or functional information contained in the brain of a database used as a reference (different from the database of the experiment). New approaches are parcellating the brain according to both, structure and function, as in the new parcellation scheme recently published by Glasser et al. [2016]. Examples of this parcellation schemes are the AAL [Tzourio-Mazoyer et al., 2002] , Harvard-Oxford [Desikan et al., 2006], Craddock [Craddock et al., 2012], among others.

The other approach is a data-driven parcellation. According to Thirion et al. [2014], they do not reflect a pre-defined scheme of brain structures but they may represent the measurements or features of interest in a more efficient way. The most popular techniques to achive data driven parcellations are based on clustering algorithms, such as mixture models Golland et al. [2007], variations of k-means Kahnt et al. [2012], hierarchical clustering Eickhoff et al. [2011], spectral clustering Thirion et al. [2006], Craddock et al. [2012] and dense clustering Hanson et al. [2007]. Other methods such as ICA, can also be applied to obtain data-driven brain parcellations.

In this thesis, we analyse how some of this parcellation schemes influence the reliability of functional connectivity.

Filtering

Temporal filtering aims to remove or attenuate frequencies that are not of interest within the signal. As I have mentioned previously, time series extracted from rs-fMRI have to be filtered to select frequencies below 0.1Hz.

Temporal filtering usually relies on the Fourier Transform and band pass filtering is the most common technique to perform this frequency selection, usually ranging from [0.01-0.1]Hz or [0.008-0.08]Hz.

But, there are other techniques to perform this band pass filtering. Wavelet transforms perform a time-scale decomposition that partitions the total energy of a signal over a set of compactly supported basis functions, or little waves, each of which is uniquely scaled in frequency and located in time [Daubechies, 1992]. In this thesis, we applied the maximal overlap discrete wavelet transform (MODWT) to each regional mean time series and estimated the pairwise inter-regional correlations at each of the the wavelet scales [Achard et al., 2006]. Then, we select the wavelet whom frequency band is below 0.1 Hz, and perform the analysis of the rs-fMRI data at that scale.

3.4.4 Advantages and limitations of rs-fMRI

Limitations

Functional MRI does not provide a direct measure of brain functional activity. The slow fluctuations measured can be neuronal but also may reflect hemodynamic changes related to other mechanisms of physiological regulation. Heart rate variability, for example, presents rhythm between 0.003 Hz to 0.4 Hz which are related to the regulation of heart rate, blood pressure, breathing movements, thermoregulation, etc. This technique is also subject to artifacts that can be induced by the equipment, and the movements that people make inside the scanner.

The temporal resolution in fMRI is dependent on the TR of the acquisition (usually around 2 s) which is not very high taking into account that the action potential of a neuron is in the order of milliseconds. But even if the TR was lower, it is still limited by the slow spread of the BOLD signal, which lasts around 20 seconds after the stimuli presentation.

Advantages of fMRI and rs-fMRI

According to Carter et al. [2012b], there are three main advantages of rs-fMRI with respect to fMRI:

- It can be easily obtained even in severe patients that cannot participate in cognitive testing in the scanner.
- In a single scan it is possible to obtain a survey of multiple networks at once, in contrast to task fMRI in which only regions driven by the a-priori will be seen.
- Rs-fMRI measures are expected to be robust at the group level, as in most task fMRI studies, but also in single subjects.

Due to the degree of the brain damage, some stroke patients are not able to perform a task during the fMRI acquisition. This is why we consider that rs-fMRI is the ideal technique to measure the functional connectivity of patients with large lesions, such as the stroke patients studied in this thesis.

Chapter 4

Brain connectivity

4.1 Introduction to brain connectivity

As defined by Olaf Sporns in 2007: "Brain connectivity refers to a pattern of anatomical links ("anatomical connectivity"), of statistical dependencies ("functional connectivity") or of causal interactions ("effective connectivity") between distinct units within a nervous system. The units correspond to individual neurons, neuronal populations, or anatomically segregated brain regions. The connectivity pattern is formed by structural links such as synapses or fiber pathways, or it represents statistical or causal relationships measured as cross-correlations, coherence, or information flow. Neural activity, and by extension neural codes, are constrained by connectivity. Brain connectivity is thus crucial to elucidating how neurons and neural networks process information"[1].

At the macroscale level, functional connectivity (FC) can be studied with MRI with a good spatial resolution but limited temporal resolution, or with electrophysiological methods (EEG, MEG, NIRS)[2] at poor spatial resolution but high temporal resolution. Functional connectivity permits to study how activity in one region is related to activity in other regions forming a functional network in the brain. It assumes that two or more regions belong to the same functional network if their activation time-courses correlate with each other . Functional connectivity enables us to investigate:

- Brain functioning in normal condition.
- Specific contributions of brain areas to recovery of function.
- Effect of therapies on cortical reorganization
- The reasons why some patients respond to treatment and others do not.

[1] `http://www.scholarpedia.org/article/Brain_connectivity`

[2] Electroencephalography (EEG), magnetoencephalography (MEG) and near-infrared spectroscopy (NIRS).

4.2 Main brain functional connectivity techniques

In the last few years, functional connectivity has been widely used to investigate the neuronal networks in several clinical conditions such as Alzheimer's [Yong et al., 2009], Parkinson's disease [Wu et al., 2011], autism [Müller et al., 2011], epilepsy [Qiao et al., 2012], schizophrenia [Hahamy et al., 2014], and also in studies that involve normal human brain (development, aging, gender differences) [Ferreira and Busatto, 2013, Gao et al., 2016, Tian et al., 2011, Nielsen et al., 2013].

There are three main approaches to analyse functional connectivity: seed-based connectivity, independent component analysis (ICA) and graph theory.

4.2.1 Seed-based connectivity

This method is appropriate when having hypothesis on specific brain regions (few), called "seed". The method aims at providing precise and detailed look at specific functional connectivity between these areas of interest or between one region and the rest of the brain. This way, the seed is used to compute correlations with other voxels/regions of the brain. This method relies on a priori information, the hypothesis of the seed location can highly influence the results. It is not possible to explore all the brain connections with this technique. In Fig. 4.1, we show one of the first approaches that used seed-based connectivity, where Fox et al. [2005] demonstrated that regions with apparently opposing functionality were found to be negatively correlated (anticorrelated) within their spontaneous activity. They found that regions that exhibit an increased activity in response to attention demanding cognitive tasks were anticorrelated with a set of regions that usually exhibits a decrease in activity.

4.2.2 ICA

In rs-fMRI, ICA aims to separate the different brain functional networks, known as resting state networks (RSN). It is a technique to separate linearly mixed sources by decomposing a signal into independent spatial and temporal components. Thus, it is a data-driven method that does not need any apriori information. Among all the components, several relate to different noise sources (motion, scanner drift, etc). The rejection of the noise component is said to be an efficient way of denoising. The classical ICA model assumes that the source signals are not observable, statistically independent, non-Gaussian and linearly mixed. As limitations, this approach divides the brain in different networks impeding to study the brain globally, or how a particular region behaves [Beckmann and Smith, 2004, Cabral et al., 2014, Damaraju et al., 2010]. The sources of interest represent only 10% - 20% of the signal variance. For an example illustration of ICA, see Fig. 4.2.

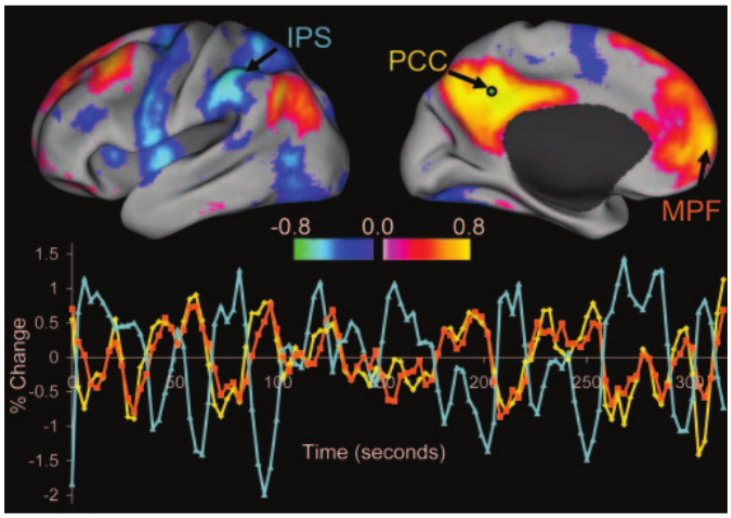

Figure 4.1: The illustration shows an example of seed based connectivity analysis in stroke done by Fox et al. [2005]. Positive nodes (warm colors) are significantly correlated with seed regions involved in attention and working memory (task-positive regions) and significantly anticorrelated with seed regions de-activated during attention-demanding cognitive tasks (task-negative seeds). Negative nodes (cold colours) are significantly correlated with task-negative seeds, and anticorrelated with task-positive seeds.

4.2.3 Graph analysis

When considering that the brain could be regarded as a network with nodes that represent different brain areas and edges representing communication pathways, the graph theory that applies to networks can be used. The communication is coded by temporal dependencies between the activity of different brain regions.

Currently, the study of the brain using graph analysis quantifies brain dysfunctions in terms of aberrant topographic features of functional brain networks [De Vico Fallani et al., 2014]. This technique allows to describe whole brain patterns and all inter-regional interactions. It is thus an approach that requires no a priori on the brain. However, this technique is dependent on the parcellation of the brain in different areas. In Fig. 4.3, we show an example of brain graph performed by Wang et al. [2010].

4.3 Brain functional connectivity in Stroke

Several studies have applied brain MRI to explore how stroke affects the brain but also how spontaneous recovery and treatment help the brain to recover. These studies involve human but also small rodent animals and non-human

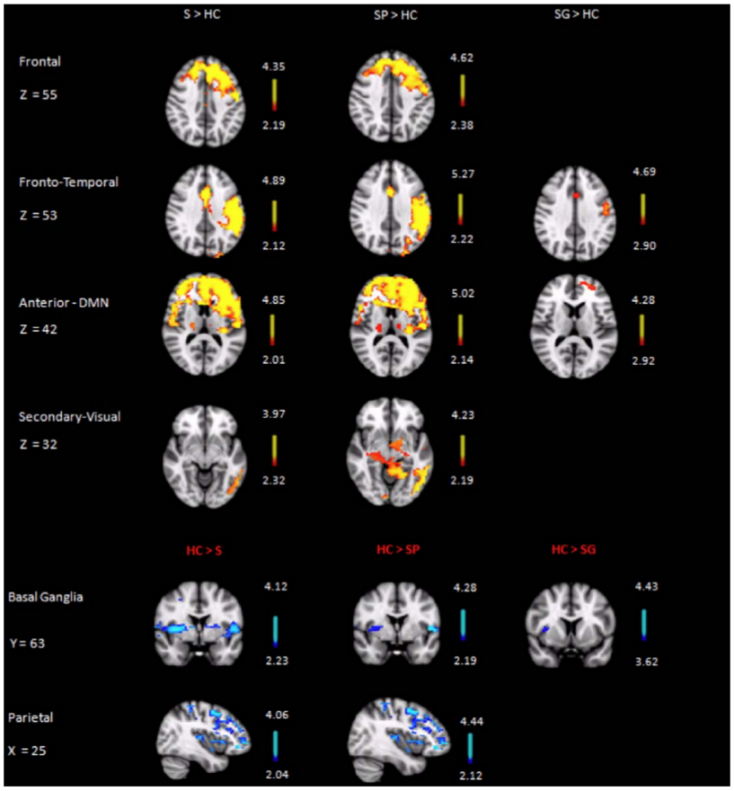

Figure 4.2: The illustration shows an example of ICA based connectivity in stroke, extracted from [Dacosta-Aguayo et al., 2014]. Axial (Frontal, Fronto-Temporal, DMN and Secondary Visual), coronal (Basal Ganglia), and sagittal (Parietal) slices showing significant between-group differences in resting activity. HC: healthy control group; S: whole stroke group; SP: stroke patients with poor cognitive recovery; SG: stroke patients with good cognitive recovery.

primates and they were developed using different MRI techniques.

Next, we review the literature of human brain functional connectivity after stroke using rs-fMRI, mainly. First, we introduce some studies that focus on the motor network, followed by studies focused on other networks. Then, approaches that study prognostic values of networks for recovery, and finally, literature dealing with therapeutic interventions. Detailed information related to the subjects and methods of these studies can be found in Tables 4.1 and 4.2.

Motor network

In Park et al. [2011], they aimed to carry out long-term follow-up of rs-fMRI in ischemic stroke patients with supratentorial lesions for delineation of the neural

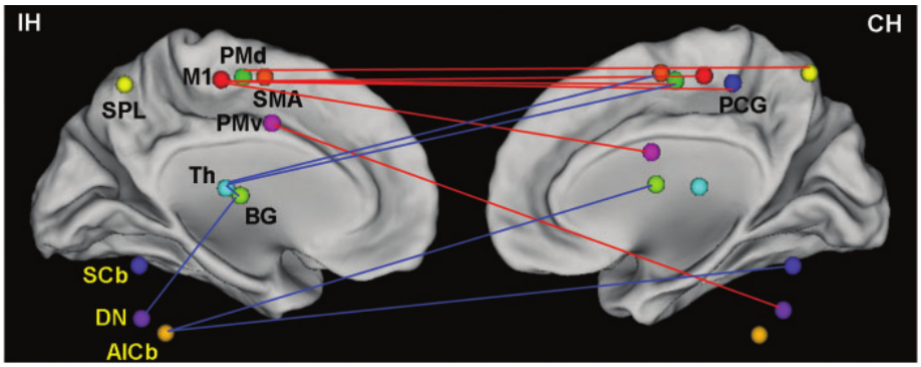

Figure 4.3: Monotonically increased and decreased functional connectivity over time. Increased connections (red lines) are mainly located between ipsilesional primary cortex area and contralesional key motor areas, whereas the decreased connections (blue lines) involve ipsilesional subcortical areas and cerebellum. Each area is displayed with a unique color and homologous areas show the same color. IH = ipsilesional hemisphere; CH = contralesional hemisphere.

substrates of motor recovery after stroke. Using a seed in the ipsilesional primary motor cortex (M1), they compared the functional connectivity of stroke patients and healthy subjects. They also investigated neural correlates associated with long-term motor recovery at 6 months after stroke. Their results demonstrated that patients had higher functional connectivity with the ipsilesional frontal and parietal cortices, bilateral thalamus, and cerebellum. Instead, functional connectivity with the contralesional M1 and occipital cortex were decreased in patients with stroke. Functional connectivity between the ipsilesional and contralesional M1 showed the most asymmetry at 1 month after onset to the ipsilesional side. Functional connectivity of the ipsilesional M1 with the contralesional thalamus, supplementary motor area (SMA), and middle frontal gyrus (MFG) at onset was positively correlated with motor recovery at 6 months after stroke.

The role of the contralesional motor cortex for motor recovery in acute stroke was studied by Rehme et al. [2011]. Using task fMRI, they measured hand movement-related neural activity 3 times during the first 2 weeks after stroke. They found that an increasing activity in contralesional M1 and premotor cortex correlated with improved functional recovery in severely affected patients, indicating early cortical reorganization supporting motor function of the affected hand.

In a recent review, Thiel and Vahdat [2015] focused on structural and rs-fMRI brain connectivity studies of motor networks after stroke. Consistent findings across studies were that the interhemispheric functional connectivity between homologous sensory and motor areas was decreased compared with controls and that it correlated with the degree of behavioral impairments in the acute stage. Higher connectivity between ipsilesional motor cortex and con-

tralesional thalamus and SMA was predictive of a better chronic motor recovery as was the progressive restoration of interhemispheric, but not intrahemispheric somatomotor connectivity. At chronic stage, decreased interhemispheric connectivity between homologous areas tends to return back to normal in patients who recovered well, whereas in poorly recovered patients, the degree of decreased interhemispheric connectivity correlates with motor function. This reduction in interhemispheric connectivity coincided with reduced structural integrity. Both, structural and functional connectivity measures, were independently correlated with clinical outcome measurements, suggesting that both measures may provide complementary information.

Volz et al. [2015] combined transcranial magnetic stimulation (TMS) and task fMRI to investigate to which degree recovery of hand function depends on corticospinal tract damage (CST) and biomarkers of cerebral plasticity in chronic stroke patients. Their main finding was that the "active motor threshold" [3] of the ipsilesional hemisphere explained the largest amount of variance in individual motor impairment in chronic stroke patients (73%), followed by reduced interhemispheric connectivity (64%) and the amount of structural CST damage (51%).

One example of the application of brain graphs in stroke was performed by Wang et al. [2010], see Fig. 4.3. The aim of this study was to identify dynamic changes in the functional organization of the motor execution network along the stroke recovery process. They selected 21 brain regions of interest (nodes) associated with the motor network finding that the functional connectivity of these regions showed consistent alterations over time. They also found that the functional connectivity measures were correlated with clinical variables suggesting an adaptive reorganization of the motor execution network in stroke patients.

The topological properties of the cortical motor-related network in response to subcortical motor pathway stroke was investigated by Yin et al. [2013]. They focus their approach in 20 ROIs remote from the primary lesion for constructing the cortical motor-related network. Focusing on graph theory, they found alterations in betweenness centrality of regions in stroke patients in contralesional supplementary motor area, dorsolateral premotor cortex, and anterior inferior cerebellum.

Inman et al. [2012] studied the association between motor performance and the effective connectivity of motor networks in stroke patients with hemiparesis in comparison to healthy volunteers. They found diminished connectivity in stroke survivors in connections from the superior parietal cortex to primary and supplementary motor cortex.

In Liu et al. [2016], they aimed to investigate the dynamic of evolutionary

[3] They assessed excitability of the corticospinal system using the "active motor threshold" (AMT) of the motor hotspot, which predominantly reflects the cortical motor output compared to the "resting motor threshold" which is also influenced by spinal and other influences The AMT was defined as the lowest stimulator intensity needed to evoke motor evoked potentials of 200 lV in five out of ten consecutive trials during mild tonic contraction of the first dorsal interosseus (FDI) muscle

patterns of functional connectivity density (FCD) and strength (FCS) after subcortical stroke involving in the motor pathways. This study included 8 right-handed male patients with first-onset subcortical infarctions in the left internal capsule and neighboring regions involving the motor pathways. They found that both FCD and FCS initially decreased in the sensorimotor regions and increased in the cognitive regions and finally returned to normal levels.

With the hypothesis that motor impairment might reflect the dual contribution of corticospinal damage and altered network functional connectivity, Carter et al. [2012a] study the connectivity between 6 core regions of the somatomotor network in subacute stroke patients. To study the relationship between corticospinal damage and resting functional connectivity or behavior, bivariate correlations were calculated. They found that corticospinal damage was negatively correlated with inter-hemispheric resting functional connectivity, in particular with connectivity between the left and right central sulcus, conluding that dysfunction of cortical functional connectivity can occur after interruption of corticospinal outflow tracts, and can contribute to impaired motor performance.

In Golestani et al. [2013], authors wanted to test if resting-state fMRI can elucidate the disruption of functional connections within hours of ischemic stroke as well as during recovery. They computed the interhemispheric connectivity of the primary and sensorimotor cortex (SM1) and seed based analysis of the ipsilesional SM1 with the rest of the brain. They found that Within hours poststroke, patients with motor deficits exhibited significantly lower connectivity than controls and patients with no motor impairment. Connectivity was reestablished after 7 days in recovered participants. After 90 days, recovered patients exhibited normal motor connectivity, but reduced connectivity with subcortical regions associated with effort and cognitive processing remained.

The hypothesis that alterations in motor transcallosal and corticospinal connections correlate with motor impairment in patients with chronic stroke was studied by Chen and Schlaug [2013]. They computed the temporal coupling in neural activity between interhemispheric motor cortex, and white matter integrity, in the transcallosal motor fibers and corticospinal tract. Within the patient group those with higher interhemispheric motor cortex connectivity and higher fractional anisotropy in the transcallosal motor fibers were less impaired.

In a pilot study, Jung et al. [2013] computed the inter-hemispheric connectivity in 8 stroke patients with severe left upper limb motor impairment. They found that inter-hemispheric connectivity score in patients with progressive motor recovery was much greater than the scores in patients with fast late-onset and poor motor recovery.

Other networks

The default mode network (DMN) was studied in stroke patients with and without post-stroke cognitive impairment (PSCI) in Ding et al. [2014]. They found that both groups of patients showed significantly decreased functional connectivity in the posterior cingulate cortex/precuneus (PCC/PCu) and increased

functional connectivity (higher in the non-PSCI group) in the medial prefrontal cortex and left hippocampus. They also found that fhe functional connectivity in the PCC/PCu was related to the MoCA score [4] measured at a 10-day follow-up, and the connectivity in the left hippocampus predicted the MoCA score measured at 3 months follow-up.

Other study aiming to identify dynamic changes in the functional organization of the DMN after stroke was performed by Dacosta-Aguayo et al. [2015]. They used probabilistic ICA, seed-based connectivity analysis, and graph based analysis to determine the functional connectivity of the DMN in a group of subacute stroke patients (at 3 months) after a right hemispheric stroke. Applying ICA, they found increased DMN activity in the left precuneus and left anterior cingulate gyrus when compared with healthy controls; with seed based analysis, had significant impairment in the connectivity between different DMN nodes; finally, with graph analysis, they found that impairment of the functional integration of the DMN was negatively associated with the size of the lesion in stroke patients, and that there were more impaired nodes in the right and left (contralesional) frontal gyrus, the PCC, the right parietal cortex, and the left parahippocampal gyrus.

Lassalle-Lagadec et al. [2012] found that a dysfunction of DMN functional connectivity involved in emotional control is associated with the severity of post-stroke depression. They used ICA to to isolate the DMN in mild to moderate stroke patients, observing that after stroke, anxiety severity was correlated with functional connectivity in the middle temporal cortex and the anterior midcingulate cortex, while at 3 months after stroke, a correlation was observed with the middle temporal cortex and the posterior cingulate cortex.

Other study dealing with the default mode connectivity in stroke patients was performed by Tuladhar et al. [2013]. ICA was conducted to identify the DMN and to compare the group differences of the DMN. ROI based analysis was performed to explore the functional connectivity between the regions of the DMN. They found sigificantly decreased functional connectivity in the left medial temporal lobe, posterior cingulate and medial prefrontal cortical areas of the DMN.

Park et al. [2014] examined longitudinal changes in the DMN during the 6 months after stroke, and investigated the relationship between DMN changes and cognitive recovery. Applying ICA and ROIs based analysis, they found that stroke patients restored most of their DMN connectivity at 3 months after stroke, and that the increased connectivity shown during recovery indicated a correlation with cognitive improvement, suggesting that reorganization plays an important role in cognitive recovery.

In Gratton et al. [2012], they used graph theory to examine the effects of lesions on the structure of large-scale functional brain networks. They included patients with focal brain lesions because of stroke, traumatic brain injury, and tumors. They study how the modularity (a measure of the integrity of network

[4] Montreal cognitive assessment (MoCA) is a test that assesses several cognitive domains such as short-term memory recall, visuospatial abilities, executive functions, language, and orientation to time and place.

organization) is affected by a focal lesion, finding that focal brain damage can have a widespread, nonlocal impact on brain network organization when the regions damaged are important for the communication between networks.

Nomura et al. [2010] test the hypothesized functional independence of the fronto-parietal (FP) and cingulo-opercular (CO) cognitive control networks in patients with heterogeneous lesions. Using graph theory, they found that anatomical damage to portions of FP and CO networks differentially engaged during different cognitive control processes specifically affects only the damaged network.

Ovadia-Caro et al. [2013] investigated the distal effects of lesions on a global level in a stroke population with heterogeneous lesions. Longitudinal rs-fMRI was analyzed using an eight-network template taken from Beckmann et al. [2005]. They applied whole-brain spatial concordance as a measure of change in the connectivity over time finding that concordance preferentially decreases in affected networks across a heterogeneous lesion population.

In Zhang et al. [2014], they tried to identify altered functional connectivity (FC) of the affective network in patients with poststroke depression (PSD) and to explore the correlation between functional connectivity and the severity of PSD. Using seed-based analysis, they computed the connectivity of the bilateral anterior cingulated cortices with the rest of the brain among the three groups, stroke patients with PSD, stroke patients without PSD, and healthy controls. They found that connectivity of the affective network was disrupted in PSD patients compared to stroke patients without depression and normal controls. Also, left inferior frontal gyrus (which indicated altered functional connectivity) was significantly correlated with depression scores in PSD patients. They conclude that dysfunction of the affective network may be one of the reasons of the development of PSD.

Changes in functional connectivity within 11 resting-state network (RSN) and between these RSNs in subcortical stroke patients who were well recovered in global motor function were studied in Wang et al. [2014]. They used ICA to extract the RSN finding that, subcortical stroke may induce connectivity changes in multiple functional networks, affecting not only the intranetwork functional connectivity within RSNs but also the internetwork FC between these RSNs.

Nair et al. [2015] investigated functional connectivity changes after stroke in the language network (23 seed regions based on a previous study) using resting-state fMRI and performance on a verbal fluency task in patients without clinically documented language deficits. They found decreased functional connectivity in the language network and verbal fluency deficits in early stroke patients without clinically documented language deficits.

Prognostic value of networks measure for recovery

Several studies in the literature have tried to link clinical scores with functional connectivity measures. Authors in Carter et al. [2010] evaluated the relationship between the performance and functional connectivity of motor and

attention networks in rs-fMRI in patients with a first ever stroke, using seed based analysis. They performed a previous task fMRI study to identify core regions of the somatomotor and attention networks. Then, they used those regions as seeds to generate voxel-wise functional connectivity maps. Separately, they also conducted behavioral measurements of spatial attention and arm function. They found that FC was significantly correlated with abnormal detection of visual stimuli in attention networks and with upper extremity impairment in the somatomotor network. Also, performance was correlated with intra- and inter-hemispheric connectivity, separately. This study demonstrated a significant association between impaired performance and disrupted interhemispheric functional connectivity. (a similar relationship was not observed for intra-hemispheric connectivity).

In Dacosta-Aguayo et al. [2014], they applied probabilistic ICA to identify resting state brain activity patterns in a group of 18 patients with focal ischemic stroke in the territories of the anterior, middle, or posterior cerebral arteries with absence of severe aphasia (8 with good cognitive recovery; 10 with poor cognitive recovery) and 18 matching healthy controls. They identified 6 brain networks with different results between groups: frontal, fronto-temporal, default mode network, secondary visual, parietal and basal ganglia. The esxtension of the networks beyong the lesion suggest a possible brain plasticity compensation. They found that patients with good recovery show normalization of these compensatory changes and also, that there is a correlation between functional connectivity changes in patients and performance on cognitive tasks (see Fig. 4.2 for an illustration of these results).

In the graph based analysis performed in Dacosta-Aguayo et al. [2015], they found that mean path length showed positive correlations with semantic fluency test, phonetic fluency test and the mini mental state examination (MMSE).

Xu et al. [2014a] investigated longitudinal changes in the resting-state functional connectivity of the contralesional primary sensorimotor cortex (CL-PSMC) and their association with motor recovery. Dynamic changes in the connecctivity of the CL-PSMC within the whole brain were evaluated and correlated with the Motricity Index (MI) scores. Compared with healthy controls, the connectivity of the CL-PSMC with the bilateral PSMC was initially decreased, then gradually increased, and finally restored to the normal level 1 year later. These dynamic changes in the inter-hemispheric connectivity between the bilateral PSMC was positively correlated with the MI scores, but the intra-hemispheric connectivity of the CL-PSMC was not correlated with the MI scores. They suggest that increased inter-hemispheric connectivity between the bilateral PSMC may facilitate motor recovery in stroke patients.

Zhu et al. [2014] combined ICA and network connectivity analysis methods to investigate the association between resting state functional connectivity and language function in aphasic patients. They found that brain lesions may influence language comprehension by altering functional connectivity between regions and that the patterns of abnormal functional connectivity may contribute to the recovery of language deficits.

How recovery of somatosensory function in the first 6 months after stroke was

associated with functional network changes was investigated by Bannister et al. [2015]. Six seeds involving somatosensory regions were selected and voxel-wise whole brain correlation analysis was performed. Patients demonstrated a wide range of severity of touch impairment 1 month post-stroke, followed by variable improvement over time. In the stroke group, at 6 months, significantly stronger inter-hemispheric functional correlations were found between somatosensory regions, and with visual and frontal areas.

New et al. [2015] examined functional connectivity within a network of regions previously hypothesized as being associated with apraxia of speech (AOS). Fifteen individuals were categorized as AOS and 17 were AOS-absent. They found that AOS patients had reduced connectivity between bilateral premotor cortex, and this reduction correlated with the severity of AOS impairment. Also, AOS patients showed negative connectivity between the left premotor and right anterior insula and this effect decreased with increasing severity of non-verbal oral apraxia.

Therapeutic intervention

Different therapeutic interventions after stroke have been studied. Methods such as transcranial magnetic stimulations (TMS), introduced in the first chapter of this thesis, or neurofeedback. Using fMRI to monitor the aspects of task-related changes in neural activation or brain connectivity, neurofeedback allows investigators to offer feedback of neural signals/patterns back to the participant on a quasireal-time basis (real time fMRI neurofeedback, rt-fMRI-NF).

Hoyer and Celnik [2011] reviewed several papers to discuss the contributions of TMS to understand how different motor areas, such as the ipsilesional hemisphere, secondary motor areas, and contralesional hemisphere are involved in motor recovery. They conclude that altogether, the reviewed studies in stroke patients suggest that using repetitive TMS (rTMS) may be an effective strategy to improve motor functional outcomes. They observed that inhibitory rTMS over the contralesional hemisphere may be a more effective method of enhancing paretic limb function, although ipsilesional stimulation is still beneficial. However, significant limitations remain and further investigation with larger sample sizes, more global motor tasks and at different stages of the recovery process (i.e., acute, subacute or chronic) are needed to make more definitive conclusions.

In a recent review, Linden and Turner [2016] explored studies were rt-fMRI-NF was applyed in healthy subjects but also in Parkinson disease and stroke victims. Even if the evidence for clinical effects of rt-fMRI-NF in neurological motor conditions is currently limited to data from small proof-of-principle studies and small randomized trials, they concluded that the preliminary evidence suggests that rt-fMRI-NF may be useful in improving clinical measures of motor impairment in stroke recovery.

Author	Total n	Mean age (years)	Stroke type	Lesion side	Symptons	# Exams	Method
Park et al., 2011	12 (5 M; 7 F)	58.4 ± 6.9	12 I	8 L, 4 R	Motor deficit	4	SBA
Volz et al., 2015	12 (9 M; 3 F)	63 ± 10	12 I	3 L, 9 R	Unilateral hand motor deficit	3	TMS & Effective connectivity
Inman et al., 2012	13 (9 M; 4 F)	59	6 I, 4 H, UN	6 L, 7 R	Motor deficit	1	Effective connectivity
Ding et al., 2014	18 (10 M; 8 F)	63.9 ± 9.2	18 I	UN	2 groups: PSCI; non-PSCI	1	ICA
Dacosta-Aguayo et al., 2015	11 (8 M; 3 F)	63.8 ± 3.6	11 I	11 R	UN	2	SBA, ICA, GBA
Liu et al., 2016	8 (8 M)	49.0 ± 5.1	UN	8 L	Lesion in the left internal capsule and neighboring regions	5	FCD & FCS
Ovadia-Caro et al., 2013	12 (8 M; 4 F)	64.2 ± 12.0	12 I	UN	UN	3	ICA
Carter et al., 2010	23 (11 M; 12 F)	59.6 ± 13.0	18 I; 5 H	11 L; 12 R	Motor deficit neglect and aphasia	1	SBA
Dacosta-Aguayo et al., 2014	18 (13 M; 5 F)	63.9 ± 8.3	18 I	3 L; 15 R	UN	1	Probabilistic ICA
Lassalle-Lagadec et al., 2012	24 (19 M; 5 F)	60.0 ± 12.3	24 I	UN	No aphasia	2	ICA
Carter et al., 2012	23 (11 M; 12 F)	59.6 ± 13.0	UN	10 L; 13 R	UN	1	ROI analysis, SBA

Tuladhar et al., 2013	20 (13 M; 7 F)	55.1 ± 12.8	20 I	11 L; 9 R	UN	1	ROI analysis, ICA
Golestani et al., 2013	31 (16 M; 15 F)	67 ± 15	31 I	17 L; 14 R	Unilateral motor weekness and/or paresthesia	3	IHC, SBA
Chen et al., 2013	11 (8 M; 3 F)	57.5 ± 9.1	11 I	8 L; 3 R	Stroke in the MCA, movement in wirst or fingers.	3	IHC
Jung et al., 2013	8 (3 M; 5 F)	59.0 ± 14.5	8 I	8 R	Severe hemiplegia	1	IHC
Xu et al., 2014	13 (13 M)	49.2 ± 7.1	13 I	8 L; 5 R	Motor deficits in upper and lower extremities.	5	IHC, SBA
Zhang et al., 2014	50 (39 M; 11 F)	58.3 ± 10.0	50 I	UN	Depression diagnosis for PSD group	1	SBA
Wang et al., 2014	25 (18 M; 7 F)	56.2 years range [42-72]	25 I	12 L; 13 R	Lesion in the internal capsule and neighboring regions, motor deficit	1	ICA
Zhu et al., 2014	13 (12 M; 1 F)	49.4 ± 10.7	10 I; 3 H	13 L	Apahsia	2	ICA, network connectivity analysis of LFPN
Park et al., 2014	11 (8 M; 3 F)	57.5 ± 8.9	7 I; 4 H	11 R	UN	3	ICA, ROIs based analysis
Bannister et al., 2015	10 (8 M; 3 F)	58.8 ± 18.4	10 I	6 L; 4 R	Impaired touch discrimination of the upper limb	2	SBA
Nair et al., 2015	26 (16 M; 10 F)	62.2 ± 7.7	26 I	UN	UN	2	SBA

New et al., 2015	32 (27 M; 5 F)	62 ± 10	UN	32 L	Difficulty with speech or language	1	SBA

Table 4.1: Demographic data and study details of stroke human brain functional connectivity approaches using rs-fMRI. F, female; FC, functional connectivity; FCD, funtional connectivity density; FCS, funtional connectivity strength; GBA, graph based analysis; H, haemorrhagic; I, ischemic; ICA, independent component analysis; IHC, inter hemispheric connectivity; L, left; LFPN, left frontoparietal network; M, male; MCA, middle cerebral artery; PSCI, post-stroke cognitive impairment; R, right; SBA, seed based analysis; TMS, transcranial magnetic stimulation; UN, undefined.

Author	**Total** n	**Mean age (years)**	**Stroke type**	**Lesion side**	**Symptons**	**# scans**	**Regions**
Wang et al., 2010	10 (9 M; 1 F)	48.7 ± 5.00	10 I	10 L	Motor deficit	5	24 regions in motor execution network
Yin et al., 2013	24 (19M; 5F)	61.04 ± 7.33	12 I, 12 H	24 L	Motor deficit	1	17 regions in motor execution network + bilateral middle frontal gyri + ipsilesional postcentral gyrus
Gratton et al., 2012	31 (Gender: UN)	60	UN	21 L 10 R	UN	1	90 regions Whole brain
Nomura et al., 2010	17 (Gender: UN)	58 ± 14	16 I; 1 H	UN	UN	1	18 regions based on previous seed

Table 4.2: Demographic data and study details of graph based human brain functional connectivity approaches using rs-fMRI. F, female; H, haemorrhagic; I, ischemic; L, left; M, male; R, right; UN, undefined.

Chapter 5

Graph theory applied to brain functional connectivity

5.1 Introduction to graph theory

A great diversity of real life applications or problems are configured as nodes and connections. They may represent a roadmap, a molecule or a galaxy distribution, for example. They are used by your GPS to find the shortest path to home, to explain the social media interaction, or how the brain works, among other applications.

Any mathematical object concerning points and connections between them could be called a graph. A graph is an abstract representation of a set of objects where some pairs of the objects are connected by links.

5.1.1 History of graphs

Some time ago, the people of Königsberg amused themselves by trying to find a walking path around their city which would cross each of their seven bridges once and only once, and return them to the same starting point, Fig. 5.1.

This problem came to the attention of Euler in 1736. He represented the walking path as a sequence of the land mass letters A, B, C, and D, as in Fig. 5.2. In modern terms, he replaced each land mass for a node, and each bridge for an edge. Euler answered that the problem had no solution, and represented the beginning of graph theory.

5.1.2 Basic concepts

Definition 1. *A **graph** G is an ordered pair, $G = (V, E)$, comprising*

- *a set V of vertices (or nodes),*
- *a set E of edges, which are 2-element subsets of V.*

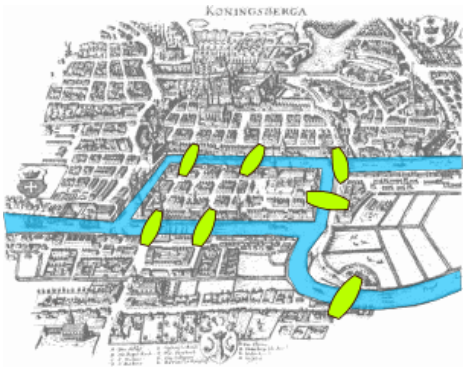

Figure 5.1: Map of Königsberg in Euler's time showing the layout of the seven bridges.

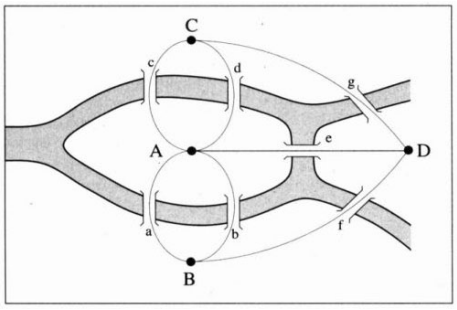

Figure 5.2: Graph with the four land masses represented by points and the seven bridges by lines which connect the points.

Definition 2. *A node $u \in V$ is **adjacent** to node $v \in V$ if they are joined by an edge.*

Definition 3. *Two adjacent nodes are called **neighbors**.*

Definition 4. *A **self-loop** (or loop) is an edge that joins a single endpoint to itself.*

In Fig. 5.3, we show an example of a graph with their respective set of nodes and edges.

5.1.3 Types of graphs

We have introduced the simplest properties of a graph. But other additional attributes allow them to serve as mathematical models for a broad variety of applications. Two common attributes are the direction and the weight of a graph (Fig. 5.4).

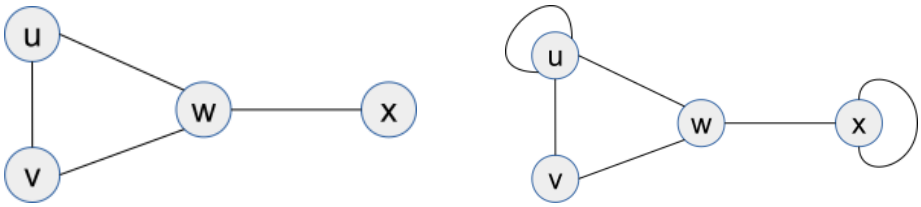

Figure 5.3: Left: Example of a simple graph $G = (V, E)$, where the set of nodes is defined as $V = \{u, v, w, x\}$ and the set of edges as $E = \{\{u, v\}, \{u, w\}, \{v, w\}, \{w, x\}\}$. Right: the same graph with loops on nodes u and x.

Definition 5. *A **directed graph** (or digraph) is a graph where the edges have a direction associated with them.*

Definition 6. *A **weighted graph** is a graph whose nodes or edges have been assigned weights (numerical values). More specifically,*

- *a **vertex-weighted** graph has weights on its nodes,*
- *a **edge-weighted** graph has weights on its edges.*

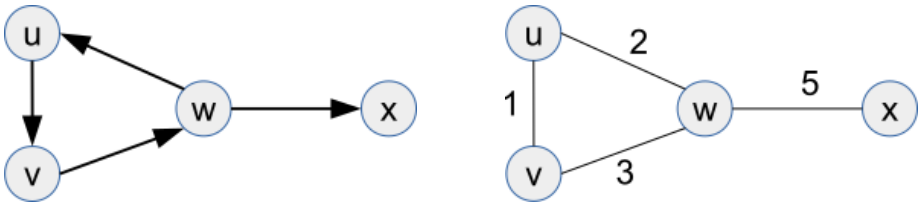

Figure 5.4: Left: Example of a directed graph and the set of edges as $E = \{\{u, v\}, \{u, w\}, \{v, w\}, \{w, x\}\}$. Right: Example of an edge-weighted graph.

Definition 7. *A **fully-connected** graph is a graph where all the nodes have at least one edge associated with them.*

Directly related to fully-connected graphs is the concept of **minimum spanning tree (MST)** [Prim, 1957, Alexander-Bloch et al., 2010]. It consists of removing, from a connected graph, as many edges as possible while all the nodes remain connected. In a graph with n nodes, the MST has $n - 1$ edges. There could be multiple MST for the same graph.

There are many other graph properties, see Gross et al. [2013] for detailed information. Along this thesis, we focus only in fully-connected, loop-less, undirected and unweighted graphs. Following definitions and explanations are related only to these type of graphs.

5.1.4 Graphs basic representation

The most basic representation of a graph is named adjacency matrix. It is a square matrix where its elements indicate if each possible pair of nodes are adjacent or not in the graph, see Fig. 5.5. In loop-less graphs, the diagonal of the adjacency matrix is full of Os. In the case of undirected graphs, this matrix is symmetric.

It is properly defined as:

Definition 8. *An **adjacency matrix** representation of a simple graph $G = (V, E)$ is a $\mid V \mid \times \mid V \mid$ matrix A, where*

- $A_{i,j} = 1$ *if there is an edge from vertex i to vertex j;*
- $A_{i,j} = 0$ *otherwise.*

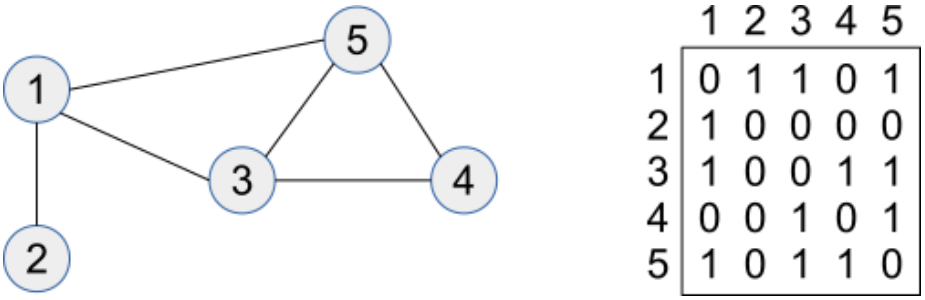

Figure 5.5: Example of an adjacency matrix representation associated to the graph shown on the left of the image.

5.1.5 Concept of cost

The **cost** (also known as density or sparsity) of a graph, is the ratio between the number of edges and all the possible edges in the graph. In the case of undirected graphs, the number of possible edges is divided by 2. In Fig. 5.6, we give a graphical example of different cost in a graph.

Definition 9. *The **cost** of an undirected graph G, C_G, with x number of nodes and y number of edges is defined as*

$$C_G = \frac{y}{x(x-1)/2}.$$

5.2 Graphs of the brain

One of the most important characteristics of the brain graphs is the small world regime [Bullmore and Sporns, 2012, Watts and Strogatz, 1998]. Brain networks

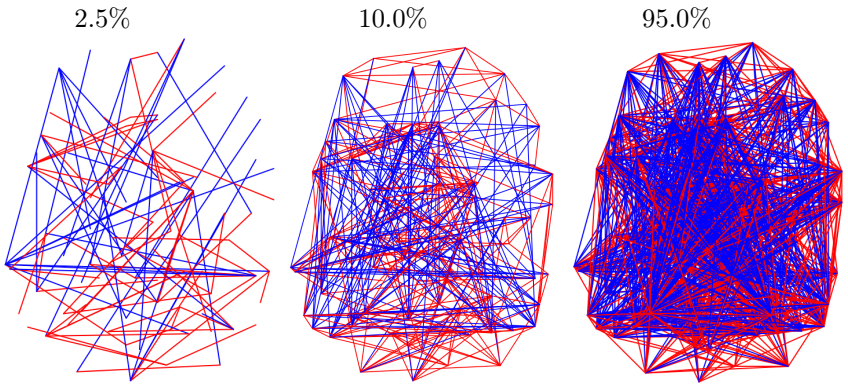

Figure 5.6: Example of different cost of a graph in the brain. On the left, there is a graph with very low cost (2.5%) and thus, very poorly connected. Contrary, on the right, there is a graph highly connected (95%) where almost all the nodes are connected between them. In the middle, there is a graph at 10% cost with a good trade-off between the number of nodes and the number of edges where we can observe some of the topology of the graph.

wired to minimize cost would have a lattice-like topology. For example (see Fig. 5.7, left panels), each node could have two nearest neighbors topologically that were also its closest neighbors spatially. However, this topology does not favor global integration of information processing because there are not enough direct connections between regions that are physically far apart.

Brain network efficiency would be maximized by a random topology where each node is expected on average to connect to any two other nodes (see Fig. 5.7, right panels). But, this topology results in a high wiring cost due to the large number of long-distance connections. Human brain networks appear to be between these two extreme cases (see Fig. 5.7, middle panels): there are clusters of short-distance connections between spatially neighboring nodes (lattice-like), also including high-cost components, such as long-distance short-cuts between connector hubs in different modules and different anatomical regions.

Topologically direct connections between spatially remote brain regions will increase the efficiency of information processing. Brain networks can therefore be said to negotiate an economical trade-off between minimizing physical connection cost and maximizing topological value.

5.3 Brain graphs computation

The computation of graph based brain functional connectivity requires several steps that have to be applied to each participant separately. These steps consist on the preprocessing of the acquired MRI images, the parcellation of the brain in several brain regions to extract the time series that contain the functional activity of each region of the brain, the computation of a brain connectivity

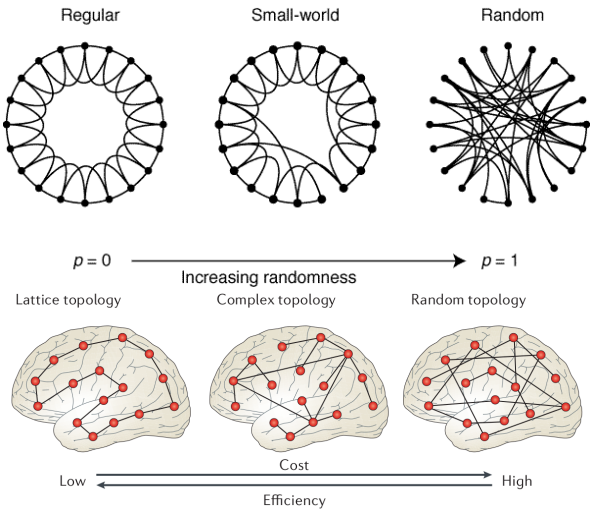

Figure 5.7: Small world property. Combines high levels of local clustering among nodes and short paths that globally link all nodes of a network. Image above taken from Watts and Strogatz [1998], image below from Bullmore and Sporns [2012].

matrix that explains the functional connectivity relation between the different regions of the brain and finally, the extraction of the graphs and their associated graph metrics that give detailed information about the brain functional connectivity of each particular participant. There are multiple ways to perform this steps, in the following paragraphs, we detail how we apply each of these steps, that are represented in Fig. 5.8.

Image acquisition

Before acquiring the images, it is important to take into account the acquisition parameters. The repetition time (TR), the number of volumes (scan duration) and the resolution at the voxel level, are the most important to consider. Once the image is obtained, it must be preprocessed to match with other subjects of a study and with the parcellation scheme.

Brain parcellation

Next step is the parcellation of the brain in different areas. As we have already seen, there are several ways to perform this step. Graphs can be computed using each voxel as a node in the graph, or we can apply any type of parcellation (structural, functional, subject based or standarized template). All the experiments performed in this thesis were done using parcellation schemes, mainly the AAL scheme Tzourio-Mazoyer et al. [2002]. The voxels of each volume that

belong to a region are extracted; then, they are weighted by a gray matter probability map (that is obtained during the preprocessing) and the mean value of each region for each volume is computed. This way, a time series is obtained that represents the evolution of the BOLD signal across time for each selected region in the brain. Finally, the head movements and motion outliers are regressed out from the time series to clean the signal from movement related noise.

Connectivity matrices computation

Obtained time series are then decomposed in several scales using wavelet transformation. This approach applies a time-scale decomposition that partitions the total energy of a signal over a set of compactly supported basis functions, or little waves, each of which is uniquely scaled in frequency and located in time [Akansu and Haddad, 2001]. We apply the maximal overlap discrete wavelet transform (MODWT) to each regional mean time series to estimate the pairwise inter-regional correlations (applying Pearson's correlation) between wavelet coefficients at each of the four scales. Our analysis is mainly focused on the wavelet scales that represent functional connectivity in the frequency intervals below 0.1 Hz, where relevant information for rs-fMRI data is contained [Biswal et al., 1995].

Graph computation

To keep fully connected graphs, we first extract the minimum spanning tree (MST) [Pettie and Ramachandran, 2002] based on the absolute correlation matrix. The remaining absolute correlation values are thresholded to create an adjacency matrix that defines an unweighted graph for each subject. The threshold R is calculated to produce a fixed number of edges M. The number of edges is fixed to be able to compare the extracted graphs among the different participants in the study; as a consequence, the values of the threshold are subject dependent. Once the maximum number of edges is reached, the graph is defined.

The computation of the graph is based on the minimum spanning tree (MST) [Pettie and Ramachandran, 2002]. Applying the MST, we obtain the minimum graph where all the nodes are connected. Then, we add links between nodes according to the highest correlation values until a fixed number of edges is reached. Once the graph is defined, there are several metrics that can be extracted in order to study the characteristics of the graph.

5.4 Graph metrics

No matter what definition or type of graph is used, one of the basic steps in graph analysis is to calculate or extract basic graph (or network) properties. The majority of networks are too complex to analyze them visually. It is necessary to extract the metrics from the graphs to be able to study the importance or roles of certain nodes and edges.

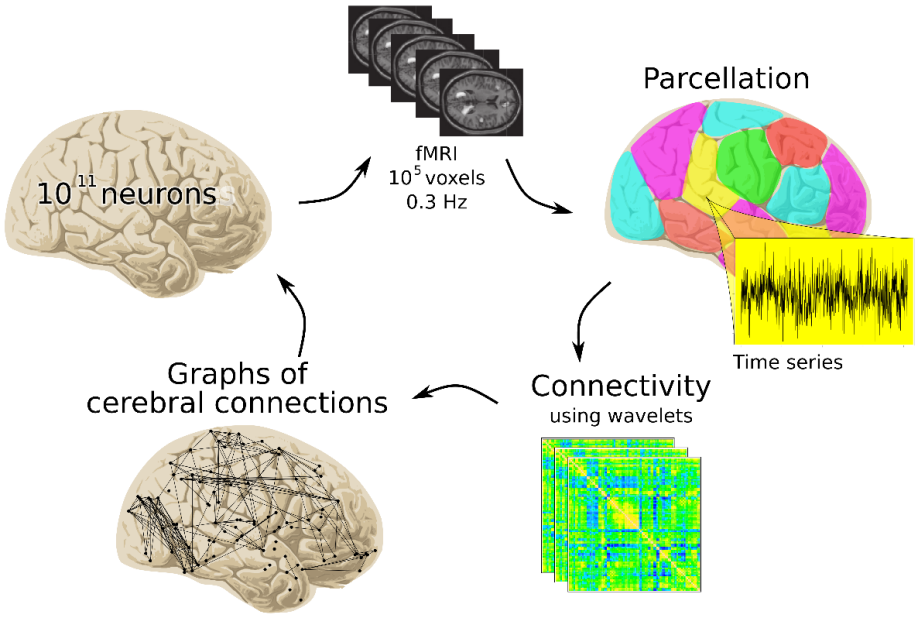

Figure 5.8: Graph computation pipeline. Several steps are required to obtain a graph based representation from a rs-fMRI acquisition. Courtesy of Sophie Achard.

Each graph metric gives a particular description of the topology of a graph. They can be computed at different levels, providing information at the global level (global metrics), about clusters inside the graph (intermediate metrics) or about each particular node (nodal metrics).

5.4.1 Classical graph metrics

Some metrics, such as local efficiency (e_{l_i}) or clustering coefficient (c_i), rely on the connectivity properties in the neighborhood of a node; while other metrics, such as global efficiency (e_{g_i}) and betweenness centrality (b_i), describe the influence of a particular node in the propagation of the information along the whole network.

In the following paragraphs, the formulation of the graph metrics that have been applied more often along this thesis is given.

Definition 10. *The **degree** of a node i, k_i, corresponds to the number of edges that connect the node with the rest of nodes in the graph*

$$k_i = \sum_{j \in N} A_{ij},$$

where N is the number of nodes in the network.

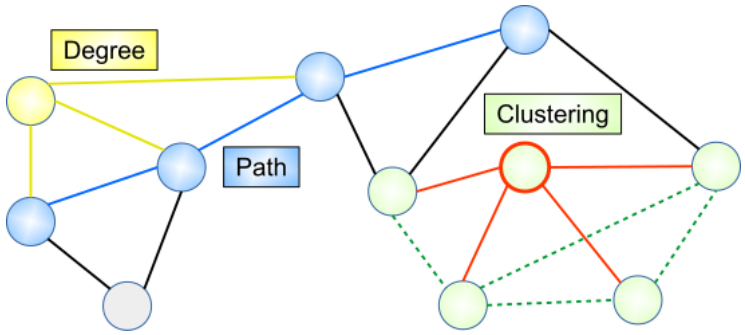

Figure 5.9: Graphical example of the following graph metrics: node degree (in yellow), clustering coefficient (in green) and minimum path length (in blue).

In the graph shown in Fig. 5.9, we show an example of the degree of a node, where $k_i = 3$.

The **minimum path length** is the minimum number of edges that must be traversed to go from one node to another. In Fig. 5.9, the shortest path to go from one node on the left to another node on the right is shown in blue (where $l_{ij} = 3$).

Definition 11. *The **minimum path length** (distance), between nodes i and j is defined as*

$$l_{ij} = \sum_{a_{uv} \in g_{i \leftrightarrow j}} a_{uv},$$

where $g_{i \leftrightarrow j}$ is the (geodesic) shortest path between i and j.

Definition 12. *The **global efficiency** measures how the information in the network is propagated. It is defined as the inverse of the harmonic mean of the minimum path length l_{ij} between a node i and the rest of nodes in the graph [Latora and Marchiori, 2001]. It is computed as*

$$e_{g_i} = \frac{1}{N-1} \sum_{j \in N, j \neq i} \frac{1}{l_{ij}}.$$

Definition 13. *The number of shortest paths going through a node i is known as **betweenness centrality** (b_i) [Freeman, 1977, Brandes, 2001]*

$$b_i = \sum_{i \neq j \neq k} \frac{\rho_{jk}(i)}{\rho_{jk}},$$

where ρ_{jk} is the number of shortest paths between nodes j and k, and $\rho_{jk}(i)$ is the number of shortest paths between nodes j and k that pass through i.

Definition 14. *The **local efficiency** (e_{l_i}) is a measure of information transfer in the immediate neighborhood of each node [Latora and Marchiori, 2001]. It is*

computed as follows:

$$e_{l_i} = \frac{1}{N_{G_i}(N_{G_i}-1)} \sum_{j,k \in G_i} \frac{1}{l_{jk}},$$

where G_i is a subgraph of G extracted from the set of nodes that are the nearest neighbours of node i, and where N_{G_i} is the number of nodes in G_i.

The clustering coefficient is defined as the fraction of one node's neighbors that are also neighbors of each other. In Fig. 5.9, is possible to see an example of clustering coefficient (in green).

Definition 15. *The **clustering coefficient** (c_i) [Watts and Strogatz, 1998] is a measure of the degree to which nodes in a graph tend to cluster together:*

$$c_i = \frac{1}{N} \sum_{i \in N} \frac{2t_i}{k_i(k_i-1)},$$

where t_i is the number of triangles around a node i, defined as $t_i = \frac{1}{2} \sum_{i \neq j \neq k} a_{ij} a_{jk} a_{ik}$ [Watts and Strogatz, 1998].

The degree to which the network may be subdivided into delineated and nonoverlapping groups is quantified by the modularity. Each module is composed of several nodes densely connected between them, and with relatively few connections to nodes in different modules. In Fig. 5.10, we show an example of a graph with two modules.

Definition 16. *The **modularity** (Q) of a network is defined as*

$$Q = \sum_{u \in M} [e_{uu} - (\sum_{v \in M} e_{uv})^2],$$

where the network is fully subdivided into a set of nonoverlapping M modules, and e_{uv} is the proportion of all edges that connect nodes in module u with nodes in module v.

For more detailed information of the graph metrics, see Rubinov and Sporns [2010]. To extract the network parameters, we used *brainwaver* and *igraph* R libraries, tools that are freely available on CRAN[1,2].

Concept of hub

A **hub** in a network is a node that interacts with many other nodes, facilitating functional integration, and playing a key role in network resilience to insult Rubinov and Sporns [2010]. The importance of an individual node to network efficiency can be evaluated by removing it and estimating the efficiency of the resultant "damaged" network.

[1] http://cran.r-project.org/web/packages/brainwaver/index.html
[2] http://cran.r-project.org/web/packages/igraph/index.html

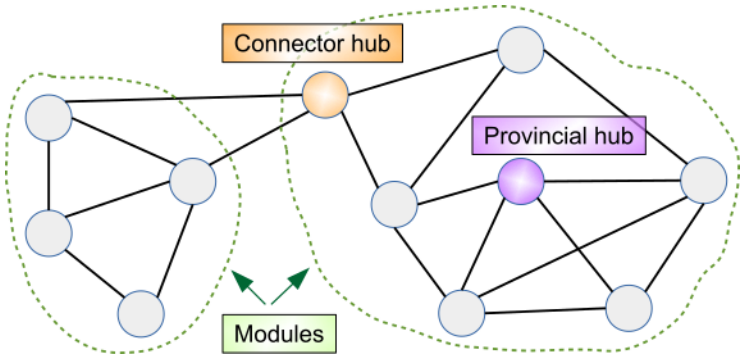

Figure 5.10: Graphical example of the concept of hub and modularity of a graph. The differences between a connector hub and a provincial hub are shown.

Even if there is no clear definition of a hub, some authors identify hubs as nodes with high node degree or high betweenness centrality [Bullmore and Sporns, 2009]. According to them, hubs can be described in terms of their roles in the modular structure. For example, there are hubs considered as **provincial hubs** because they are connected mainly to nodes in their own modules, while some other hubs are considered as **connector hubs** because they are connected to nodes in different modules. In Fig. 5.10, we show a simple example of this type of hubs classification.

5.4.2 Hub disruption index (κ)

The hub disruption index (κ) was first introduced by Achard et al. [2012]. It is a metric that evaluate the nodal network topology of a subject in relation to a referential network topology (i.e. the normative network topology of a healthy control group). It can be used to compare the behavior of the network of a single subject (healthy or patient) with respect to a referential network topology, but also to compare the differences between two groups with respect to a referential network topology.

Consider the case of a single healthy volunteer compared to the healthy control group (Fig. 5.11A). Choosing one graph metric at the nodal level, for example the node degree in this figure, we plot the value of each node of the individual volunteer against the average degree for the same nodes of the healthy control group, taken as a reference. We can observe that the points fall approximately on a positive slope line of the type $y = x$. This means that the nodes' value of a healthy volunteer is similar to the average value of the same nodes from the group of controls. Contrary, if we proceed similarly with a stroke patient (Fig. 5.11B), we observe that the slope line is not around the $y = x$ line. This means that the degree of any particular node in a stroke patient is not well predicted by the average degree of the same node in a group of healthy controls. To compute κ, we proceed as follows: we subtract the healthy group mean nodal

degree (or any other nodal metric) of the same node in an individual volunteer before we plot that difference against the healthy control group mean. In this case, for a healthy volunteer (Fig. 5.11C), the data will be scattered around an horizontal line ($\kappa \sim 0$) and for an individual patient (Fig. 5.11D) around a negatively slope line ($\kappa < 0$).

5.5 Test-retest analysis of brain graphs

The validation of sensitive longitudinal imaging biomarkers relying on graphs requires rigorous evaluation of the test-retest (TRT) reliability of graph metric measures [Nakagawa and Schielzeth, 2010]. TRT reliability is typically evaluated by acquiring at least two scanning sessions of the same subject at different times. The second session is performed after a time interval varying from a few minutes, when the two acquisitions are performed during the same session (intra-session reliability), to several hours, days or months, for the assessment of intersession reliability. The analysis of TRT data on brain connectivity is necessary to identify network features that are intrinsic to the functioning of brain (called biomarkers in this paper) and not biased by subject variability or artefacts from acquisition. To our knowledge, graph metrics TRT reliability of the whole brain using a parcellation scheme has been assessed in 6 studies [Braun et al., 2012, Cao et al., 2014, Liang et al., 2012, Wang et al., 2011, Schwarz and McGonigle, 2011, Guo et al., 2012], or at the voxel level [Liao et al., 2013, Du et al., 2015], and in a recent meta-analysis [Andellini et al., 2015].

Intraclass correlation coefficient (ICC) [Shrout and Fleiss, 1979] has been used as a measure of reliability, resulting in a large range of ICC values, presumably due to considerable heterogeneity in the methodological approaches. In Appendix A, we show the how ICC is computed. Despite this heterogeneity, several factors have been shown to influence graph reliability, such as the preprocessing steps (smoothing, global signal regression, movement regression) [Braun et al., 2012, Shirer et al., 2015], the frequency range [Liang et al., 2012, Liao et al., 2013, Shirer et al., 2015], the computation of the edges of the graph [Liang et al., 2012, Fiecas et al., 2013], the type of graph metrics [Wang et al., 2011, Braun et al., 2012, Cao et al., 2014], the cost/sparsity [Braun et al., 2012], the type of network (binary or weighted [Braun et al., 2012, Guo et al., 2012, Liang et al., 2012, Liao et al., 2013, Schwarz and McGonigle, 2011], the brain parcellation scheme [Wang et al., 2011, Cao et al., 2014], the use of voxel-wise metrics [Zuo and Xing, 2014], and most importantly, the scan duration [Braun et al., 2012, Liao et al., 2013, Wang et al., 2011]. In a seed-based approach, Birn et al. [2013], exploring TRT reliability of rs-fMRI connectivity for scan duration ranging from 3 to 27 min, found improvement in intersession reliability by increasing scan duration up to 9 min, suggesting that functional connectivity computed from a 10 min acquisition duration averages slow changes and provides a more stable estimate of the connectivity strength. In a recent meta-analysis based on graph theory TRT studies, the same trend was observed with increased reliability for longer acquisition duration [Andellini et al., 2015].

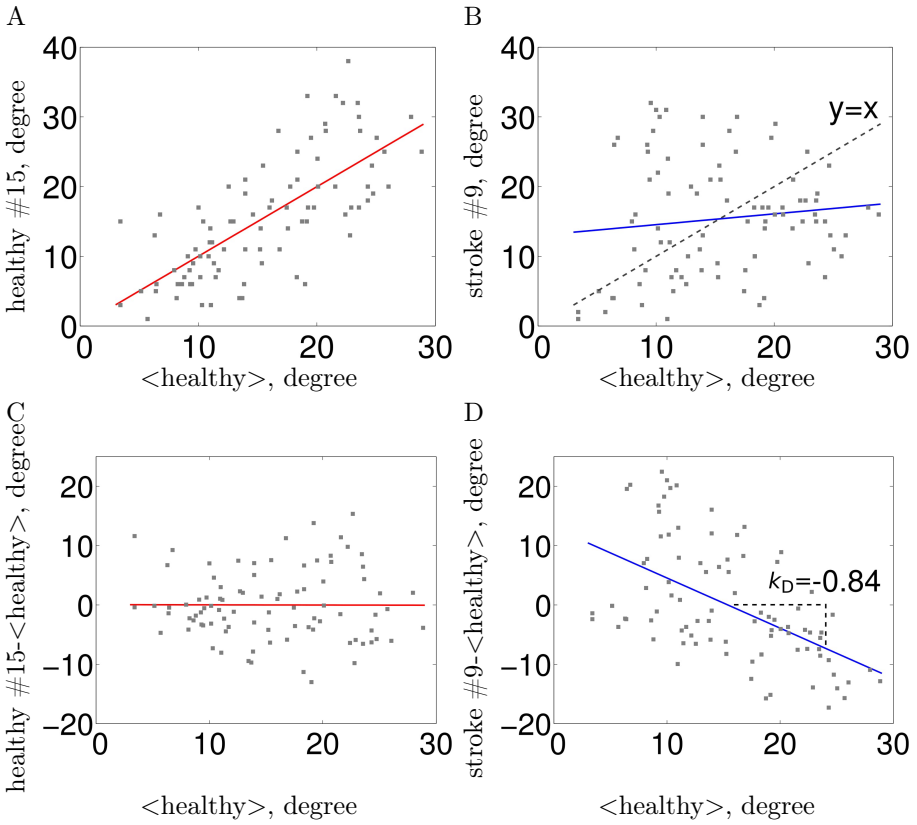

Figure 5.11: Estimation of κ. The nodal network topology (here, node degree) of an individual subject in relation to the normative network topology of the healthy control group (A) for one healthy volunteer and (B) for one stroke patient. To construct the hub disruption index κ for the degree, we subtract the healthy group mean nodal degree from the degree of the corresponding node in an individual subject before plotting this individual difference against the healthy group mean. κ is the slope of the regression line computed on this scatter plot. This transformation means that the data for an individual healthy volunteer (C) will be scattered around a horizontal line ($\kappa \sim 0$), whereas the data for a patient in a stroke (D) will be scattered around a negatively sloping line ($\kappa < 0$).

Author	# **Subj**	**Scan length**	**Parcellation**	E_g	k_i
Schwarz et al, 2011	25	7 min 197 tp	AAL	ICC $\sim$ 0.5	-
Wang et al, 2011	25	7 min 197 tp	AAL, HO, 160 func ROIs	ICC $<$ 0.25	0.40 $<$ ICC (precuneus)
Braun et al, 2012	33	5 min 150 tp	AAL	ICC = 0.5	-
Liang et al, 2012	22/25	5 min 150 tp	AAL	ICC $<$ 0.02	0.25 $<$ ICC $<$ 0.4 (precuneus)
Cao et al, 2014	26	5 min 150 tp	AAL, func ROIs	ICC $\sim$ 0.5	0.4$<$ ICC $<$ 0.55 (precuneus)
Guo et al, 2012	24	8 min 240 tp	68 ROIs (salience)	-	ICC $<=$ 0.6

Table 5.1: Test-retest reliability studies using graphs with rs-fMRI. AAL: Automated anatomical labeling; E_g: Global efficiency; func ROIs: functional regions of interest; HO: Harvard-Oxford; ICC: Intraclass correlation coefficient; k_i: node degree; tp: time points.

In Table 5.1, I show a comparison between several studies that have analized the TRT reliability of brain graphs using a parcellation scheme to divide the brain in several regions. Among other reliability measures, all of them computed the ICC. This fact made possible the comparsion of the results across studies, although the results are not always coherent among them. These studies reported multiple results according to different preprocessing steps, frequency ranges, types of networks, parcellation schemes, and so on; Table 5.1 reflects the results that are more closely related to the graph methodology we apply.

In this thesis, we tested for the first time the combined effect of the sample size and duration on TRT reliability. Also, we studied the influence of the cost and the influence of the parcellation schemes, as we show in the following part.

Chapter 6

Aim of this thesis

In the Chapter 4 of this thesis, we introduced the main techniques to study the functional connectivity of the brain. Among these three techniques, we decided to use graph analysis. This election is motivated by two different reasons. First, after reviewing the literature dealing with brain functional connectivity in stroke, we concluded that the effect that stroke causes in the brain is not only focal damage, it also involves remote brain regions. On the contrary, recent publications on stroke suggest a global reorganization of the brain function 4.3. Graph analysis is potentially an adequate technique to explore the global effect of brain lesions such as stroke, without using any *a*-priori infomation. Second, the previous expertise using graph analysis of one of the co-supervisors of this thesis, also motivated this choice.

This observed global reorganization justifies also the introduction of the hub disruption index, a graph measure specially dedicated to detect functional brain connectivity patterns that differ from a reference considered as normal.

As we will see in the last part of this thesis, almost all the experiments performed with stroke patients are focused on the contralesional hemisphere. When stroke lesions are extended, they may cause deformations in the brain that are difficult to treat in the preprocessing steps. Even if we have designed a specific pipeline (detailed in Chapter 11) to deal with the stroke lesion in the preprocessing of the images, we prefered to focus on the contralesional hemisphere only. In one hand, we limited the randomly introduction of edges in empty nodes of the graph due to the minimum spanning tree (explained in Chapter 5); in the other hand, we explore the effect of stroke in the contralesional hemisphere alone, without the influence of the ipsilesional hemisphere. This approach is not common, because stroke studies are usually centered on the motor system and the areas surronding the lesion, ignoring the remote brain regions also affected by the infarct.

Why so much effort to study the reliability of graph based brain functional connectivity? Reliability is defined as the complete consistency of a measure. One measure has a high reliability if it produces similar results under similar conditions. That is, if the same experiment is repeated two or more times, with

the same sample group under consistent conditions, and the results obtained are equal or near to each other, then the measure is highly reliable. A reliable measure means that it is accurate, reproducible and consistent between different test.

In general, but specially in clinical applications, to assess the reliability of new measures is of paramount importance to be sure that the results obtained are trustable. As we have seen in the last part of Chapter 5, the reliability of graph based analysis of the functional connectivity of the brain has been previously assessed by several authors. The results given by these studies, listed in Table 5.1, were not always coherent across them. Some of these studies reported huge confidence intervals on their results, making difficult to extract any reliable conclusions from them. In line with statisticians [Button et al., 2013, Ioannidis, 2014], we think that this variability in their results may be due to low statistical power. This low power relies on two main causes: the small sample size of the studies and the the small number of independent timepoints (associated to short scan duration of the rs-fMRI acquisitions). This is why we decided to work on a freely available test-retest database, from the Human Connectome Project (HCP), that consists in 100 subjects with two rs-fMRI acquisitions, using a long acquisition duration (more than 14 minutes), to look for the impact of the sample size and scan duration on the reliability of graph metrics applied to the human brain. The results should provide tools for best practices in rs-fMRI.

The kind of approach we present in this PhD thesis is strongly encouraged both by institutions such as the Meta Research Innovation Center at Stanford [1] and by the neuroimaging community (Consortium for Reliability and Reproducibility (CoRR) [2]

The aim of this thesis is to investigate how the trade-off between the sample size and the scan duration, the cost (the density of connections in a graph), and the parcellation scheme influence the reliability of graph based brain functional connectivity in resting state (Part II of this thesis). Once we have a deeply knowledge of the circumstances under the measures we are using are reliable, we proceed to study the differences between a stroke group and a group of healthy volunteers, the reorganization along time of the brain after a stroke and the outcome prediction (Part III of this thesis).

The data used in this thesis is part of an innovative research project that studies the effect of stem cells treatment in the recovery of stroke victims. Thus, the final aim of this thesis is to investigate if a treatment based on stem cells may improve the recovery of stroke patients.

[1] http://metrics.stanford.edu/
[2] http://fcon_1000.projects.nitrc.org/indi/CoRR/html/

Part II

Methodological contributions

Introduction

In this second part of the thesis, we will address the issue of the duration of rs-fMRI acquisition, of the sample size required in group studies, and of the way we compute graphs in order to achieve reliability in published studies.

We will take the opportunity of using a freely available dataset with long acquisition duration, and large sample size (n=100 subjects) of test-retest data (2 acquisitions per subject) provided by the Human Connectome Project (HCP).

In Chapter 7, we evaluate the effect of some preprocessing steps in graph based brain connectivity. In Chapter 8, we present the results of the test-retest reliability of brain graphs using the HCP database. In Chapter 9, the reliability of the hub disruption index is presented and finally, in Chapter 10, we analyze the reliability of other factors that can also influence the brain graphs. Such factors are the parcellation scheme, the time series filtering procedure and the computation of the connectivity measure.

Chapter 7

Evaluating the effect of MRI preprocessing in graph based brain connectivity

7.1 Introduction

There are several ways to perform data preprocessing, and the way the different preprocessing methodologies influence the final results is still a topic of interest. Authors in Andronache et al. [2013] study the impact of five different preprocessing procedures of increasing complexity in the detection of the default-mode network in subjects with disorders of consciousness. They strongly underlined the importance of performing high-grade preprocessing, including rejection of outlier volumes, ventricle masking, removal of movement related and global signal covariance and band-pass filtering.

Although the preprocessing is performed to correct systematic variability due to the physics of MRI, subject motion, physiological processes, random noise, and so on; it introduces other type of variability when manipulating the original data with several interpolations.

Here, we tested four different preprocessing pipelines, focusing on the importance of inter-individual image registration, and the choice of the referential space, in order to see if there are significant differences in the resulting graphs. Our hypothesis was that if the graph theory methodology is robust, there should not be significant differences between preprocessing pipelines whenever the quality of the preprocessing is good enough.

A standard rs-fMRI preprocessing pipeline involves several steps Smith et al. [2013b]:

- Realignment of functional echo planar imaging (EPI) images.
- Slice time correction of EPI.

- Anatomical T1 segmentation in different tissues: gray matter (GM), white matter (WM), cerebrospinal fluid (CSF) and non-brain tissues.
- GM and WM affine/non-linear registration to a standard template.
- Co-registration to GM/WM, fMRI data and template.

The first three steps are common to all the proposed pipelines while the rest varies among them. Commonly, a template is used as reference to determine that one particular voxel (or region) corresponds to the same voxel (or region) in all the subjects in the study, but when using these templates, a new problem appears because each of the subjects and the referential template are in different anatomical spaces. Two strategies are possible for individual parcellation: either we match the atlas onto the subjects anatomical space (that means minimal transformation of fMRI images), or we match each subjects anatomical and rs-fMRI images onto the atlas space. Additionally, it was previously shown that an accurate inter-individual registration (such as DARTEL) permits a better matching with a predefined parcellation scheme and an increase in the statistical significance in task fMRI [Pizzagalli et al., 2013]. We then aim at exploring the effect of diffeomorphic registration on graph metrics.

We wanted to answer two questions related with the preprocessing of rs-fMRI data:

1. Is it better to remain in the subject specific referential space with minimal transformation of the rs-fMRI data, or to place all the subjects to a similar referential space?
2. Is it better to apply a diffeomorphic transformation of the data to register them more accurately, rather than a standard normalization procedure?

7.2 Preprocessing pipelines

Common steps (see Fig. 7.1) involve realignment and slice timing correction performed on the EPI images. Structural images are then co-registered to the mean EPI and segmented in different tissues. This segmentation tool is known as *unified segmentation* and it enables image registration, tissue classification, and bias correction combined within the same generative model Ashburner and Friston [2005]. It is based on a mixture of Gaussian distributions incorporating a smooth intensity variation and nonlinear registration with tissue probability maps (TPM)[1].

7.2.1 Pipeline 1: Non linear registration in MNI space

Previously estimated deformation fields are applied to corrected EPI data. In order to obtain all the data in the same spatial resolution, images are resliced

[1] All the preprocessing steps are done using the toolbox SPM12 in Matlab.

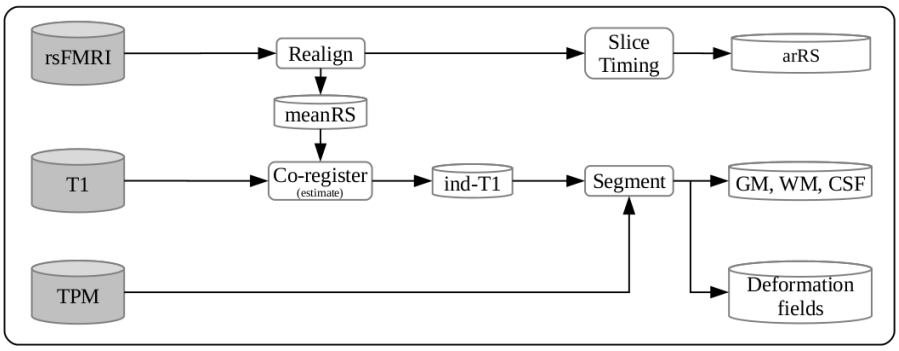

Figure 7.1: Common steps in the preprocessing of rs-fMRI. arRS: RS data after realignment (r) and slice timing (a); TPM: tissue probability maps (provided by SPM software).

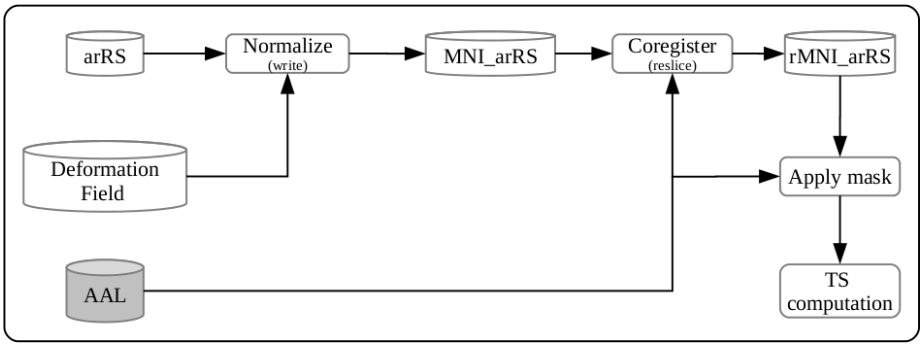

Figure 7.2: Non linear registration pipeline in MNI space.

to match voxel to voxel. In Fig. 7.2, we show the pipeline used to co-register all the data to MNI space.

In this experiment, to determine the ROIs to build the graphs, we use a predefined brain atlas, the Automated Anatomical Labeling (AAL) map. As this template is already in MNI space, no transformation is needed in this case.

7.2.2 Pipeline 2: Non linear + diffeomorphic transformation in MNI space

A diffeomorphic transformation from one image to another can be described as a vector field, where the vector (at every point) describes the movement of a particular voxel from the original to the transformed image Poldrack et al. [2011]. This approach is based on computational anatomy methods which uses models based on physical phenomena, such as the deformation of elastic materials, to align structures across individuals respecting the anatomical constraints.

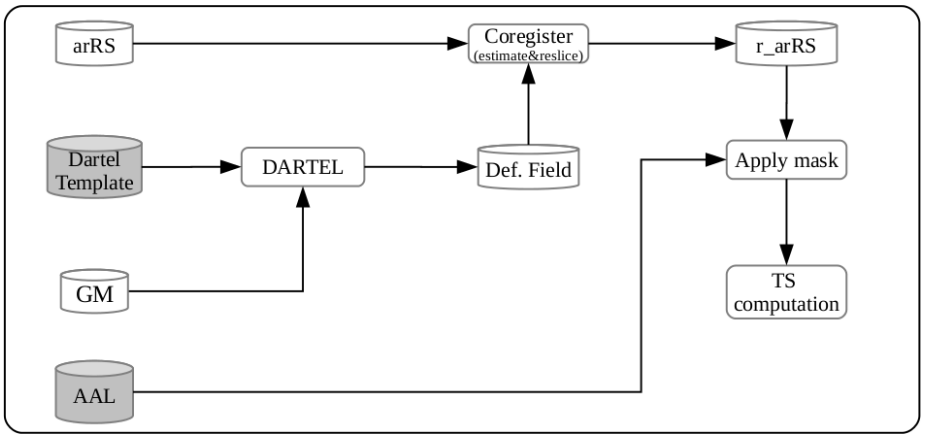

Figure 7.3: Diffeomorphic transformation pipeline in MNI space.

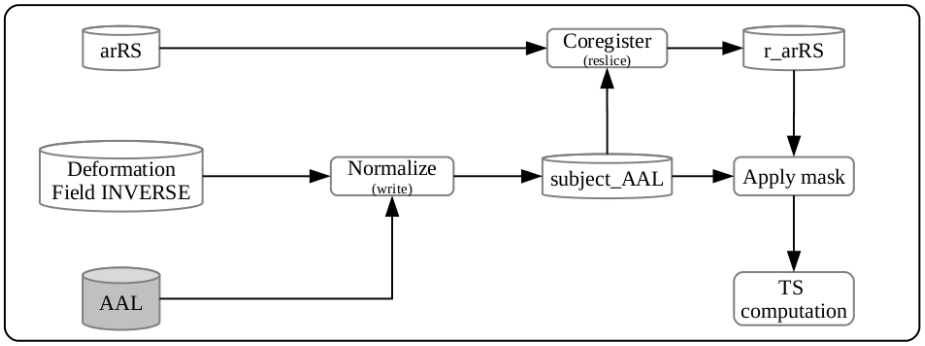

Figure 7.4: Non linear registration pipeline in subject space.

In SPM, this tool is known as DARTEL Ashburner [2007]. After non-linear registration, this diffeomorphic transformation is applied to register the data more accurately allowing registration of fine structures. We show the preprocessing with diffeomorphic transformation to MNI space in Fig. 7.3. After Dartel, new deformation fields are obtained, which are applied to corrected EPI data.

7.2.3 Pipeline 3: Non linear transformation in subject's space

In this case, the inverse of the deformation field is applied to the AAL parcellation scheme, in order to transform it to the subject space. Corrected EPI data are not transformed, but they need to be resliced to match voxel by voxel. Steps are shown in Fig. 7.4.

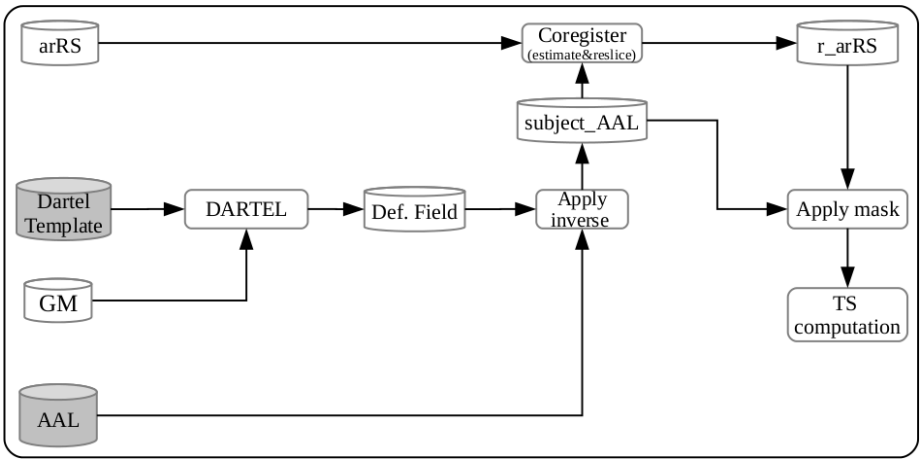

Figure 7.5: Diffeomorphic transformation pipeline in subject space.

7.2.4 Pipeline 4: Non linear + diffeomorphic transformation in subject's space

Similar to steps explained in Subsection 7.2.3, the inverse of the deformation field is computed to apply it to the AAL parcellation scheme, obtaining an adapted anatomical template for each subject. In Fig. 7.5, we show the standard preprocessing, with diffeomorphic transformation co-registering all the data to each subject's referential space.

7.3 Evaluation methods

7.3.1 Database

The database used in this experiment corresponds to 31 healthy controls that belong to the HERMES study. MRI data were acquired at 3T (Achieva 3.0TTX, Philips, NL) at IRMaGe MRI facility (Grenoble, France). The resting-state functional images were acquired using a gradient-echo EPI imaging sequence with the following parameters: in plane 3 mm isotropic voxels, 36 axial slices of 3.5 mm thick, gap = 0.25 mm TR = 2000 ms, TE = 30 ms, flip angle = 75°, field of view = 192x192 mm^2. A total of 400 volumes was acquired for a total scan duration of 13 min and 20 s.

7.3.2 Graph metrics

The graph metrics computed to compare the 4 pipelines are:

- Global metrics: E_g, E_l, Q and Edg per subject and per pipeline.
- Regional metrics: e_{g_i}.

Global metrics

Three global measures of network integration are computed for each subject: global efficiency (E_g) which is the mean across nodes of e_{g_i} (definition 12 of Chapter 5) , local efficiency (E_l) which is the mean across nodes of e_{l_i} (definition 14 of Chapter 5) and modularity (Q), definition 16 of Chapter 5. We also include as a variable the maximum number of possible edges (Edg), taking into account the amount of significant absolute correlations, to check if the number of significant edges in the graph was altered depending on the preprocessing pipeline.

For each subject, we compute the global efficiency at both, global and regional level. The values for all subjects of the global efficiency is shown in Fig. 7.6a. We also compute E_l and Q (but only at the global level), their values for all subjects is shown in Fig. 7.6b and Fig. 7.6c, respectively. Finally, the values for all subjects of the maximum number of edges is shown in Fig. 7.6d.

Also, the mean and standard deviation of the regional global efficiency between subjects is computed for each of the 89 regions (Fig. 7.7)

Regionl metrics

At the regional level, we only computed regional global efficiency, e_{g_i}. This metric is defined in the definition 12 of Chapter 5 of this thesis.

7.3.3 Statistical analysis

In order to test the effect of the pipeline on regional global efficiency, e_{g_i}, we performed a repeated ANOVA analysis with two factors (regions and pipeline). Then we computed similarity measures (Pearson correlation) between the different pipelines. Finally, significant differences between regions were tested (t-test), with p-value adjusted method *holm* [Holm, 1979].

7.4 Results

No statistically significant differences on e_{g_i} values across regions were found when computing repeated ANOVA. Several correlation values across pipelines are shown in Table 7.1. In Fig. 7.8, we show the correlation value across pipelines for each of the 89 regions. Looking at the correlation values in Table 7.1, we can conclude that the obtained graph metrics are highly correlated between the different pipelines. Lowest correlation values were found for Q when comparing pipeline 1 and 3, and pipeline 2 with pipelines 3 and 4, meaning that Q values are influenced by preprocessing. Highest correlation values when comparing the e_{g_i} were found when comparing pipeline 1 and 3 (both with no diffeomorphical transformation - Dartel) and between pipeline 2 and 4 (both with Dartel tool applied). This trend was also seen for the E_l correlations, and also for the majority of the regions in Fig. 7.8.

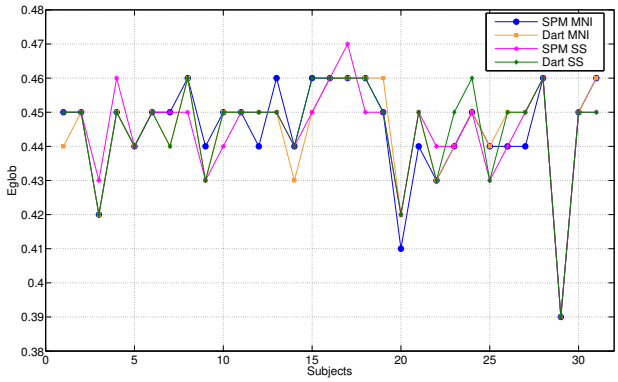

a)

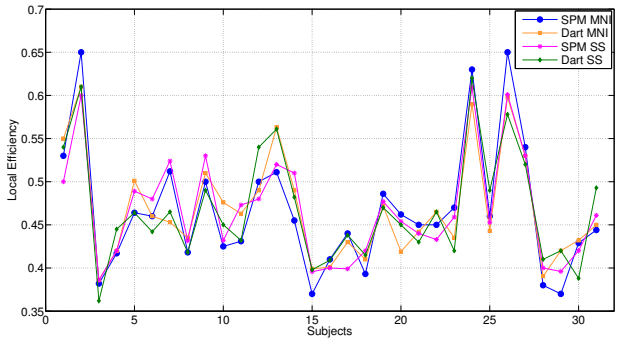

b)

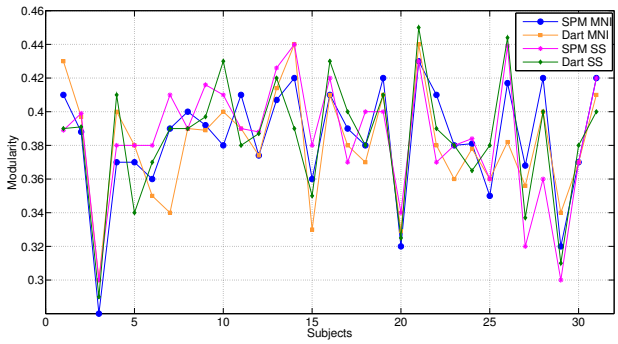

c)

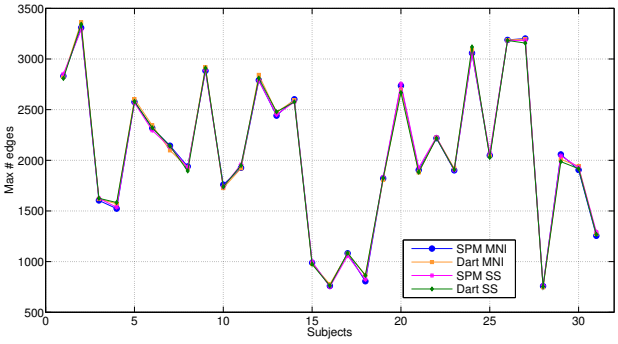

d)

Figure 7.6: Mean global measures per subject for each preprocessing pipelines: a) global efficiency per subject; b) local efficiency per subject; c) graph modularity per subject; d) maximum number of edges per subject.

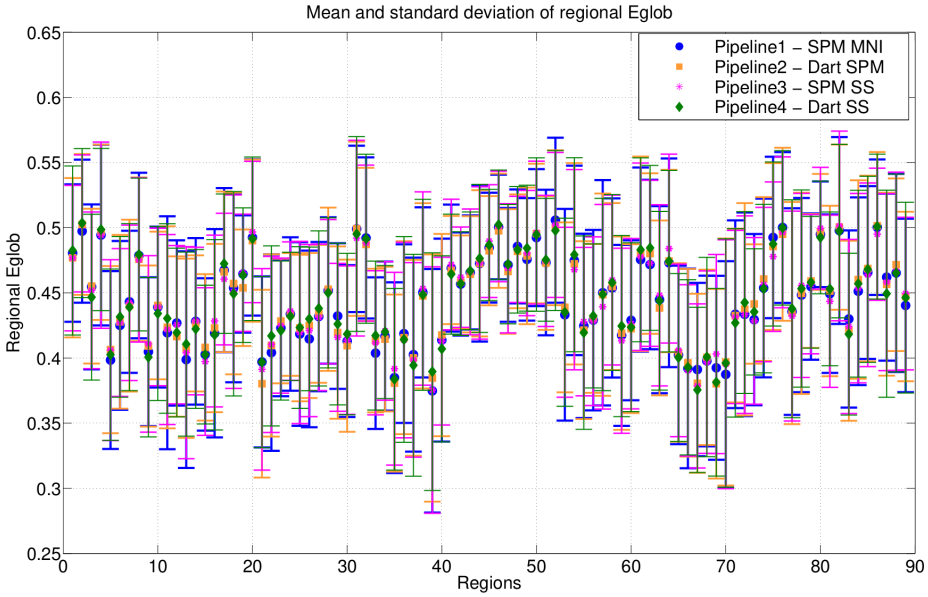

Figure 7.7: Regional mean global efficiency (e_{g_i}) + one standard deviation of the proposed pipelines.

In the other hand, pairwise t-tests were computed to see which regions are significantly different between pipelines. In several regions, results significantly differe between pipelines after t-test computation: region 19 (left supplementary motor area), region 29 (left anterior cingulum), region 52 (right postcentral gyrus), region 62 (right precuneus) and region 75 (left temporal superior). Despite of there is no significant differences between the pipelines, lowest correlation values are reached for region 69 (pallidum left) and region 73 (left Heschl), both small regions in the template.

Same statistical tests where computed for each of the global measures (E_g, E_l, Q and Edg) but no significant differences were found.

When plotting the global measures in 3D, as shown in Fig. 7.9, it is possible to see that the majority of the data were all clustered together, therefore difficult to separate. But, it is also possible to appreciate that some subjects, like number 3 (ADV03), number 20 (mapvs06a) and number 29 (tem15a), were separated from the grouped data.

7.5 Discussion

The results obtained in this experiment show that there was no significant differences in graph metrics between the tested preprocessing pipelines. However, some metrics such as Q may differ.

The impact of registraton of rs-fMRI data has not been addressed yet. To

rho	**1vs2**	**1vs3**	**1vs4**	**2vs3**	**2vs4**	**3vs4**
e_{g_i}	0.91	0.93	0.91	0.91	0.94	0.91
E_g	0.92	0.89	0.92	0.90	0.94	0.91
E_l	0.89	0.95	0.90	0.92	0.93	0.89
Q	0.84	0.79	0.82	0.71	0.76	0.83
Edge	0.99	0.99	0.99	0.99	0.99	0.98
Global	0.92	0.90	0.91	0.88	0.91	0.91

Table 7.1: Correlation values between the different preprocessing pipelines: e_{g_i} is the mean correlation value of the 89 regions; E_g, E_l, Q and Edg shows the correlation of each of those values between the different pipelines and *Global* is the mean correlation value of the three values (E_g, E_l and Q); 1vs2 refers to comparison between pipeline 1 and pipeline 2, and so on.

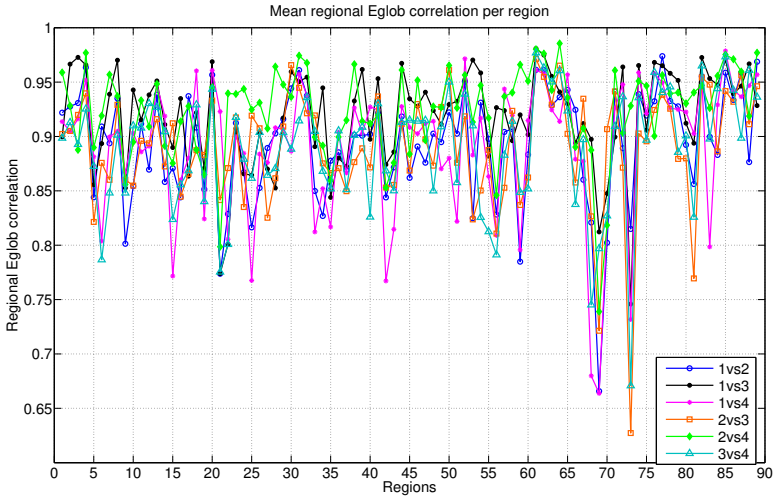

Figure 7.8: Correlation values of the regional global efficiency between different pipelines.

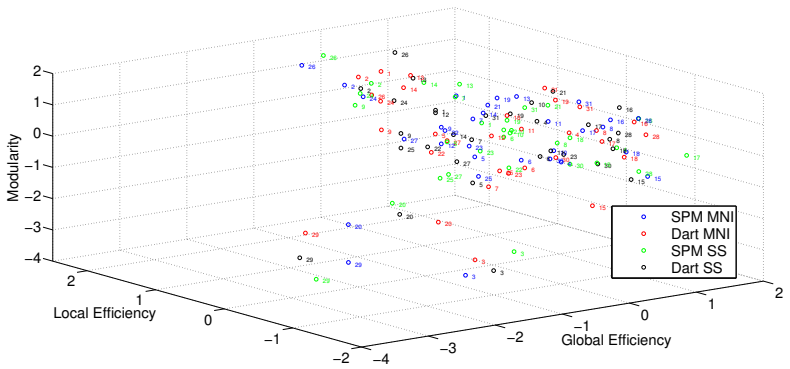

Figure 7.9: 3D representation of the global measures for each subject.

us, it seems important to choose an accurate registration, since in task fMRI it provides more accurate localization and higher size effect than standard registration.

Therefore, graph based brain connectivity seems to be robust between the proposed pipelines because we were not able to find significant differences between the final measures extracted from the brain graphs. In particular, regions with the highest e_{g_i} remain the same, whatever the pipeline applied (Fig. 7.7). In other words, hubs are independent of the pipeline. Also, it seems to be a highest correlation between pipelines related to the same type of non linear registration.

This experiment was performed as an initial step for the thesis with the aim of fixating the type of preprocessing that would be used along this work.

Our final decision was to apply the preprocessing 2 (Fig. 7.2), that is the non linear diffeomorphic transformation in MNI space. The controls database used in this thesis to compare to the stroke patients database, were preprocessed this way.

The schemes of the selected preprocessing pipeline are given in Figs. 7.10 to 7.13.

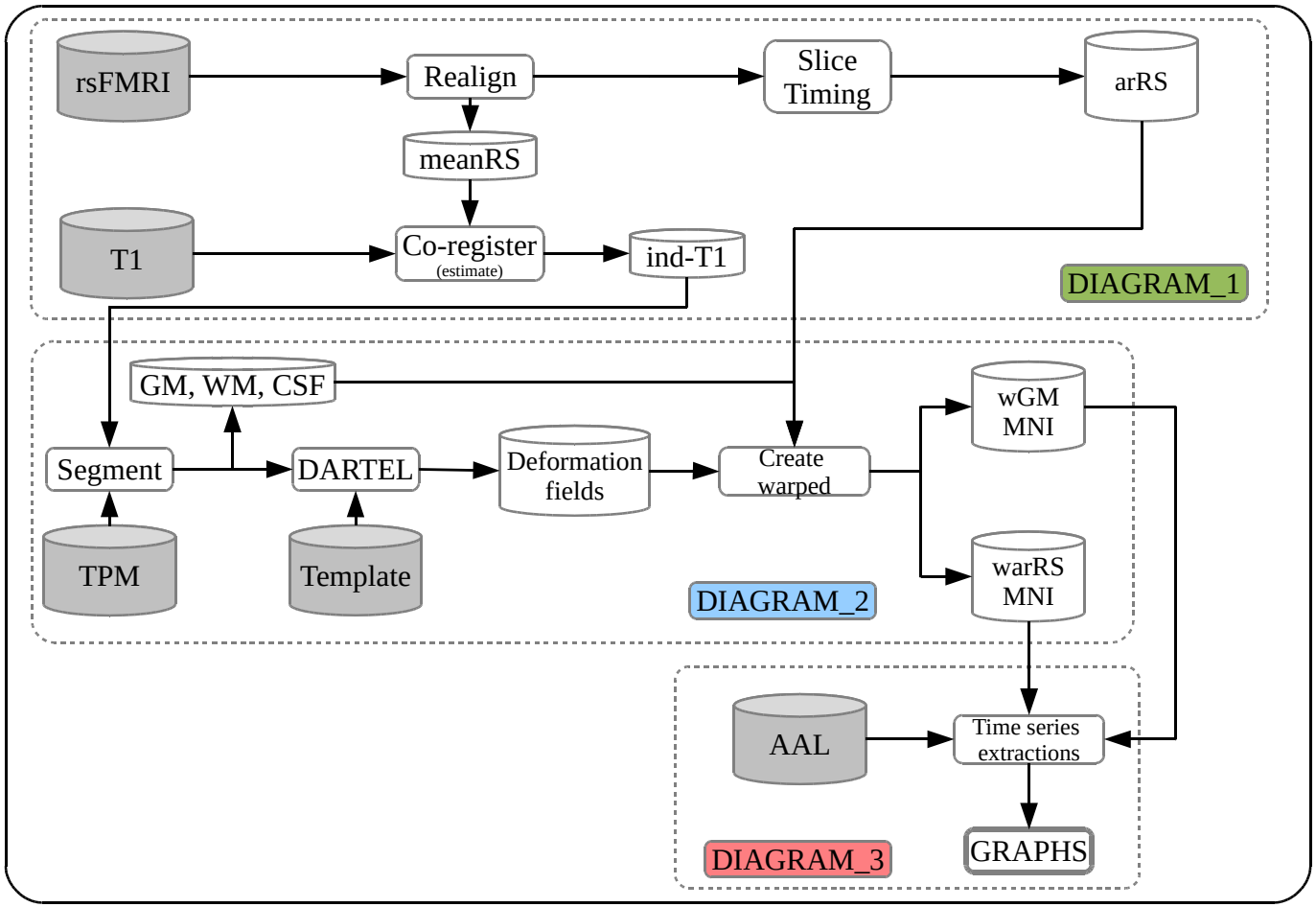

Figure 7.10: Complete outline with all the required steps to preprocessed the data upto the time series computation.

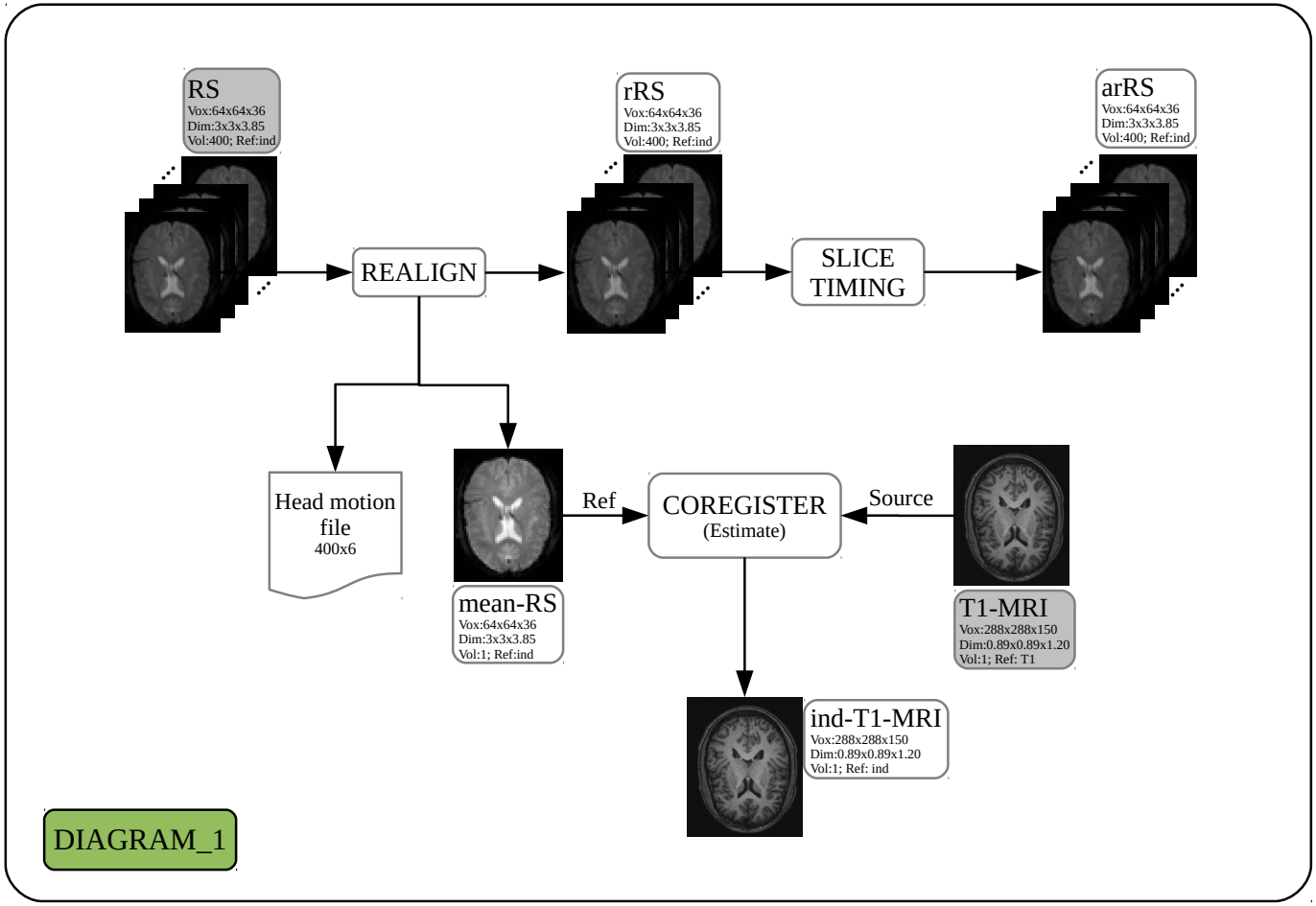

Figure 7.11: Detailed steps of the first part of the preprocessing pipeline involving realignment and slice time correction of EPI data and the coregistration of the anatomical T1 and the mean resulting image of the realigned EPI data.

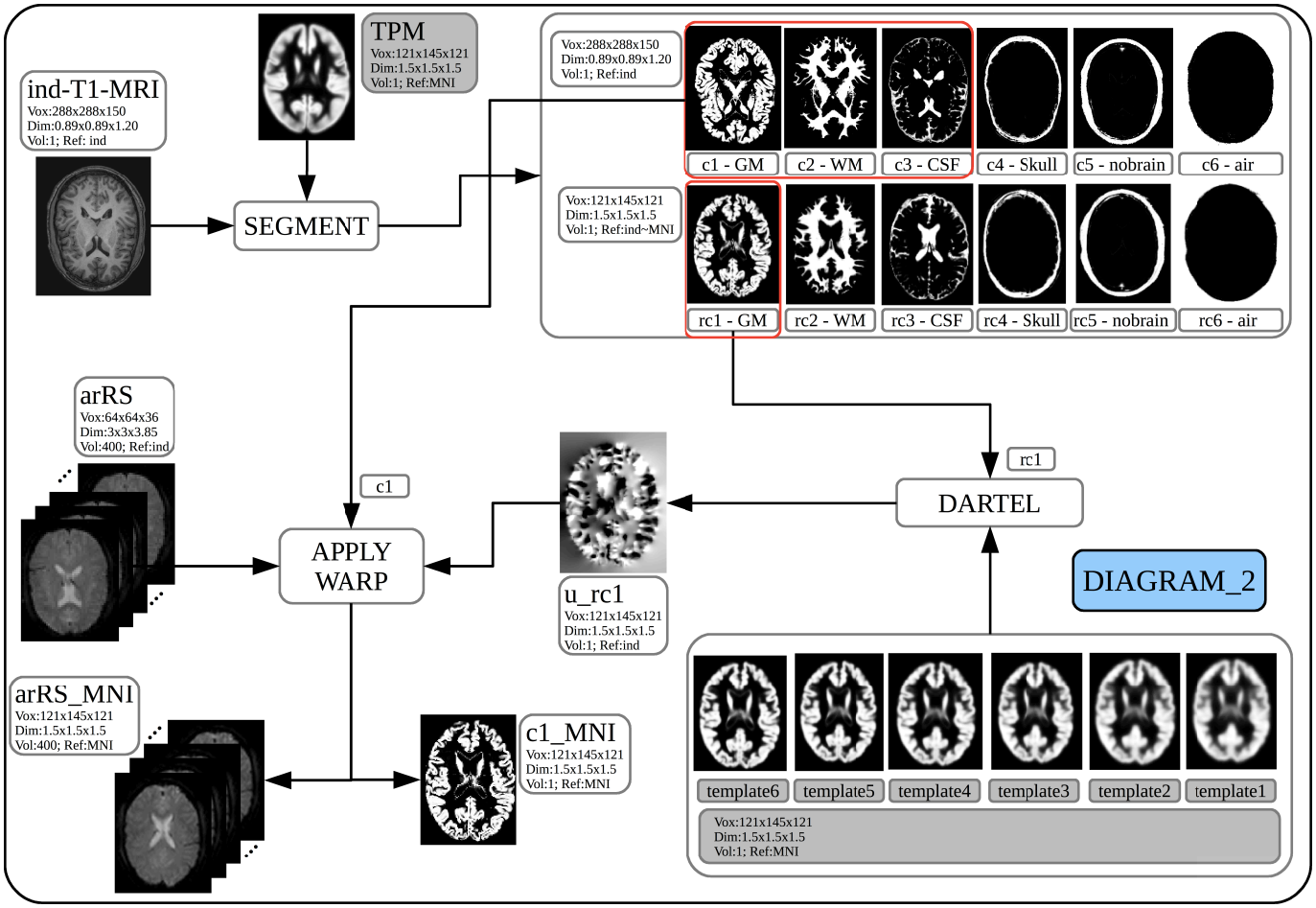

Figure 7.12: Detailed steps of the second part of the preprocessing pipeline involving the segmentation of the structural T1 into 6 different tissues and the extraction of the deformation fields after diffeomorphic transformation of the grey matter volume.

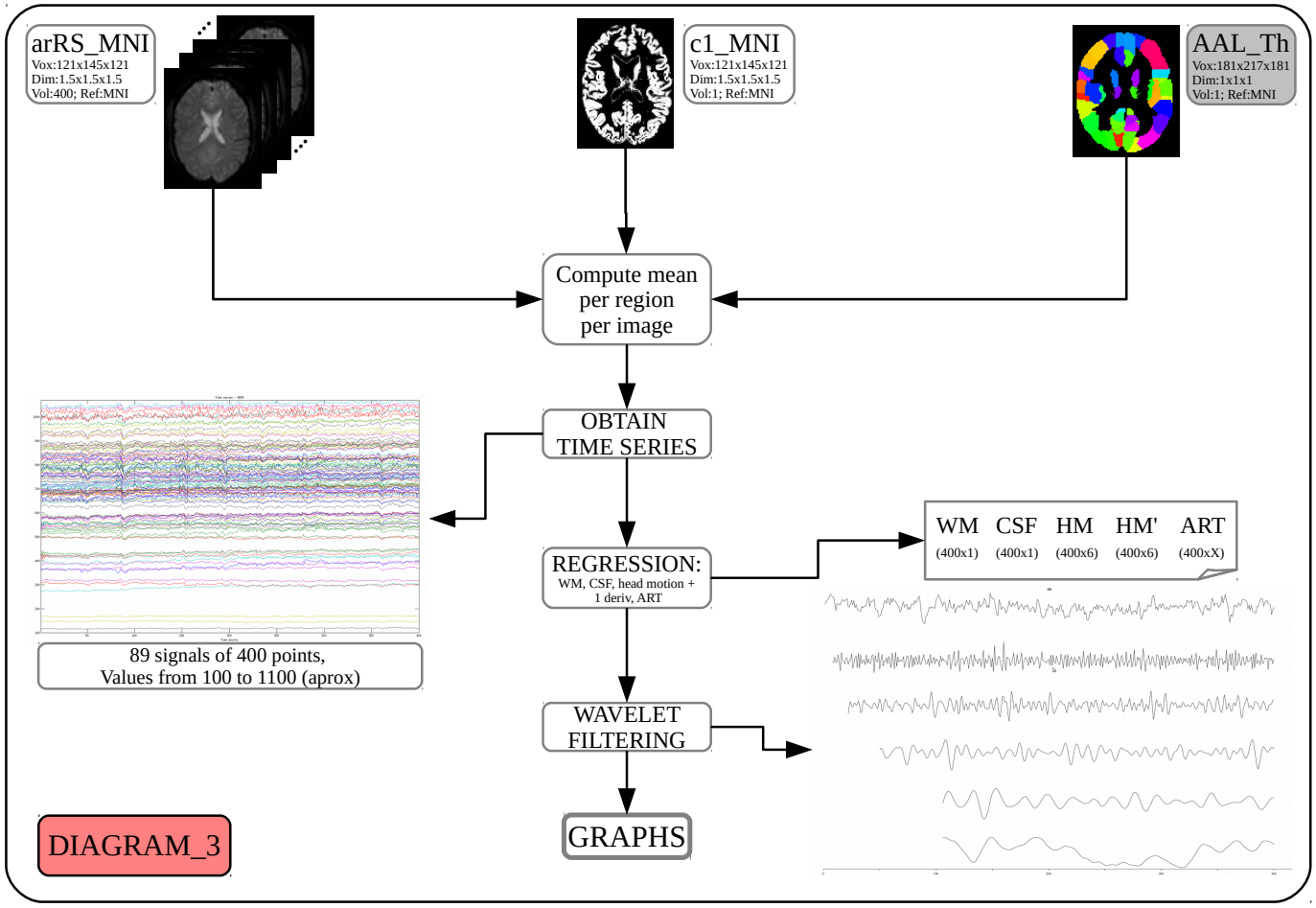

Figure 7.13: Detailed steps of the last part of the preprocessing pipeline involving the computation of the mean voxel value per region to obtain the time series, the confound removal of motion parameters, and the division of the time series into different frequency bands applying discrete wavelet decomposition. AAL-Th: Parcellation scheme; ART: outlier detection toolbox.

Chapter 8

Test-retest reliability of graph based brain functional connectivity

This chapter corresponds to our Neuroimage publication:

M. Termenon, A. Jaillard, C. Delon-Martin, S. Achard, **Reliability of graph analysis of resting state fMRI using test-retest dataset from the Human Connectome Project**, NeuroImage, Available online 6 June 2016, ISSN 1053-8119, http://dx.doi.org/10.1016/j.neuroimage.2016.05.062

8.1 Introduction

The exploration of brain networks with resting-state fMRI (rs-fMRI) combined with graph theoretical approaches has become popular, with the perspective of finding network graph metrics as biomarkers in the context of clinical studies. A preliminary requirement for such findings is to assess the reliability of the graph based connectivity metrics. In previous test-retest (TRT) studies, this reliability has been explored using intraclass correlation coefficient (ICC) with heterogeneous results. But the issue of sample size has not been addressed. Using the large TRT rs-fMRI dataset from the Human Connectome Project (HCP), we computed ICCs and their corresponding p-values (applying permutation and bootstrap techniques) and varied the number of subjects (from 20 to 100), the scan duration (from 400 to 1200 time points), the cost and the graph metrics, using the Anatomic-Automatic Labelling (AAL) parcellation scheme. We quantified the reliability of the graph metrics computed both at global and regional level depending, at optimal cost, on two key parameters, the sample size and the number of time points or scan duration.

8.2 Methods

8.2.1 Subjects and data acquisition

The dataset used for this experiment was selected from a large sample of rs-fMRI dataset publicly released as part of the Human Connectome Project (HCP), WU-Minn Consortium. Our sample includes 100 subjects: 99 young healthy adults from 20 to 35 years old (54 females) and 1 healthy adult older than 35. Each subject underwent two rs-fMRI acquisitions on different days. Subjects were instructed to keep their eyes open and to let their mind wander while fixating a cross-hair projected on a dark background [Smith et al., 2013a].

Data were collected on the 3T Siemens Connectome Skyra MRI scanner with a 32-channel head coil. All functional images were acquired using a multiband gradient-echo EPI imaging sequence with the following parameters: 2 mm isotropic voxels, 72 axial slices, TR = 720 ms, TE = 33.1 ms, flip angle = 52, field of view = 208x180 mm^2, matrix size = 104x90 and a multiband factor of 8. A total of 1200 images was acquired for a scan duration of 14 min and 24 s. For more detailed parameters, see [Smith et al., 2013a]. Two high resolution structural images T1-weighted (T1w) and T2-weighted (T2w) were further collected. They were acquired with a 3D MPRAGE sequence and a 3D T2-SPACE sequence, respectively. The main MR parameters for the T1w image were: TR = 2.4 s, TE = 2.14 ms, TI = 1000 ms, flip angle = 8, field of view = 224 x224 mm^2 and 0.7 mm isotropic voxels and for the T2w: TR = 3.2 s, TE = 565 ms, flip angle = variable, field of view = 224 x224 mm^2 and 0.7 mm isotropic voxels.

8.2.2 Data preprocessing

Structural data were preprocessed according to the pipeline described by Glasser et al. [2013]. In brief, it corrects T1w and T2w for bias field and distortions, coregisters them together and registers them to the MNI152 atlas using linear and nonlinear registrations, using FSL's FLIRT and FNIRT functions. After registration to the atlas image, we segmented the individual T1w in six different brain tissues to obtain a grey matter (GM) probability maps that will be later used to extract the time series to compute the graphs.

Functional data were corrected for distortions and subject motion. They were registered to the individual structural image and further to the MNI152 atlas space using the transforms applied to the structural image. All of these preceding transforms were concatenated, together with the structural-to-MNI nonlinear warp field, so that a single resulting warp (per time point) was applied to the original time series to achieve a single resampling into MNI space with a final isotropic voxel size of 2 mm. Finally, the 4D image was normalized to a global mean and the bias field was removed, and non-brain voxels were masked out. No spatial smoothing was applied. For more details of the spatial preprocessing pipeline, see Glasser et al. [2013].

8.2.3 Time series extraction and analysis using wavelets

Based on anatomical features, we used a modified version of the classical Anatomic-Automatic Labeling (AAL) [Tzourio-Mazoyer et al., 2002] composed of 89 regions (see Appendix A for more information). In each parcel, regional mean time series were estimated by averaging, at each time point, the fMRI voxel values weighted by the GM probability of these voxels. This weighting limits the contamination of the time-series by white matter signals and cerebrospinal fluids. We reduce the influence of the partial volume effect related to voxels that contains both GM and WM or GM and CSF. The problem of regressing out WM and CSF in the functional data is that it may remove also some GM signal. The mean white matter and cerebrospinal fluid signals were thus not regressed. Residual head motion were eventually removed by regressing out motion parameters and their first derivative's time series. Global signal regression was not applied, since it was shown to introduce severe artifacts [Murphy et al., 2009], resulting in correlation pattern distortions [Saad et al., 2012].

The resulting time series were decomposed in 5 scales using discrete dyadic wavelet transformation. Wavelet transforms perform a time-scale decomposition that partitions the total energy of a signal over a set of compactly supported basis functions, or little waves, each of which is uniquely scaled in frequency and located in time [Achard et al., 2006]. We applied the maximal overlap discrete wavelet transform (MODWT) to each regional mean time series and estimated the pairwise inter-regional correlations at each of the five wavelet scales[1]. We performed our analysis at wavelet scale 4. Indeed, resting state signal is currently analyzed in frequencies below 0.1 Hz [Biswal et al., 1995, Fox and Raichle, 2007], thus the relevant information for rs-fMRI data is mainly contained within the scale 4 that represents the frequency interval $[0.043 - 0.087]$ Hz. Scale 3 is omitted because it belongs to the frequency range between $[0.087 - 0.17]$, thus it contains signal from frequencies higher than 0.1 Hz. The frequency bands extracted using wavelets are reported in the table A.1. For a comparison with classical acquisitions using a higher TR, the table reports also the wavelet frequency bands obtained with a TR of 2 s. As the interest in resting-state fMRI study is on low frequencies, the most important parameter is the time duration of the acquisition. The table A.1 provides details to link the duration of the scan to the number of points and the corresponding frequency bands of interest.

8.2.4 Graph computation

All pairs of scale 4-specific wavelet correlations between regions are further pooled into a correlation matrix for each of the subjects. To compute the graph, we first extracted the minimum spanning tree based on the absolute correlation matrix [Alexander-Bloch et al., 2012] to keep the graph fully connected, and

[1]The comparison between wavelets and band pass filtering was already tested in Guo et al. [2012]. They found that "ROI matrix reliability improved substantially when ROI time series correlations were computed after wavelet transformation".

the remaining absolute values of correlation matrices were thresholded to create an adjacency matrix that defines an unweighted graph for each subject. A threshold R was calculated in order to produce a fixed number of edges M to be able to compare the extracted graphs. As a consequence, the threshold value is subject dependent. The ratio between the number of selected edges and all possible edges is termed "cost", implying that the higher the cost the larger number of edges is considered in the computation of the graph. For example, with a parcellation of 89 regions, the number of edges are 391 at 10% cost and 1564 at 40% cost. Each of these extracted graphs comprised N=89 nodes corresponding to the anatomical regions, and M undirected edges corresponding to the significant correlation values above the threshold R [Achard et al., 2012]. There exists no straightforward way to select the appropriate cost [De Vico Fallani et al., 2014]. Achard and Bullmore [2007] introduced the small-world regime which defines a range of cost that is a vector of values of cost. The low limit of the range is defined by a sufficiently large number of edges so that the graph is different from regular or random graphs. The upper limit is reached when the graph has too many edges and cannot be differentiated from random or regular graphs.

8.2.5 Computation of graph metrics

It has been shown that graph metrics have different properties and highlight different topological characteristics of the graphs, see Boccaletti et al. [2006] for a review. Global efficiency, minimum path length or betweenness centrality are interpreted as measures to facilitate functional integration [Rubinov and Sporns, 2010], quantifying how information is propagating in the whole network. Moreover, local efficiency or clustering coefficient are measures associated to segregation functions [Rubinov and Sporns, 2010] and can be regarded as measures of information transfer in the immediate neighborhood of each node. All these measures were used to quantify the graph metrics at the global level with the extraction of one quantity for each graph, subject and session. However, these metrics can also be evaluated at the nodal or regional level, i.e. one value is computed for each node of the graph or region of the brain. For each subject, session and graph, we computed a vector of parameters quantifying the same characteristics but at the regional level. Table 8.1 presents a summary of each metric used in the paper. The detailed formulas can be found in [Rubinov and Sporns, 2010]. Network parameters computation was preformed in R using *brainwaver* and *igraph* libraries, tools that are freely available on CRAN[2,3].

8.2.6 Test-retest reliability

The assessment of reliability using proper statistical methods needs caution in terms of interpretation. The first studies date back to the last century and the work of Fisher [Fisher, 1925], who proposed to use an ANOVA with a separation

[2]http://cran.r-project.org/web/packages/brainwaver/index.html
[3]http://cran.r-project.org/web/packages/igraph/index.html

Parameter	Character	Description
Regional networks parameters		
Degree	k_i	Number of edges connected to a node i.
Global efficiency	e_{g_i}	Communication efficiency of a node i with all other nodes.
Local efficiency	e_{l_i}	Communication efficiency of a node i with its neighbors.
Betweenness centrality	b_i	Influence of a node i over the information flow between all other nodes.
Clustering coefficient	c_i	Fraction of the neighbors of a node i that are also neighbors of each other.
Global network parameters		
Global efficiency	E_g	Mean of e_{g_i}.
Local efficiency	E_l	Mean of e_{l_i}.
Modularity	Q	Strength of division of a network into clusters of nodes highly connected between them.
Betweenness centrality	B	Mean of b_i.
Small world topology	σ	Extent of a network between randomness and order.
Clustering coefficient	C	Mean of c_i.

Table 8.1: Description of the network metrics. Detailed information and metrics computation can be found in [Rubinov and Sporns, 2010]. We explored both regional metrics computed at the level of the nodes of the graphs and global metrics that correspond to the average of the regional metrics other the whole graph.

of within-subject and between-subject variability. In this study, the adopted statistical model for the observations Y_{ij} for the jth session of the ith subject, is defined as

$$Y_{ij} = \mu + S_i + e_{ij},$$

where μ is the mean of all the observations in the population, the group effects S_i are identically distributed with mean 0 and variance σ_A^2, the residual errors e_{ij} are identically distributed with mean 0 and variance σ_e^2, and the S_i and e_{ij} are independent [Donner, 1986]. This model is frequently used in several fields of research, such as, for example, epidemiology, psychology and neuroimaging as shown in a recent review on graph metrics [Welton et al., 2015], and in a meta-analysis of reliability graph metrics of rs-fMRI brain networks [Andellini et al., 2015]. The intraclass correlation coefficient is then defined as the following ratio, $\rho = \sigma_A^2/(\sigma_A^2 + \sigma_e^2)$.

In Müller and Büttner [1994], authors highlight the difficulties to choose proper statistical measures of reliability depending on the design of the experiment. In this study, our aim was to test the reliability of inter-session acquisitions. To determine the level of reliability between two acquisitions [McGraw and Wong, 1996], we used intraclass correlation coefficient (ICC), which is based on the comparison of the within-subject and between-subject variability. This coefficient may not be adequate to test the conformity of methods or interchangeability as pointed out by [Bland and Altman, 1986], however it provides a quantitative value to easily build statistical comparisons.

8.2.6.1 Intraclass correlation coefficient (ICC)

ICC, as defined in the previous section, assesses the reliability of graph connectivity metrics by comparing the variability of these metrics during different sessions of the same subject to the total variation across all sessions and all subjects.

In line with several previous studies [Birn et al., 2013, Wang et al., 2011, Liang et al., 2012], we have applied a one-way random effect model, noted ICC(1,1) following Shrout and Fleiss [1979]. This provides an estimation of ρ defined by,

$$ICC = \frac{s_b - s_w}{s_b + (k-1)s_w} \tag{8.1}$$

where s_b is the variance between subjects, s_w is the variance within subjects and k is the number of sessions per subject. ICC is close to 0 when the reliability is low, and close to 1 when the reliability is high. Note that ICC, as estimation of ρ using equation (8.1), may take negative values when the variance within subjects is larger than between subjects. This is due to statistical errors given a particular data set and should be considered as non reliable estimation.

A first approach to interpret the ICC is to classify its values into different categories with commonly-cited cutoffs [Cicchetti, 1994, Sampat et al., 2006]: less than 0.4 indicates low reliability, 0.4 to 0.6 indicates fair reliability; 0.6 to 0.75 indicates good reliability and greater than 0.75 indicates excellent reliability. However, there are several limitations of ICC approaches, as described by Müller and Büttner [1994]. First, ICC estimation may vary according to the estimation method leading to different versions of ICCs, based usually on parametric and non parametric approaches. In parametric approaches, ICCs vary according to the distribution and the equality of variances of the population. In addition, ICCs are dependent on the range of the measuring scale. Consequently, there is no reason to judge an absolute ICC as indicating good consistency, and it has been recommended to calculate confidence intervals (CI) in addition to ICCs [Shrout and Fleiss, 1979].

The ICCs and their CI evidenced a large range for different graph metrics throughout the test-retest literature. CI are computed using F-distribution (*e.g.* the reviews of Boardman [1974], Donner and Wells [1986]) with degrees of freedom depending on the number of groups and number of subjects. In Cao et al. [2014], the authors computed the CI of ICCs and they reported, for example, that for an ICC of 0.45 for the E_g, the confidence interval was evaluated to be equal to $[0.09-0.71]$, for an ICC of 0.26 in b_i, the confidence interval was ranging between $[0.05-0.55]$, and for an ICC of 0.24 for e_{g_i}, the confidence interval was evaluated to be equal to $[0.04-0.55]$. These values of CI were computed with 26 subjects scanned twice. This example where ICCs were ranging from not reliable to good reliability, highlights that confidence intervals are unstable and difficult to interpret, especially in the context of fMRI studies with small sample size. In order to cut the margin of error in half, it is needed to approximately quadruple our sample size [Shrout and Fleiss, 1979]. In a paper exploring several methods for constructing intervals for ICC, small sample size studies and

normality assumption violation resulted in wide average interval width [Ionan et al., 2014].

8.2.6.2 p-values of ICC using permutation tests

In addition to the study of absolute values of ICC, p-values of ICC can be used. The addition of p-values allows a precise statistical analysis to evaluate the accuracy and significance of the extracted ICCs. The difficulty of working with p-values comes from the necessity to have access to the law of the estimators under the null hypothesis. In the case of ICC, it is possible to define an F-test to determine whether the ICC is significantly different from zero for a given level of confidence [McGraw and Wong, 1996]. However, this parametric approach can be too restrictive when the sample of the data is too small or far from the Gaussian assumption.

Therefore, we propose to use a recent development of permutation tests to get a data-driven non parametric approach [Boardman, 1974]. Each permutation consists in shuffling the acquisition sessions so that for each new subject the two sessions correspond to two different initial subjects, in particular, we shuffle the order of the subjects in the second session. The aim is to model the randomness of the measurements. For each permutation, we computed ICCs which produce a distribution of values where the two sessions correspond to a random choice of subjects, all or some of the paired sessions were disturbed. The true value of ICC obtained with the correct pairs of session of the same subject was then compared to the obtained distribution, hence the p-value is computed. The up-to-date statistical methods, based on Monte Carlo simulation [Metropolis and Ulam, 1949], test the reliability of our sample by randomly permuting the sessions between subjects. Two different tests were constructed. The first one concerns the global network level, where the goal is, for a given cost, to compute the p-value of the ICC for each metric. For that purpose, we use Simctest [Gandy, 2009]. It is an open-ended sequential algorithm for computing the p-value of a test using Monte Carlo simulation. It guarantees that the resampling risk, the probability of a different decision than the one based on the theoretical p-value, is uniformly bounded by an arbitrarily small constant. Although the algorithm is open-ended, the expected number of steps is finite, except when the p-value is on the threshold between rejecting and not rejecting. In the sequel of the paper, the ICC is used with p-values (of ICCs), with the aim of modeling the randomness of the measurements. We consider as reliable ICCs with a p-value≤ 0.05.

A second issue concerns the regional network level, where the tests are applied for each region of the parcellation scheme. In this case, we apply MMCtest [Gandy and Hahn, 2014] which is based on Simctest and includes a correction for multiple comparisons that is crucial when manipulating a large number of regions. Here, we applied the Benjamini-Hochberg procedure that controls the false discovery rate (FDR). These tools are freely available on CRAN [4].

[4] http://cran.r-project.org/web/packages/simctest/index.html

In addition to the permutation, a step of bootstrap was associated to take advantage of the large size of the data set. For example, the results derived for 20 subjects were performed by first choosing at random without replacement a set of 20 subjects among the 100 in the original data set, and the p-values were computed using permutations of the restricted 20 subjects data set. This bootstrap test is repeated N times with a new set of 20 subjects for each repetition. We performed these tests considering 20, 30, 40, 60, 80 and 100 subjects to study how the reliability of the graph metrics depends on the subjects sampling procedure. In the case of $20 - 80$ subjects, we repeated the Simctest $N = 1000$ times and MMCtest, $N = 100$ times, selecting each time a random subsample of the data. We also repeated these bootstrap tests considering different number of volumes/time points. The original scan duration has 1200 time points at a TR=720ms, corresponding to a total duration of 14 min 24 s. We split it into four: 400 time points (4 min 48 s), 600 time points (7 min 12 s), 800 time points (9 min 36 s) and 1000 time points (12 min 00 s). All the subdivisions were extracted from the beginning of the time series up to each threshold.

8.3 Results

We analyzed the reliability of the graphs with respect to different factors that may influence ICCs and p-values: the sample size (number of subjects), the number of time points (duration), the graph metrics (global and regional), and the cost.

8.3.1 Between, within variances, ICC and p-values for E_g with respect to cost

ICC is based on the variance between and within subjects (see Eq. (8.1) and Fig. 8.1). Fig. 8.1 illustrates the computations of ICC, and p-values. The p-values are obtained using permutation techniques, and the error bars are obtained by using bootstrap on the number of subjects (no error bars can be computed using the whole set of 100 subjects). The first column of Fig. 8.1 displays the values of the between-subject variance s_b, and the within-subject variance s_w. Whatever the cost, for E_g, the between-subject variance s_b was found higher than the within-subject variance s_w with a maximum difference in the 15%-30% range. At high cost, these values are very small, and very close to each other so that the denominator of the ICC formula (s_b+s_w) is small, and results in high values of ICC (second column of Fig. 8.1). The p-values are displayed in the third column, so that in addition to the absolute values of ICC, the p-values are given an indication of confidence of these values compared to the randomness of the measurements.

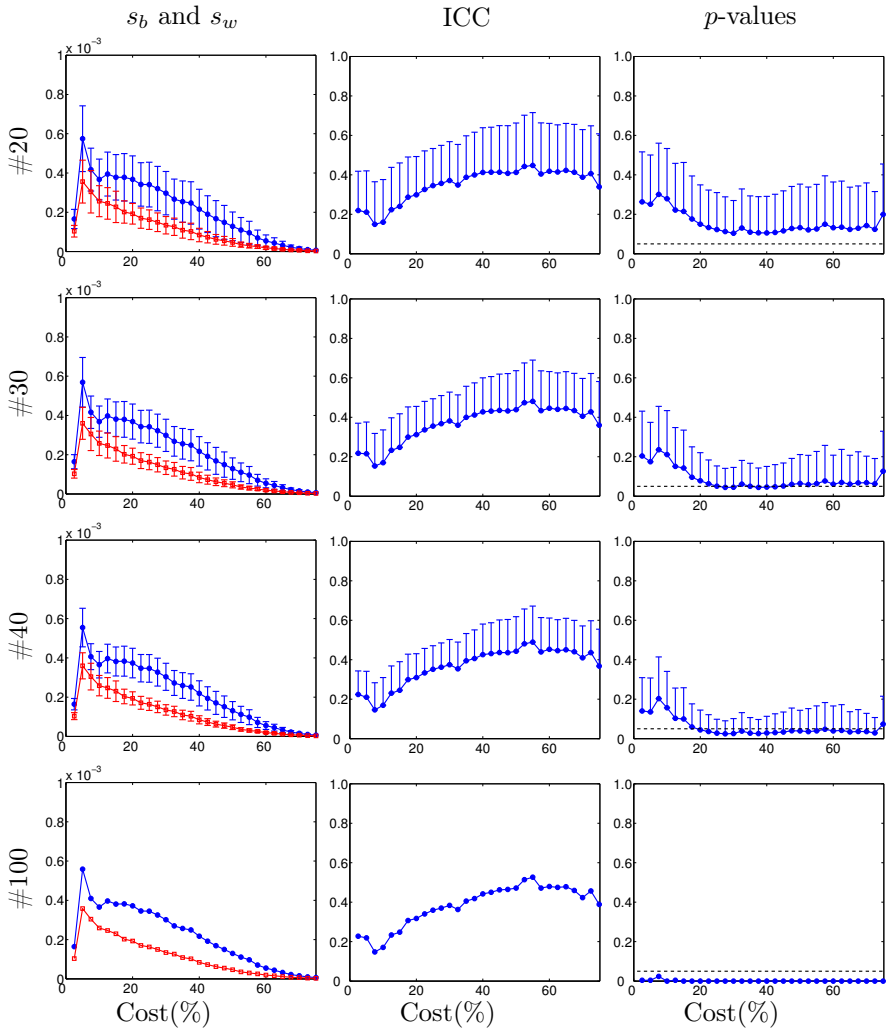

Figure 8.1: Reliability measures using ICC for global efficiency (E_g) and AAL89 as parcellation scheme. Each curve represents the between and within subjects variance (first column, respectively s_b in blue and s_w in red), values of ICC (second column) and associated p-values (third column) for E_g at 1200 time points as a function of the cost from 2.5% to 75%, in steps of 2.5%. Each row represents a different number of subjects (20, 30, 40 and 100 subjects). Error bars indicate one standard deviation of the bootstrap procedure. 1000 bootstraps were computed to select different subsamples of 20, 30 and 40 subjects. As the number of subjects is increasing, the p-values are decreasing, and the reliability is increasing. For 20 subjects, no p-values are significant, showing a poor reliability. However, for 40 subjects, p-values are significant for a large range of cost and reliable results are expected.

8.3.2 Influence of the number of subjects

On average, s_b, s_w and ICC values are very similar whatever the number of subjects (see Fig. 8.1) but we can observe a decrease in the standard deviation as the number of subjects increases, resulting in a decreasing p-value with increasing number of subjects. Below 20% cost, the p-values of the ICCs reach significance only with 100 subjects. With 20 subjects the ICCs are only significant by chance. On average, with 30 subjects the ICCs are only significant from around 25% to 45% cost while with 40 subjects, they are significant from around 20% to 72.5% cost. In the case of 100 subjects, ICCs remain significant from 2.5% to 75%.

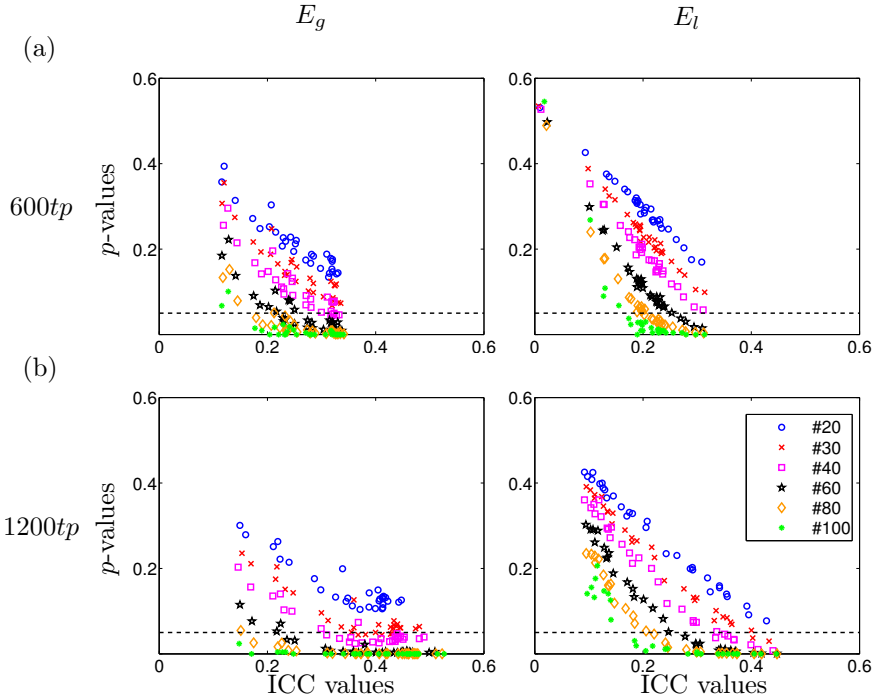

Figure 8.2: Reliability results in terms of number of subjects and scan duration. p-values of ICC (y-axis) as a function of ICC values (x-axis) for different number of subjects and different scan duration. (a) Using 600 time points, which corresponds to a scan duration of 7 min 12 s and (b) using 1200 time points (14 min 24 s). Mean result after 1000 bootstraps for cost values ranging from 2.5% to 75% are plot for 20, 30, 40, 60 and 80 subjects and for two global network parameters: E_g (left panels) and E_l (right panels). Note that increasing the scan duration and the number of subjects resulted in decreased p-values and that ICCs increase as the scan duration increases. Results correspond to the AAL89 parcellation scheme.

At global level, we plot in Fig. 8.2 the ICCs and their respective p-values

of E_g and E_l for costs between 2.5% to 75.0% at 600 and 1200 time points. The results for 20, 30, 40, 60, 80 and 100 subjects are displayed (computing the mean ICC and p-values of 1000 bootstraps in the first five cases). We observed that for a given ICC value, its significance depends on the number of subjects and on the cost range. The less significant results were observed for costs below 20%.

Considering the experimental conditions with 1200 time points, with 20 subjects, ICCs were not significant for the analyzed metrics. With 30 subjects, we can obtain significant ICCs from 25% to 45% cost for E_g and for E_l from 30% to 35% cost. When considering 40 subjects, significant ICCs are observed for E_g in the cost range from 20% to 72.5%, and for E_l, in the cost range between 7.5% to 35%. With 60 subjects, significant ICCs are observed from 12.5% to 75% cost for E_g and for E_l from 7.5% to 40% cost. With 80 subjects, ICCs are significant from 5% to 75% cost for E_g and for E_l from 5% to 45% cost. With 100 subjects, in the case of E_g, ICCs were found significant at any cost, while with E_l, in the range between 2.5% to 52.5%.

With 600 time points (Fig. 8.2 (a)), a similar evolution with the number of subjects is observed but with less significant values corresponding to smaller cost range.

8.3.3 Influence of the number of points in time

At global level, we found that the reliability increases with the number of time points. In Fig. 8.2 (b), the p-values are plot with respect to ICC for 1200 time points (corresponding to 14 min 24 s) and in Fig. 8.2 (a) for 600 time points (7 min 12 s), a duration currently used in the rs-fMRI literature (though, usually, with a TR=2s). We can observe that with 600 time points, the ICCs are reliable from 60 subjects, whereas with 1200 time points, reliable E_g and E_l can be achieved with groups of 40 and even 30 subjects at different cost range, as we mentioned in previous section.

In Fig. 8.3, we display the p-values of ICC for E_g at 20% cost with respect to the number of time points for different groups of subjects. This result shows that it is not possible to achieve reliable results with 400 time points at 20% cost, even with 100 subjects. At 20% cost, significant p-values of the ICC are found to be achieved with 1200 time points and 40 subjects or for length above 600 time points and 60 subjects. At 400 time points, ICCs for the E_g are only significant for the range $37.5 - 55.0\%$ cost in 100 subjects (not shown).

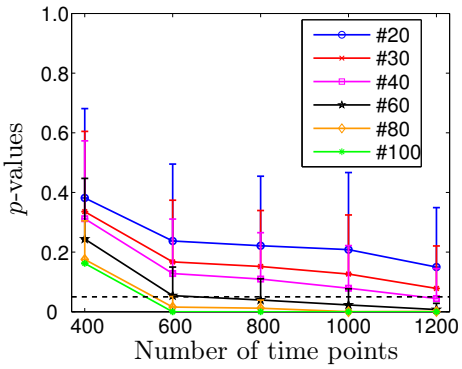

Figure 8.3: Reliability trade-off between number of subject and number of points in time using AAL89 as parcellation scheme. Evolution of the significance of global efficiency at global network level when increasing the number of points in time and the number of subjects. E_g mean p-values at different points in time applying 1000 bootstraps of 20, 30, 40, 60 and 80 subjects and for 100 subjects. All the results shown are computed at 20% cost. The number of subjects to achieve reliable results depends on the number of time points: a larger number of subjects is needed for a short scan duration. The correspondence between scan duration and time points is as follows: 400 time points (4 min 48 s), 600 time points (7 min 12 s), 800 time points (9 min 36 s), 1000 time points (12 min 00 s) and 1200 time points (14 min 24 s). All the subdivisions were extracted from the beginning of the time series up to each threshold.

8.3.4 Graph metrics reliability

At the global network level, in Fig. 8.4, we plot the p-values of ICC at different costs and for 6 different graph metrics. Plots on the left six panels correspond to 40 subjects randomly chosen 1000 times, and on the right panels computed with 100 subjects. In the former, with 40 subjects, E_g and B are significant from $20-60\%$ cost, E_l and C from $7.5-35\%$ cost, σ from $7.5-20\%$ cost and Q from $10-25\%$ cost, approximately. In the latter, with 100 subjects, all metrics are significant from 10% to around 40% cost.

At the nodal network level, Fig. 8.5 represents Pearson's correlation matrix between the p-values of the ICC of the different graph metrics at 1200 time points, with 30 subjects and 20% cost. It is possible to see that p-values of the ICC of e_{l_i} and c_i are highly correlated (89.00%) and p-values of the ICC for e_{g_i} and k_i are correlated (72.49%), while the rest of the metrics are not. This high correlation between p-values of the ICC of metrics means that same regions in the brain have similar significance reliability between those metrics.

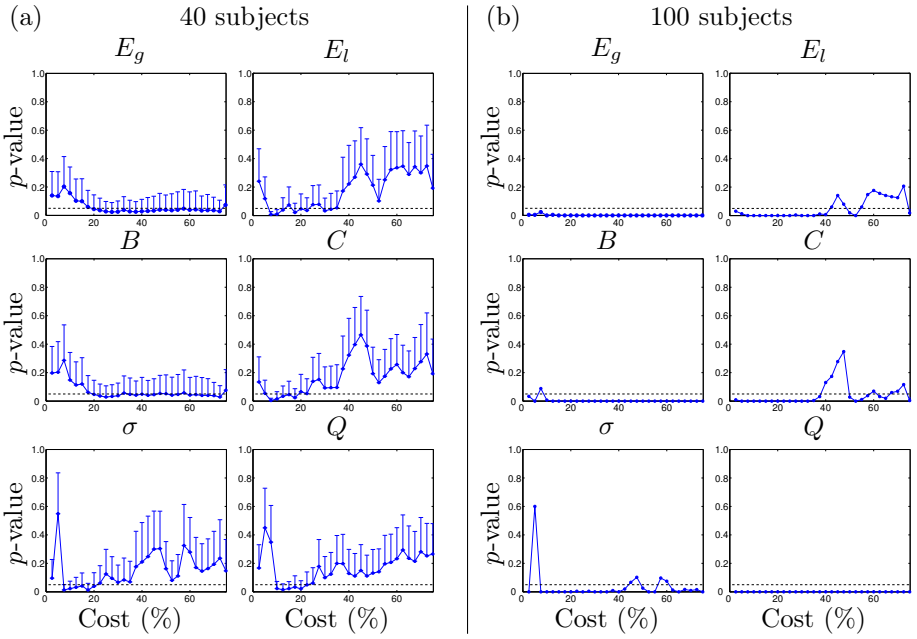

Figure 8.4: Reliability evaluation of different metrics using AAL89 as parcellation scheme. Mean p-values of ICC and standard deviation of 6 different global network parameters: global efficiency (E_g), local efficiency (E_l), betweenness centrality (B), clustering (C), small worldness (σ) and modularity (Q). Cost ranges from 2.5 to 75%. (a) 1000 bootstraps with 40 subjects randomly selected are shown using error bars with one standard deviation; (b) with 100 subjects.

8.3.5 Regional metrics reliability

Fig. 8.6 illustrates our first finding in terms of the number of regions that reach significant ICCs; the number of significant regions is dependent on the number of subjects and scan duration. When increasing the number of subjects from 20 to 100, the number of regions with significant reliability is 21 for 20 subjects, 42 for 30 subjects, 57 for 40 subjects, 77 for 60 subjects, 85 for 80 subjects and up to 87 for 100 subjects. The e_{g_i}, e_{l_i} and b_i with their p-values of all the AAL89 ROIs for 1200 tp at 20% cost can be found at the end of this chapter in Table 8.3 for 40 subjects and Table 8.5 for 100 subjects.

The locations of these regions are displayed in Fig. 8.7. Only significant regions are shown for 20, 30 and 40 subjects (100 permutations) and for 100 subjects at 20% cost for e_{g_i} and e_{l_i}.

We finally analyze the reliability of the regional values of global efficiency metrics with the p-values. As high values of regional e_{g_i} and b_i graph metrics are potential indicators of brain key regions [Bullmore and Sporns, 2009], we plot these metrics with their respective p-values at two different costs (20% in blue and 40% in red) for 40 subjects and 1200 tp in Fig. 8.8.

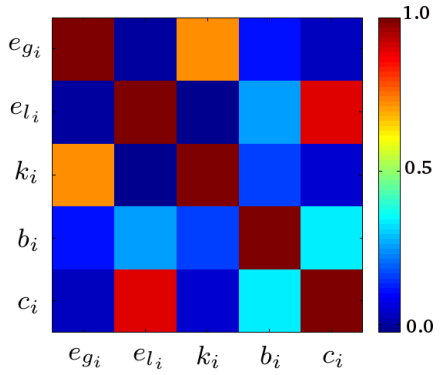

Figure 8.5: Correlation of reliability of graph metrics. Correlation matrix between the p-values of the ICCs of the AAL89 using 5 different regional network parameters. Results are computed at 1200 time points, 20% cost and 100 bootstraps of 30 subjects randomly selected: global efficiency (e_{g_i}), local efficiency (e_{l_i}), node degree (k_i), betweenness centrality (b_i) and clustering (c_i). A high correlation value between two metrics implies that the regions in the brain present similar reliability between those metrics.

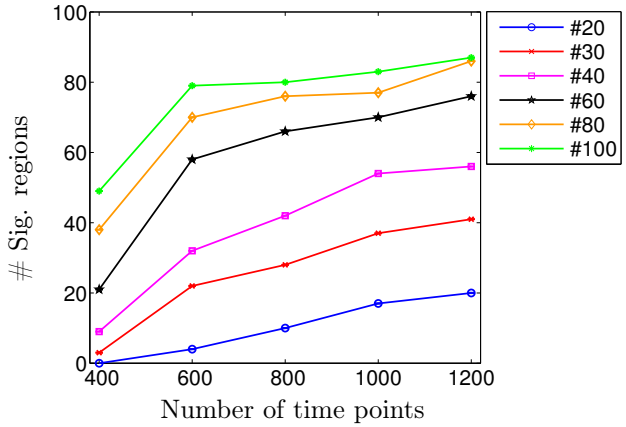

Figure 8.6: Reliability at the regional level using global efficiency and AAL89 parcellation scheme. Number of significant regions, computed using e_{g_i}, as function of the points in time for different number of subjects (corrected for multiple comparisons using a false discovery rate procedures at 0.05%). All the results shown are computed at 20% cost. The correspondence between scan duration and time points is as follows: 400 time points (4 min 48 s), 600 time points (7 min 12 s), 800 time points (9 min 36 s), 1000 time points (12 min 00 s) and 1200 time points (14 min 24 s). All the subdivisions were extracted from the beginning of the time series up to each threshold.

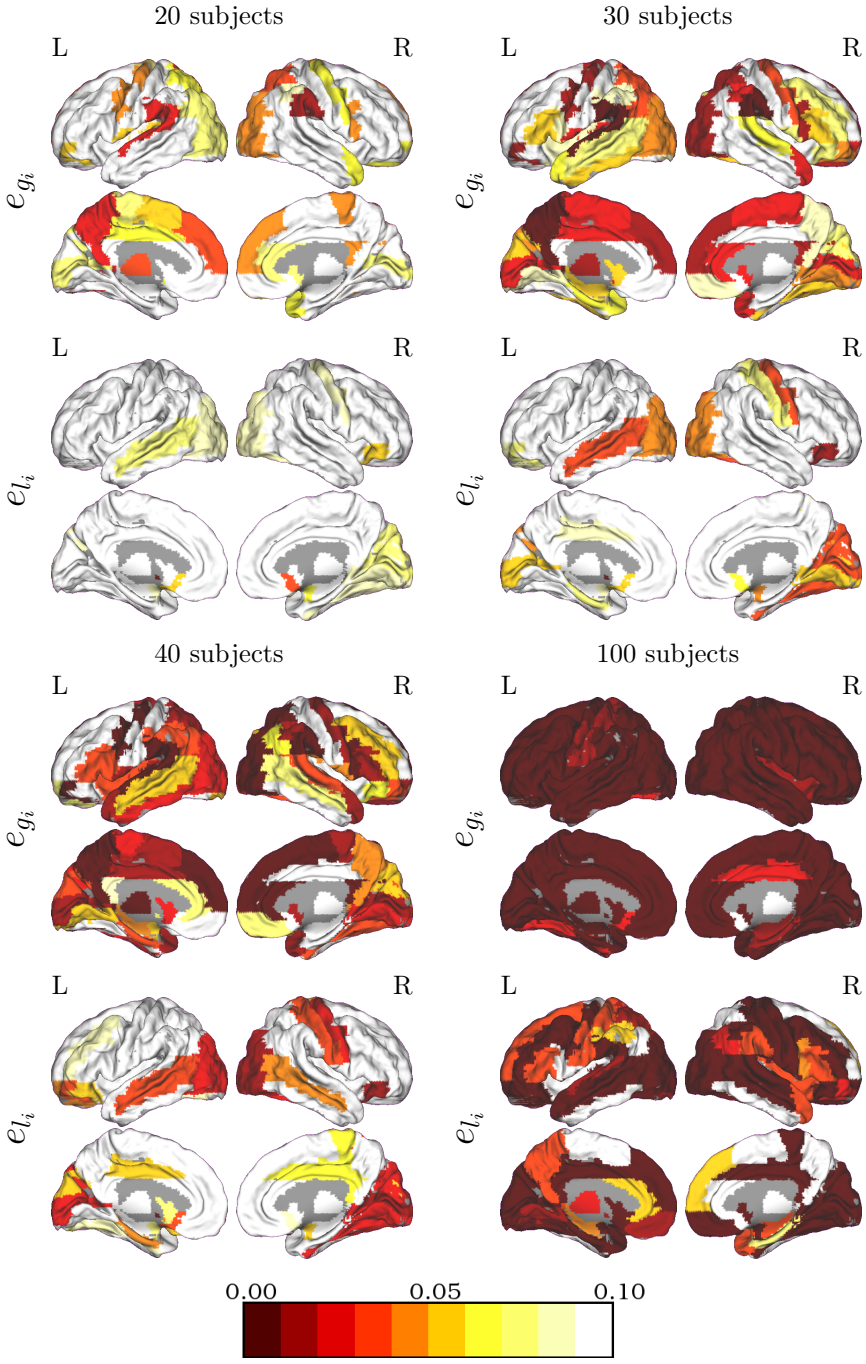

Figure 8.7: Brain maps of reliable regions for AAL89 parcellation scheme. Cortical surface representation of nodes that demonstrated significant regions on the brain using two regional network parameters: global efficiency (e_{g_i}) and local efficiency (e_{l_i}). The displayed p-values are the ones corrected for multiple comparisons using a false discovery rate at 0.05%. First two rows, e_{g_i} for 20, 30, 40 (100 bootstraps) and 100 subjects. Last two rows, e_{l_i} for 20, 30, 40 (100 bootstraps) and 100 subjects. Results were obtained at 1200 time points and 20% cost. The tables of ROI's names with their p-values from 20 to 100 subjects can be found in Appendix together with the e_{g_i} and e_{l_i} of the ROI for 40 subjects.

On average, higher e_{g_i} values are associated with smaller p-values (but not always) at both costs. At 20% cost, with an e_{g_i} of $0.35 - 0.45$, we found a 53% of nodes that are significantly reproducible, while from $0.55 - 0.65$, there are 69%. Contrary, in the case of b_i, there are few significant nodes at both costs, not necessarily the nodes with highest b_i value. In terms of brain networks, this suggests that reliable key regions are better determined using e_{g_i} than b_i. Accordingly, we propose a classification of regions (Table 8.2) based on high e_{g_i} and on their p-values higher or lower than 0.05 to define: regions with high e_{g_i} and low p-value as 'reliable key regions', regions with high e_{g_i} and high p-value as 'non-reliable key regions', regions with low e_{g_i} and low p-value as 'reliable non-key regions', regions with low e_{g_i} and high p-value as 'non-reliable non-key regions'. The threshold for the proposed classification of e_{g_i} was set at the 65th percentile corresponding to values higher than 0.58.

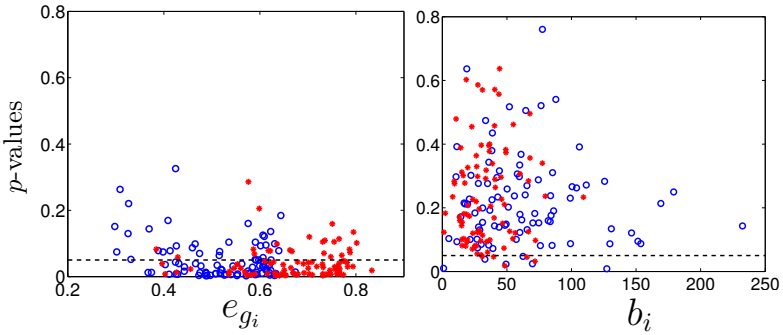

Figure 8.8: Reliability of brain regions in terms of cost using AAL89 as parcellation scheme. Mean e_{g_i} (left) and b_i (right) with their mean p-values. Computed for 40 subjects, 20% cost (in blue), 40% cost (in red) with 100 bootstraps (error bars are not shown) at 1200 points in time. Interestingly, the number of significant reliable regions obtained with betweenness is less than the one obtained with global efficiency. This may show that global efficiency is better at characterizing reliable hubs.

At the end of the chapter, in Tables 8.3-8.5, we show the regional values for different cost, metrics and number of subjects.

8.4 Discussion

The present study has investigated the test-retest reliability of brain network properties/metrics derived from graph theory methods using rs-fMRI acquisition. Original extensive statistical analyses have been conducted by using a large number of subjects (100 healthy participants) and a high number of time points (1200 time points/volumes; 14 min 24 s duration) provided by the test-retest data set of the Human Connectome Project.

	$p \leq 0.05$	$p > 0.05$
$e_{g_i} >= 0.58$	PrecGy (L/R), FrontMid (R), SMA (L/R), CingMid (L), Calcarine (L/R), Cuneus (L/R), Lingual (R), Occipital (L/R), Fusiform (R), ParietalSup (L/R), Precuneus (L/R), TempSup (L/R), TempMid (L), TempInf(L), RolandOperc (L/R), Cereb (VII, VIII, IX, X) (R)	FrontSup (L/R), FrontMid (L), CingMid (R), Lingual (L), Fusiform (L), PoscGy (L/R), TempMid (R), TempInf (R), Insula (R), Cuneus(R), FrontMid (L)
$e_{g_i} < 0.58$	FrontSupOrb (R), FrontMidOrb (L/R), FrontInfOperc (L/R) FrontInfTri (L/R), RolandOperc (L), FrontSupMed (L/R), Insula (L), CingAnt(R), CingPost(R), Hippocampus (L), ParaHippoc (L), ParietalInf (L/R), SupraMarginal (L/R), Angular (L), ParacentralLob (L/R), Caudate (L/R), Putamen (L), Thalamus (L), Heschl (L), TempPole (L/R), TempInf (L), Cereb (I, II) (L/R), Cereb (III, IV, V, VI) (L/R) Cereb (VII, VIII, IX, X) (L), Vermis	FrontSupOrb (L), FrontInfOrb (L/R), Olfactory (L/R), FrontMedOrb (L/R), CingAnt(L), CingPost(L), Hippocampus (R) ParaHippoc (R), Amygdala (L/R), Angular (R) Putamen (R), Pallidum (L/R), Thalamus (R), Heschl (R)

Table 8.2: Regions with strong global efficiency (e_{g_i}) for AAL89 parcellation scheme. Classification of regions according to their e_{g_i} value and their p-value. We consider as key regions the nodes with the 33% of the highest e_{g_i} values (in this case the threshold is $e_{g_i} \geq 0.58$) and p-value $p \leq 0.05$, corrected for multiple comparisons. Some regions not classified as key regions are also found to be reliable. Results are computed using 100 bootstraps of 40 subjects at 1200 time points and a 20% cost.

In this paper, we first showed that ICC can measure reliability only when combined with confidence intervals or p-values. For each tested parameter, we found a smaller within subjects variance in comparison to the between subjects variance. This suggests that the extraction of graph metrics from rs-fMRI brings valuable information that are consistent with a test-retest analysis. However, having a positive difference does not mean that it is statistically significant, and the use of p-values is crucial to quantify the reliability of the rs-fMRI brain connectivity using graph metrics. These p-values were found to be significant for a whole set of parameters showing that the rs-fMRI brain connectivity networks present common characteristics that are shared by a large number of subjects and also individual features that make each subject unique.

Although ICCs are widely used to quantify test-retest reliability, a large discrepancy in ICC values was found in a systematic review of the literature [Welton et al., 2015]. As ICC values depend on both cost and scan length (Fig. 8.2), high ICC scores do not necessarily indicate reliable results. Therefore using confidence intervals [Braun et al., 2012, Cao et al., 2014, Liang et al., 2012, Liao et al., 2013, Birn et al., 2013] or p-values in addition to ICCs offers an efficient procedure for dealing with sometimes inconsistent results among studies jointly characterized by small sample sizes, short scan duration and different fMRI acquisition and analysis techniques. As shown in this work, the advantage of p-values is to provide direct information on the significance of the ICCs, and permutations tests are a very efficient way to compute p-values, when suf-

ficient data are available. Accordingly, we recommend that ICC values should be accompanied by p-values to assess TRT reliability.

The main parameters analyzed in this study are the sample size i.e. number of subjects, scan length, i.e. the duration, choice of metrics and optimal cost. The increase of sample size and scan length was characterized by a decrease on the p-values of ICC illustrating the major role of these two parameters in reaching statistical significance to obtain reliable metrics at the global level. The ability of graph methods to quantify the role of each node of the graph (or region of the brain) allows us to study regional reliability. The p-values of ICC scores were extracted for each region separately and after a correction for multiple comparisons, the decrease of the p-values was confirmed when increasing the sample size or scan length. Major reliable regions, for study with 40 subjects, were found in the default mode network, the motor and the visual networks.

8.4.1 Brain connectivity graphs to find potential biomarkers

Up to now, brain connectivity is mainly studied for the discrimination of groups of patients and used to characterize the disruption in the connectivity affected by a certain disease [De Vico Fallani et al., 2014]. Moreover, graph representation of brain connectivity has the potential to extract a unique representation for each patient and to provide a unique tool to quantify the brain connectivity networks at the individual level. However, from a translational perspective, graph metrics could serve as biomarkers for diagnosis, follow-up and treatment efficacy only if it is proved to be reliable across acquisitions and subjects. We provide in this study the combination of parameters that allow the graph representation of brain connectivity networks to be used as potential biomarkers. As we have observed along the results, the reliability of the graph metrics depends on the number of subjects, the number of time points and the cost of the graph.

Influence of the number of subjects Reliability of global metrics is strongly related to the number of participants that are included in the study, as shown in Fig. 8.1, where the p-values progressively decrease when adding participants. As can be observed in Fig. 8.2 and 8.3, there is a scale in effect for both E_g and E_l, with a threshold number of 40 subjects. Indeed, a minimum number of 80 to 100 participants is recommended to carry out reliable graph analysis at both global and regional network level. This is, to our knowledge, the first report showing the influence of the number of participants in the resting state literature, since previous studies were all performed with a limited number of subjects (between 11 and 33). Indeed, the poor reproducibility of scientific works reported by statisticians [Button et al., 2013, Ioannidis, 2014] would be, at least for a part, due to the low statistical power because of low sample size. This is a strong push for running multisite studies that are powered to obtain reliable results [Button et al., 2013]. This kind of approach is strongly encouraged both by institutions such as the Meta Research Innovation Center

at Stanford [5] and by the neuroimaging community (Consortium for Reliability and Reproducibility (CoRR) [6], with the need to quantify site-related variance. Our findings are derived using a population of healthy volunteers and we focus on reliability as established by TRT studies. The goal of identifying difference between groups of subjects is different and our recommendations may be over evaluated. Indeed, the potentiality to find differences depends on the amplitude of the unknown differences between the two groups. However, if very few assumptions are known when comparing two groups of subjects using our recommendations would minimize the risk of not being able to identify differences between groups.

Influence of scan duration on TRT reliability The amount of time points or the duration of the acquisition required to obtain reliable results is also another open issue in brain connectivity fMRI analysis with graphs. Thanks to the long scan acquisition (1200 time points) and short repetition time (720 ms) of the HCP data set, we could assess test-retest reliability with different numbers of time points, i.e. different scan duration. We considered 5 different number of time points (from 400 to 1200) corresponding to scan duration ranging from 4 min 48 s to 14 min 24 s. As scan duration increases, reliability increases in parallel with a minimum of 600 time points or 7 min duration that is required to achieve reliable results for global metrics (Fig. 8.3). In the literature on whole brain graph analysis of rs-fMRI, the issue of the influence of scan duration on test-retest (TRT) reliability has been previously addressed [Liao et al., 2013, Cao et al., 2014]. Liao et al. [2013] found increased ICC values as the scan duration increased during the first 5-6 min and confidence intervals above 0 for a minimum duration of 5 min. No gain was observed for the ICC values after 6 min [Liao et al., 2013], but the confidence intervals are not shown after 5 min, limiting the validity of their findings for longer duration. Similarly, Braun et al. [2012] observed that shortening in a group of 33 subjects the scan duration from 5 to 3 min led to decrease significantly the reliability, leading the authors to recommended the acquisition of longer time series. In a recent meta-analysis based on TRT reliability of graph metrics studies, Andellini et al. found a significant increase in the TRT reliability for time series longer than 5 min compared to times series shorter than 5 min [Andellini et al., 2015]. As an effect of scan duration was questioned for longer duration ($5 - 15$ min) by studies outside TRT [Van Dijk et al., 2010, Whitlow et al., 2011], Birn et al. [2013] explored the influence of scan duration using 9 different scan duration from 3 to 27 min, in the context of a seed based approach TRT study (25 subjects). Increase duration had a significant effect on TRT reliability, until a plateau reached around 13 min for intra-session reliability and 9 min for inter-session reliability. Authors concluded that TRT reliability can be improved by increasing the scan duration to 12 min. Although the methodology of analysis applying graphs is different from theirs, our findings are consistent with those

[5] http://metrics.stanford.edu/
[6] http://fcon_1000.projects.nitrc.org/indi/CoRR/html/

of Birn et al. [2013].

Influence of the cost At low cost, typically 10.0% or below, global metrics such as global efficiency E_g and betweenness centrality, B, are not reliable up to 40 subjects (Fig. 8.4). This might be explained by the low sparsity of the graph, thus preventing robust calculation of these metrics. Conversely, above 30.0% cost, more edges are added to the graph that becomes more uniform so that potential variability within the network is reduced. For such costs, the metrics related to local features in the graph such as clustering coefficient C, modularity Q or local efficiency E_l appear poorly reliable. This might be related to an insufficient sparsity in the graph. In the literature, costs are currently in a range from 1.0% to 40.0%, or computed using values integrated on all the cost range. The influence of cost ranging from 10.0% to 40.0% on the reliability of global and local metrics has been previously investigated by Braun et al. [2012] and Wang et al. [2011] without clear results, given the large uncertainty on ICC values. Here, aiming at finding reliability for all global metrics, we considered a cost around 20.0% or 25.0% to be a good trade off. Accordingly, most of the figures presented in this study were performed at 20.0% cost.

Reliability of the different graph metrics The sample size appears to be a key parameter to achieve reliable global graph metrics (Fig. 8.4). At the global network level, Fig. 8.4 also shows that in small samples global metrics are cost dependent. Global efficiency, and in a lesser extent betweenness centrality, appear to be the most robust metrics in small samples (40 subjects) in a large cost range, while all metrics are reliable at intermediate costs in larger samples, here 100 subjects (Fig. 8.4). At regional level, for 20.0% cost, we found that degree and global efficiency present similar reliability, in line with Du et al. [2015] and Wang et al. [2011], as well as clustering coefficient and local efficiency (Fig. 8.5).

Trade off between number of subjects, number of time points and cost Our findings showed that reliability of the graph metrics computed at both global and regional level depends on two main factors, the number of subjects and the number of time points. This suggests that good reliability of graph metrics cannot be easily achieved with a sample size of 10 to 30 subjects and relative short duration (5 to 10 min.) that are sometimes used in studies of human cognition and clinical research. Fig. 8.4 shows how reliability is also influenced by the cost and the type of graph metric. Therefore, reaching the appropriate sample size may become an issue given the particular study design (recruitment of patients, rare inclusion criteria, complex cognitive study) and hypothesized effects. An alternative way to obtain reliable metrics consists of increasing the scan duration and to select the cost according to the metric of interest. For instance, as shown in Fig. 8.3, at the global network level and at 20.0% cost, global efficiency is significantly reliable at 1200 time points for 40 subjects or above, or at 600 time points for 60 subjects. Taking together the

influence of the number of subjects, the number of time points, the cost and the metrics, it appears that reliability at the global level can be achieved through a trade off between these parameters.

8.4.2 Exploring reliability at the regional network level

Another option to design clinical and cognitive studies for graph analysis is to focus at the regional network level to target reliable regions of interest. Fortunately, when a large number of subjects is available (80 or 100), almost all the brain parcellated regions are reliable (Table 8.5), and the values of the graph metrics can be used to classify nodes in terms of specific roles in networks. However, it is important to keep in mind that with a small sample size (below 40), the characterization of key regions has first to be referred for their reliable value, as only a part of the brain regions are reliable. Fig. 8.7 shows that, even with a small number of subjects (20 to 40 participants), e_{g_i} and e_{l_i} can be explored in a set of significantly reliable regions. The number of reliable regions depends on the time points and, for a given number of subjects, it increases from 400 to 800 time points to reach a plateau at 1000-1200 time points (Fig. 8.6). This plateau corresponds to 12 min., a duration that is also recommended by Birn et al. [2013] using a different methodological approach. Reliable regions as a function of sample size subgroups (20, 30, 40 and 100 participants) can be found in Table 8.4 for global efficiency at a cost of 20.0% with the AAL89 parcellation. As indicated in this table, the number of subjects can be adapted to the set of regions of interest in the study. For example, a sample size of 20 subjects is nearly sufficient to study the DMN, whereas, the exploration of SMA connectivity requires at least 30 subjects. To determine the regions which are most reliable depending on the type of metric in small samples, we report the values of e_{g_i}, e_{l_i} and b_i with their p-values for each AAL89 regions in Table 8.3 for graphs computed at 20.0% cost, for 40 subjects and 1200 time points. In these conditions, e_{g_i} presents the highest number of significant regions (58 regions among 89), e_{l_i} (19 regions) and b_i the lowest number of significant regions (6 among 89). It should be noted that the low reliability of betweenness centrality has been previously reported by Guo et al. [2012] when studying the default mode and the salience networks and by Du et al. [2015]. Therefore, we recommend to explore e_{g_i} and e_{l_i} rather than b_i for exploring graphs in small sample studies. These figures and table are thought to be useful for designing future rs-fMRI studies. In order to determine reliable key region in small samples, we used e_{g_i} values to rank the regions with their p-value of ICC at regional level for 1200 time points (corresponding to 14 min and 24 sec) in 40 subjects, at 20.0% cost (Table 8.2). Considering as reliable key regions the ones above $65th$ percentile for e_{g_i} values (higher or equal 0.58) and p-value$\leq$ 0.05, we found a set of 25 reliable key regions, which are listed in bold in Table 8.3.

Defining reliable key regions with graph metrics in small samples In parallel, the measure of the metrics reliability can also be applied to identify significant or robust key regions in small samples. The present study showed

that global efficiency (or similarly minimum path length) and node degree were the most reliable metrics. As commented above, considering 40 subjects, we found 25 regions that remain highly connected and reliable over time, printed in bold in Table 8.3 and in the upper left part of Table 8.2. All these regions belong to three main groups of resting state networks: the default mode networks (bilateral precuneus, left middle part of the cingulum and left inferior, left middle and bilateral superior temporal lobe), the sensorimotor networks (bilateral precentral gyri, bilateral SMA, right rolandic operculum) and the visual networks (bilateral calcarine cortex, bilateral occipital areas, bilateral cuneus, right lingual and right fusiform gyri), in agreement with previous studies [Liao et al., 2013, Wang et al., 2011, Agcaoglu et al., 2015].

Defining reliable key regions in subcortical regions At subcortical level, all cerebellar regions show significant reliability, even for 20 subjects (Table 8.4). Tomasi and Volkow [2012] have found the cerebellum to be a reliable and global key region using high functional connectivity density. The lobules VII, VIII, IX and X that are comprised in the posterior lobe of the cerebellum, are incorporated into a distributed neural circuits subserving complex movement, language, working memory and emotion [Stoodley and Schmahmann, 2009, O'Reilly et al., 2010]. Indeed, impairment in motor control, behavioral and cognitive functions can be observed after cerebellar lesions [Stoodley et al., 2012]. Of note, the left cerebellar lobe did not show high graph metrics, which could be related to acquisition limitations (Table 8.5). In this study, when examining graph metrics in the basal ganglia and the thalamus, we found the caudate nucleus to be reliable in the small sample of 40 subjects, although graph metric values were average (Table 8.3). In the 100 subject sample, the striatum (putamen and caudate), pallidum and left thalamus regions that are part of the basal ganglia network [Agcaoglu et al., 2015, Malherbe et al., 2014] are all reliable (Table 8.5). The engagement of the basal ganglia and more particularly the implication of the dorsal caudate in executive functioning, working memory and learning has been documented in a body of neuroimaging, anatomical and behavioral studies [Middleton and Strick, 2000, Grahn et al., 2009, Malherbe et al., 2014]. Although previous TRT graph studies have not reported the basal ganglia as key regions [Liao et al., 2013], the fact that striatal regions show relatively high b_i values, combined with a possible loss of signal related to acquisition and segmentation limitations (see limitations subsection) suggest that their role as a multimodal key region needs to be more specifically addressed.

8.4.3 Methodological considerations

The normal resting adult human heart rate ranges from $60 - 80$ bpm, which belongs to a frequency band between $[1.00 - 1.33]$ Hz. Given the short TR acquisition value, the maximal frequency is $1/(2\ \text{TR}) = 0.69$Hz. This band is aliased within the frequency range of $[0.05 - 0.38]$ Hz mainly located within wavelet scales 2, 3 and 4. Thus, there could be some contamination of our results by cardiac signal. The respiratory signal at rest is in the frequency band

between $[0.20 - 0.25]$ Hz, typically located in the wavelet scale 2. It is, thus, not contaminating our results.

While in most rs-fMRI studies the sampling rate used is about 0.5 Hz (corresponding to TR = 2 s), the multiband acquisition technique applied to fMRI [Feinberg et al., 2010] offers the advantage of increasing the sampling rate up to 1.67 Hz (corresponding to TR = 0.6 s) for a whole brain coverage. Previous studies have used multiband rs-fMRI data to test the reliability of brain network regions [Liao et al., 2013, Tomasi et al., 2015]. A main limitation of low sampling rate (or long TR) is that the cardiac and respiratory contributions are aliased in the data leading to artifacts. An advantage of multiband sequence is thus to prevent artifacts related to these physiological factors. Thus, as heart and respiration rates are not aliased within the frequency range of interest, there is no need of regressing them out.

The equivalence between time points and scan duration may be questionable, as number of time points used in the wavelet approach depends on the duration, the repetition time, and the frequency band. In Table A.1 (see Appendix A), we show the equivalences between these parameters. For example, in order to compute the graphs with at least 50 independent points in time, we need 800 time points for a TR = 720 ms (scan duration of 9 min 36 s) or 400 time points for a TR = 2 s (scan duration of 13 min 20 s).

Finally, the dyadic wavelet transform applied in this study splits the frequency band in five sub-bands. This permits to compute correlations that relate to each particular sub-band, a strategy which was found to improve reliability [Guo et al., 2012]. The results obtained here are thus not fully comparable with those found with larger frequency bands, such as the currently used 0.01 to 0.1 Hz band. Because of these differences as compared to other graph preprocessing, the results found here might not be strictly equivalent to other preprocessing strategies.

8.4.4 Limitations

The dataset used in this study was acquired in healthy young adults aged from 20 to 36 years old and included 54 females and 46 males. The analysis performed in this study did not attempt to discriminate between gender and age. Age effect was reported in structural and functional connectivity among resting-state networks across the human lifespan [Betzel et al., 2014] but in the small age range of this study, this effect was considered as negligible. Moreover, during adulthood, the age effect might be moderate [Song et al., 2012] and the results found here could probably be extended to subjects up to 60 years old. Gender effect has also been reported in youth (between 9 and 22 years of age) [Satterthwaite et al., 2015] and in the lateralization of the resting-state networks [Agcaoglu et al., 2015]. Agcaoglu et al. [2015] found that differences related to gender are consistent in samples above 250 subjects. Given the relatively lower number of subjects studied here, the effect of gender was not considered.

In order to compute the time series in the gray matter alone, the T1w structural images were segmented to obtain a gray matter mask. This permits to

eliminate most of the white matter and cerebrospinal fluid contribution in the time series. The T1w structural image was acquired with a MPRAGE sequence, which is efficient at presenting a good gray matter/white matter contrast in the cortical surface. However, the high iron content of the subcortical nuclei (especially caudate, pallidum and putamen) [Haacke et al., 2005] further shortens the T1 in these deep structures. As a consequence, they exhibit reduced contrast from white matter in T1w images and are often misclassified by segmentation algorithms [Helms et al., 2009]. The time series may thus not be optimally extracted in these deep structures, reflecting the relative low reliability of the graph metrics in the basal ganglia (putamen, pallidum, caudate) and in the thalamus.

The dataset provided by the Human Connectome Project comprised two different acquisitions, one with the phase encoding direction from left to right and the other one from right to left. As the mental state of the subjects may differ between them, rather than pooling them, we chose to use only the first dataset, the left to right one. Despite the distortion corrections schemes that were applied in the preprocessing stage, the inhomogeneity of the static field may have led to some residual distortions which can be seen in the inferior part of the temporal lobe, and to some loss of signal in regions such as the olfactory, orbito-frontal and amygdala regions.

Region	e_{g_i}(*p*-value)	e_{l_i}(*p*-value)	bc_i(*p*-value)	**Region**	e_{g_i}(*p*-value)	e_{l_i}(*p*-value)	bc_i(*p*-value)
CingMid L	**0.67(0.014)**	**0.74**(0.054)	**232.41**(0.143)	FrontInfTri R	0.52(0.020)	0.74(0.122)	59.89(0.334)
CingMid R	0.64(0.184)	0.76(0.065)	179.12(0.250)	ParacentralLob L	0.52(0.022)	0.86(0.399)	28.01(0.140)
TempMid R	0.64(0.078)	0.75(0.048)	169.19(0.214)	ParacentralLob R	0.52(0.011)	0.83(0.063)	25.22(0.184)
PrecGy L	**0.63(0.009)**	**0.80**(0.131)	99.23(0.087)	CingAnt L	0.52(0.076)	0.75(0.284)	64.58(0.505)
TempInf R	0.63(0.099)	0.79(0.255)	130.84(0.134)	Angular R	0.52(0.064)	0.77(0.127)	38.77(0.435)
Precuneus L	**0.63(0.003)**	0.76(0.191)	**153.70**(0.087)	FrontInfTri L	0.51(0.034)	0.72(0.129)	49.42(0.149)
TempMid L	**0.62(0.050)**	0.75(0.031)	**151.43**(0.095)	Heschl L	0.51(0.009)	0.85(0.155)	14.31(0.172)
Fusiform L	0.62(0.136)	0.82(0.089)	99.07(0.230)	FrontSupMed R	0.51(0.009)	0.75(0.368)	74.32(0.288)
ParietalSup L	**0.62(0.019)**	**0.83**(0.150)	60.01(0.122)	FrontInfOperc R	0.50(0.004)	0.80(0.224)	29.02(0.131)
TempSup L	**0.62(0.005)**	**0.80**(0.142)	83.81(0.238)	Cereb I_II R	0.49(0.003)	0.83(0.158)	64.14(0.240)
PrecGy R	**0.62(0.012)**	**0.82**(0.025)	74.67(0.153)	CingAnt R	0.49(0.010)	0.79(0.516)	27.89(0.276)
TempSup R	**0.62(0.034)**	**0.80**(0.117)	**103.94**(0.262)	TempPole R	0.49(0.011)	0.74(0.239)	55.78(0.237)
Occipital L	**0.61(0.024)**	**0.84**(0.021)	62.49(0.047)	Cereb I_II L	0.49(0.003)	0.81(0.068)	61.48(0.162)
Calcarine L	**0.61(0.019)**	**0.84**(0.023)	**75.93**(0.081)	ParietalInf R	0.49(0.013)	0.80(0.125)	18.93(0.636)
FronMid L	0.61(0.095)	0.73(0.089)	146.52(0.121)	Angular L	0.48(0.032)	0.75(0.358)	31.14(0.154)
FronSup R	0.61(0.121)	0.75(0.327)	125.63(0.283)	TempPole L	0.48(0.012)	0.65(0.111)	60.95(0.368)
Lingual R	**0.61(0.028)**	**0.86**(0.027)	50.15(0.259)	FrontInfOrb R	0.47(0.070)	0.68(0.012)	51.94(0.517)
Precuneus R	**0.61(0.045)**	0.79(0.694)	**100.46**(0.266)	Vermis	0.47(0.004)	0.74(0.092)	36.74(0.192)
Lingual L	0.61(0.057)	0.86(0.123)	44.19(0.316)	FrontInfOperc L	0.47(0.039)	0.80(0.458)	22.13(0.302)
PostcGy L	0.61(0.125)	0.85(0.262)	48.53(0.145)	FrontInfOrb L	0.47(0.099)	0.69(0.057)	42.94(0.234)
Fusiform R	**0.61(0.031)**	**0.82**(0.025)	65.66(0.131)	CingPost L	0.46(0.087)	0.73(0.104)	35.04(0.276)
SMA L	**0.61(0.010)**	**0.82**(0.300)	71.60(0.182)	Caudate L	0.44(0.029)	0.59(0.073)	77.52(0.760)
PostcGy R	0.60(0.093)	0.84(0.039)	57.24(0.101)	Caudate R	0.44(0.016)	0.59(0.093)	85.00(0.082)
Cuneus L	**0.60(0.033)**	**0.87**(0.054)	39.14(0.072)	ParaHippoc L	0.43(0.039)	0.49(0.047)	60.10(0.179)
FrontMid R	**0.60(0.050)**	0.75(0.138)	**129.74**(0.087)	CingPost R	0.43(0.007)	0.65(0.068)	16.84(0.215)
Calcarine R	**0.59(0.013)**	**0.86**(0.015)	43.95(0.139)	FrontMedOrb L	0.43(0.093)	0.55(0.115)	65.49(0.270)
Occipital R	**0.59(0.007)**	**0.87**(0.016)	35.87(0.083)	FrontMidOrb L	0.43(0.008)	0.54(0.037)	42.26(0.295)
RolandOperc R	**0.59(0.050)**	**0.83**(0.132)	51.07(0.202)	Thalamus R	0.42(0.326)	0.55(0.428)	20.92(0.228)
FronSup L	0.59(0.104)	0.75(0.180)	111.42(0.272)	Hippocampus L	0.42(0.044)	0.46(0.194)	86.15(0.190)
ParietalSup R	**0.59(0.006)**	**0.85**(0.323)	33.00(0.038)	FrontMedOrb R	0.41(0.078)	0.57(0.107)	59.63(0.298)
Cuneus R	**0.59(0.052)**	**0.88**(0.024)	26.84(0.101)	Thalamus L	0.41(0.007)	0.55(0.182)	27.27(0.074)
TempInf L	**0.59(0.028)**	0.78(0.644)	82.00(0.160)	ParaHippoc R	0.41(0.169)	0.47(0.251)	35.96(0.343)
SMA R	**0.58(0.009)**	**0.82**(0.705)	76.42(0.521)	FrontalMidOrb R	0.40(0.036)	0.53(0.165)	33.49(0.474)
Cereb VII - X R	**0.58(0.011)**	0.78(0.050)	**127.37**(0.009)	FrontSupOrb L	0.40(0.074)	0.53(0.042)	21.50(0.101)
Insula R	0.58(0.160)	0.79(0.118)	87.87(0.540)	Putamen R	0.39(0.078)	0.37(0.113)	106.10(0.391)
RolandOperc L	**0.58(0.017)**	**0.85**(0.245)	38.44(0.225)	FrontSupOrb R	0.37(0.013)	0.44(0.090)	17.55(0.212)
SupraMarginal R	0.57(0.002)	0.80(0.138)	49.30(0.023)	Hippocampus R	0.37(0.144)	0.34(0.186)	30.14(0.085)
ParietalInf L	0.56(0.038)	0.77(0.169)	58.04(0.306)	Putamen L	0.37(0.012)	0.38(0.046)	70.07(0.152)
Cereb VII - X L	0.55(0.008)	0.80(0.097)	83.54(0.157)	Amygdala L	0.33(0.052)	0.07(0.072)	19.59(0.212)
SupraMarginal L	0.55(0.003)	0.84(0.092)	40.41(0.143)	Olfactory L	0.33(0.220)	0.09(0.036)	10.61(0.297)
Insula L	0.54(0.032)	0.83(0.532)	38.32(0.379)	Amygdala R	0.33(0.130)	0.08(0.057)	11.23(0.392)
FrontSupMed L	0.54(0.006)	0.74(0.139)	84.19(0.176)	Olfactory R	0.31(0.263)	0.04(0.081)	5.01(0.103)
Heschl R	0.54(0.104)	0.87(0.254)	31.25(0.199)	Pallidum L	0.30(0.075)	0.01(0.005)	0.96(0.010)
Cereb III - VI R	0.53(0.007)	0.78(0.144)	69.77(0.024)	Pallidum R	0.30(0.151)	0.11(0.178)	11.25(0.094)
Cereb III - VI L	0.53(0.004)	0.77(0.074)	85.33(0.310)				

Table 8.3: Regional network parameters and their *p*-values for each region in AAL89 parcellation at 20% cost, considering 40 subjects at 1200 tp. Key regions are defined as regions with high e_{g_i} and significant *p*-value. The threshold to consider a high e_{g_i} is fix to the percentile 65%, in this case, $e_{g_i} \geq 0.58$. Other regional network parameters and their respective *p*-values are also shown: local efficiency e_{l_i} and betweenness centrality b_i.

Region	e_{g_i} (#40)	#20	#30	#40	#100	Region	e_{g_i} (#40)	#20	#30	#40	#100
PrecGy L	0.63	0.044	0.018	0.009	0.004	Lingual L	0.61	0.152	0.080	0.057	0.004
PrecGy R	0.62	0.070	0.039	0.012	0.004	Lingual R	0.61	0.099	0.046	0.028	0.004
FontSup L	0.59	0.162	0.122	0.104	0.004	Occipital L	0.61	0.078	0.043	0.024	0.004
FontSup R	0.61	0.218	0.144	0.121	0.009	Occipital R	0.59	0.046	0.015	0.007	0.004
FrontSupOrb L	0.40	0.182	0.122	0.074	0.004	Fusiform L	0.62	0.277	0.223	0.136	0.021
FrontSupOrb R	0.37	0.063	0.029	0.013	0.004	Fusiform R	0.61	0.114	0.059	0.031	0.004
FrontMid L	0.61	0.222	0.146	0.095	0.009	Postcentral L	0.61	0.195	0.142	0.125	0.018
FrontMid R	0.60	0.148	0.073	0.050	0.004	Postcentral R	0.60	0.180	0.113	0.093	0.004
FrontMidOrb L	0.43	0.057	0.017	0.008	0.004	ParietalSup L	0.62	0.066	0.035	0.019	0.004
FrontMidOrb R	0.40	0.099	0.049	0.036	0.004	ParietalSup R	0.59	0.039	0.015	0.006	0.004
FrontInfOperc L	0.47	0.153	0.083	0.039	0.004	ParietalInf L	0.56	0.151	0.090	0.038	0.004
FrontInfOperc R	0.50	0.048	0.012	0.004	0.004	ParietalInf R	0.49	0.087	0.029	0.013	0.004
FrontInfTri L	0.51	0.113	0.054	0.034	0.004	SupraMarginal L	0.55	0.020	0.005	0.003	0.004
FrontInfTri R	0.52	0.105	0.056	0.020	0.004	SupraMarginal R	0.57	0.011	0.003	0.002	0.004
FrontInfOrb L	0.46	0.203	0.141	0.099	0.009	Angular L	0.48	0.072	0.036	0.032	0.004
FrontInfOrb R	0.47	0.126	0.079	0.070	0.004	Angular R	0.51	0.158	0.100	0.064	0.004
RolandOperc L	0.57	0.057	0.022	0.017	0.004	Precuneus L	0.63	0.021	0.006	0.003	0.004
RolandOperc R	0.59	0.131	0.071	0.050	0.004	Precuneus R	0.61	0.134	0.083	0.045	0.004
SMA L	0.60	0.058	0.024	0.010	0.004	ParacentralLob L	0.52	0.079	0.028	0.022	0.004
SMA R	0.58	0.098	0.030	0.009	0.004	ParacentralLob R	0.52	0.047	0.023	0.011	0.004
Olfactory L	0.33	0.290	0.265	0.220	0.028	Caudate L	0.44	0.110	0.057	0.029	0.004
Olfactory R	0.31	0.325	0.291	0.263	0.118	Caudate R	0.44	0.074	0.029	0.016	0.004
FrontSupMed L	0.54	0.035	0.010	0.006	0.004	Putamen L	0.37	0.068	0.027	0.012	0.004
FrontSupMed R	0.51	0.044	0.014	0.009	0.004	Putamen R	0.39	0.156	0.116	0.078	0.004
FrontMedOrb L	0.43	0.186	0.149	0.093	0.004	Pallidum L	0.30	0.192	0.120	0.074	0.004
FrontMedOrb R	0.41	0.127	0.088	0.078	0.004	Pallidum R	0.30	0.245	0.202	0.151	0.011
Insula L	0.54	0.119	0.084	0.032	0.004	Thalamus L	0.41	0.038	0.014	0.007	0.004
Insula R	0.58	0.220	0.166	0.160	0.014	Thalamus R	0.42	0.347	0.341	0.326	0.160
CingAnt L	0.52	0.183	0.130	0.076	0.004	Heschl L	0.51	0.050	0.016	0.009	0.004
CingAnt R	0.49	0.073	0.026	0.010	0.004	Heschl R	0.53	0.158	0.092	0.104	0.004
CingMid L	0.67	0.067	0.024	0.014	0.004	TempSup L	0.62	0.029	0.009	0.005	0.004
CingMid R	0.64	0.241	0.188	0.184	0.028	TempSup R	0.62	0.098	0.060	0.034	0.004
CingPost L	0.46	0.136	0.101	0.087	0.004	TempPole L	0.47	0.118	0.067	0.012	0.004
CingPost R	0.43	0.047	0.017	0.007	0.004	TempPole R	0.49	0.068	0.023	0.011	0.004
Hippocampus L	0.42	0.113	0.059	0.044	0.004	TempMid L	0.62	0.145	0.072	0.050	0.004
Hippocampus R	0.37	0.243	0.171	0.144	0.014	TempMid R	0.64	0.222	0.130	0.078	0.009
ParaHippoc L	0.43	0.117	0.060	0.039	0.004	TempInf L	0.58	0.112	0.057	0.028	0.004
ParaHippoc R	0.41	0.283	0.213	0.169	0.018	TempInf R	0.63	0.184	0.124	0.099	0.004
Amygdala L	0.33	0.126	0.059	0.052	0.004	Cereb I II L	0.49	0.009	0.003	0.003	0.004
Amygdala R	0.32	0.196	0.168	0.130	0.018	Cereb I II R	0.49	0.014	0.003	0.003	0.004
Calcarine L	0.61	0.078	0.026	0.019	0.004	Cereb III - VI L	0.53	0.021	0.005	0.004	0.004
Calcarine R	0.59	0.071	0.028	0.013	0.004	Cereb III - VI R	0.53	0.047	0.013	0.007	0.004
Cuneus L	0.60	0.105	0.050	0.033	0.004	Cereb VII - X L	0.55	0.035	0.008	0.008	0.004
Cuneus R	0.59	0.138	0.079	0.052	0.004	Cereb VII - X R	0.58	0.038	0.015	0.011	0.004
						Vermis	0.47	0.036	0.010	0.004	0.004

Table 8.4: *P*-values for each brain region of the AAL89 for 20, 30, 40 and 100 subjects. Graph metric: regional global efficiency (e_{g_i}). Cost of 20% at 1200 time points.

Region	e_{g_i} (p-value)	e_{l_i} (p-value)	b_i (p-value)	Region	e_{g_i} (p-value)	e_{l_i} (p-value)	b_i (p-value)
CingMid L	**0.67(0.005)**	0.74(0.002)	**232.75**(0.005)	ParacentralLob L	0.52(0.005)	0.86(0.140)	28.06(0.050)
CingMid R	**0.64(0.028)**	0.76(0.002)	**180.31**(0.026)	FrontalInfTri R	0.52(0.005)	0.74(0.023)	61.55(0.273)
TempMid R	**0.64(0.009)**	0.75(0.002)	**168.89**(0.064)	ParacentralLob R	0.52(0.005)	0.83(0.002)	25.84(0.026)
Precentral L	**0.63(0.005)**	0.79(0.004)	99.96(0.003)	CingAnt L	0.52(0.005)	0.75(0.062)	63.55(0.607)
TempInf R	**0.63(0.005)**	0.79(0.124)	**129.30**(0.017)	Angular R	0.51(0.005)	0.77(0.034)	38.34(0.413)
Precuneus L	**0.63(0.005)**	0.76(0.032)	**154.14**(0.004)	FrontInfTri L	0.51(0.005)	0.72(0.023)	49.18(0.038)
Fusiform L	**0.62(0.021)**	**0.82**(0.007)	98.74(0.036)	Heschl L	0.51(0.005)	0.85(0.011)	14.26(0.084)
TempSup L	**0.62(0.005)**	**0.80**(0.013)	83.03(0.051)	FrontSupMed R	0.51(0.005)	0.74(0.052)	76.78(0.033)
ParietalSup L	**0.62(0.005)**	**0.83**(0.017)	58.00(0.006)	FrontInfOperc R	0.50(0.005)	0.80(0.043)	29.97(0.028)
TempMid L	**0.62(0.005)**	0.75(0.004)	**149.03**(0.002)	Cereb I II R	0.49(0.005)	0.83(0.011)	63.00(0.114)
TempSup R	**0.62(0.005)**	**0.80**(0.002)	**104.30**(0.102)	Cereb I II L	0.49(0.005)	0.81(0.002)	63.90(0.136)
Precentral R	**0.62(0.005)**	**0.82**(0.002)	76.88(0.026)	CingAnt R	0.49(0.005)	0.79(0.457)	28.05(0.219)
FrontMid L	**0.61(0.009)**	0.73(0.002)	**150.74**(0.005)	ParietalInf R	0.49(0.005)	0.80(0.007)	19.00(0.679)
Occipital L	**0.61(0.005)**	**0.84**(0.002)	60.29(0.002)	TempPoleSupMid R	0.49(0.005)	0.73(0.029)	57.68(0.147)
Calcarine L	**0.61(0.005)**	**0.84**(0.002)	74.92(0.001)	Angular L	0.48(0.005)	0.75(0.140)	31.19(0.021)
FrontSup R	**0.61(0.009)**	0.75(0.284)	**127.58**(0.142)	TempPoleSupMid L	0.48(0.005)	0.65(0.007)	63.09(0.353)
Precuneus R	**0.61(0.005)**	0.78(0.846)	**103.00**(0.037)	Vermis	0.47(0.005)	0.74(0.004)	38.09(0.060)
Lingual R	**0.61(0.005)**	**0.86**(0.002)	49.49(0.112)	FrontInfOrb R	0.47(0.005)	0.68(0.002)	52.25(0.412)
Postcentral L	**0.61(0.018)**	**0.85**(0.047)	47.79(0.021)	FrontInfOper L	0.47(0.005)	0.79(0.413)	22.07(0.284)
Fusiform R	**0.61(0.005)**	**0.82**(0.002)	66.48(0.028)	FrontInfOrb L	0.46(0.009)	0.68(0.002)	43.92(0.110)
SMA L	**0.61(0.005)**	**0.82**(0.295)	72.68(0.044)	CingulumPost L	0.46(0.005)	0.73(0.004)	35.81(0.081)
Lingual L	**0.61(0.005)**	**0.86**(0.011)	44.14(0.258)	Caudate R	0.44(0.005)	0.59(0.007)	87.00(0.002)
Postcentral R	**0.60(0.005)**	**0.84**(0.004)	56.75(0.001)	Caudate L	0.44(0.005)	0.59(0.004)	76.01(0.857)
Cuneus L	**0.60(0.005)**	**0.87**(0.002)	38.57(0.002)	CingulumPost R	0.43(0.005)	0.66(0.002)	16.93(0.069)
FrontMid R	**0.60(0.005)**	0.75(0.002)	**128.87**(0.005)	ParaHippocampal L	0.43(0.005)	0.50(0.002)	60.74(0.008)
Occipital R	**0.59(0.005)**	**0.87**(0.002)	35.48(0.003)	FrontalMidOrb L	0.43(0.005)	0.54(0.004)	44.60(0.080)
Calcarine R	**0.59(0.005)**	**0.86**(0.002)	42.86(0.011)	Thalamus R	0.42(0.160)	0.54(0.500)	20.98(0.104)
RolandicOper R	**0.59(0.005)**	**0.83**(0.007)	50.88(0.084)	FrontMedOrb Rectus L	0.42(0.005)	0.55(0.013)	64.40(0.148)
ParietalSup R	**0.59(0.005)**	**0.85**(0.368)	32.56(0.003)	Hippocampus L	0.42(0.005)	0.46(0.042)	87.67(0.037)
Cuneus R	**0.59(0.005)**	**0.88**(0.002)	26.68(0.013)	FrontMedOrb Rectus R	0.41(0.005)	0.57(0.004)	58.91(0.184)
FrontSup L	**0.59(0.005)**	0.75(0.029)	**110.37**(0.029)	Thalamus L	0.41(0.005)	0.54(0.033)	27.34(0.013)
TempInf L	**0.58(0.005)**	0.78(0.923)	81.56(0.024)	Parahippocampal R	0.41(0.018)	0.46(0.080)	36.05(0.219)
SMA R	**0.58(0.005)**	**0.82**(0.923)	75.50(0.571)	FrontMidOrb R	0.40(0.005)	0.52(0.027)	33.21(0.413)
Cereb VII - X R	**0.58(0.005)**	0.78(0.017)	**125.59**(0.001)	FrontSupOrb L	0.40(0.005)	0.53(0.002)	20.68(0.038)
RolandicOper L	**0.58(0.005)**	**0.85**(0.108)	38.65(0.097)	Putamen R	0.39(0.005)	0.37(0.007)	107.80(0.326)
Insula R	**0.58(0.014)**	0.79(0.032)	89.42(0.607)	FrontSupOrb R	0.37(0.005)	0.43(0.013)	17.18(0.068)
SupraMarginal R	0.57(0.005)	0.80(0.035)	48.93(0.001)	Hippocampus R	0.37(0.014)	0.33(0.025)	31.04(0.012)
ParietalInf L	0.56(0.005)	0.78(0.056)	58.13(0.103)	Putamen L	0.37(0.005)	0.38(0.002)	69.49(0.008)
SupraMarginal L	0.55(0.005)	0.84(0.011)	40.08(0.052)	Amygdala L	0.33(0.005)	0.07(0.002)	21.03(0.062)
Cereb VII - X L	0.55(0.005)	0.80(0.021)	84.82(0.053)	Olfactory L	0.33(0.028)	0.09(0.002)	11.09(0.441)
Insula L	0.54(0.005)	0.83(0.607)	38.01(0.337)	Amygdala R	0.32(0.018)	0.08(0.002)	11.35(0.536)
FrontSupMed L	0.54(0.005)	0.73(0.004)	83.51(0.024)	Olfactory R	0.31(0.118)	0.04(0.194)	4.38(0.153)
Heschl R	0.54(0.005)	0.87(0.127)	31.73(0.045)	Pallidum L	0.30(0.005)	0.01(0.004)	0.87(0.017)
Cereb III - VI R	0.53(0.005)	0.78(0.004)	70.97(0.001)	Pallidum R	0.30(0.011)	0.11(0.154)	12.45(0.084)
Cereb III - VI L	0.53(0.005)	0.77(0.002)	88.47(0.157)				

Table 8.5: P-values of each brain region (AAL89) for 100 subjects using different graph metrics: regional global efficiency (e_{g_i}), regional local efficiency (e_{l_i}) and regional betweenness centrality (b_i). Cost of 20% at 1200 time points.

Chapter 9

Reliability of the hub disruption index (κ)

In this chapter, I use the same methodology and database explained in Chapter 8 to address the reliability of the hub disruption index. This step is essential when aiming at using this type of metrics in clinical applications. The results shown in this chapter are part of our publication in Frontiers in Computational Neuroscience:

M. Termenon, S. Achard, A. Jaillard, C. Delon-Martin, **The "Hub Disruption Index", a Reliable Index Sensitive to the Brain Networks Reorganization. A Study of the Contralesional Hemisphere in Stroke**, Frontiers in Computational Neuroscience, 2016, 10:84, `http://dx.doi.org/10.3389/fncom.2016.00084`

9.1 Introduction

In the recent years, there has been a great amount of work developing new investigation methods of the brain connectivity based on fMRI. Among those, the graph theoretical approach seems particularly useful in the context of pathology since it underlines the role of key communicating regions (hubs) in the graph. Since there was no graph metric aiming at capturing this type of reorganization after brain damage, the Hub Disruption Index (κ) was introduced in Achard et al. [2012] to capture it. κ index summarizes graph metric changes at the nodal level in a single value. It is thus a global index capturing changes at the nodal level. For a given graph metric, κ is computed as the slope of the linear regression model between the mean nodal metric value of a reference group and the differential nodal metric value between a given subject (patient or control) and that reference (see Fig. 5.11 for a graphical explanation). If the subject's nodal values are close to those of the reference group (Fig. 5.11.C), the κ will be close to 0. Contrary, if the subject's nodal values are different from those of

the reference group (Fig. 5.11.D), with reduced values in nodes with high metric values in the reference group, the κ will be negative. Once the reference group is computed, the kappa can be calculated for each control and each patient individually and statistical tests can be applied to compare the differences between groups.

According to Bullmore and Sporns [2009], hubs are crucial nodes for an efficient communication in the network and are identified as nodes with high degree or high centrality values. In this paper, we computed κ using metrics that directly relate to hubs: node degree, betweenness centrality and global efficiency; and also in metrics that explore the neighborhood of the node, such as, local efficiency and clustering coefficient.

In order to translate the use of κ in clinical context, an essential requirement to achieve meaningful results is to investigate the reliability of this index. Applying similar techniques than the one explained in the previous chapter, we assessed the reliability of κ, over different graph metrics, by computing the ICC in a cohort of 100 healthy subjects using the database from the Human Connectome Project (HCP) [1]. We calculated the ICCs and their p-values, applying bootstrap and permutation techniques to check for the influence of the number of subjects and of the number of edges (cost) in brain graphs.

9.2 Reliability of κ using HCP database

The κ index is proposed as a measure to capture network disorganization in individuals or groups as compared to a reference group. The assessment of its reliability in controls is a complementary step because if it is found as a reliable index, it will increase the chance of finding differences between groups, even if it does not assure that differences between groups will be found [Shirer et al., 2015].

We used HCP database to assess the reproducibility of κ in control subjects calculated over the five metrics explained above, for costs ranging between 10% and 75%. We used the mean of session 1 as reference to compute κ for each subject's session 1 and the mean of session 2 as reference for the κ of session 2. The between and within subjects variances were computed and ICC values for κ were derived following the formulae above. This was done for the whole group of 100 subjects and for subgroups of 20, 40 and 60 subjects applying bootstrap sampling.

For each subgroup size, to provide uncertainty and p-values on ICC, we randomly permuted the sessions between subjects. For that purpose, we used Simctest [Gandy, 2009]. It is an open-ended sequential algorithm to compute the p-value of a test using Monte Carlo simulation. It guarantees that the resampling risk, the probability of a different decision than the one based on the theoretical p-value, is uniformly bounded by an arbitrarily small constant. A more detailed description can be found in [Termenon et al., 2016].

[1] `http://www.humanconnectome.org/`

In a complementary experiment, we also tested whether the intra-hemispheric κ index could be different between the right and the left hemispheres. Intra-hemispheric κ was computed among all the nodes of a single hemisphere. Then, we compared the intra-hemispheric κ of the left versus the right hemisphere using as reference the mean between left and right metric values for each session of HCP database independently. We also tested across sessions the reliability of the left intra-hemispheric connectivity and of the right intra-hemispheric connectivity, separately. As reference, we used the mean between both sessions of the left hemisphere and the mean between both sessions of the right hemisphere, respectively. To evaluate the significance of these differences, statistical tests were performed using Wilcoxon rank-sum test (p-value< 0.05).

In case of no laterality effect in the intra-hemispheric connectivity in controls, we consider that the contralesional intra-hemispheric connectivity in stroke could be pooled together, independently of the side of the lesion.

9.3 Results

To test the reliability of κ, we computed the ICC on subgroups of 20, 40, 60 and 100 subjects. We applied permutations and bootstrap techniques to assess the p-values of the obtained ICC. In Fig. 9.1, we show the ICCs and their p-values of κ_D with respect to cost, for the different subgroups' sizes. We considered separately the left intra-hemispheric connectivity (LEFT), the right intra-hemispheric connectivity (RIGHT) and the whole brain connectivity including both intra- and inter-hemispheric connections (ALL).

In the case of intra-hemispheric connectivity, for a cost equal to or above 20%, we observed an ICC value that is roughly independent of the cost, with an uncertainty on the ICC that depends on the number of subjects (it is reduced with an increasing number of subjects). Below 17.5% cost, the graph is too sparse and the κ_D index was not reliable. When considering connections from all the brain, we achieved higher reliability than when considering only intra-hemispheric connections for costs below 40%. When the cost is high, it means that the graph is highly connected, and thus the between and within variance differences can be reduced. We have to underline here that these ICC values are also dependent on the acquisition duration, as was shown in Birn et al. [2013], Termenon et al. [2016].

Similar results were found with the other graph metrics we tested: global efficiency (Fig. 9.2), betweenness centrality, clustering and local efficiency. For the sake of comparison, under the same experimental conditions (same database, graph methodology, permutation and bootstrap sampling), the ICC(E_g) was lower considering the whole brain (ranging between 0.30 at 20% cost and 0.40 at 40% cost) and also, the intra-hemispheric connectivity (Fig. 9.3). These results show that κ_{E_g} is more reliable than the average E_g metric obtained by averaging all the nodes.

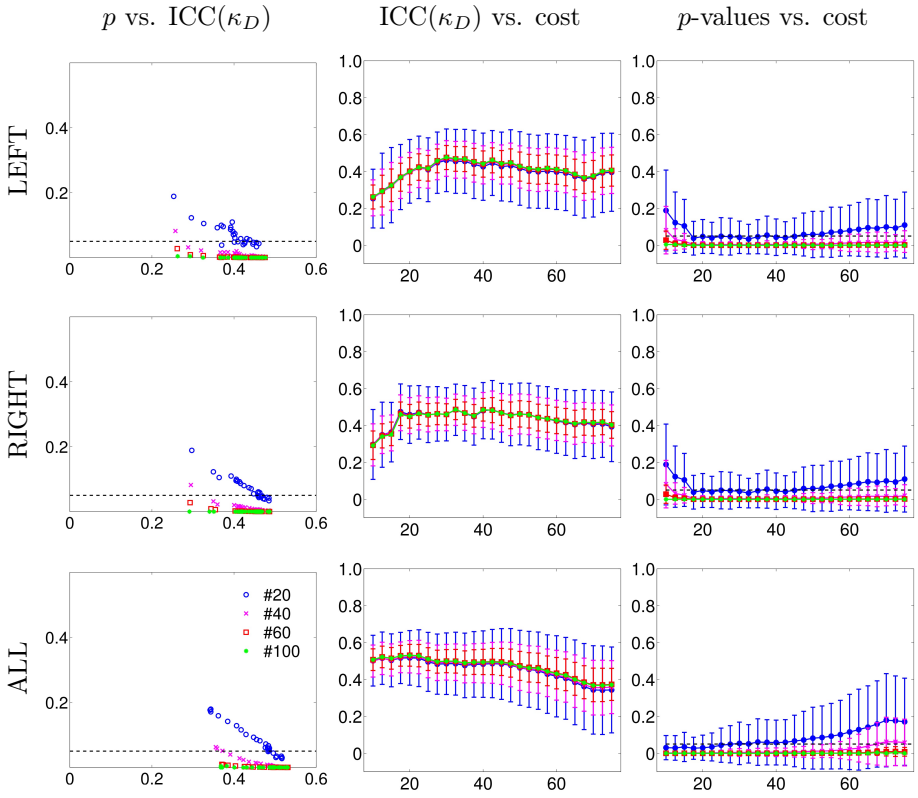

Figure 9.1: Reliability results for κ degree (κ_D) in terms of number of subjects as a function of the cost from 10% to 75%, in steps of 2.5%. Results are given for subgroups of 20, 40, 60 and finally, 100 subjects using the database of the HCP project. First column, p-values of ICC (y-axis) as a function of ICC values (x-axis) for different number of subjects. Second column, values of ICC (y-axis) as a function of the cost (x-axis) for different number of subjects. Third column, ICC associated p-values (y-axis) as a function of the cost (x-axis) for different number of subjects. LEFT refers to the graph built from the left intra-hemispheric connections, RIGHT for the right intra-hemispheric connections. ALL refers to the graph built from connections of the whole brain. In addition, we found that κ_D is more reliable than classical metrics.

Comparison of κ per hemisphere in controls The differences between left and right intra-hemispheric connections using the 100 subjects of the HCP are shown in Fig. 9.4 . We compared the intra-hemispheric connectivity of left and right hemispheres for each session independently (upper row). To compute the κ_D, we used the mean between left and right hemispheres as reference, considering only the intra-hemispheric connections (inter-hemispheric connections were excluded). We found no significant differences between the left and the

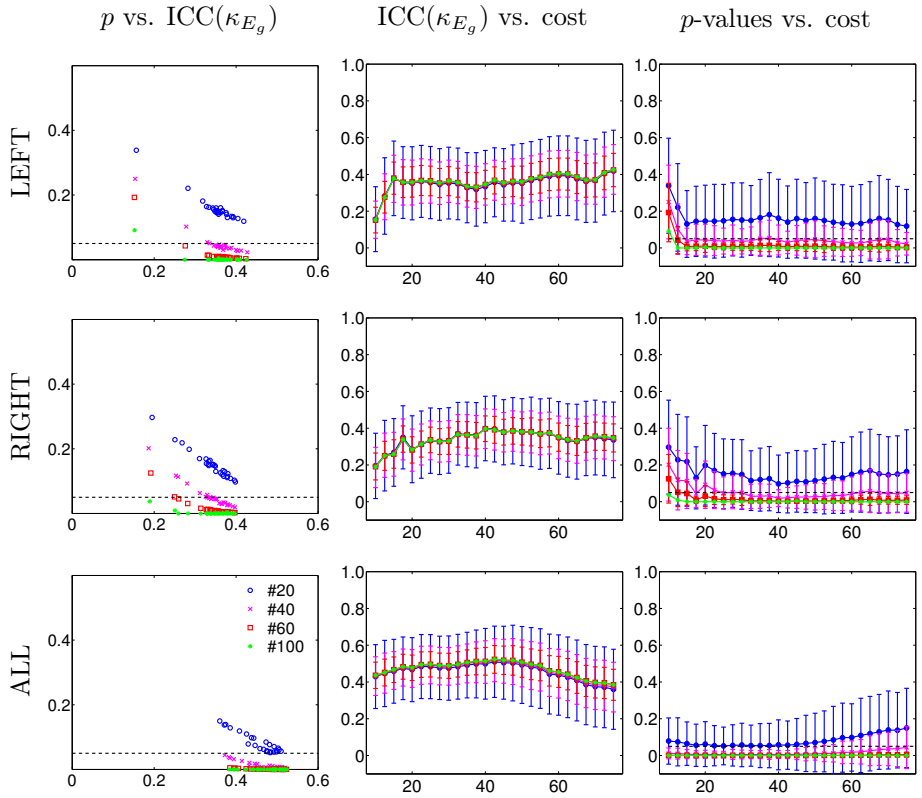

Figure 9.2: Reliability results for κ global efficiency (κ_{E_g}) in terms of number of subjects as a function of the cost from 10% to 75%, in steps of 2.5%. Results are given for subgroups of 20, 40, 60 and finally, 100 subjects using the database of the HCP project. First column, p-values of ICC (y-axis) as a function of ICC values (x-axis) for different number of subjects. Second column, values of ICC (y-axis) as a function of the cost (x-axis) for different number of subjects. Third column, ICC associated p-values (y-axis) as a function of the cost (x-axis) for different number of subjects. LEFT refers to the graph built from the left intra-hemispheric connections, RIGHT for the right intra-hemispheric connections. ALL refers to the graph built from connections of the whole brain. We found that κ_{E_g} is more reliable than mean global efficiency E_g (compare to Fig. 9.3)

right intra-hemispheric connectivity, neither in the first session nor in the second session.

In the second comparison (lower row of Fig. 9.4), we studied if there were differences across sessions for each hemisphere, independently. For each session, we compared the intra-hemispheric connectivity of the left hemisphere, using as reference the mean between sessions of the left intra-hemispheric connectivity. Same procedure was applied for the right hemisphere. We found no effect of

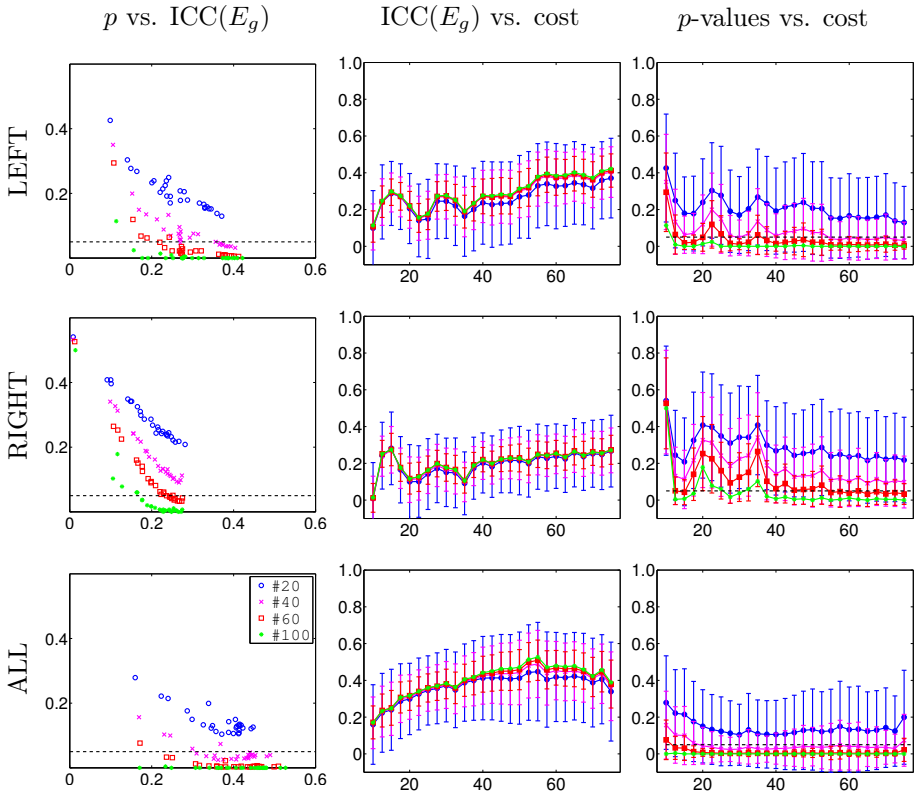

Figure 9.3: Reliability results for mean global efficiency (E_g) using the database of HCP project in terms of number of subjects as a function of the cost from 10% to 75%, in steps of 2.5%. Results are given for subgroups of 20, 40, 60 and finally, 100 subjects using the database of the HCP project. First column, p-values of ICC (y-axis) as a function of ICC values (x-axis) for different number of subjects. Second column, values of ICC (y-axis) as a function of the cost (x-axis) for different number of subjects. Third column, ICC associated p-values (y-axis) as a function of the cost (x-axis) for different number of subjects. LEFT refers to the graph built from the left intra-hemispheric connections, RIGHT for the right intra-hemispheric connections. ALL refers to the graph built from connections of the whole brain. We found that E_g is less reliable than κ global efficiency (κ_{E_g}) (compare to Fig. 9.2).

the sessions on the intra-hemispheric connectivity, nor for the left hemisphere neither for the right hemisphere.

The lack of laterality effect in the intra-hemispheric connectivity supports the view that contralesional intra-hemispheric connectivity, independently of the hemispheric location of the stroke lesion, could be pooled together. This motivates the fact that, in the study on stroke patients, we pooled together

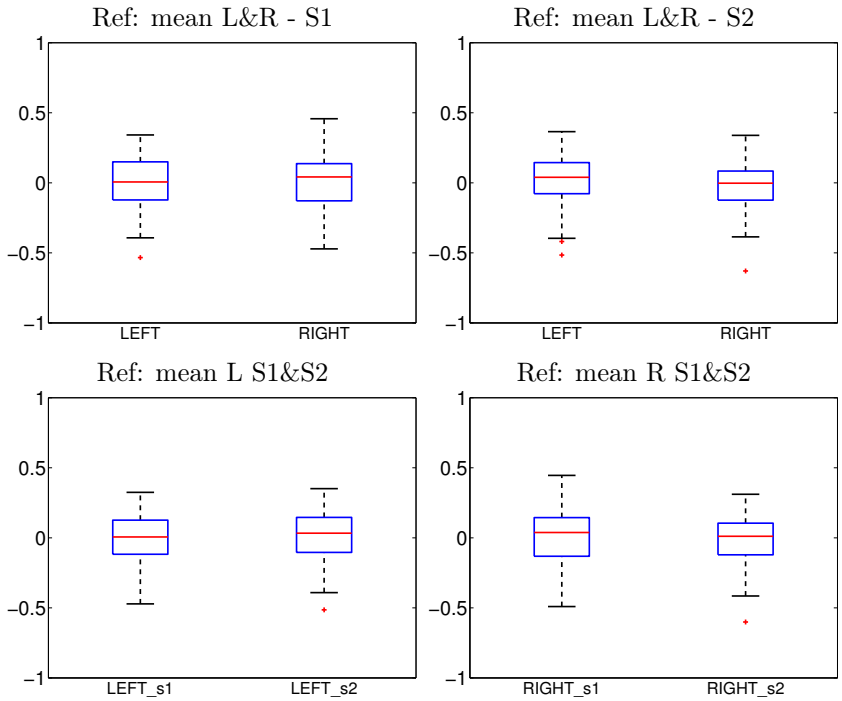

Figure 9.4: Boxplots of the differences between left and right hemispheres of κ degree (κ_D) considering the 100 healthy subjects together with their two sessions (S1 and S2) of the HCP database. First row shows the comparison between left and right hemispheres for each session independently. Second row shows the comparison between the two sessions of the left and right hemispheres separately, considering as reference the mean between both sessions of each hemisphere. Results show no significant differences in κ_D neither between left and right hemispheres, nor between different sessions of the same subjects.

the data of patients with right-sided and left-sided lesions. We also eventually performed the statistics in separated sub-groups.

Similar results were obtained with the other tested graph metrics: κ_{E_g}, κ_{E_l}, κ_B and κ_C.

9.4 Discussion

In this study, we explored the 'hub disruption index' (κ) that aims at capturing brains' networks reorganization in order to propose it as a new tool for clinical investigation of brain lesions.

Characteristics of κ: reliability, group discriminability We first showed that κ is more reliable than global graph metrics in healthy subjects. We then

applied it to explore the reorganization of the brains' contralesional hemispheric networks in the post-acute stage of severe stroke patients. We found significantly lower κ values in the contralesional hemispheres of the patients' brain networks indicating the presence of reorganization in the contralesional hemisphere, a result that was not found when using classical graph metrics. Through this clinical example, we showed here that κ is more reliable than graph metrics and more sensitive to detect differences between groups of patients as compared to healthy controls.

Sample size and group discriminability with κ The ICC reliability relates to the variance of the measures. ICC is commonly classified into different categories [Cicchetti, 1994, Sampat et al., 2006]: less than 0.4 indicates low reliability, 0.4 to 0.6 indicates fair reliability; 0.6 to 0.75 indicates good reliability and greater than 0.75 indicates excellent reliability. However, there are several limitations of ICC approaches, as described by Müller and Büttner [1994]. ICC estimation may vary according to the estimation method leading to different versions of ICCs and ICCs are dependent on the range of the measuring scale. Consequently, it has been recommended to calculate confidence intervals or p-values in addition to ICCs [Shrout and Fleiss, 1979].

Here, with a group of 20 subjects or higher, we showed that we can achieve reliable κ estimation for the whole brain connectivity analysis (p-value ~ 0.05) even if the ICC values are not very high. For the intra-hemispheric connectivity, κ estimation presents less reliability and thus a larger variance. As a consequence, in this case, the discriminability between two groups is more difficult to achieve, but when differences between groups are large enough, even small groups can be sufficient to detect the effect. This situation could be compared to the Student t-test: when the difference between two Gaussian curves is sufficient, this difference can be statistically significant even with large variance in the Gaussian curve and with a low number of degrees of freedom.

Chapter 10

Influence of parcellation, filtering and connectivity measure on test-retest reliability

Some of the results presented in this chapter related to the influence of the parcellation schemes at the global level were published in our Neuroimage publication:

M. Termenon, A. Jaillard, C. Delon-Martin, S. Achard, **Reliability of graph analysis of resting state fMRI using test-retest dataset from the Human Connectome Project**, NeuroImage, Available online 6 June 2016, ISSN 1053-8119, http://dx.doi.org/10.1016/j.neuroimage.2016.05.062

10.1 Introduction

The influence of the parcellation scheme used to study the brain functional connectivity, is still an issue under debate. Among the neuroimaging community, there is no consensus about the best parcellation and the number of regions for the investigation of the test-retest reliability of brain networks.

Mainly, two types of templates exist: those based on **anatomical features** (either structural T1 or diffusion based) and those based on **functional features**. Among the structural based templates, the AAL has attracted lots of interest since it is a precisely defined template based on a single subject that includes parcellation of the cerebellum [Tzourio-Mazoyer et al., 2002] and additionally it was mainly used in the previous test-retest studies. The brain parcellation done by this template is shown in Fig. 10.1. However, it may not be representative of the brain populations and thus another atlas based on the

structural images of 37 healthy adult subjects was developed, currently known as the Harvard-Oxford atlas [Desikan et al., 2006]. More recently, functional connectivity based atlases have been proposed by for example aggregating regions based on their functional similarity using different algorithms such as spatially-constrained spectral clustering algorithm [Craddock et al., 2012] (see Fig. 10.2) or by using independent component analysis [Filippini et al., 2009].

According to Thirion et al. [2014], predefined parcellations are limited in two regards: i) there exist many different parcellation schemes, but they are mutually inconsistent; ii) a given parcellation may not fit the data properly. These authors carried out a comparison between data-driven parcellation methods in task based fMRI.

Two other factors that can influence the reliability of graph-based functional connectivity were also explored.

The first one corresponds to the filtering method used to select frequencies below 0.1 Hz. We compared two methods based on Fourier transformation (Butterworth and Boxcar) to the wavelets decomposition approach we used along all the experiments of this thesis.

The second one relates to the computation of the connectivity measure. Here, we compared the reliability of computing graphs using Pearson's correlation and partial correlation. The former measures the general dependence between variables, whereas the latter estimates the direct interdependence after excluding third-party effects. Smith et al. [2011] demonstrated that both correlation methods provide excellent performance at estimating functional connections, but Pearson's correlation outperformed partial correlation when the number of nodes in brain networks significantly increased. It is important to take into account that the computation of partial correlation is based on the covariance matrix and it needs to be inverted; this inversion can be numerically unstable if the length of the time series is shorter than the number of regions in the analysis.

10.2 Methods

The methods applied in these experiments were the same as explained in Section 8.2 but with the following parcellation schemes.

Parcellation scheme

In order to evaluate the influence of the parcellation scheme on the TRT reliability, we tested several parcellation schemes. Based on anatomical features, we used a modified version of the classical Anatomic-Automatic Labeling (AAL) [Tzourio-Mazoyer et al., 2002] composed of 89 regions and a finer one derived from the same parcellation but subdivided into 459 regions [Alexander-Bloch et al., 2012], denoted **AAL89** and **AAL459** respectively. The Harvard-Oxford template[1] (**HO117**) was used together with the cerebellar atlas [Diedrich-

[1] Available in `http://fsl.fmrib.ox.ac.uk/fsl/fslwiki/Atlases`

sen et al., 2009] (note that we merged some parts of the cerebellum to have the same parcellation as in AAL89). As a functional alternative, we used a parcellation with 100 regions provided by Craddock[2] (**Crad100**), using temporal correlation between voxel-time courses as similarity metrics and a group level clustering based in a two-level scheme in which the data of each participant are clustered separately. Finally, we used the ICA maps available from the "node timeseries" in the HCP website[3] for 50, 100 and 200 independent spatial maps (named **ICA50**, **ICA100** and **ICA200**, respectively), in which the full set of ICA maps was used as spatial regressors against the full data, estimating one time series for each ICA map.

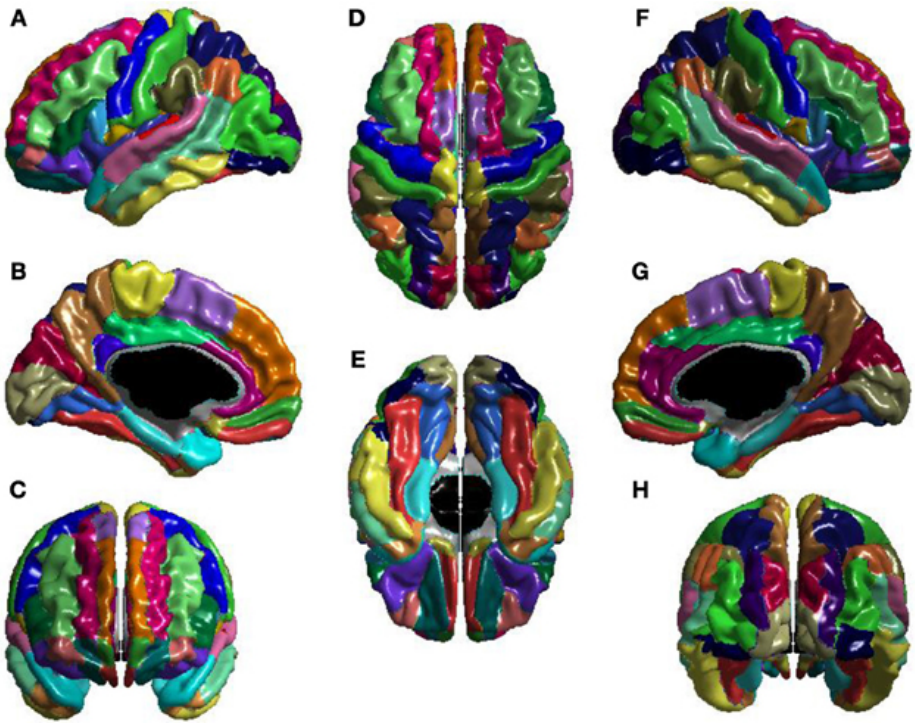

Figure 10.1: Example of the standard AAL parcellation scheme without the cerebellum, comprising 90 regions in the cortical and subcortical areas.

Fourier transform

Graphs using Fourier transformation were computed using two different frequencies: $F1 = [0.008 - 0.08]$ Hz, that corresponds with the standard frequency

[2] http://ccraddock.github.io/cluster_roi/atlases.html

[3] http://www.humanconnectome.org/documentation/S500/HCP500_GroupICA+NodeTS+Netmats_Summary_28aug2014.pdf

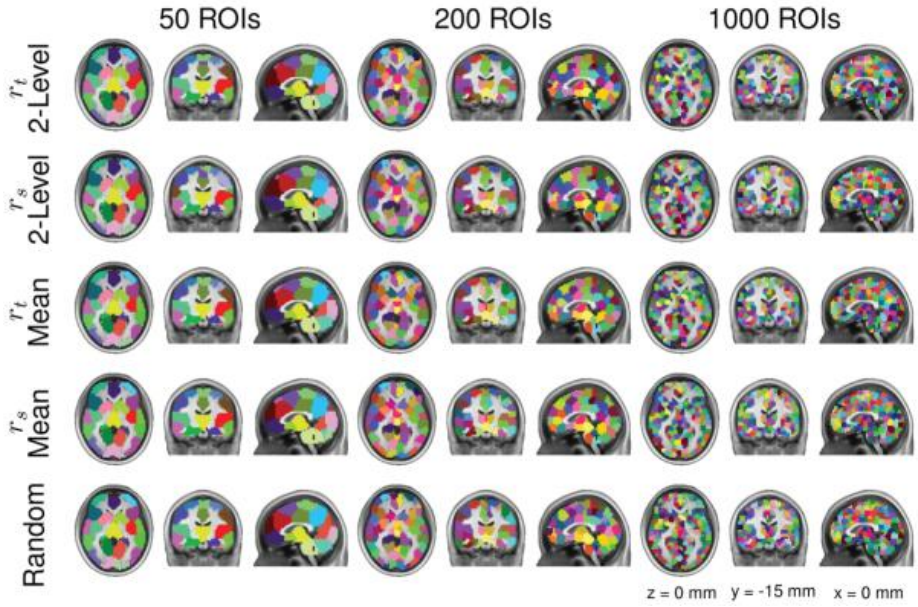

Figure 10.2: Example of Craddock parcellation scheme showing different parcellations according to the number of regions (50, 200 and 1000 regions). ROI: regions of interest.

band used in the majority of resting state experiments and $F2 = [0.04 - 0.08]$ Hz, that corresponds to the same frequency band of wavelet 4. We also applied to different band pass filtering: butterworth (BW) filter and boxcar filter.

We applied Simctest to the extracted global efficiency to compare the reliability of this metric computed using wavelets and Fourier transform. Results are shown in Fig. 10.8.

Partial correlation

For the computation of partial correlation, we used a package in R named 'parcor'[4], which estimates partial correlations based on regularized regression. In particular, we used the computation of partial correlations with adaptive lasso.

We applied Simctest to the extracted global efficiency to study the reliability of this metric using partial correlations for both, wavelet 3 and 4 and also using Fourier transformation at frequency $F1 = [0.008 - 0.08]$ Hz. Results are shown in Fig. 10.9.

[4]https://cran.r-project.org/web/packages/parcor/parcor.pdf

10.3 Results

10.3.1 Comparison between parcellation at the global level

In Fig. 10.3, we show the p-values for E_g and E_l using the parcellation AAL459 and we compare the results for 40 and 100 subjects. With 40 subjects, both E_g and E_l becomes significant; from $5-40\%$ cost in the case of E_l and $10-37.5\%$ cost for E_g. When considering 100 subjects both metrics are significant at almost every cost. This figure can be compared to the first row of Fig. 8.4 that displays the same plot with the AAL89 parcellation scheme. Both E_g and E_l are showing also more reliable measures with the finer parcellation scheme as compared to the coarse ones.

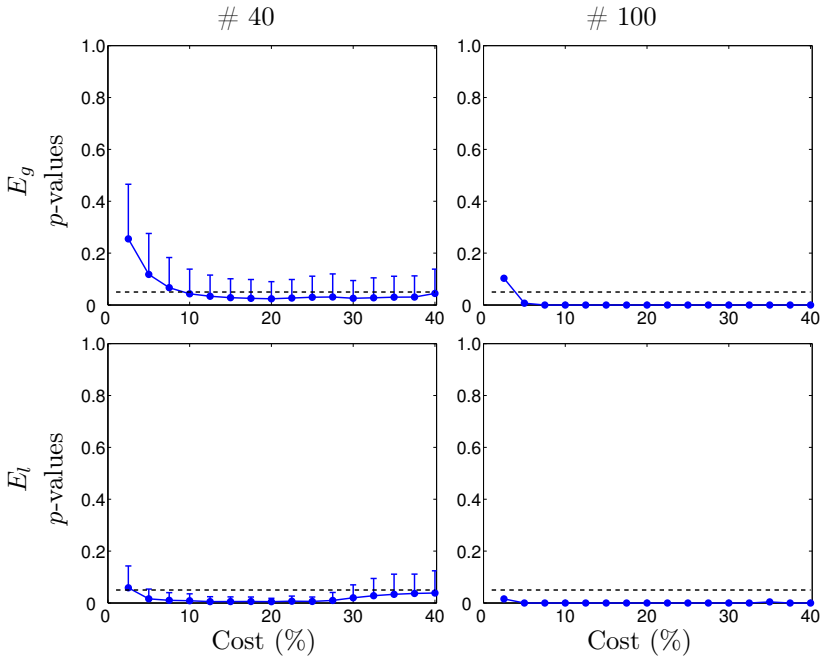

Figure 10.3: Comparison between the reliability of 40 and 100 subjects using the parcellation of 459 regions. Two global network parameters (Global and local efficiency) are compared. E_g (first row) and E_l (second row) p-values; on the left, 40 subjects (1000 bootstraps) and 100 subjects on the right. Results computed for cost from 2.5 to 40%. This figure can be compared to the first row of Fig. 8.4.

The ICCs and their respective p-values for E_g, E_l and B using several anatomical and functional parcellation schemes at 20% cost and 1200 tp are shown in Fig. 10.4. For E_g, we observe that the p-values are very close for the different parcellations except for HO117. A number of subjects between 30 and 40 is sufficient to achieve reliability on ICC except for HO117, where 60 subjects

are required.

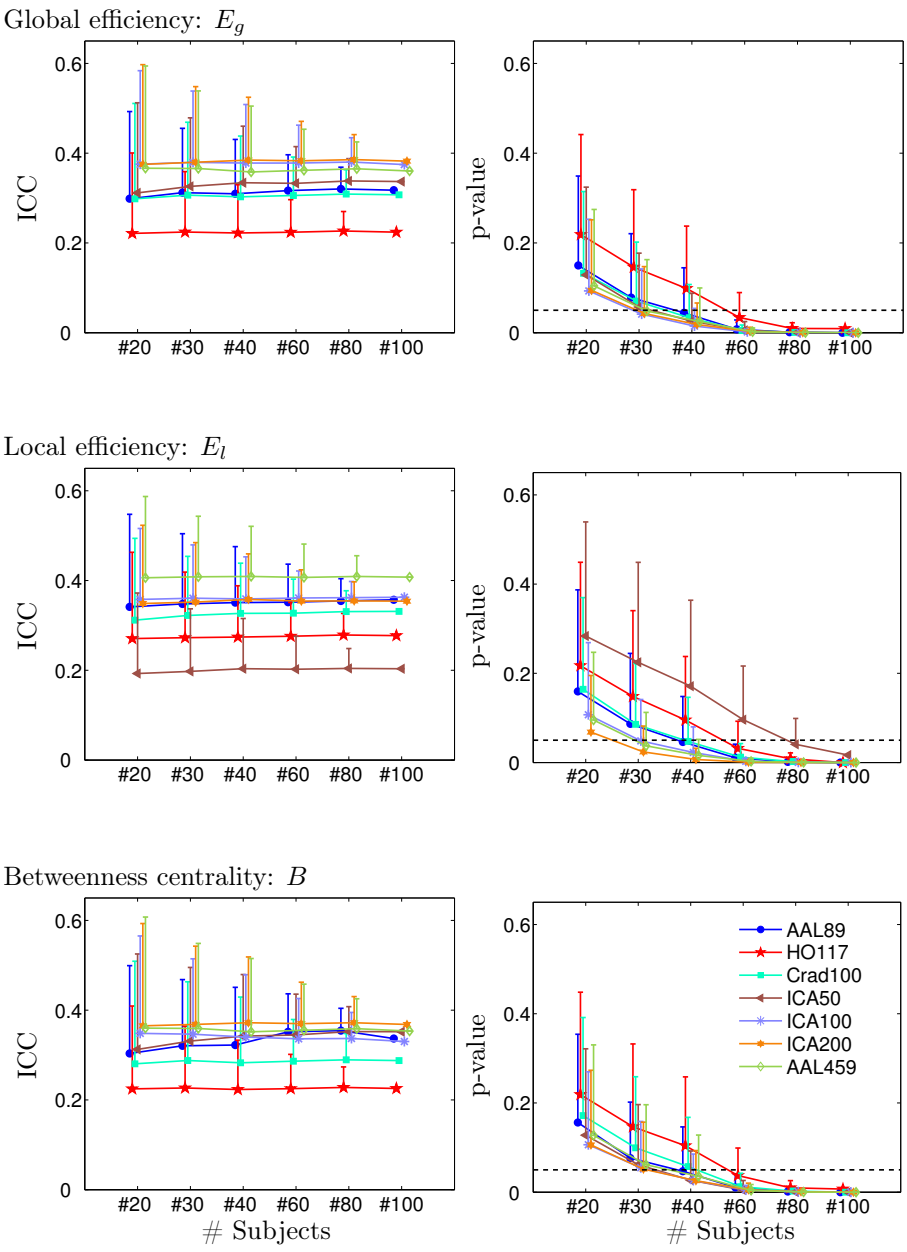

Figure 10.4: ICCs and their p-values for different parcellation schemes and different number of subjects. Results are shown for global efficiency (E_g), local efficiency (E_l) and betweenness centrality(B), at 1200tp and 20% cost.

Similar results are observed for B. In the case of E_l, p-values present higher differences between parcellation schemes with lowest p-values for ICA200, followed by AAL459, then ICA100, Crad100 and AAL89, then HO117 and finally ICA50. Accordingly, for E_l, the number of subjects required to achieve reliability on ICC depends on the parcellation (middle row). We also show that ICC values of the three metrics are dependent on the parcellation scheme (left column). With E_g and B, we found the highest ICC values for the finer parcellations: ICA200, ICA100 and AAL459; then for ICA50, AAL89 and Crad100 and finally, for HO117 parcellation. With E_l, highest ICC values were found with AAL459, followed by ICA200, ICA100 and AAL89, then Crad100 and HO117 and finally ICA50.

10.3.2 Comparison between parcellations at the regional level

Similarly, as we computed the percentage of significant regions for the AAL89, we repeated the same computation for the rest of parcellations in the study. In Fig. 10.5, we show the results for regional global efficiency (e_{g_i}) at 1200tp and 20% cost.

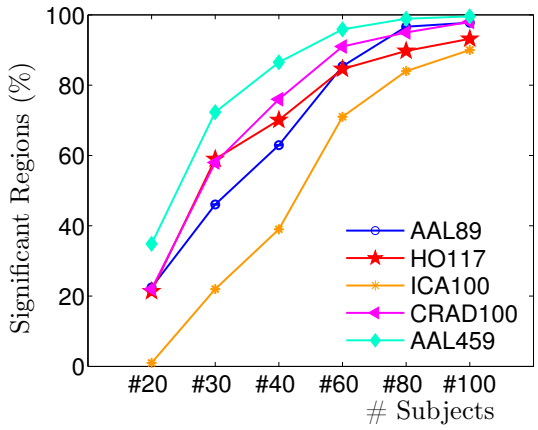

Figure 10.5: Percentage of significant number of regions according to the number of subjects included in the analysis and the parcellation template. Results are shown for global efficiency (Eglob) at 1200tp and 20% cost.

Each parcellation divides the brain into different regions. In order to see if the significant regions are located in the same regions of the brain, we show in Figs. 10.6 and 10.7 the location of the significant regions for 20, 30, 40 and 100 subjects and all the structural based parcellations. We can observe that the finer parcellation (AAL459) prsents the highest percentage of significant regions whatever the sample size, followed by Crad100, HO117, AAL89 and ICA100.

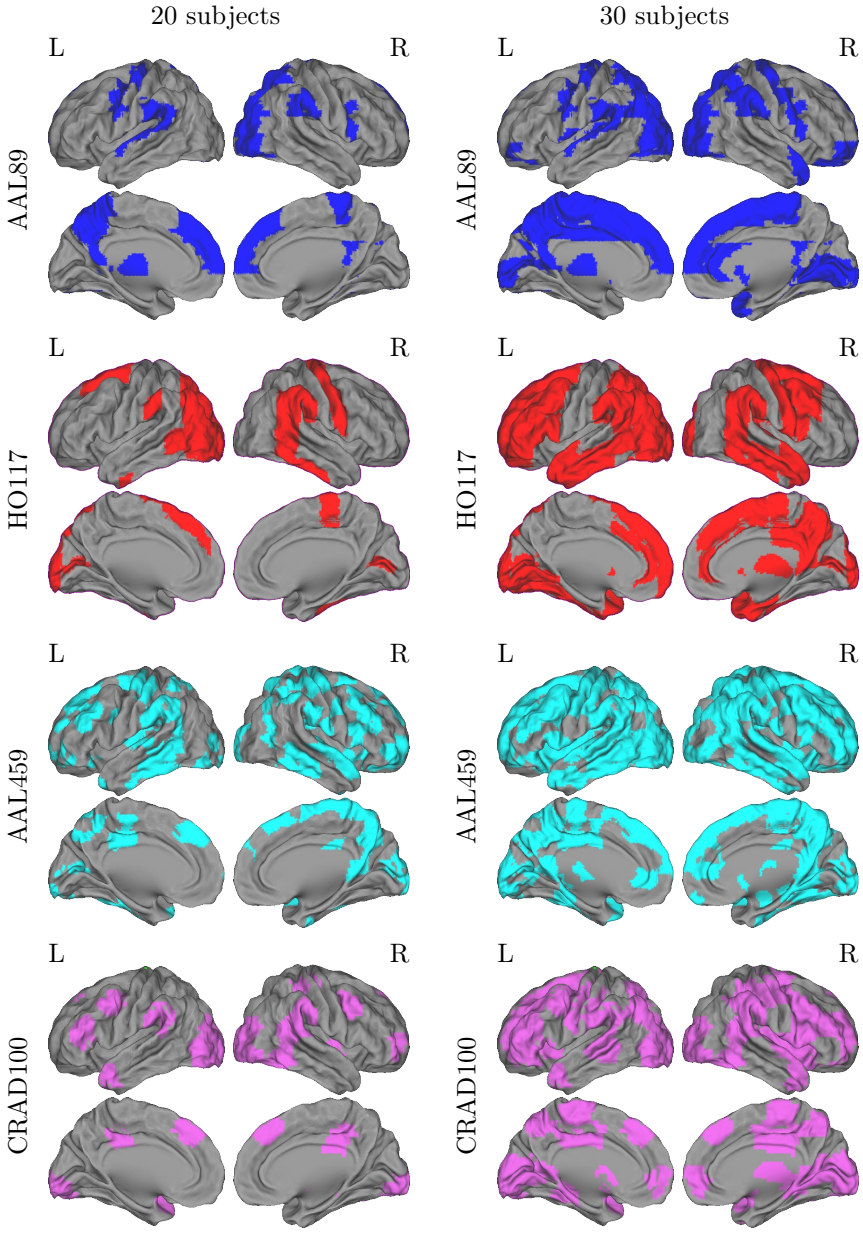

Figure 10.6: Comparison between the significant regions of the brain for 20 and 30 subjects, using AAL89, HO117, AAL459 and CRAD100. Results are obtained for e_{g_i} at 20% cost and 1200 tp.

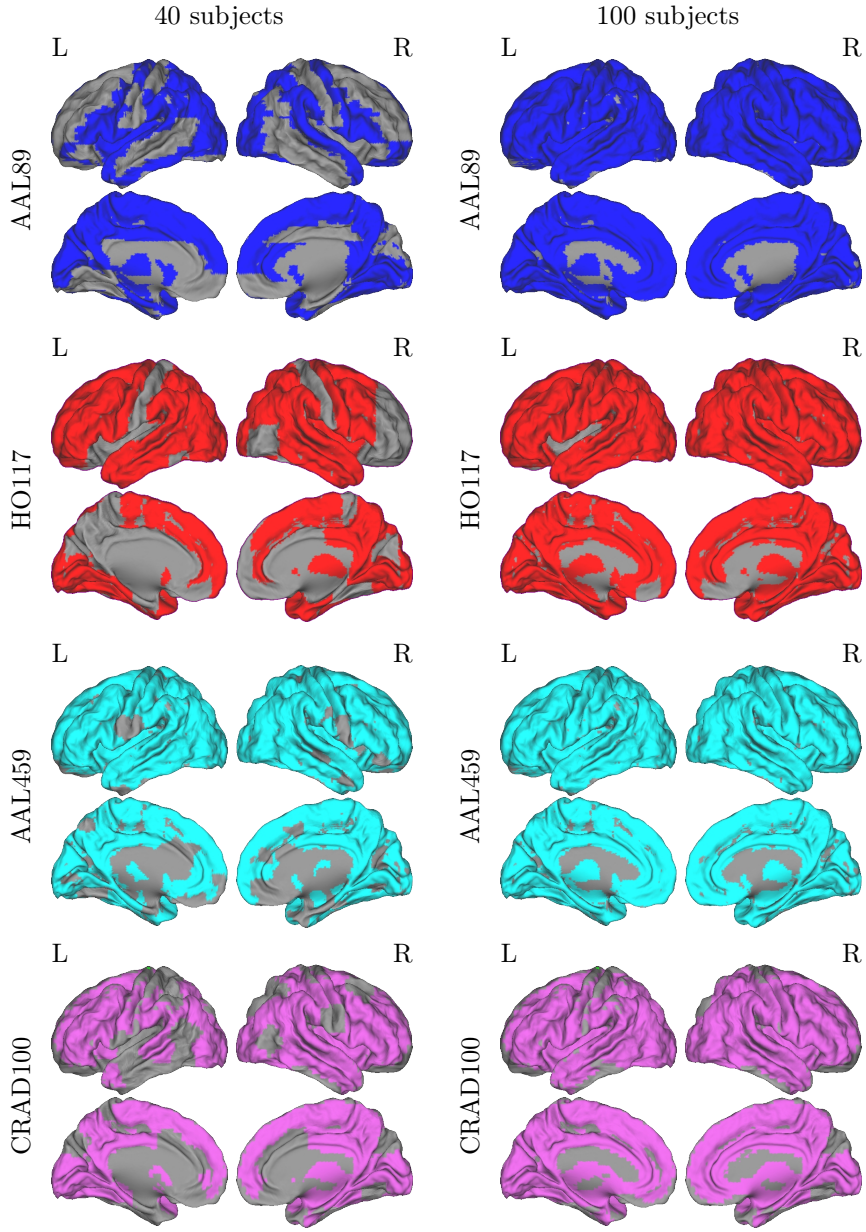

Figure 10.7: Comparison between the significant regions of the brain for 40 and 100 subjects, using AAL89, HO117, AAL459 and CRAD100. Results are obtained for e_{g_i} at 20% cost and 1200 tp.

Whatever the template, with 20 subjects, it can be observed that the percentage of reliable regions is low, ranging from 0 to 35%, suggesting that only a

few set of regions can be considered as reliable with a sample size of 20 subjects.

Taken together, using the finest parcellation scheme (AAL459) seems to be a good choice for achieving reliability of global and regional graph metrics. However, for small sample size, only few regions are reliable and their location depends on the parcellation choice (Figs. 10.6 and 10.7). For sample size above 60 subjects, the reliability is achieved at both global and local level, with very few influence of the template.

10.3.3 Comparison of reliability between graphs computed using Fourier transform and using wavelets

The reliability differences of E_g between graphs computed using Fourier transform and using wavelets are shown in Fig. 10.8. We can observe that the reliability of Fourier transform at frequency F1 ($[0.008 - 0.08]$ Hz) are more compactly grouped, almost achieving significant values with 20 subjects, first row of Fig. 10.8.

The comparsion between wavelets and Fourier at the same frequency interval ($F2 = [0.04 - 0.08]$ Hz), shows very similar results, second and third rows of Fig. 10.8.

10.3.4 Comparison of reliability between graphs computed using partial correlation and graphs using Pearson's correlation

The reliability of partial correlation is shown in Fig. 10.9. In the first row, the reliability of both wavelets 3 and 4 are shown. There are several costs with negative ICC scores and very few significant values. Wavelet 3 seems to be very unstable, with ICCs ranging from -0.8 to 1. These negative ICC values are difficult to interpret because they mean that the between subjects variance is smaller than the within subjects variance.

In the case of Fourier, second row of Fig. 10.9, results are slightly better, but still far from the reliability achieved with Pearson's correlation.

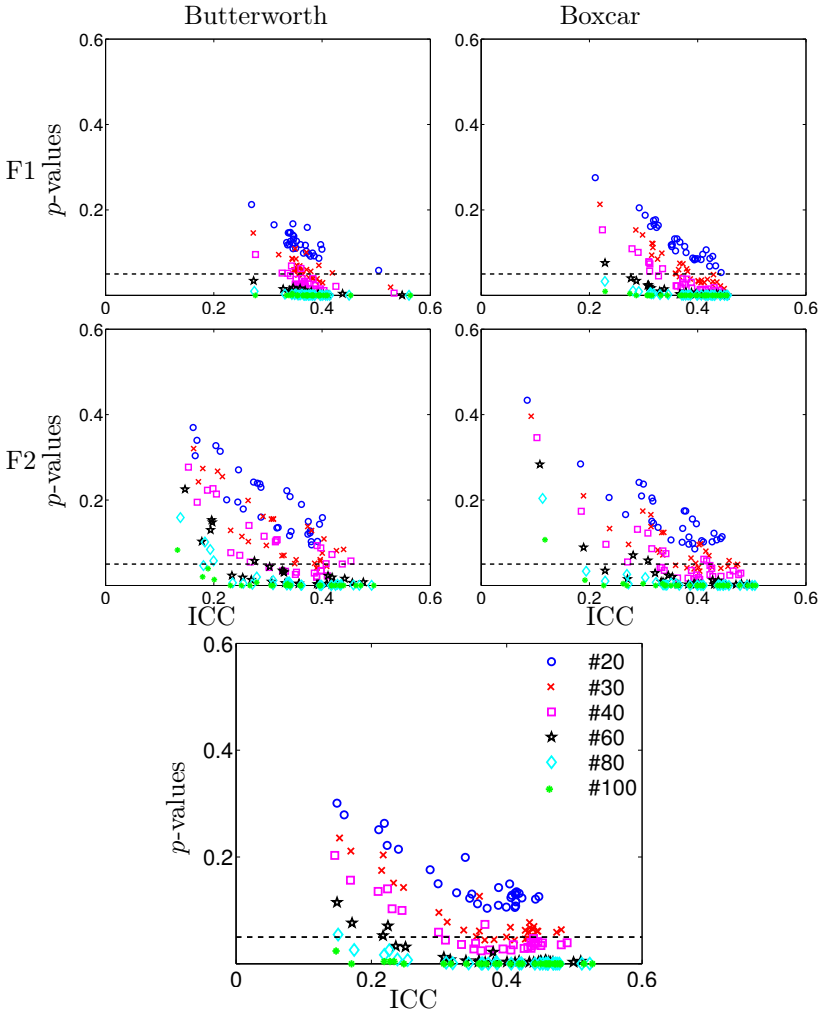

Figure 10.8: Comparison of the reliability of E_g between Fourier transform and wavelets. First row, results for Fourier transform at frequency $F1 = [0.008 - 0.08]$ Hz; second row, results for Fourier transform at frequency $F2 = [0.04 - 0.08]$ Hz; last row, results using wavelet at the same frequency band than F2. Results are shown for different number of subjects at 1200 tp in the cost range between 2.5 - 70%.

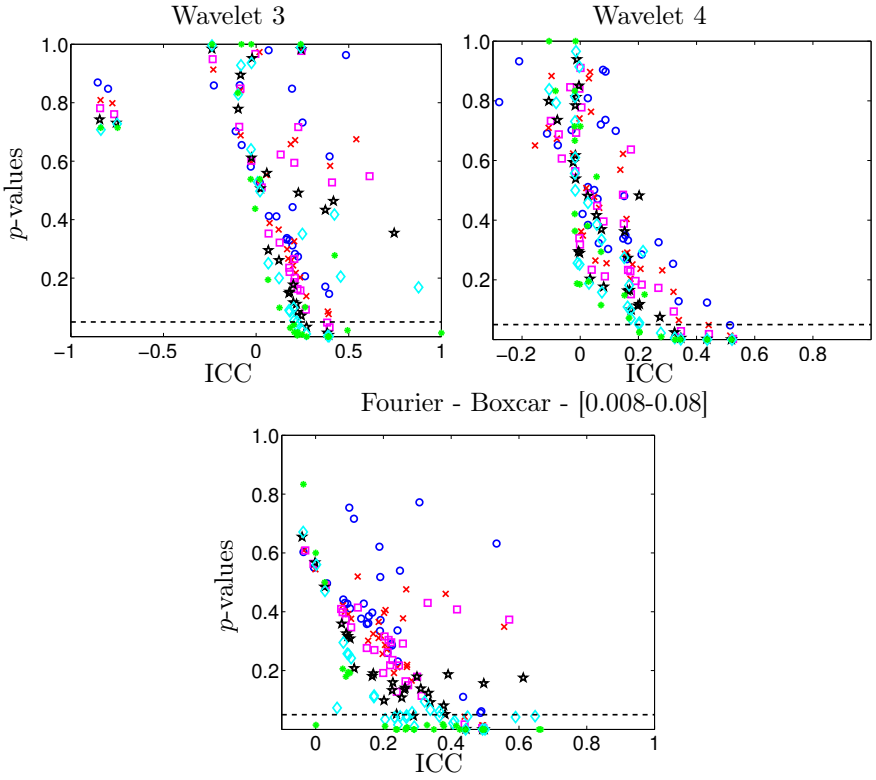

Figure 10.9: Comparison of the reliability of E_g using adaptive lasso partial correlation. Results are shown for wavelet 3 and 4 (first row), and for band pass Fourier filter using boxcar in the frequency band [0.008-0.08] Hz. Results are computed for different number of subjects at 1200 tp in the cost range between 2.5 - 70%.

10.4 Conclusion

10.4.1 Influence of the parcellation scheme

In an attempt to evaluate the influence of the choice of the nodes of the graphs on the connectivity results, we investigated in this chapter the test-retest values of graph metrics using different brain atlases. We found that the choice of atlas matters with different results depending on them. Although we believe that the ultimate atlas is not here yet, we can try to compare their respective influences. Here, we will discuss:

1. The comparison between anatomical atlases based on a single subject (AAL89) or on multiple subjects (HO117);

2. The comparison with respect to the number of parcels, using two parcel-

lation schemes based on the same atlas (AAL89) vs. (AAL459);

3. The comparison between different types of atlases having about the same number of parcels: anatomical atlases (AAL89 or HO117) vs. data-driven parcellations (Crad100 or ICA100).

Comparison between structural atlases:

The AAL89 atlas is based on the manual labeling of the anatomical structures of the Collin27 brain. This brain image presents a high signal to noise ratio since Collin was scanned 27 times for this acquisition and borders of this atlas are then accurate. The paper of Tzourio-Mazoyer which describes it was one of the earliest published in the literature, in 2002 and as such, achieved a high number of citations. Its main drawback is to be not representative of the population.

Since then, the so-called 'Harvard-Oxford' template [Desikan et al., 2006] combined the efforts of the Harvard and Oxford teams to automatically delineate gyral structures from 40 healthy subjects. As the 40 brain images are individual-specific, they were inflated and coregistered together using an automatic algorithm that lead to uncertainties at some borders. Yet, it contains 117 structures from the neocortex, subcortical structures and the cerebellum.

Both atlases are used in the literature but without direct comparison between them. Here, we found that global graph metrics with HO117 present lower ICC and larger p-values than with AAL89. At regional level, we found different percentage of reliable regions depending on the atlas and on the sample size. In particular, the regions that present good reliability are dependent on the chosen atlas. For instance, in Fig. 10.7 with 40 subjects, we see that the reliable regions are different in the temporal lobe, in the frontal lobe, in the precuneus between the two parcellations. It is thus impossible to conclude that one atlas is better than the other. One reason could be related to the region size that may be too large and inhomogeneous. Indeed the studies based on cytoarchitecture of the cortex had permitted to find finer parcels than the parcels of these atlases. This point could be investigated using a finer atlas.

Comparison of number of nodes in anatomical atlases:

With the finer template (AAL459) derived from the standard AAL [Tzourio-Mazoyer et al., 2002], the number of nodes is higher and the surface of each node is then smaller, leading more chance for an intra-nodal homogeneity. The ICC values for the global graph metrics obtained with AAL459 are higher than those with AAL89, while p-values remain very close. At regional level also, we achieve a higher percentage of significant regions with the finer parcellation that covers nearly the whole brain with 40 subjects. This clearly indicate that a finer parcellation is better than a coarse one.

But what is the best number of parcels? One indication could come from previous work on task-based fMRI data provided by 67 subjects from the Human Connectome Project [Thirion et al., 2014]. In this work, where atlases varied in their number of parcels, the authors found that a number of about 200

to 500 parcels is relevant while 100 parcels is unsufficient. The result found here with resting-state is compatible with the results found with task-based fMRI. Interestingly, the team of Van Essen published this summer a multi-modal parcellation of the human cerebral cortex, that lead to the extraction of a set of 180 cortical areas per hemisphere, providing a total of 360 cortical areas, that is in the same order of magnitude [Glasser et al., 2016].

Comparison of the atlas types:

The type of atlas available by and for the neuroimaging community are different: they may be based on anatomical structures, on functional regions or derived from the data using some classifiers. By comparing the results derived from templates with about the same number of parcels (AAL89, HO117, Crad100 and ICA100), we could observe at global level that ICC are the highest and p-values the smallest with ICA100 (Fig. 10.4).

At regional level, the 3 parcellations (Crad100, HO117 and AAL89) provide different reliability according to their type (Figs. 10.6 and 10.7). This result is particularly important with sample size of 20 or 30 subjects. **This results suggests that conclusions drawn in the literature with a given template might not apply with another one.**

10.4.2 Influence of the filtering method

Others points that were poorly investigated in the literature related to the frequency filtering were addressed here since wavelets filter more narrow frequency bands. We did not find clear differences with frequency filtering of the same band, but slightly higher ICC values than standard frequency band. This latter result seems to be on line with observations made by Guo et al. [2012].

10.4.3 Influence of the connectivity measure

According to the results observed in Fig. 10.9, partial correlation is not reliable. Partial correlation needs a very big sample size, or a very long scan duration (much more than 1200 time points), or a very low number of regions to be a reliable measure [Smith et al., 2011]. In the context we performed this experiment, 100 subjects, scan duration of around 14 minutes and parcellation scheme of 89 regions, we do not recommend the use of partial correlations.

These results are in line with those of Liang et al. [2012], where they found that Pearson's correlation was more reliable than partial correlation.

Part III

Role of the contralesional hemisphere in stroke using graphs

Introduction

Stroke, resulting in focal structural damage, induces changes in brain function at both local and global levels. Following stroke, cerebral networks present structural and functional reorganization to compensate for the functional impairment provoked by the lesion itself and its remote effects. As several recent studies underlined the role of the contralesional hemisphere during recovery, we studied its role in the reorganization of brain function of stroke patients using resting state fMRI and graph theory.

We explored this reorganization using the 'hub disruption index' (κ), a global index sensitive to the reorganization of nodes within the graph. For a given graph metric, κ of a subject corresponds to the slope of the linear regression model between the mean local network measures of a reference group, and the difference between that reference and the subject under study.

In numerous neurological conditions, the adult central nervous system retains an impressive capacity to recover and adapt following injury. Such so-called spontaneous recovery occurs after spinal cord injury, traumatic brain injury and stroke. Therefore, a basic understanding of the mechanisms that underlie spontaneous recovery of function is the initial step in the development of modulatory therapies that may improve recovery rates and endpoints [Nudo, 2013].

In subacute stroke, it has been shown that initial damage disrupts communication in distributed brain networks. This initial disorganization is followed by a dynamic reorganization at subacute and chronic stage that may determine the level of post-stroke recovery [Carter et al., 2012b]. Not only disorganization in structural connectivity has been reported and related to outcome of patients [Moulton et al., 2015] but also functional reorganization in the motor network of both ipsilesional and contralesional hemispheres [Gerloff et al., 2006, Loubinoux et al., 2003, Jaillard et al., 2005, Favre et al., 2014] to compensate for the lesion itself and for remote effects (see Grefkes and Fink [2014] for a review).

While the role of the contralesional hemisphere in the recovery process after stroke is supported by several studies using motor task fMRI paradigms [Rehme et al., 2011, Riecker et al., 2010, Grefkes and Fink, 2014, Gerloff et al., 2006, Lotze et al., 2006, Teki et al., 2013] , its role in recovery is still debated. On one hand, atypical interhemispheric balance with higher contralesional hemisphere activity can be associated with poor recovery [Calautti et al., 2007, Wiest et al., 2014], and impaired motor performance is often attributed to disruption in inter-hemispheric inhibition, where an overactive contralesional area is believed to suppress activity in the lesioned hemisphere [Auriat et al., 2015]. On the other hand, higher activity observed soon after severe stroke in contralesional primary motor and premotor cortices has been related to good recovery [Rehme et al., 2011]. In large stroke lesions, where the ipsilesional hemisphere is too damaged to support complete recovery, additional compensatory mechanisms might involve contralesional motor areas, explaining response variability to rTMS in stroke [Auriat et al., 2015]. Indeed, deleterious effects of contrale-

sional motor cortex inhibition using rTMS that have been observed following severe stroke Bradnam et al. [2012], suggest a compensatory role for the contralesional hemisphere.

In the recent years, there has been a great amount of work developing new investigation methods of the brain connectivity based on fMRI. Among those, the graph theoretical approach seems particularly useful in the context of pathology since it underlines the role of key communicating regions (hubs) in the graph. Furthermore, graph approach allows the exploration of each hemisphere independently of the interhemispheric connectivity. It is thus of clinical interest to study the reorganization of the contralesional hemisphere in stroke patients by means of functional connectivity fMRI at rest. Since there was no graph metric aiming at capturing this type of reorganization after brain damage, the Hub Disruption Index (κ) was introduced in Achard et al. [2012] to capture it. κ index summarizes graph metric changes at the nodal level in a single value. It is thus a global index capturing changes at the nodal level. A more detailed description of this index can be found in Subsection 5.4.2. In a previous chapter, we studied the reliability of this index, resulting in more reliable results than with standard global graph metrics.

We performed two experiments to explore the role of the contralesional hemisphere. Clinical and fMRI data was acquired in 25 patients with an ischemic stroke, at one and six month follow-up, in the context of the ISIS-HERMES study (see Chapter 11).

- Assessment of kappa index in stroke patients to explore contralesional global reorganization

In the first experiment, we computed κ using metrics that directly relate to hubs: node degree, betweenness centrality and global efficiency; and also in metrics that explore the neighborhood of the node, such as, local efficiency and clustering coefficient. The aim, thus, of this experiment was to quantify the impact of the lesion on the brain network reorganization of the contralesional hemisphere in severe stroke patients at subacute stage. For this purpose, κ index is a perfect tool to assess such reorganization by comparing nodal metrics between healthy volunteers and patients. We measured intra-hemispheric κ index in the contralesional hemisphere of 20 subacute stroke patients compared to 20 age-matched healthy controls.

Statistical analysis showed a significant reduction of κ for the contralesional hemisphere of right stroke patients compared to healthy controls. Similar results were observed for the right contralesional hemisphere of left stroke patients. We showed that κ, is more reliable than global graph metrics and more sensitive to detect differences between groups of patients as compared to healthy controls. Using new graph metrics as κ, allows us to show that stroke induces a network-wide pattern of reorganization in the contralesional hemisphere whatever the side of the lesion. Graph modeling combined with measure of reorganization at the level of large-scale networks can become a useful tool in clinical applications.

- Can kappa values in the contralesional hemisphere predict cognitive outcome?

In the second experiment, I introduce preliminary results obtained trying to predict clinical outcome of stroke at six months from variables measured during the first month after stroke. These variables are from diverse sources; patients characteristics such as the age, sex, lesion side; patients clinical scores such as RBANs, MMSE, treatment; and finally, measures obtained applying graph based analysis to the rs-fMRI acquisition, such as κ_{e_g}, κ_{e_l}, κ_b. As we have already seen in Chapter 4 of this thesis, it is important to relate clinical values to functional connectivity measures.

Based on the results of experiment 1, we investigated whether the kappa values derived from the graph metrics could predict the main cognitive outcome, i.e. the RBANS assessed at six months, through three steps.

First, we investigated whether one month kappa measures were associated with cognitive scores measured concurrently and six months later.

Second, we used multivariable regression to assess whether kappa measures predict cognitive outcome (six month RBANS). To test whether kappa measures could predict cognitive recovery, we first entered baseline RBANS in the model and then introduced the other predictors. In this process, lesion volume, lesion side, gender, age, level of education and delay from stroke onset were introduced as additional predictors in the multivariable predictive model

Third, baseline RBANS was removed from the model to determine whether kappa measures alone can be used as a biomarker of cognitive outcome. A limitation of multivariable linear regression is the possible model overfitting by including too many variables. Internal validation can overcome this problem by indicating an upper limit to the expected performance of the model in different datasets. Thus, multiple regression was coupled with bootstrap resampling with 5000 replications to reconstruct 95% confidence intervals and obtain unbiased estimates of prediction accuracy [Steyerberg et al., 2001].

Chapter 11

Stroke database and methods

In this chapter, I will introduce the relevant information related to the stroke patients group. Also, I will explain the steps we need to follow to include the lesion mask in the preprocessing of the data. I also explain the particularities of the time series extraction and graph computation, that will remain constant along all the experiments presented in this last part of the thesis. Finally, I describe the methods applied for each of the two experiments performed.

11.1 The ISIS-HERMES study

ISIS-HERMES is phase II monocentric clinical controlled trial (CCT) where 31 patients were enrolled. The objective of the clinical part of the CCT, was to assess feasibility and tolerance of intravenous injection (IV) of autologous mesenchymal stem cells (MSC) in patients with carotid ischemic stroke. HERMES (PHRC2010) is a neuroimaging study whose primary outcome is to identify MRI biomarkers of stroke recovery. These biomarkers will be used to assess the efficacy of MSC in a multicenter European CCT, RESSTORE (Horizon 2020). A group of 41 healthy subjects was included in HERMES as controls for MRI experiments.

The main inclusion criteria were: (1) right or left carotid ischemic stroke in the prior 14 days confirmed by MRI, (2) persistent moderate to severe movement deficits at one month post stroke, (3) optimal medical treatment (antithrombotic, antihypertensive, statins) (4) clinical status compatible with participating in the hospital rehabilitation program, and (5) willingness to participate. Patients with a previous history of neurological disease with a consequent movement deficit, claustrophobia, or psychiatric disease were excluded. Following informed consent, they received either intravenous autologous stem-cell or no treatment. Patients were studied using fMRI at inclusion one month after stroke, before stem-cell treatment. They received standard medical care and were admitted to a stroke rehabilitation center.

Patients had a pre-inclusion medical visit (V1), were randomized, and then

had an inclusion visit at one month post stroke (V2), where treatment was administered. The follow-up included visits that took place at two weeks (V3), two months (V4), four months (V5), six months (V6), one year (V7) and two years (V8) post inclusion. The MRI protocol was performed at V2, V3, V4, V6 and V8.

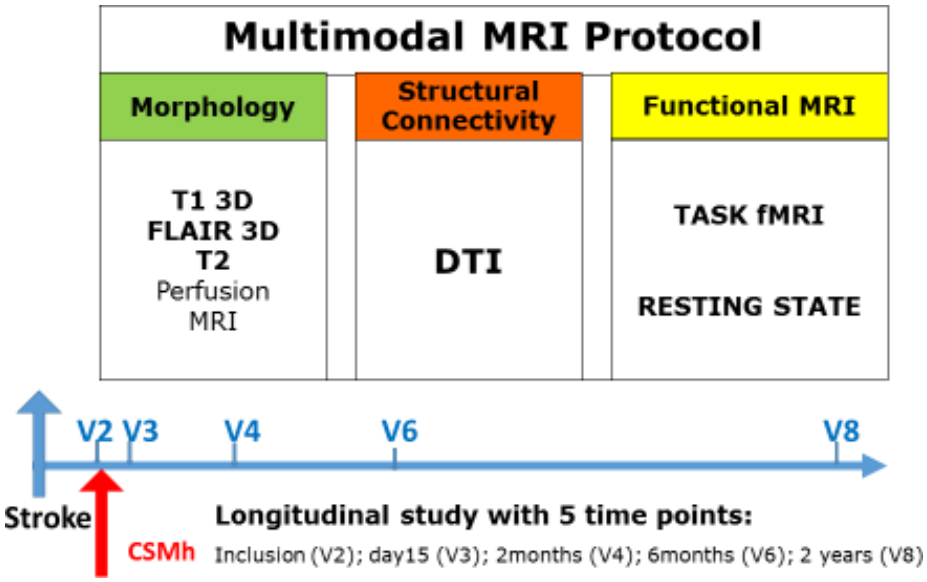

Figure 11.1: HERMES longitudinal study, from inclusion to 2 years after stroke.

Behavioral motor assessment, blinded to treatment allocation, included the motor Fugl-Meyer score (FMS) and NHISS at one and six months post-stroke. The FMS was used to determine the initial motor performance at V2 and motor outcome at V6.

The NIHSS [Brott et al., 1989] was used for patient inclusion and to classify baseline stroke severity as moderate (7-15 NIHSS range) or severe (16-24 NIHSS range). Independence was measured using the Barthel Index [Mahoney and Barthel, 1965], and the Modified Rankin Score (mRS) [Rankin, 1957].

The cognitive assessment included:

1. RBANS (Repeatable Battery for the Assessment of Neuropsychological Status) [Randolph et al., 1998]. It is a multidimensional neuropsychological test assessing five neurocognitive domains, with scaled score profiles:

    - Immediate Memory: List Learning (10 words with 4 trials) and Story Memory (2 trials)
    - Visuospatial/Constructional: 1 Figure Copy and Line Orientation (10 x 2 lines)

- Language: Picture naming (10 pictures) and Semantic Fluency (1 min)
- Attention: Digit Span and Coding (90 sec)
- Delayed Memory: List Recall, List Recognition, Story Memory, and Figure Recall

2. The BAWL battery (Battery Attention William Lennox [Leclercq and Chipp, 1989]) a computerized tool for assessing different attentional components with three reactions time (RT) tests: the Visual centred RT, the Auditory RT and the simple binary RT test.

3. The mini-mental state examination (MMSE [Folstein et al., 1975]) to assess dementia.

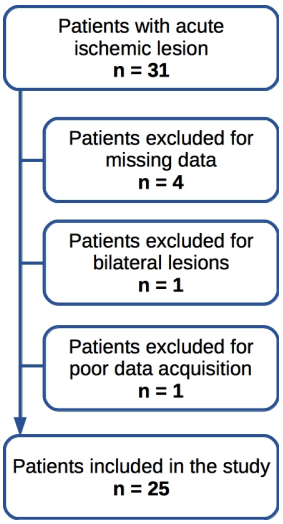

Figure 11.2: Flowchart illustrating the selection of patients.

All patients underwent RBANS assessment with short term memory, visuospatial, language, attention and delayed memory subscores generated. Adding these subscores resulted in the RBANS that was used as the main cognitive outcome measure. Note that higher scores indicate better cognitive performance. A score of zero is given for patients who were not able to perform the test. Behavioral assessment was performed by a stroke neurologist (neurological examination, NIHSS, Barthel, mRS) and a neuropsychologist (RBANs, BAWL, MMSE) blind to treatment allocation at baseline (one month after stoke) and at six month follow-up. Stem-cell therapy effects are explored in another manuscript that is in preparation.

Out of 31 patients enrolled, the rs-fMRI could be performed in 25 patients, see Fig. 11.2. In Table 11.1, we show the demographics of the patients included in these experiments.

Patient	**Age**	**Gender (M/F)**	**Lesion side**	**Lesion vol (ml)**	**NIHSS**	**RBANS V2**	**RBANS V6**
h02	51	M	L	97	16	40	45
h03	38	F	L	47	11	61	78
h04	53	M	L	181	22	0	44
h05	48	M	R	241	13	61	79
h06	50	M	R	9	12	77	90
h07	60	F	L	119	20	10	50
h08	48	F	L	123	12	46	63
h09	59	M	L	73	16	43	52
h10	57	M	R	36	13	70	84
h13	45	M	R	60	9	87	108
h15	41	F	L	112	11	49	69
h16	52	M	R	83	12	78	77
h17	59	F	R	52	14	102	110
h18	58	M	L	220	23	0	0
h19	27	M	R	30	11	95	106
h20	42	F	R	55	12	97	110
h22	59	M	L	43	10	60	90
h24	65	M	L	72	7	55	78
h25	57	M	L	33	8	74	84
h26	47	F	L	34	12	44	66
h27	53	M	L	133	12	44	47
h28	62	M	L	70	10	57	77
h29	57	M	R	176	10	57	77
h30	67	M	L	150	23	0	25
h31	63	M	R	180	12	69	77
	52.7 ± 10.2	7F/18M	10R/15L	97.2 ± 64.0	13.2 ± 4.4	55.2 ± 30.0	72.2 ± 26.5

Table 11.1: Demographics of the stroke group. F, female; L, left; M, male; R, right.

Dataset of first experiment

Three out of the 31 enrolled patients were excluded: one for claustrophobia, one for refusal to continue, and one for psychiatric disease. Data from 6 patients were further rejected due to large motions (more than 12% of fMRI volumes rejected), and 2 of them had lesions in both hemispheres. Thus the final sample comprised the 20 remaining patients, whose demographic characteristics are given in Table 11.2. The 20 patients were matched for age and gender with 20 healthy controls.

Lesion	#	Age	Gender(M/F)	NIHSS	Lesion vol (ml)
Right	9	49 ± 11 [27-63]	7/2	12 ± 1 [9-14]	71 ± 72 [09-241]
Left	11	56 ± 9 [38-67]	7/4	13 ± 6 [7-23]	95 ± 59 [33-220]

Table 11.2: Demographics of the stroke group. Mean, SD and range for age, clinical score NIHSS and lesion volume are given.

Dataset of second experiments

In the second experiment, we included 25 stroke patients shown in Table 11.1 and a dataset of 41 healthy controls. We used the dataset of healthy controls, only to compute the reference of the κ index.

11.2 Data acquisition and preprocessing

Resting state fMRI parameters Image Acquisition

Participants were studied with Philips 3T ACHIEVA MRI system with a 32 channel head coil. Echo planar images (EPI) were acquired during one session (400 EPI volumes per session) using the following parameters: TR 2 s, voxel $3x3x3.5$ mm; time 13 min 40 sec. High resolution ($1mm^3$ voxel) structural images were acquired including sagittal T1-weighted (TR 9.9 ms, TE 4.6 ms,) 3D-FLAIR (TR 8 s, TE 342 ms) and 3D-T2-weighted images (TR: 2.5 ms, TE: 223 ms), FOV: 256*256*160, 160 slices. All subjects were instructed to remain still and relaxed during the scan with eyes closed and to avoid to fall asleep.

Preprocessing steps of stroke patients taking into account the lesion

A lesion in the brain can influence the preprocessing of the data in several steps. For example, when the T1w image is segmented to obtain the GM information, some lesioned parts of the brain can be wrongly detected as GM (as shown in Fig. 11.3). If this case, the GM segmentation can be very different from the template that the diffeomorphic registration tool (DARTEL) uses as reference. Trying to adapt the GM segmentation to the template, may cause non-desired deformations around the lesioned part that can lead to a non adequate registration of the volume.

This is the main reason why we designed a special pipeline for the stroke patients (see Fig. 11.4 for a detailed diagram). Stroke lesion volume was determined by manual delineation based on FLAIR images using MRIcron [1], and then used to mask T1-weighted images before preprocessing (T1w-hole in Fig. 11.4). We apply two segmentation steps, one for the T1w and one for the T1w-hole. This way we obtain two different GM segmentation (GM and GM-hole, respectively, in Fig. 11.4). GM-hole is then used for the non-linear registration, as the lesion is not included, the algorithm will not run in that part, and no

[1] `http://people.cas.sc.edu/rorden/mricron/index.html`

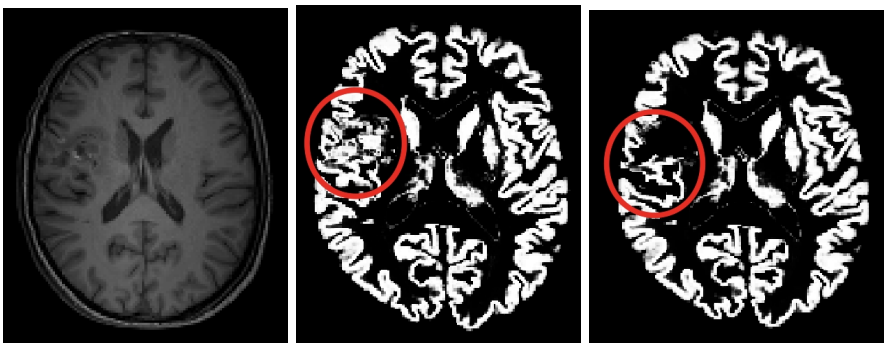

Figure 11.3: Example of GM segmentation with brain lesions. On the left, the structural T1w image, lesion can be observed on the left hemisphere. On the middle, the lesion mask was not applied when segmenting the GM. On the right, the lesion mask was applied when segmenting the GM. It is possible to observe some lesion parts included as GM in the segmentation of the middle image, that do not appear on the segmentation on the right.

non-desired deformations will be created. The deformation field is then applied to the GM segmentation and to the rs-fMRI volumes.

In order to do the segmentation the most accurate, we also included the T2w and/or FLAIR images (depending on availability).

11.3 Time series extraction and graph computation

Time series extraction The structural brain images were parcellated according to a modified version of the classical Anatomic-Automatic Labeling (AAL) [Tzourio-Mazoyer et al., 2002] composed of 89 regions (see Appendix A for more information). For the computation of the intra-hemispheric graphs, each hemisphere was divided in 44 regions, and the vermis of the cerebellum was removed from the parcellation template. Inter-hemispheric graphs were only computed to assess the reliability of κ in the whole brain. In this case, the complete parcellation scheme was used for the computation of the graphs.

In each parcel, regional mean time series were estimated by averaging, at each time point, the fMRI voxel values weighted by the GM probability of these voxels. This weighting limits the contamination of the time-series by white matter signals and cerebrospinal fluids. Residual head motion were eventually removed by regressing out motion parameters and outliers detected using the ART toolbox[2].

[2] `https://www.nitrc.org/projects/artifact_detect/`

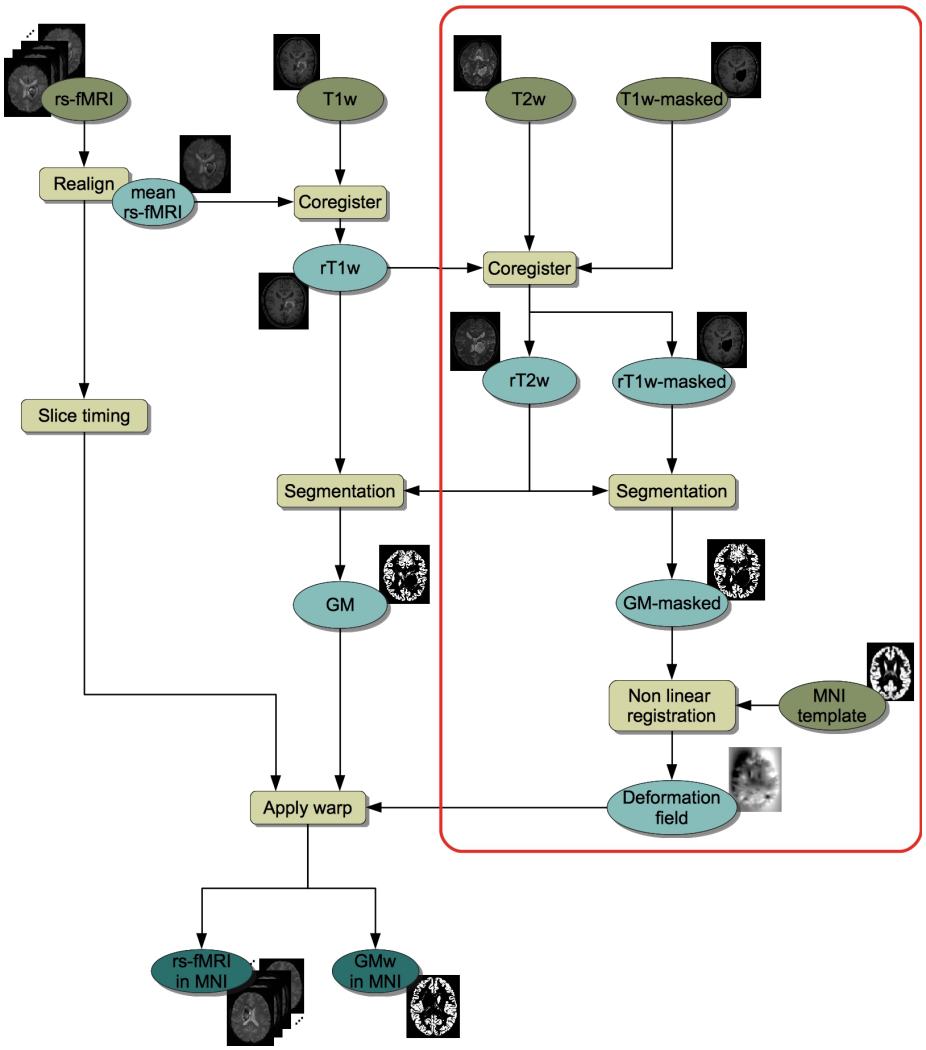

Figure 11.4: Preprocessing pipeline of stroke patients taking into account the lesion mask. In red, we show the new parts that were added in comparison to the pipeline of the healthy controls group.

Wavelets decomposition Wavelet transforms perform a time-scale decomposition that partitions the total energy of a signal over a set of compactly supported basis functions, each of them uniquely scaled in frequency and located in time [Achard et al., 2006]. We applied the maximal overlap discrete wavelet transform (MODWT) to each regional mean time series and estimated the pairwise inter-regional correlations at each of the wavelet scales.

The wavelet decomposition is dependent on the repetition time (TR) of

the rs-fMRI acquisition protocol. The databases used in this experiment have different TR. In the HCP database the TR = 0.72 s, while in the HERMES database the TR = 2.00 s, providing a maximum frequency $f = 1/(2\text{TR})$ of f = 0.69 Hz and f = 0.25 Hz, respectively. Each time a dyadic wavelet frequency band is obtained, the frequency is divided by 2. The relevant information for rs-fMRI data is then mainly contained within the scale 3 for HERMES data, that represents the frequency interval $0.032 - 0.065$ Hz. This choice was guided by the fact that, for resting-state fMRI data, frequencies below 0.1 Hz contain the most relevant information [Biswal et al., 1995].

Graph computation All pairs of correlations between regions are further pooled for each of the subjects into a correlation matrix. To compute the graph, we first extracted the minimum spanning tree based on the absolute correlation matrix to keep the graph fully connected [Prim, 1957, Alexander-Bloch et al., 2010]. The remaining absolute values of correlation matrices were thresholded to create an adjacency matrix that defines, for each hemisphere of each subject, an unweighted and undirected graph $G = [a_{ij}]_{1 \leq i,j \leq N}$, where N is the number of nodes in G and where $a_{ij} = 0$ or 1 for all the $1 \leq i, j \leq N$. A threshold R was computed to produce a fixed number of edges M. This way the comparison between the extracted graphs is easier. Graphs are computed for different costs, which is defined as the ratio between the number of selected edges among all possible edges in the graph. More detailed information can be found in [Achard et al., 2006].

We extracted κ for 5 different graph metrics: Global efficiency (E_g), local efficiency (E_l), node degree (D), betweenness centrality (B) and clustering coefficient (C). All this metrics were introduced in the first part of this thesis, Chapter 5.

11.4 Methods applied in stroke experiments

The methodology applied depends on the question we were addressing in each experiment. Here, we will describe what we did for each particular experiment.

11.4.1 Experiment 1

Comparison of κ in patients and controls

We studied the differences between controls and patients at different costs by computing the κ index for the five graph metrics introduced above.

We performed two types of analysis: in the first one, we pooled all the patients ($n = 20$), whatever the side of the lesion, and compared the κ of the contralesional hemisphere against the mean of left and right hemispheres in controls, without taking into account the inter-hemispheric connectivity. In the second analysis, we explored each sub-group of stroke patients according to the side of the lesion ($n = 9$ and $n = 11$ for right and left side lesions

respectively). Therefore, we compared 9 left contralesional hemispheres against 20 left hemispheres of controls and 11 right contralesional hemispheres against 20 right hemispheres of controls. In both analysis, to evaluate the significance of these differences, non-parametric tests were performed using Wilcoxon rank-sum test (p-value< 0.05).

Robustness of κ results in patients

For rigorous purpose, we replicated the experiment explained above on healthy subjects from the HCP database using bootstrap techniques. Due to the small number of patients and controls, 20 in each group, we wanted to check whether the statistically significant differences obtained when comparing both groups were reproducible in a group of healthy controls of the same size.

For each bootstrap iteration, we randomly selected 20 subjects which played the role of reference group and another 20 subjects that played the role of test group. As in the previous section, we performed two different analysis: in the first one, for the reference group, we computed the mean between left and right hemispheres (same way we did with the HERMES study); for the test group, we selected 9 left hemispheres and 11 right hemispheres and pooled them together in the same group. In the second analysis, we selected 11 right hemispheres (that played the role of the 11 right contralesional hemispheres of stroke patients) and compared them to 20 right hemispheres (corresponding to the 20 controls) and similarly, we selected 9 left hemispheres that were compared to 20 left hemispheres. For each of the 1000 bootstrap iterations corresponding to a selection of 2 groups, we computed the 5 mean graph metrics, the κ related to each metric and the z-value of the differences between groups.

11.4.2 Experiment 2

Prediction in multiple regression

When multiple regression is used for prediction, the sample is used to create a regression equation that would optimally predict a particular phenomenon within a particular population, in this case, the stroke patients. The final goal is to use the equation to predict outcomes for new individuals not included in the sample used in the analysis.

In this experiment, we want to design a model that predicts the outcome of stroke patients at 6 months (V6) using information at one month (V2). In particular, we would like to predict clinical outcome from variables from diverse sources; patients characteristics such as the age, sex, lesion side; patients clinical scores such as RBANs[3], MMSE[4], treatment; and also, measures obtained applying graph based analysis to the rs-fMRI acquisition: κ_{e_g}, κ_{e_l}, κ_d, κ_b and κ_c,

[3]RBANs: Repeatable Battery for the Assessment of Neuropsychological Status. It consists of ten subtests which give five scores, one for each of the five domains tested (immediate memory, visuospatial/constructional, language, attention, delayed memory).

[4]MMSE: Mini-Mental State Examination. It is a 30-point questionnaire extensively used in clinical and research settings to measure cognitive impairment.

in both the lesioned and the contralesional hemisphere. Among these variables, we want to select the ones that better predict the outcome.

In our predictive model we included the variables shown in Table 11.3.

Variables	**Mean**	**Std. deviation**	**N**
Treatment	-	-	-
Age	52.72	9.31	25
Sex	18M/7F	-	25
Years of education	11.28	3.42	25
Lesion vol. cm^3	97.08	63.98	25
Lesion side	10R/15L	-	25
Cognitive performance (V2)	55.2	29.98	25
Contral. κ_{e_g} V2	-0.15	0.43	25
Contral. κ_{e_l} V2	-0.27	0.51	25
Contral. κ_d V2	-0.12	0.42	25
Contral. κ_b V2	-0.15	0.55	25
Contral. κ_c V2	-0.16	0.51	25

Table 11.3: Mean and standard deviation values of the variables used in the predictive model. Values of treatment are not shown because they are still confidential. Contral.: contralesional; F: female; L: left; M: male; R: right.

Bootstrapping

Here, we propose the use of bootstrapping for ordering potential predictors according to their importance. We took a 5000 bootstrap samples from the original data.

11.5 Cortical surface rendering

Cortical surface representations of the distribution of the mean differences between healthy controls' and stroke patients' groups was done with Caret v5.64 software [Van Essen et al., 2001]. The significance of the group differences in the above mentioned graph metrics at each region were tested using Wilcoxon test with the following correction $p < (1/N) = 0.023$ (as in Lynall et al. [2010]), where N is the number of regions, in our case 44 in each hemisphere. This correction was done only with visualization purposes.

Chapter 12

Experiment 1: Brain networks reorganization in the contralesional hemisphere of stroke patients

The results shown in this chapter are part of our publication in Frontiers in Computational Neuroscience:

M. Termenon, S. Achard, A. Jaillard, C. Delon-Martin, **The "Hub Disruption Index", a Reliable Index Sensitive to the Brain Networks Reorganization. A Study of the Contralesional Hemisphere in Stroke**, Frontiers in Computational Neuroscience, 2016, 10:84, doi:10.3389/fncom.2016.00084.

12.1 Results

12.1.1 Hub disruption index κ in patients

We performed two different experiments. First, as we did not find any significant difference between left and right hemispheres in controls, we pooled the left and right contralesional hemispheres of stroke patients into a single group and compared them against the mean between left and right hemispheres of the controls.

The results for graph metrics and κ are shown in Fig. 12.1. Second, we analyzed each hemisphere independently in patients and controls. Results are shown in Fig. 12.2 for κ_D and in Figs. 12.3-12.6 for the other tested graph metrics.

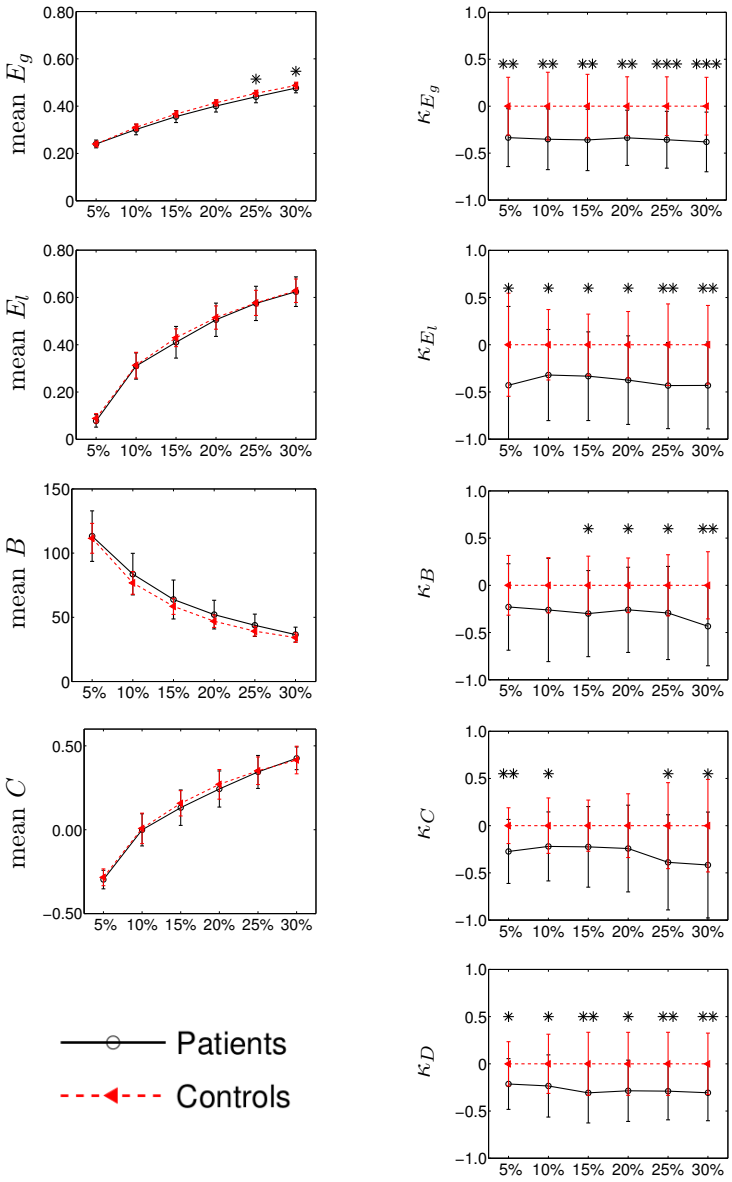

Figure 12.1: Group differences between mean intra-hemispheric connectivity in controls and contralesional hemispheric connectivity in stroke patients according to classical graph metrics (left column) and κ index (right column). Metrics (y-axis) correspond to global efficiency (mean E_g and κ_{E_g}, respectively), local efficiency (E_l and κ_{E_l}), betweenness centrality (B and κ_B), clustering coefficient (C, and κ_C) and node degree (κ_D). Cost (x-axis) ranges from 5% to 30%. Error bars indicate standard deviation and significant differences (Wilcoxon, $p < 0.05$) are indicated with asterisk (*) ($* < 0.05$; $** < 0.01$; $*** < 0.001$). Using κ, we found huge significant differences between the two groups while with classical graph metrics, differences were difficult to observe.

κ in patients versus controls

In the right column of Fig. 12.1, we show the comparison among the κ values of E_g, E_l, B, C and D between the mean controls' left and right intra-hemispheric connectivity and patients' contralesional hemispheric connectivity, for costs ranging between 5% and 30%.

We found that κ index was significantly reduced in patients as compared to controls for κ_{E_g}, κ_{E_l} and κ_D at all costs and for κ_B at costs above 10%. In the case of κ_C, we found a significant reduction in patients only with a graph density corresponding to costs above 20% or below 10%. Taken together, the results obtained with κ_{E_g}, κ_D and κ_B indicate that a global reorganization is occurring in the contralesional hemisphere of patients. The results related to κ_{E_l} and κ_C suggest also a reorganization using metrics at the neighborhood level.

The comparison of the intra-hemispheric connectivity between patients and controls using the classical graph metrics are shown in the left column of the Fig. 12.1. Global efficiency (E_g), local efficiency (E_l), betweenness centrality (B) and clustering (C) are displayed in the left column for cost values ranging between 5% and 30%. The only significant difference between both groups was found for E_g at 25% and 30% costs (Wilcoxon test, $p < 0.05$).

κ per hemispheric lesion side

In order to explore whether our results could differ between left-sided and right-sided lesions, we computed the differences of κ between controls and patients at 20% cost, comparing left control hemispheres against left contralesional patients hemispheres (9 subjects) and right controls hemispheres against right contralesional patients hemispheres (11 subjects). In Fig. 12.2A, we show the values of κ_D estimated for all the subjects, while in Fig. 12.2B we plot the mean D of each node in the control group against the difference between groups in mean D of each node. We found a $\kappa_D = -0.27$ for the right-sided lesioned patients and $\kappa_D = -0.36$ for the left-sided lesioned patients. The cortical surface representation of the mean D differences between stroke patients and controls is shown in Fig. 12.2C, where red denotes increased D, on average, in patients compared to controls while blue denotes abnormally decreased D in stroke patients. Finally, in Fig. 12.2D, we show the brain regions that demonstrated significant between group differences in D, corrected for multiple comparison applying Wilcoxon test ($p < 1/N$) as indicated in Section 11.5. In right-sided stroke lesion, we found that the occipital cortex, which was high-D region in the normal brain networks, became a low-D region in the stroke brain networks. When the lesion is on the left side, we found the same trend in the lingual gyrus.

Similar results were obtained in the case of κ_{E_g} (see Fig. 12.3), where $\kappa_{E_g} = -0.35$ for the right-sided lesioned patients and $\kappa_{E_g} = -0.37$ for the left-sided lesioned patients.

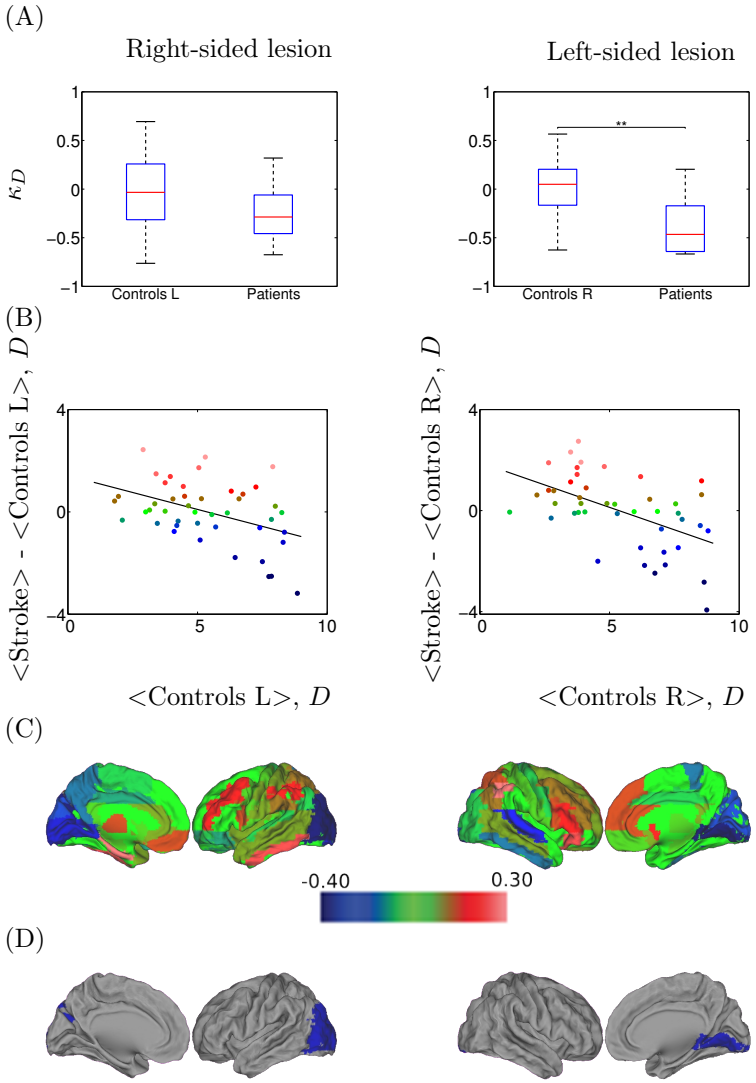

Figure 12.2: κ_D hub disruption of functional networks in stroke patients contralesional hemisphere, computed at a 20.0% cost, using node degree (D). A: Boxplots of the individually estimated hub disruption indices for the healthy volunteer group and the stroke patient group. On the left, healthy volunteer group left hemisphere and stroke contralesional left hemisphere; on the right, healthy volunteer group right hemisphere and stroke contralesional right hemisphere. B: On the left, results of the healthy volunteer group left hemisphere and the stroke group with left contralesional hemisphere, where $\kappa = -0.27$; on the right, results of the healthy volunteer group right hemisphere and the stroke group with right contralesional hemisphere, where $\kappa = -0.36$. C: Cortical surface representation of the difference in mean D between both groups; red denotes increased D, on average, in patients compared with healthy volunteers; blue denotes abnormally decreased D in stroke patients. D: nodes that demonstrated significant between-group difference in nodal D; Wilcoxon test, $p < 0.023$; red denotes significantly increased D and blue denotes significantly decreased D in the patients on average.

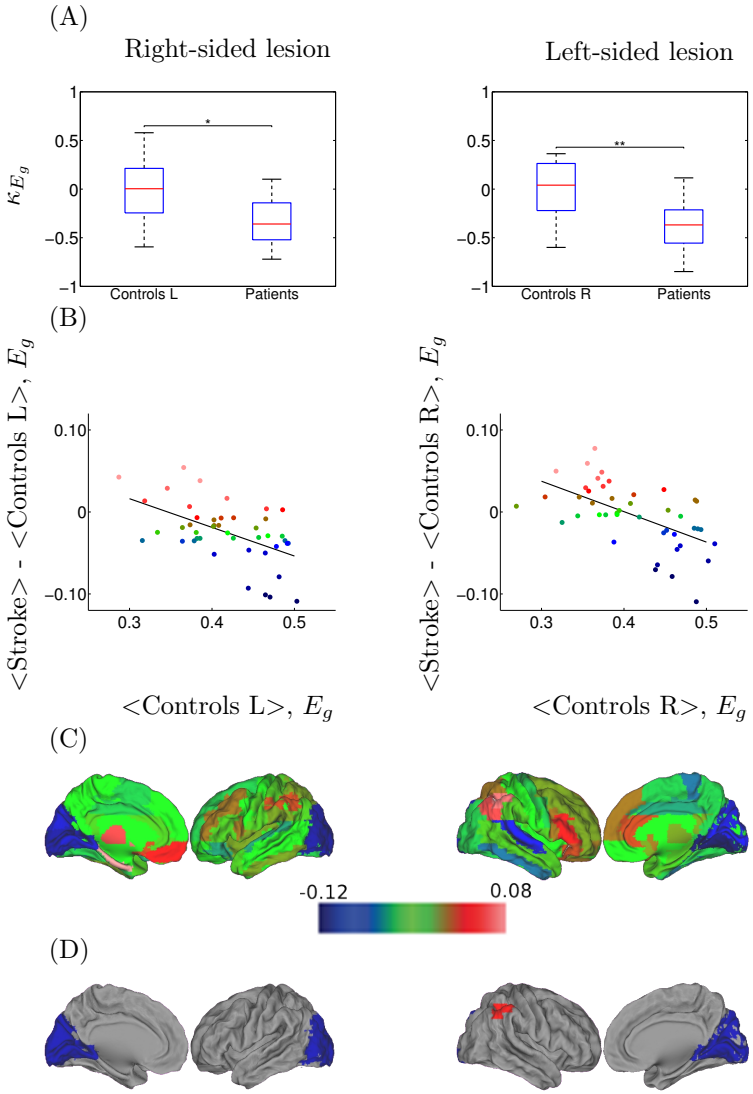

Figure 12.3: κ_{E_g} hub disruption of functional networks in stroke patients contralesional hemisphere, computed at a 20.0% cost, using global efficiency (E_g). A: Boxplots of the individually estimated hub disruption indices for the healthy volunteer group and the stroke patient group. On the left, healthy volunteer group left hemisphere and stroke contralesional left hemisphere; on the right, healthy volunteer group right hemisphere and stroke contralesional right hemisphere. B: On the left, results of the healthy volunteer group left hemisphere and the stroke group with left contralesional hemisphere, where $\kappa = -0.35$; on the right, results of the healthy volunteer group right hemisphere and the stroke group with right contralesional hemisphere, where $\kappa = -0.37$. C: Cortical surface representation of the difference in mean E_g between both groups; red denotes increased E_g, on average, in patients compared with healthy volunteers; blue denotes abnormally decreased E_g in stroke patients. D: nodes that demonstrated significant between-group difference in nodal E_g; Wilcoxon test, $p < 0.023$; red denotes significantly increased E_g and blue denotes significantly decreased E_g in the patients on average.

We observed that calcarine area, cuneus and lingual gyrus, which were high-E_g regions in the normal brain networks, became low-E_g regions in the stroke brain networks (in both, left and right hemispheres), and also occipital lobe in left hemisphere; whereas the parietal inferior gyrus, which was low-E_g region in the normal group became high-E_g region in the patient group.

Same analysis was performed on each subgroup of patients with κ_{E_l}, κ_B and κ_C. The corresponding results are displayed in Figs. 12.4, 12.5 and 12.6, respectively.

12.1.2 Robustness of the patients' results

We are concerned that the sample of patients is small, even smaller if we separate the patients into two subgroups, left and right sided lesions. In order to test if the significant differences found between patients and controls are robust, we performed a repeated bootstrap sampling from the HCP data.

We randomly selected 20 subjects that simulated the healthy controls, 11 subjects that played the role of left-sided lesion patients and 9 more subjects as right-sided lesion patients. For each random selection, we computed the κ of each subject and the z-values (Wilcoxon test) of the comparison of κ values between the control and patient groups for each graph metric. We repeated the same procedure 1000 times. The p-value was computed counting how many times the z-values were lower than the one we obtained with our true control and patient groups.

Two different experiments were performed: first, pooling left and right contralesional hemispheres (to test the results obtained in Fig. 12.1 but only at 20% cost) and second, comparing left contralesional hemisphere in patients to left hemisphere in controls and right contralesional hemisphere in patients to right hemisphere in controls (to test the results obtained in Figs. 12.2-12.6). Results are shown in Fig. 12.7. With the limitation that our on-site data are not acquired in the same conditions than the HCP data, the bootstrap sampling tend to show that the results obtained on κ_{E_g} (left, p-value= 0.019; right, p-value= 0.005; pooling left and right, p-value= 0.003), κ_{E_l} (left, p-value= 0.016; right, p-value= 0.013; pooling left and right, p-value= 0.012) in the three cases and κ_D (left, p-value= 0.111; right, p-value= 0.011; pooling left and right, p-value= 0.006) in the left-sided lesion subgroup and pulling both sides lesions are significant. With κ_B, there is only a trend of significance (left, p-value= 0.072; right, p-value= 0.075; pooling left and right, p-value= 0.096), while with κ_C (left, p-value= 0.073; right, p-value= 0.236; pooling left and right, p-value= 0.041), results are significant when pooling both sides lesions in the same group, and not significant dividing the patients into subgroups.

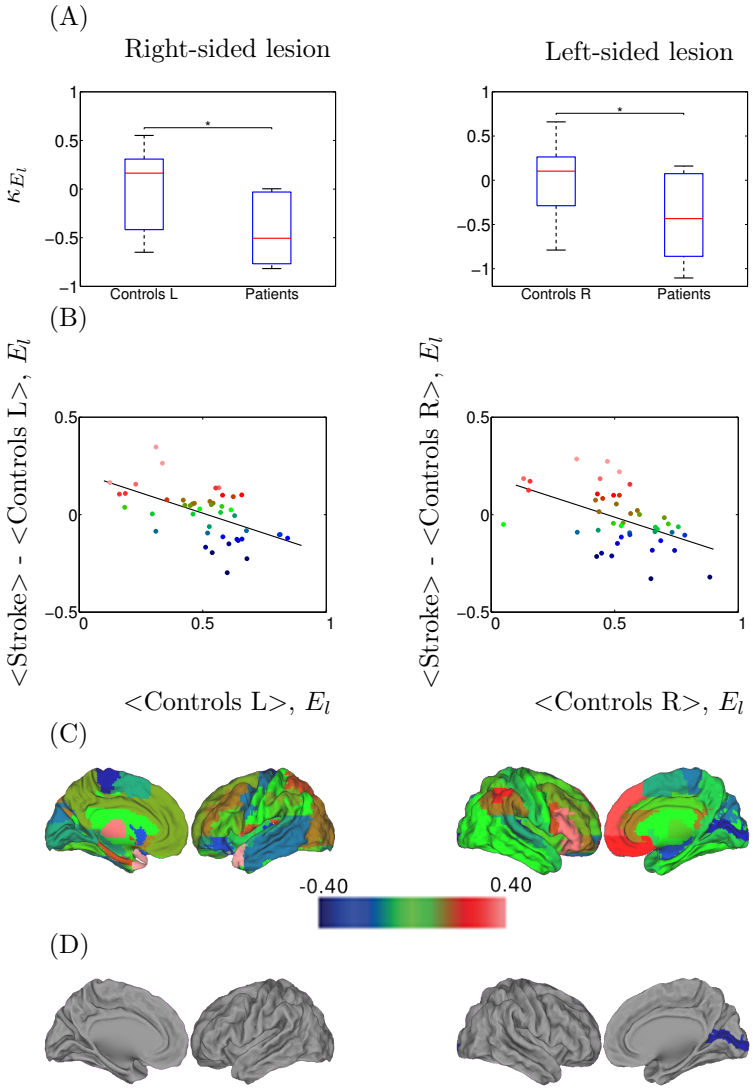

Figure 12.4: κ_{E_l} hub disruption of functional networks in stroke patients contralesional hemisphere, computed at a 20.0% cost, using local efficiency (E_l). A: Boxplots of the individually estimated hub disruption indices for the healthy volunteer group and the stroke patient group. On the left, healthy volunteer group left hemisphere and stroke contralesional left hemisphere; on the right, healthy volunteer group right hemisphere and stroke contralesional right hemisphere. B: On the left, results of the healthy volunteer group left hemisphere and the stroke group with left contralesional hemisphere, where $\kappa = -0.41$; on the right, results of the healthy volunteer group right hemisphere and the stroke group with right contralesional hemisphere, where $\kappa = -0.41$. C: Cortical surface representation of the difference in mean E_l between both groups; red denotes increased E_l, on average, in patients compared with healthy volunteers; blue denotes abnormally decreased E_l in stroke patients. D: nodes that demonstrated significant between-group difference in nodal E_l; Wilcoxon test, $p < 0.023$; red denotes significantly increased E_l and blue denotes significantly decreased E_l in the patients on average.

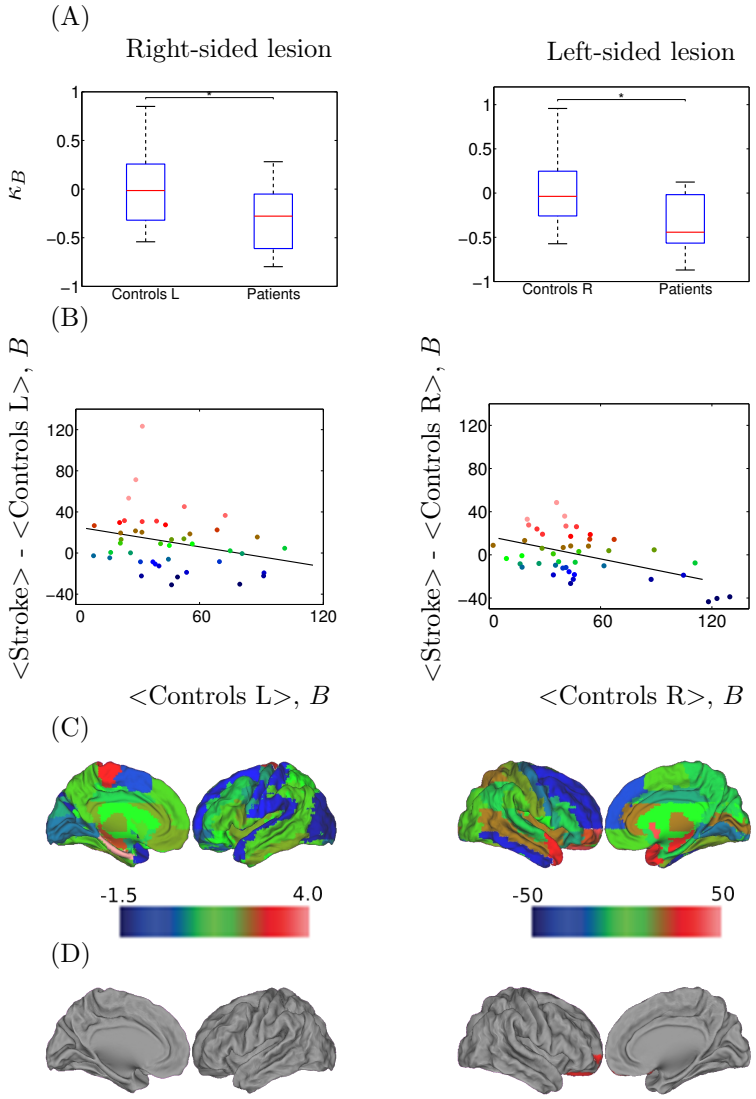

Figure 12.5: κ_B Hub disruption of functional networks in stroke patients contralesional hemisphere, computed at a 20.0% cost, using betweenness centrality (B). A: On the left, results of the healthy volunteer group left hemisphere and the stroke group with left contralesional hemisphere, where $\kappa = -0.32$; on the right, results of the healthy volunteer group right hemisphere and the stroke group with right contralesional hemisphere, where $\kappa = -0.35$. B: Boxplots of the individually estimated hub disruption indices for the healthy volunteer group and the stroke patient group. On the left, healthy volunteer group left hemisphere and stroke contralesional left hemisphere; on the right, healthy volunteer group right hemisphere and stroke contralesional right hemisphere. C: Cortical surface representation of the difference in mean B between both groups; red denotes increased B, on average, in patients compared with healthy volunteers; blue denotes abnormally decreased B in stroke patients. D: nodes that demonstrated significant between-group difference in nodal B; Wilcoxon test, $p < 0.023$; red denotes significantly increased B and blue denotes significantly decreased B in the patients on average.

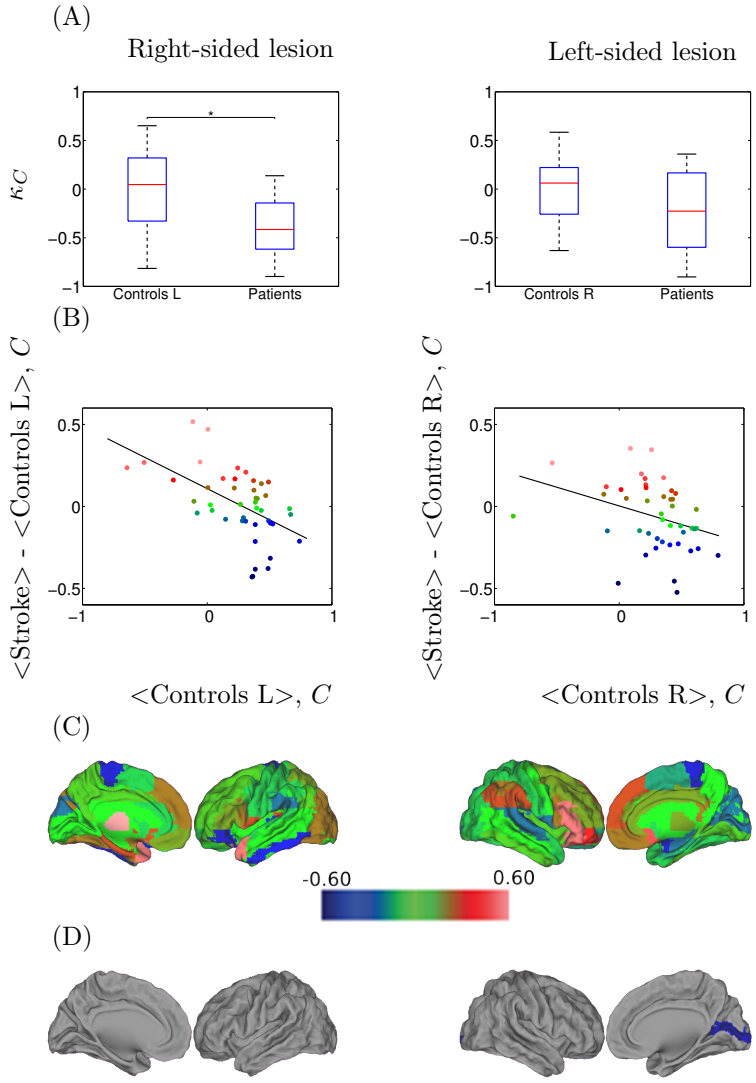

Figure 12.6: κ_C hub disruption of functional networks in stroke patients contralesional hemisphere, computed at a 20.0% cost, using clustering coefficient (C). A: Boxplots of the individually estimated hub disruption indices for the healthy volunteer group and the stroke patient group. On the left, healthy volunteer group left hemisphere and stroke contralesional left hemisphere; on the right, healthy volunteer group right hemisphere and stroke contralesional right hemisphere. B: On the left, results of the healthy volunteer group left hemisphere and the stroke group with left contralesional hemisphere, where $\kappa = -0.38$; on the right, results of the healthy volunteer group right hemisphere and the stroke group with right contralesional hemisphere, where $\kappa = -0.23$. C: Cortical surface representation of the difference in mean C between both groups; red denotes increased C, on average, in patients compared with healthy volunteers; blue denotes abnormally decreased C in stroke patients. D: nodes that demonstrated significant between-group difference in nodal C; Wilcoxon test, $p < 0.023$; red denotes significantly increased C and blue denotes significantly decreased C in the patients on average.

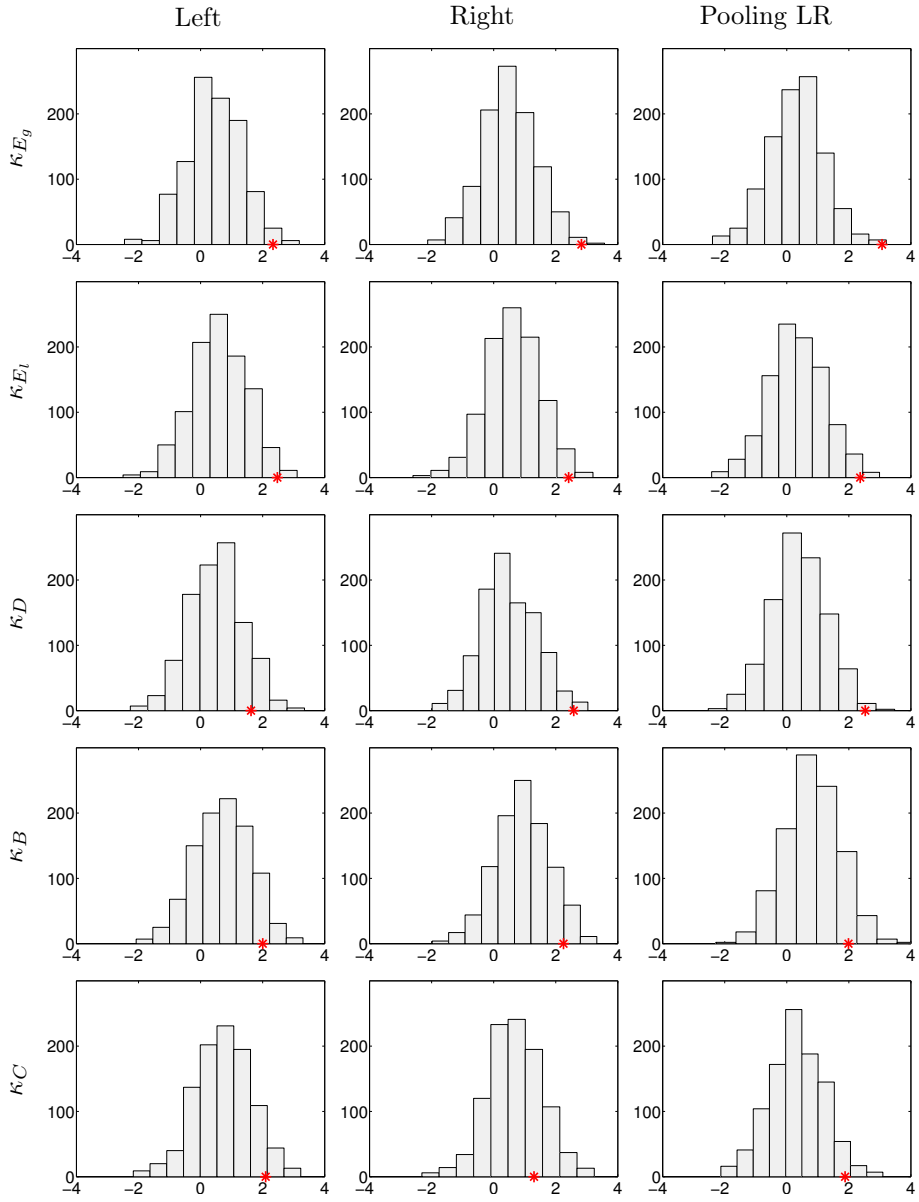

Figure 12.7: Analysis of the robustness of the significant differences between controls and stroke patients using the HCP database. 1000 bootstrap sampling iterations were performed. In each iteration, 40 subjects were randomly selected (20 subjects as healthy controls, 11 subjects as left-sided lesion patients and 9 subjects as right-sided lesion patients), their respective κ index and the z-values (Wilcoxon test) of the comparison of κ between the control and patient groups for each graph metric were computed. Histograms with the bootstrap sampling of κ_{E_g}, κ_{E_l}, κ_D, κ_B and κ_C at 20% cost are shown. First column, replication of left lesioned stroke; middle column, of right-sided lesion stroke; last column, pooling left and right-sided lesion groups and compared against the mean between left and right hemispheres in controls. The red star corresponds to the true z-value obtained from the comparison of κ between patients and controls.

12.2 Discussion

In this study, we explored the 'hub disruption index' (κ) that aims at capturing brains' networks reorganization in order to propose it as a new tool for clinical investigation of brain lesions.

κ as a measure of brain network reorganization Since κ, for a given individual, is computed by linear regression of all nodal metric differences between this individual and the mean nodal metric computed on a group of controls (see Fig. 5.11), the larger the differences between nodal metrics, the larger the κ. This index is thus specially sensitive to the combination of underconnected and overconnected brain regions, a situation that occurs in different neurological and psychiatric brain disorders in comparison to a control group. The significantly disconnected regions were found mainly in the occipital lobes and overconnected regions were in the superior parietal cortex. This pattern presents some similarities with the one found in the post-anoxic comatose patients [Achard et al., 2012]. However, it should be noticed that resting state data were acquired with eyes open in controls, and that patients with severe subacute stroke were not all capable to keep their eyes opened during the whole session. Reorganization of the functional network in the eye-opened state compared to the eye-closed state has been reported in previous works, with decreased or increased efficiency at the nodes related to the default mode network and the visual network [Xu et al., 2014b]. Therefore, a question that remains to be addressed is how eye closure may have influenced the changes observed in the brain network.

Potential clinical interest of κ The clinical interest of κ has been shown in different pathological conditions such as in disorders of consciousness [Achard et al., 2012], in epilepsy [Ridley et al., 2015], or in neuromyelytis optica [Hemmert et al., 2013]. In comatose patients, we found that the brain connectivity was profoundly modified with both disconnected and overconnected nodes. κ was indeed deeply reduced in these patients as compared to healthy subjects [Achard et al., 2012].

To the best of our knowledge, this is the first time that a global change of connectivity is observed within the contralesional hemisphere in stroke. In a computational model of focal brain lesions, Alstott et al. [2009] found that lesions produced specific patterns of altered functional connectivity among distant regions of cortex, often affecting both cortical hemispheres. In the clinical situation of reversible single hemisphere sedation, currently known as 'Wada test', that mimics single hemispheric lesions, large topological modifications affecting in particular the hubs of the networks were found with EEG investigation [Douw et al., 2009].

In many other brain disorders thought to be subtended by hubs lesions [Crossley et al., 2014], such as Alzheimer disease [Buckner et al., 2009], we argue here that this κ metric deserves to be used. However the relationship between κ and behavioral clinical scores remains to be explored to assess whether κ could be

used as a surrogate biomarker.

Remaining issues about κ Few methodological issues remain in the exploration of networks reorganization with κ. First, the variance within the reference group is not taken into account in the computation of κ. Second, the work done here was performed using the template AAL [Tzourio-Mazoyer et al., 2002] but few studies are using finer parcellation schemes with more reliable results [Termenon et al., 2016]. Thus, the influence of the parcellation template needs to be explored in order to be able to choose the template providing the highest reliability together with a high group discriminability.

Chapter 13

Experiment 2: Prediciting clinical outcome in stroke using graphs

13.1 Results

In this experiment, we tested two different models. In the first model, we tested if κ_b could improve the prediction of cognitive outcome using the baseline cognitive score (at V2). In the second experiment, we tested if the cognitive outcome could be predicted using clinical features and κ measures without the baseline. As the sample is relatively small, we use bootstrap to test the confidence intervals of the selected variables, repeating the same experiment 5000 times.

For the model, we adjust for the treatment as the treatment could affect the outcome. We introduced as potential predictors κ_b and stroke characteristics as the lesion volume, lesion side, demographic variables (age, years of education, sex) and finally, the delay of the stroke onset (the values of this characteristics are shown in Table 11.1). Those characteristics have been reported to potentially interfere with cognition [Saver et al., 1999, Jaillard et al., 2009, 2010, Hommel et al., 2009] .

13.1.1 Correlation

		κ_{e_g} V2	κ_{e_l} V2	κ_b V2	κ_d V2	κ_c V2
RBANs V6	**Corr**	-0.36	-0.28	**-0.60****	-0.32	-0.29
	Sig. (2 tailed)	0.08	0.17	0.001	0.12	0.16
	N	25	25	25	25	25
RBANs V2	**Corr**	-0.34	-0.25	**-0.48***	-0.33	-0.23
	Sig. (2 tailed)	0.10	0.23	0.014	0.13	0.28
	N	25	25	25	25	25
MMSE V6	**Corr**	0.11	0.12	-0.45	0.08	0.02
	Sig. (2 tailed)	0.66	0.64	0.06	0.76	0.95
	N	18	18	18	18	18
TR V6	**Corr**	0.30	0.21	0.37	0.35	0.24
	Sig. (2 tailed)	0.15	0.32	0.07	0.09	0.24
	N	25	25	25	25	25
κ_{e_g} **V2**	**Corr**	1	0.62**	0.42*	0.96**	0.56**
	Sig. (2 tailed)		0.001	0.035	<0.001	0.003
	N	25	25	25	25	25
κ_{e_l} **V2**	**Corr**	0.62**	1	0.33	0.63**	0.92**
	Sig. (2 tailed)	0.001		0.11	0.001	<0.001
	N	25	25	25	25	25
κ_b **V2**	**Corr**	0.42*	0.33	1	0.46*	0.38
	Sig. (2 tailed)	0.04	0.11		0.02	0.06
	N	25	25	25	25	25
κ_d **V2**	**Corr**	0.93**	0.63**	0.46*	1	0.61**
	Sig. (2 tailed)	<0.001	0.001	0.02		0.001
	N	25	25	25	25	25
κ_c **V2**	**Corr**	0.56**	0.92**	0.38	0.61**	1
	Sig. (2 tailed)	0.003	<0.001	0.06	0.001	
	N	25	25	25	25	25

Table 13.1: Pearson correlation between κ values and clinical scores. * Correlation is significant at the 0.05 level (2-tailed). ** Correlation is significant at the 0.01 level (2-tailed).

13.1.2 Model 1: Regression of RBANs 6 months using all covariates including RBANS at 1 month

The model selected 4 variables among the set of variables that explain the prediction of the cognitive outcome at V6 in a 87.3%. Those variables are: age, treatment, cognitive performance at V2 and contralesional κ_b at V2. The results of this model are shown in Table 13.2 and Fig. 13.1.

Variables	Steps	R	R^2	Adjusted R^2	F change	Sig F change
Treatment adjustment	1					
RBANS V2	2	0.93	0.86	0.84	98.06	<0.001
κ_b V2	3	0.95	0.89	0.87	6.48	0.019

Table 13.2: Predictors of model 1. Results for treatment are not shown because they are confidential.

The statistical test shows that both, cognitive performance at V2 and contralesional κ_b are significant.

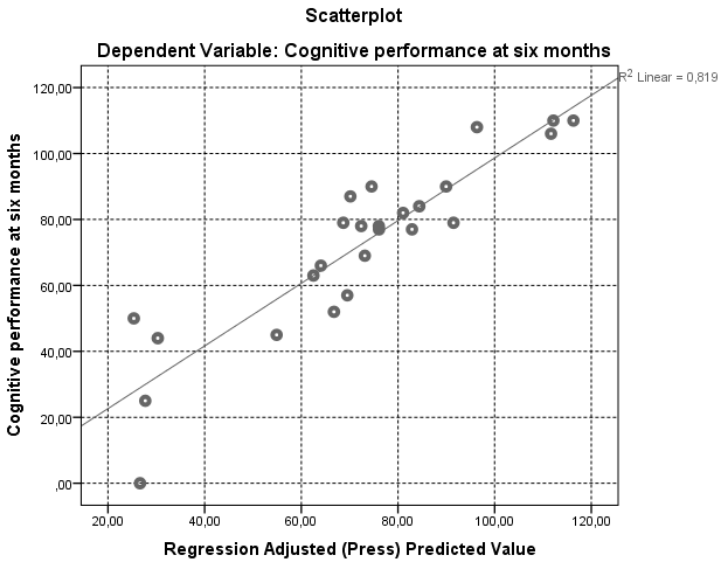

Figure 13.1: Predicted cognitive performance at 6 months using all covariates including RBANS at 1 month (V2).

The bootstrap results for model 1 are shown in Table 13.3 .

	Weights	**Bootstrap**		
		Sig. bilateral	**CI 95%**	
			Inf	**Sup**
Constant	33.72	<0.001	15.94	42.99
Treatment	-	-	-	-
RBANS V2	0.71	<0.001	0.55	0.97
κ_b **V2**	-10.07	0.035	-19.86	0.18

Table 13.3: Bootstrap results for model 1. CI: confidence interval

13.1.3 Model 2: Regression of RBANs 6 months using all covariates but RBANS at 1 month

We repeated the same experiment but removing the cognitive performance at V2. In the previous model, this variable was the one that had more influence in the prediction of the cognitive performance at V6.

This time, the model needed to add 3 more variables appart from contralesional κ_b to explain the 81.4% of the variance. Those variables are: lesion side, total volume and contralesional κ_c at V2. The results of this model are shown in Table 13.4 and Fig. 13.2.

Variables	**Steps**	**R**	R^2	**Adjusted** R^2	**F change**	**Sig. F change**
Age and treatment adjustment	1	0.45	0.20	0.13	2.83	0.08
κ_b V2 contralesional	2	0.72	0.52	0.45	13.95	0.001
Lesion side	3	0.87	0.75	0.70	18.30	0
Total vol. cm^3	4	0.91	0.82	0.78	7.95	0.011
κ_c V2 contralesional	5	0.93	0.86	0.81	4.69	0.044

Table 13.4: Predictors of model 2.

The statistical test shows that those four variables are significant.

The bootstrap results for model 2 are shown in Table 13.5 .

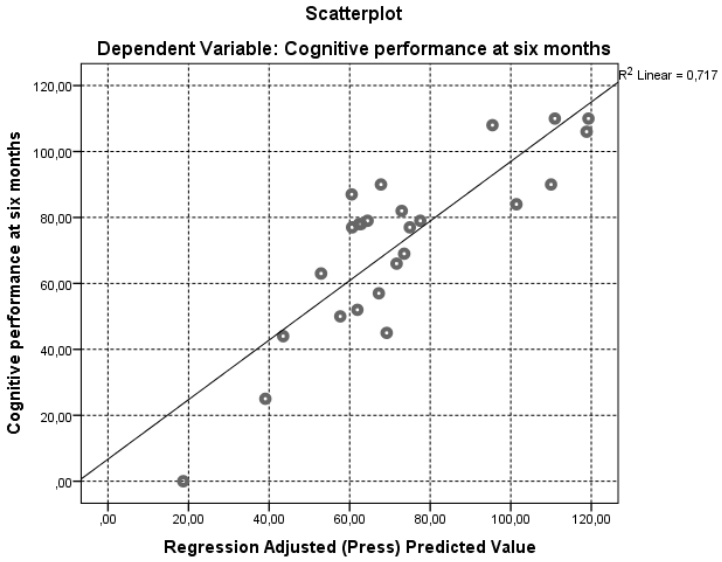

Figure 13.2: Predicted cognitive performance at 6 months using all covariates with the exception of RBANS at 1 month.

	Weights	**Bootstrap**		
		Sig. bilateral	**CI 95%**	
			Inf	**Sup**
Constant	136.92	<0.001	112.60	162.22
Treatment	-	-	-	-
Lesion vol.	-0.16	0.022	-0.30	-0.06
Lesion side	-29.70	0.001	-39.53	-16.85
κ_b **V2**	-13.96	0.023	-25.14	-0.71

Table 13.5: Bootstrap results for model 2. CI: confidence interval

13.2 Discussion

As explained in the Chapter 12 of this thesis, there are several clinical scores that measures the cognitive impairment of the stroke patients. We selected RBANS because it is a global measure that can reflect more the global functioning (disruption) of the brain, second it is correlated with κ_b (even after correcting for multiple comparison) and third, the RBANs values where available for the 25 patients, while with the other clinical scores there where missing data for 7 patients. This is why we choose to predict the cognitive outcome at 6 months using RBANS and κ_b.

According to the results, κ_b is a predictor of cognitive outcome at V6 using both, with and without including RBANs at V2. We tested the method with 5000 bootstrap repetition, and the predictors were still significant.

We can extract three main conclusions from this experiment:

- Betweenness centrality, which is a measure related to the brain hubs, reflects cognition in stroke.
- Disruption index is related to the cognitive impairment in stroke,
- Contralesional hemisphere is engaged in the recovery of cognitive function.

The better the recovery, the less disrupted are the measures as it was previously reported in Dacosta-Aguayo et al. [2015].

The clinical utility is that graph metrics can help to predict clinical outcome at the subacute phase.

Limitations

The sample is small and there is no external validation yet, they will be validated within the European project RESSTOR (ERC RESSTOR, PR O. Detante, CHU Grenoble). Thus we consider these results as exploratory results.

The criteria used to model the data need to be validated using model selection methods such as the Akaike information criterion (AIC) or Bayesian information criterion (BIC) [Vrieze, 2012].

These results need to be confirmed using data mining techniques, such as variable selection with random forest or sparse regression.

Chapter 14

Conclusions and perspectives

This thesis has been developed along two main lines of work. First, the study of the reliability of graph based brain functional connectivity. Second, the application of the graph theoretical approach to the clinical case of stroke patients.

As we have shown in the second part of this thesis, to assess the reliability of new measures is of paramount importance to be sure that the results obtained in the sample group will be representative of the population in study (stroke patients in the case of this thesis). It is important to know under which circumstances we can trust the measure we are applying. One of the main findings of this thesis is the fact that reliability of the graph metrics computed at both global and regional level depends on two main factors, the sample size and the number of time points (scan duration), as seen in Figs. 8.3 and 8.6, aiming at highlighting **good practices** in brain connectivity in rs-fMRI. This suggests that good reliability of graph metrics cannot be easily achieved with a sample size of 10 to 30 subjects and relative short scan duration (5 to 10 min.), values that are commonly used in studies of human cognition and clinical research. But, we have to take into account that our findings are obtained using a population of healthy volunteers. The goal of identifying differences between groups of subjects (i.e. diseased patients and healthy controls) is different and our recommendations may be over evaluated. Indeed, the potentiality to find differences depends on the amplitude of the unknown differences between the two groups. However, if very few assumptions are known when comparing two groups of subjects, using our recommendations would minimize the risk of not being able to identify differences between groups.

These results, however, were obtained on data from healthy subjects for a given cost in the graph, a given parcellation scheme, with time series computed using wavelets and with cross correlation as a measure of connectivity. In an attempt to evaluate the influence of these different factors, we varied each of them. We found that he influence of cost in the reliability of graph metrics depends on each particular graph metric. At low cost (typically 10% or below), when the graph is very sparse, metrics associated with centrality (such as global efficiency E_g or betweenness B) are less reliable than metrics related to local

features in the graph such as clustering coefficient C, modularity Q or local efficiency E_l. On the contrary, at higher costs (above 30%), metrics related to local features appear as less reliable. This might be related to an insufficient sparsity in the graph. According to the obtained results, we considered a cost around 20.0% or 25.0% to be a good trade off.

The influence of the parcellation scheme in the reliability of brain graphs, is still under active debate. According to our results, the influence of the parcellation in the reliability depends on the metric used. For example, E_l or C are more reliable when using a finer parcellations (more than 400 regions). While, when computing E_g, parcellations with lower number of regions (around 100 regions) are still providing reliable results. These conclusions are found using global graph metrics. At the regional level, for parcellation schemes of similar number of regions, even if the number of reliable regions are the same, the location of those regions does not belong to the same areas, as shown in Figs. 10.6 and 10.7. This make difficult to extract any conclusion. Again, the finer parcellation seems to obtain better reliability than parcellation with lower number of regions.

From the comparison between Fourier transformation and discrete wavelet decomposition, we could not observe significant differences in the reliability of both methods using the same frequency range. We prefer to keep on working with wavelets because we consider them more suitable for several reasons. One of the main reasons is that if there are not enough points in time, the wavelets approach would not be able to be computed while Fourier transformation would always give a result, even if it is only noise. Other reason is that wavelets are suitable for stationary and non stationary signals, while Fourier transformation for stationary signals only. Functional magnetic resonance images of the human brain often demonstrate scale invariant or fractal properties [Bullmore et al., 2004], making the use of wavelets more adequate in these cases.

A last issue related to reliability of brain graphs is the computation of the connectivity measure. In Chapter 10, we show the comparison between the reliability of full and partial correlation. Partial correlation needs a very big sample size, or a very long scan duration (much more than 1200 time points), or a very small number of regions to be a reliable measure. In the context we performed the experiments of this thesis (no more than 100 subjects, scan duration of around 14 minutes and parcellation schemes of at least 89 regions), we do not recommend the use of partial correlations. There are other ways to compute the connectivity matrices, but they were not explored in this thesis.

In the second part of the thesis, we translated all this knowledge to study the brain graphs of stroke patients. We mainly focus in the contralesional hemisphere because the effect of the lesion in the computation of the graph may introduce connections between brain regions that are non-existent.

Is there a global brain reorganization after stroke even in the contralesional hemisphere? To address this question, we performed a first experiment focused on the 'hub disruption index' (κ) of the contralesional hemisphere of stroke patients in comparison to healthy controls. To our knowledge, this was the first time that a global change of connectivity was observed within the contralesional

hemisphere in stroke.

The exploration of κ aimed at capturing brains' networks reorganization in order to propose it as a new tool for clinical investigation of brain lesions. We assess the reliability of κ, finding κ **more reliable than classical graph metrics**. The potential clinical interest of κ was already shown in different pathological conditions such as in disorders of consciousness [Achard et al., 2012], in epilepsy [Ridley et al., 2015], or in neuromyelytis optica [Hemmert et al., 2013].

Does clinical outcome depend on brain reorganization after stroke? This was studied by searching a relationship between κ and behavioral clinical scores to assess whether κ could be used as a surrogate biomarker, was explored in the second experiment performed with stroke patients. We observed that one of the variables that contribute to predict the several cognitive scores at 6 months after stroke was the κ betweenness centrality (κ_B). Even if we consider that more exploration is needed with other clinical scores, these results strengthen the choice of graph analysis and κ as suitable tools to analyze brain functional connectivity.

Perspectives

Other clinical questions can be addressed based on the stroke dataset. Some are on going work. We plan to explore also the whole brain, taking into account intra- and inter-hemispheric connections. We are evaluating two possible options to proceed. The first one consists in assuming that some of the connections included in the graph would be random due to the lesion and the restriction of the minimum spanning tree. We expect a small number of those random connections and thus, not cause a big influence in the results. The second option is to compare each stroke patient individually to the controls group. The lesion mask would be applied also to the controls and thus the empty regions removed from the graph. The concern with this approach is that in some cases remove the part of deleted brain would be so large that it could result in inaccurate measures.

The longitudinal study of the evolution of stroke patients is still on preliminary stage. We have explored the evolution of κ along time (at V3, V4, V6 and V8) using the values at V2 as the reference. Due to the missing values, only few patients completed all the phases and conclusions are difficult to extract. One possibility is to use Markov Chain Monte Carlo (MCMC) method to deal with the missing data, not only the missing κ but also the missing clinical scores. It is a classical approach that can be more easily accepted in the clinical context, known as imputation [Wood et al., 2008].

As mentioned above, we consider that more exploration between κ and behavioral clinical scores is needed. Scores such as reaction time, depression or NIHSS deserve to be explored at other time points.

The exploration of the effect of the treatment could not be included in the content of this thesis due to the confidentiality policy of the project. We studied the effect of the treatment in the homotopic connectivity (interhemispheric

connections that link mirror regions in the two hemispheres) of stroke patients along time (from V2 to V8). We plan to investigate the effect of treatment with other graph metrics, both in the contralesional and the whole brain. In any case, the sample size of this project is small, and the experimental results obtained should be confirmed in a larger sample. This will be done thanks to RESSTORE, a new european project to investigate the effect of stem cells treatment in a large population of stroke patients (ERC RESSTOR, PR O. Detante, CHU Grenoble).

Two important collaborations were started along this thesis. The first collaboration, with a medical doctor of the Grenoble University Hospital (CHU Grenoble) to apply the graph methodology to patients with disorders of consciousness after traumatic brain injury. The second collaboration, with Ed Bullmore group in Cambridge University, studying the repeatability of graph properties using different databases. Both, are still on-going works.

Appendix A

Aditional explanations on TRT reliability of graph based brain functional connectivity

A.1 Modified version of classical AAL parcellation scheme

The classical AAL parcellation scheme is composed by 116 regions including the cerebellum. We have merged some of the regions, reducing the parcellation to 89 regions. Merged regions are: frontal medial orbital and rectus (one region for left and one for right hemisphere); occipital superior, middle and inferior (one region for left and one for right hemisphere); temporal pole superior and medial (one region for left and one for right hemisphere); the cerebral crus (one region for left and one for right hemisphere); areas III, IV, V and VI of cerebellum (one region for left and one for right hemisphere); areas VII, VIII, IX, X of cerebellum (one region for left and one for right hemisphere) and finally, the vermis (one single region for both hemispheres).

A.2 TR, scan duration and frequency band

The problem of choosing the scan duration is linked to the sampling rate of the acquisition and the interested frequency bands. The following tables present two examples, one with a TR equal to 720 ms (the one used in this study), and a TR equal to 2 s used classically with non multiband acquisitions.

A.3 ICC computation

Considering a graph metric (e_j^i) per subject ($i \in [1, n]$) per session ($j \in [1, k]$):

	TR=2s; Fmax=0.25Hz				TR=720ms; Fmax= 0.695Hz			
	Scan duration Initial Nb Time points	$13min20s$ 400 tp	$6min30s$ 200 tp			$14min24s$ 1200 tp	$9min36s$ 800 tp	$4min45s$ 400 tp
				1	0.35-0.69 Hz	600 tp	400 tp	200 tp
1	0.12-0.25 Hz	200 tp	100 tp	2	0.17-0.35 Hz	300 tp	200 tp	100 tp
2	0.06-0.12 Hz	100 tp	50 tp	3	0.085-0.17 Hz	150 tp	100 tp	50 tp
3	0.03-0.06 Hz	50 tp	**25 tp**	4	0.042-0.085 Hz	75 tp	50 tp	**25 tp**
4	0.015-0.03 Hz	**25 tp**	**12 tp**	5	0.024-0.042 Hz	37 tp	**25 tp**	**12 tp**

Table A.1: Illustration of reliability for two different datasets using two different TR; numbers in bold indicate insufficient number of points in time to get reliability using graph analysis according to p-values obtained on ICC.

$$\mathbf{X} = [\mathbf{x_0}\, \mathbf{x_1} \ldots \mathbf{x_k}] = \begin{bmatrix} e_1^1 & e_2^1 & \ldots & e_k^1 \\ e_1^2 & e_2^2 & \ldots & e_k^2 \\ \ldots & \ldots & \ldots & \ldots \\ e_1^n & e_2^n & \ldots & e_k^n \end{bmatrix},$$

where the mean graph metric value per subject across sessions is:

$$\mathbf{t}(\mathbf{X}) = \begin{bmatrix} t^1 \\ t^2 \\ \ldots \\ t^n \end{bmatrix};$$

where $t^i = \frac{1}{k}\sum_{j=1}^{k} e_j^i$ and the total mean $\bar{x} = \frac{1}{nk}\sum_{i=1}^{n}\sum_{j=1}^{k} e_j^i$.

The within subjects mean squares (s_w) difference is then obtained by computing the mean of the square difference between each session value and the mean value among sessions:

$$s_w = \frac{1}{n(k-1)}\sum_{i=1}^{n}\sum_{j=1}^{k} p_j^i, \tag{A.1}$$

where $p_j^i = (e_j^i - t^i)^2$.

and the between subjects mean square (s_b) difference:

$$s_b = \frac{k}{n-1}\sum_{i=1}^{n} b^i, \tag{A.2}$$

where $b^i = (t^i - \bar{x})^2$.

Finally, the ICC value is computed as follows:

$$ICC = \frac{s_b - s_w}{s_b + (k-1)s_w} \tag{A.3}$$

Appendix B

Posters

In this appendix, I include the posters presented in multiple international conferences along this thesis.

2016:

M. Termenon, A. Jaillard, C. Delon-Martin, S. Achard, **Reliability of graph analysis of rs-fMRI using test-retest dataset from the Human Connectome Project**, Fifth Biennial Conference on Resting State / Brain Connectivity.

M. Termenon, S. Achard, A. Jaillard, C. Delon-Martin, **Hub disruption index (kappa), an index that measures alterations of node connectivity and captures brain networks reorganization**, Fifth Biennial Conference on Resting State / Brain Connectivity.

2014:

M. Termenon, A. Jaillard, S. Achard, C. Delon-Martin, **Hemispheric specialization in men and women using graph theory: a resting-state functional connectivity MRI study in highly educated healthy adults**, Fourth Biennial Conference on Resting State / Brain Connectivity.

M. Termenon, A. Jaillard, S. Achard, F. Renard, C. Delon-Martin **Is homotopic intramural connectivity related to cytoarchitectonic cortical classification?**, 20th Annual Meeting of the Organization for Human Brain Mapping.

185

Reliability of graph analysis of rs-fMRI using test-retest dataset from the Human Connectome Project

M. Termenon[1,2,*], A. Jaillard[3,4,5], C. Delon-Martin[1-2], S. Achard[6,7]

[1]Univ. Grenoble Alpes, Grenoble Institute des Neurosciences, Grenoble, France, [2]INSERM, U1216, Grenoble, France, [3]Pole Recherche, CHU Grenoble, France, [4]IRMaGe, Inserm US17 CNRS UMS 3552, Grenoble, France, [5]AGEIS EA7407, Univ. Grenoble Alpes, France, [6]Univ. Grenoble Alpes, GIPSA-lab, Grenoble, France, [7]CNRS, GIPSA-lab, Grenoble, France
*maite.termenon@ujf-grenoble.fr

Aim of the study

Reliability of graph metrics using:
- Human connectome project data (HCP)
- Intraclass correlation (ICC) analysis
- Permutation and bootstrap

Here, we report the influence of **sample size**, **scan duration**, graph density (**cost**) and **brain parcellation** scheme on the reliability of the graph based connectivity metrics.

Materials & Methods

Test-retest (TRT) rs-fMRI dataset from the **Human Connectome Project (HCP)**:
- **100** young healthy participants.
- 2 acquisitions (TR=0.72s)
- **Long scan duration** (14min 24s; 1200 time points).

Preprocessing:

Data were downloaded already preprocessed, (**Glasser et al (2013)**)

T1w segmentation → grey matter (GM) probability map.

Regional time series (rTS) extraction:
- Several parcellation schemes.
  - Structural:
    - **AAL89**
    - AAL459
    - Harvard-Oxford(HO117)
  - Functional:
    - Craddock (Crad100)
    - ICA based (ICA50, ICA100, ICA200)
- Voxel wise weighting by GM proportion.
- Averaging of voxels time series in each parcel → rTS.
- Regressor: head movements.
- **Discrete wavelet transform** applied to each rTS.
- Pairwise inter-regional Pearson's correlations at wavelet scale 4: **0.04-0.08 Hz**. See **Achard et al, 2006**.

Binary graph computation:
- Minimum spanning tree.
- Thresholding depending on cost → adjacency matrix.
- Cost range from 2.5% to 75%.
- Several graph metrics extracted (**Table 1**).

Reliability study:

Testing reliability of different number of subjects, scan duration, parcellation and costs for each graph metric, by computing:
- One way random **ICC(1,1)**.
- ***p*-values** (**permutations**).
- **Bootstrapping** (groups subdivision).

Parameter	Symbol	Description
Regional network level		
Degree	k_i	Number of edges connected to a node *i*.
Global efficiency	e_i	Communication efficiency of a node *i* with all other nodes.
Local efficiency	l_i	Communication efficiency of a node *i* with its neighbors.
Betweenness centrality	b_i	Influence of a node *i* over the information flow between all other nodes.
Clustering	c_i	Fraction of the neighbors of a node *i* that are also neighbors of each other.
Global network level		
Global efficiency	E_g	Mean of e_i.
Local efficiency	E_l	Mean of l_i.
Modularity	Q	Strength of division of a network into clusters of nodes highly connected between them.
Betweenness centrality	B	Mean of b_i.
Small world topology	σ	Extent of a network between randomness and order.
Clustering	C	Mean of c_i.

Table 1 - Network metrics. Details in **Rubinov and Sporns (2010).**

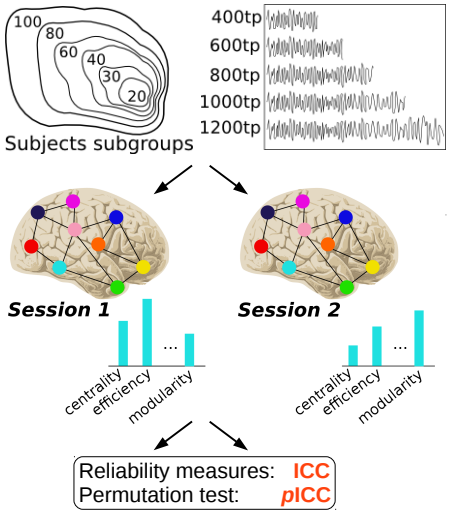

Figure 1 – Methodological overview.

Results

Influence of the number of subjects and scan duration:
- Increasing scan duration and number of subjects resulted in decreased p-values.
- ICCs increase as the scan duration increases.

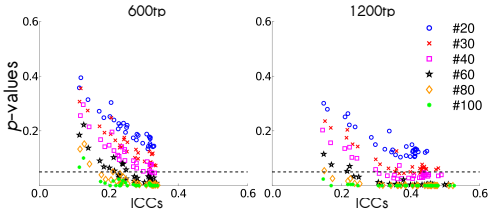

Figure 2 – E_g: *p*-values of ICC as a function of ICC values for different number of subjects and different scan duration: 600tp (7 min 12 s) and 1200tp (14 min 24 s). Mean results after 1000 bootstraps and AAL89.

- **Trade-off** between **number of subjects** and **scan duration**.
- The number of subjects to achieve reliable results depends on the scan duration: a ***larger number of subjects is needed for a short scan duration***.

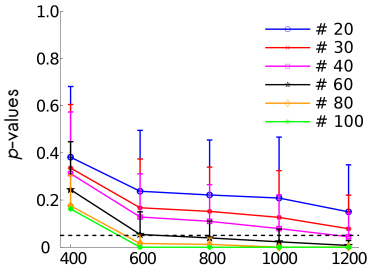

Figure 3 – E_g: mean p-values at different scan duration applying 1000 bootstraps at 20% cost and AAL89.

- The **number** of **significant regions** is **dependent** on the **number of subjects** and **scan duration**.

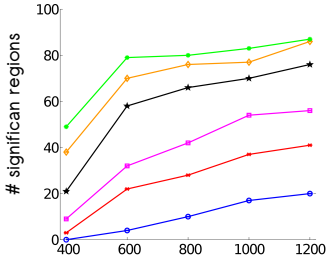

Figure 4 – Number of significant regions as function of scan duration for different number of subjects (corrected for multiple comparisons using a FDR at 0.05%). Results for e_i using AAL89 at 20% cost.

Location of the reliable regions:

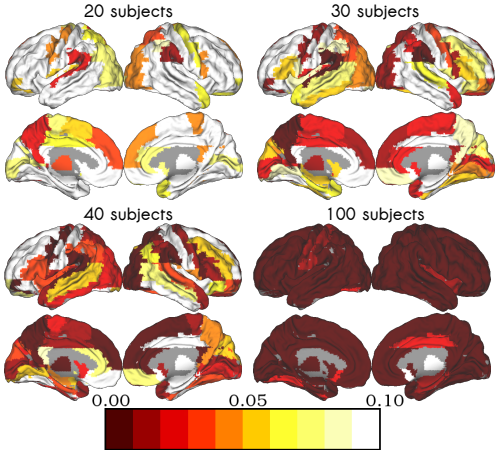

Figure 5 – Brain maps of reliable nodes that demonstrated significant regions on the brain. Displayed p-values are FDR corrected (0.05%) for multiple comparisons. Results using e_i at 1200 tp (14min 24s), AAL89 and 20% cost.

Reliability versus parcellation:
- *p*-values are very close for the different parcellations except for HO117.
- A number of subjects between 30 and 40 is sufficient to achieve reliability on ICC except for HO117, where 60 subjects are required.

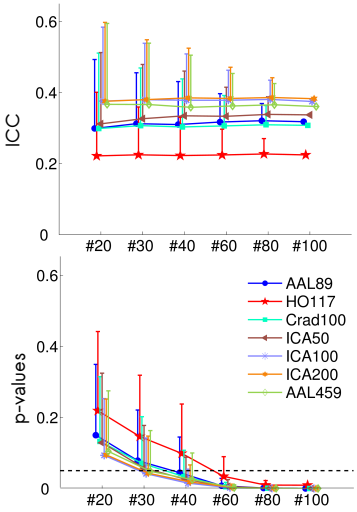

Figure 6 – ICCs and their p-values for different parcellation schemes and different number of subjects. Results are shown for E_g at 1200tp and 20% cost.

Summary

- **ICCs** should be associated with ***p*-values** to measure graph metrics reliability.
- **Sample size** and **scan duration** are key parameters for **reliable graph metrics**.
- As ICC values depend on cost, number of subjects and scan length, high ICC scores do not necessarily indicate reliable results.
- The number of regions with reliable global efficiency increased with the sample size.
- In **large samples** (N = 100), nearly all global and regional metrics are reliable.
- In **small samples** (around 40 subjects), we found reliable regions in **motor**, **visual** networks and **DMN**.
- At the global level, all the **parcellation** schemes perform **very similarly** except for HO117. At the regional level, results are more dependent on the parcellation schemes (not shown).

A deeper explanation and more results can be found in ***Termenon et al., Neuroimage, 2016***.

This work is supported by a grant from the Rhône-Alpes Région, France.

'Hub Disruption Index' (κ), an index that measures brain networks reorganization

M. Termenon[1,2,*], A. Jaillard[3,4,5], C. Delon-Martin[1-2], S. Achard[6,7]

[1]Univ. Grenoble Alpes, Grenoble Institute des Neurosciences, Grenoble, France, [2]INSERM, U1216, Grenoble, France, [3]Pole Recherche, CHU Grenoble, France, [4]IRMaGe, Inserm US17 CNRS UMS 3552, Grenoble, France, [5]AGEIS EA7407, Univ. Grenoble Alpes, France, [6]Univ. Grenoble Alpes, GIPSA-lab, Grenoble, France, [7]CNRS, GIPSA-lab, Grenoble, France *maite.termenon@ujf-grenoble.fr

What is κ?

The ***Hub Disruption Index*** (κ) measures if the functional connectivity of one brain is disorganized with respect to the functional connectivity of a reference group. It was first introduced by **Achard et al, PNAS, 2012**.

How is κ computed?

1. Compute brain graphs.
2. Select a nodal graph metric.
3. Compute the mean of this metric along a reference group ***R*** (healthy controls group).
4. Select a subject ***S*** to study.
5. Compute the difference between ***S*** and ***R***.
6. Obtain the linear fit between the difference and ***R***.

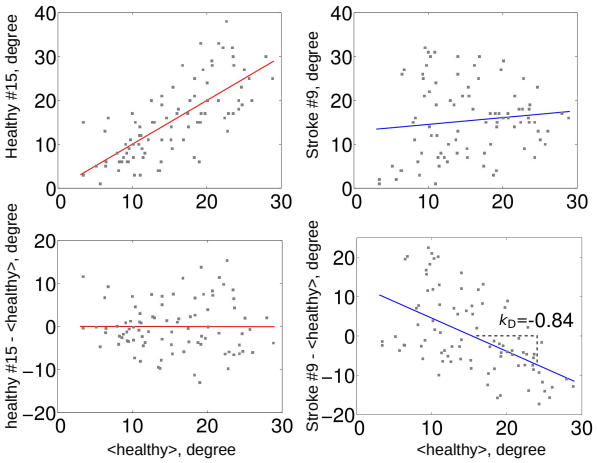

Properties:

- κ is sensitive to the nodal network topology of ***S*** in comparison to the network topology of ***R***.
- If no reorganization: κ ≈ 0.
- If reorganization: κ ≠ 0 (usually negative).
- κ index can be used to compare:
  - The behavior of the network of a single subject (healthy or patient).
  - The mean differences between a group of patients and ***R***.

κ_{Eg}: Hub disruption index using global efficiency

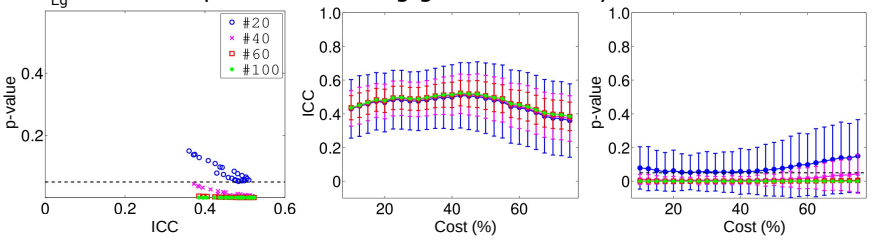

Eg: classical global efficiency

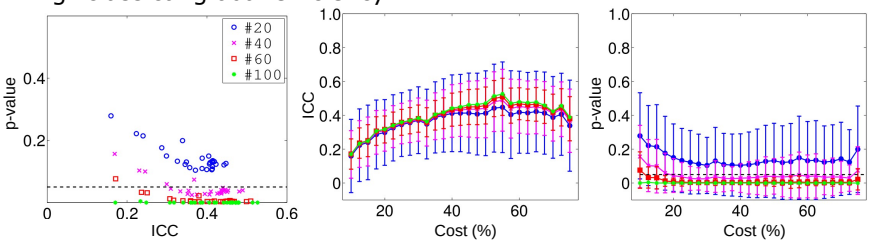

Reliability of κ in comparison with global graph metrics

- A prerequisite before translating this index to clinic is to assess its reliability.
- Testing reliability of **different number of subjects** and **costs** by computing:
  - One way random **ICC(1,1)**.
  - **p-values** (**permutations**).
  - **Bootstrapping** (group subdivision).
- Using:
  - Human Connectome Project test-retest database (100 subjects, 14min 24s scan duration).
  - AAL89 parcellation scheme.
  - Several graph metrics:global efficiency (Eg), local efficiency (El), clustering (C), betweenness centrality (B) and node degree (D).
- Results:
  - **Higher reliability** with κ index as compared to classical global graph metrics.
  - **Better sensitivity to group differences** than with global graph metrics.
  - Similar results with the other metrics.

κ in clinical applications

κ has shown its interest in:

- **Comatose patients** (**Achard et al, PNAS, 2012**):
  - Brain connectivity was profoundly modified with both disconnected and overconnected nodes.
  - κ deeply reduced in patients as compared to healthy subjects.
- **Neuromyelytis optica** (**Hemmert et al, Multiple Sclerosis, 2013**):
  - Significant differences between groups at several locations in the cortex.
  - Higher brain reorganisation in more disabled patients.
- **Epilepsy** (**Ridley et al, Neuroimage, 2015**):
  - Network-wide pattern of reorganization in the patients group.
  - Differently lateralized epileptic networks are asymmetric in their functional brain networks.
- **Stroke** (**Termenon et al, Front. Comp. Neurosci, 2016**):
  - κ deeply reduced in contralesional hemisphere of stroke patients as compared to healthy subjects.

Right contralesional hemisphere in Stroke

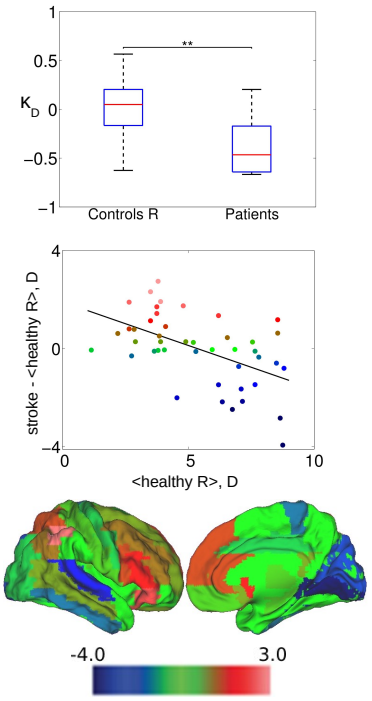

Comparison of κ vs global metrics in Stroke vs healthy controls

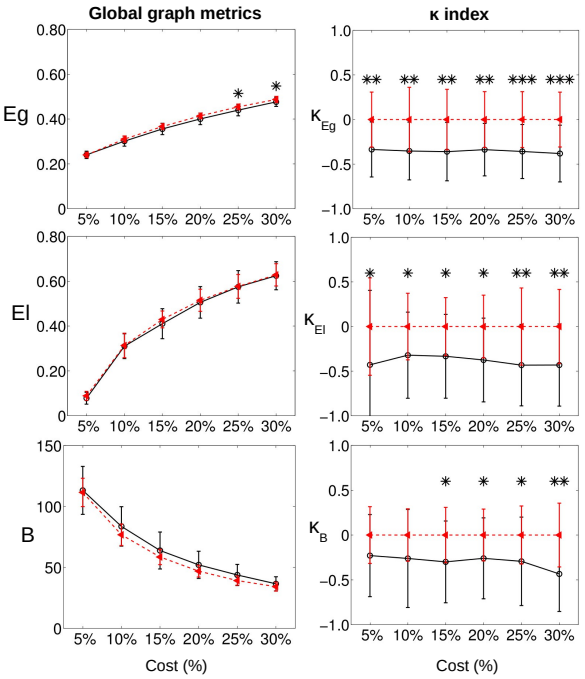

Significant differences:
*<0.05; **<0.01; ***<0.001

This work is supported by a grant from the Rhône-Alpes Région, France.

48A

Hemispheric specialization in men and women using graph theory: a resting-state functional connectivity MRI study in highly educated healthy adults

M. Termenon[1,2,*], A. Jaillard[3,4], S. Achard[1-3,5], C. Delon-Martin[1-2]

[1] Inserm, U836, Grenoble, F-38043, France. [2] Univ. Grenoble Alpes, GIN, F-38000 Grenoble, France. [3] University Hospital, Grenoble, France. [4] Pôle Recherche UMS IRMaGe, Grenoble, France. [5] GIPSA-lab UMR CNRS 5216, Grenoble, France.

*maite.termenon@ujf-grenoble.fr

Goal

To test the effect of hemispheric lateralization, sex and age in highly educated healthy adults using metrics derived from graph analysis of resting state networks.

Background

Neuropsychological findings often have found asymmetries in relation to the kind of material being processed: the left hemisphere associated with more verbal materials and the right with non-verbal materials [1].

Topological organization of human brain networks at rest can be explored using graph theory analysis [2]. Recent reports in children and young adults showed hemisphere and sex-related differences in detected hubs [3, 4]. However no significant difference was detected among global network parameters.

A recent study in structural and functional connectivity across the human lifespan [5] found age-related changes in inter-regional communication in resting-state networks.

Materials

Forty one healthy participants age range 22-62 years, 19 males, 3- to 10-year post-baccalaureate) were included in this study that was approved by local ethical committee. Participants underwent a 13 minutes resting-state fMRI acquisition session (**400 volumes**, TR=2s, spatial resolution 3x3x3.85 mm^3, 36 axial slices, FOV 192x192x138.5 mm^3, 3T Philips MR scanner). A 1x1x1 mm^3 T1 structural image was acquired for all participants. Subjects were instructed to let their mind wandering and to keep their eyes open.

Methods

Data analysis:

The fMRI data were preprocessed using **SPM12b** software. Preprocessing included **motion correction**, compensation for **time shift** between slices and **elastic registration** using DARTEL onto the **ICBM152** template. Time-series (TS) corresponding to the grey-matter voxels of **89 ROIs** from the **AAL** template were extracted by averaging the voxels of each parcel over the fMRI time series, weighted by the proportion of GM in each voxel of the segmented structural MRIs. TS were **regressed out** by 6 motion parameters and their first derivative.

Graph computation:

TS were decomposed in 4 frequency bands using **discrete wavelet transformation** and the individual graphs were computed selecting the 10% of the highest correlated connections in the **0.03-0.06 Hz** frequency band, as explained in [2]. Then, three graph metrics were computed at node level: **node degree (k)**, **global efficiency (Eglob)** and **betweenness centrality (BC)** (for a deeper explanation of the metrics, see [6]). Finally age, sex, and hemispheric side effects were assessed using GLM repeated measures analyses (SPSS software v20).

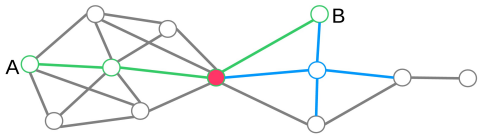

Results

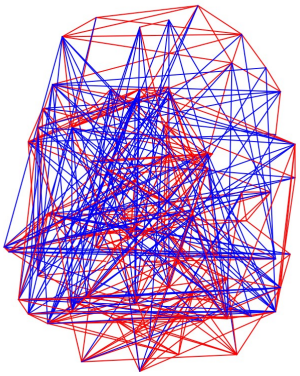

Figure 1 – Example of the functional connectivity graph of one healthy subject (transversal view).

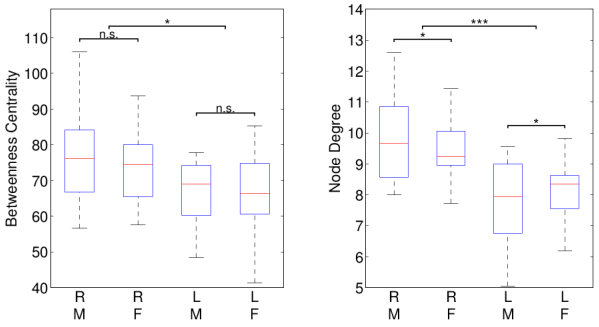

Figure 2 – Box plots of the multivariate analysis of betweenness centrality and node degree. ***(p<0.001); *(p<0.05); n.s.= no significant; R = right hemisphere; L= left hemisphere; M = male; F= female.

Multivariate analysis showed:
(i) a significant effect of hemispheric side ($p<0.0001$) and age ($p=0.005$) with a sex by side interaction ($p=0.014$): compared to females, males show higher connectivity in the right hemisphere and lower connectivity in the left hemisphere (see Fig. 2).

Univariate analyses showed:
(i) significantly higher graph metrics in the right than in the left hemisphere ($p_K<0.0001$; $p_{Eglob}<0.0001$; $p_{BC}=0.005$);
(ii) significant side by sex interaction for degree ($p_K=0.038$) and global efficiency but not for betweenness centrality ($p_{BC}=0.358$);
(iii) No significant effect was found for age at the single metric level.

References

[1] Gazzaniga M S. 2000 The Cognitive Neurosciences. MIT Press, Cambridge.
[2] Achard S et al. 2006 A resilient, low-frequency, small-world human brain functional network with highly connected association cortical hubs. *J. Neurosci.* **26**, 63-72.
[3] Tian L et al. 2011 Hemisphere- and gender-related differences in small-world brain networks: A resting-state functional MRI study. *NeuroImage* **54**, 191-202.
[4] Nielsen J A et al. 2013 An evaluation of the left-brain vs. right-brain hypothesis with resting state functional connectivity magnetic resonance imaging. *Plos ONE* **8**.
[5] Betzel R F et al. 2014 Changes in structural and functional connectivity among resting-state networks across the human lifespan. *NeuroImage* In press.
[6] Bullmore E. and Sporns O. 2009 Complex brain networks: graph theoretical analysis of structural and functional systems. *Nat. Rev. Neurosci.* **10**, 186-198.

Discussion & Conclusion

The **right hemisphere** appears to present **more connections** than the left hemisphere in highly educated healthy adults. Moreover, the differences in hemispheric graph metrics relative to sex suggest **men** and **women** may have **different hemispheric specialization**.

Our results are consistent with previous findings in children and young adults [3, 4], supporting the classical idea of greater language abilities in women and better aptitude in men for visuospatial skills.

The **mild effect of age**, has to be put into perspective with the age range (20 to 62), the high level of education of our sample, and the small number of subjects to cover the adulthood life-span. A robuster effect of age has also been reported in most RS networks [5] but in a larger age range.

These lateralization and demographic differences should be considered when using resting-state functional connectivity MRI methods in clinical studies.

Acknowledgment

This work is supported by a grant from the Rhône-Alpes Région, France.

Is homotopic intramural connectivity related to cytoarchitectonic cortical classification?

M. Termenon[1,2,*], A. Jaillard[3,4], S. Achard[5], F. Renard[3,4], C. Delon-Martin[1,2]

[1] Inserm, U836, Grenoble, F-38043, France. [2] Univ. Grenoble Alpes, GIN, F-38000 Grenoble, France. [3] University Hospital, Grenoble, France. [4] Pôle Recherche UMS IRMaGe, Grenoble, France. [5] GIPSA-lab UMR CNRS 5216, Grenoble, France. *maite.termenon@ujf-grenoble.fr

Rationale and background

Cortical regions can be classified into four types of cortex: the **paralimbic zone** (PZ), **heteromodal cortical zone** (HC), **unimodal cortical zone** (UC) and **idiotypic cortical zone** (IC), reflecting an increasing degree of specialization [1], see *Figure 1*. This classification is related to a decreasing distribution of intramural connections and neural projections between homotopic regions in the idiotypic cortex (primary sensory and motor areas) compared to the paralimbic cortex (1).
Whether the **functional connectivity** reflects differences across the different **subtypes of cortex** in the healthy human brain remains a question that can be addressed using recent methods based on resting state functional connectivity.

Goal

To test the hypothesis of an increasing connectivity between homotopic regions within the idiotypic, unimodal, heteromodal and paralimbic cortices.

A **regional inter-hemispheric correlation (rHIC)** value is computed between pairs of homotopic regions defined following the AAL [2] template, among a group of 31 healthy adults. After pooling the rHIC values by regions unambiguously pertaining to each zone, we tested for a differential connectivity related to different subtypes of cortical zones.

Methods

MR acquisitions: **Thirty one healthy** participants with no neurological or psychiatric history (age 32.7 ± 11.48 years) were included in this study (PHRC HERMES 2010 and Projet de Recherche Aviesan 'Cerveau-Intestin'). For the resting-state run, BOLD weighted fMRI images were acquired on a 3T Philips Achieva scanner at the IRMaGe platform of the University Hospital of Grenoble (France). The participants were instructed to lie still, with their eyes opened, letting their mind wandering. Acquisition parameters for the fMRI run were: **400 volumes**; TR 2sec; 35 axial slices; FOV 192x192x138.5 mm^3; voxel size 3x3x3.5 mm3; 13.5min. A 1x1x1 mm^3 T1 structural image was acquired for all participants.

Data analysis: The fMRI data were preprocessed using **SPM12b** software. Realignment and slice timing correction were performed on the EPI images. Structural images were first co-registered to the mean EPI and segmented. The deformation field permitting accurate coregistration between grey matter (GM) image and AAL is further computed using **DARTEL**. This inverse deformation field is applied to the AAL template to produce a subject-specific labeled atlas. Doing this, the EPI images, the subject-specific labeled atlas and T1 images were all in the same individual reference system. Regional mean time series (TS) were estimated by averaging the voxels of each parcel over the fMRI time series, weighted by the proportion of GM in each voxel of the segmented structural MRIs. TS were **regressed out** by global white matter and cerebrospinal fluid, 6 motion parameters and motion outliers. TS were decomposed in 4 frequency bands using **wavelet transformation** to estimate the correlations between the homotopic AAL regions [3]. The correlation matrices corresponding to the frequency interval **0.032-0.065Hz** were computed. The rHIC were extracted from the matrices for each pair of homotopic regions. We selected specific AAL areas that unequivocally belongs to each cortex type and computed the mean rHIC within the four cortical zone groups (IC, UC, MC and PZ). We compared the four groups using a repeated ANOVA test (SPSS 20.0 package).

Results

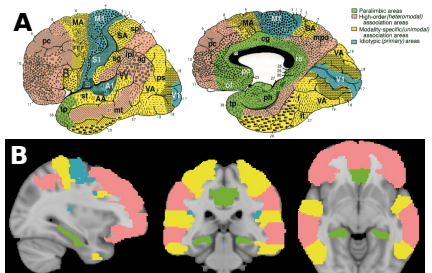

Figure 1 – Four type of cortex. A: Mesulam division [1]. B: Unambiguously regions chosen in this study.

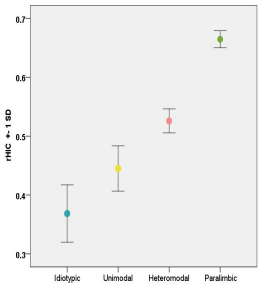

Figure 2 – Regional homotopic inter-hemispheric correlation value (rHIC) in each type of cortex.

A) The **highest** rHIC value was observed in the **PZ group** (paralimbic zone) and the **lowest** in the **IC group** (idiotypic cortical zone)**,** see *Figure 2*.
B) Repeated measures analysis showed a **significant difference** in rHIC among the 4 groups (D=19.69, p<.0001), with statistically significant differences between each group, see *Table 1*.

Cortex Type	Squares means	D	p
IC and UC	0.18	4.94	**0.034**
UC and HC	0.20	7.65	**0.010**
HC and PZ	0.60	61.14	**0.000**

Table 1 – Statistical results. Statistically significant differences between each group.

Discussion & Conclusion

- Homotopic inter-hemispheric correlations may help to **discriminate** the cortex types on the basis of the rHIC values.
- rHIC values may help to specify the **connectivity modulation** engaged in different operations according to the processing brain regions.
- Studying these rHIC measures could be of **clinical interest** in diseases impairing specific types of cortex, such as in Alzheimer, psychiatric diseases and also, in recovery.

Homotopic inter-hemispheric correlations derived from rs-fcMRI seems to reflect intramural connectivity.

References & Acknowledgment

[1] Mesulam, Oxford University Press, chapter 1, 2000.
[2] Tzourio-Mazoyer et al., NeuroImage, 2002.
[3] Achard et al., PNAS, 2012.

This work is supported by a grant from the Rhône-Alpes Région.

Bibliography

A. Abraham. *Learning functional brain atlases modeling inter-subject variability.* Theses, Université Paris-Saclay, Nov. 2015.

S. Achard and E. Bullmore. Efficiency and Cost of Economical Brain Functional Networks. *PLoS Comput Biol*, 3(2):e17, Feb. 2007. doi: 10.1371/journal.pcbi.0030017.

S. Achard, R. Salvador, B. Whitcher, J. Suckling, and E. Bullmore. A resilient, low-frequency, small-world human brain functional network with highly connected association cortical hubs. *The Journal of Neuroscience*, 26(1):63–72, Jan. 2006. ISSN 0270-6474, 1529-2401. doi: 10.1523/JNEUROSCI.3874-05.2006. 00831.

S. Achard, C. Delon-Martin, P. E. Vértes, F. Renard, M. Schenck, F. Schneider, C. Heinrich, S. Kremer, and E. T. Bullmore. Hubs of brain functional networks are radically reorganized in comatose patients. *Proceedings of the National Academy of Sciences*, page 201208933, Nov. 2012. ISSN 0027-8424, 1091-6490. doi: 10.1073/pnas.1208933109. PMID: 23185007.

O. Agcaoglu, R. Miller, A. Mayer, K. Hugdahl, and V. Calhoun. Lateralization of resting state networks and relationship to age and gender. *NeuroImage*, 104:310 – 325, 2015. ISSN 1053-8119. doi: http://dx.doi.org/10.1016/j.neuroimage.2014.09.001.

A. N. Akansu and R. A. Haddad. *Multiresolution Signal Decomposition: Transforms, Subbands, and Wavelets.* Academic Press, 2001. ISBN 978-0-12-047141-6.

A. Alexander-Bloch, R. Lambiotte, B. Roberts, J. Giedd, N. Gogtay, and E. Bullmore. The discovery of population differences in network community structure: New methods and applications to brain functional networks in schizophrenia. *NeuroImage*, 59(4):3889–3900, 2012. ISSN 1053-8119. doi: http://dx.doi.org/10.1016/j.neuroimage.2011.11.035.

A. F. Alexander-Bloch, N. Gogtay, D. Meunier, R. Birn, L. Clasen, F. Lalonde, R. Lenroot, J. Giedd, and E. T. Bullmore. Disrupted modularity and local connectivity of brain functional networks in childhood-onset schizophrenia.

Frontiers in Systems Neuroscience, 4(147), 2010. ISSN 1662-5137. doi: 10.3389/fnsys.2010.00147.

J. Alstott, M. Breakspear, P. Hagmann, L. Cammoun, and O. Sporns. Modeling the impact of lesions in the human brain. *PLoS Comput Biol*, 5(6):e1000408, 06 2009. doi: 10.1371/journal.pcbi.1000408.

M. Andellini, V. Cannatà, S. Gazzellini, B. Bernardi, and A. Napolitano. Test-retest reliability of graph metrics of resting state {MRI} functional brain networks: A review. *Journal of Neuroscience Methods*, 253:183 – 192, 2015. ISSN 0165-0270. doi: http://dx.doi.org/10.1016/j.jneumeth.2015.05.020.

A. Andronache, C. Rosazza, D. Sattin, M. Leonardi, L. D'Incerti, and L. Minati. Impact of functional mri data preprocessing pipeline on default-mode network detectability in patients with disorders of consciousness. *Frontiers in Neuroinformatics*, 7(16), 2013. ISSN 1662-5196. doi: 10.3389/fninf.2013.00016.

E. Armstrong. 1 - evolution of the brain. In G. Paxinos, editor, *The Human Nervous System*, pages 1 – 16. Academic Press, San Diego, 1990. ISBN 978-0-12-547625-6. doi: http://dx.doi.org/10.1016/B978-0-12-547625-6.50006-4.

A. Arvidsson, T. Collin, D. Kirik, Z. Kokaia, and O. Lindvall. Neuronal replacement from endogenous precursors in the adult brain after stroke. *Nat. Med.*, 8(9):963–970, Sep 2002.

J. Ashburner. A fast diffeomorphic image registration algorithm. *NeuroImage*, 38(1):95 – 113, 2007. ISSN 1053-8119. doi: http://dx.doi.org/10.1016/j.neuroimage.2007.07.007.

J. Ashburner and K. J. Friston. Unified segmentation. *NeuroImage*, 26(3):839 – 851, 2005. ISSN 1053-8119. doi: http://dx.doi.org/10.1016/j.neuroimage.2005.02.018.

A. M. Auriat, J. L. Neva, S. Peters, J. K. Ferris, and L. A. Boyd. A review of transcranial magnetic stimulation and multimodal neuroimaging to characterize post-stroke neuroplasticity. *Frontiers in Neurology*, 6:226, 2015. ISSN 1664-2295. doi: 10.3389/fneur.2015.00226.

L. C. Bannister, S. G. Crewther, M. Gavrilescu, and L. M. Carey. Improvement in touch sensation after stroke is associated with resting functional connectivity changes. *Frontiers in neurology*, 6:165, 2015. ISSN 1664-2295. doi: 10.3389/fneur.2015.00165.

C. F. Beckmann and S. M. Smith. Probabilistic independent component analysis for functional magnetic resonance imaging. *IEEE Transactions on Medical Imaging*, 23(2):137–152, Feb 2004. ISSN 0278-0062. doi: 10.1109/TMI.2003.822821.

C. F. Beckmann, M. DeLuca, J. T. Devlin, and S. M. Smith. Investigations into resting-state connectivity using independent component analysis. *Philos. Trans. R. Soc. Lond., B, Biol. Sci.*, 360(1457):1001–1013, 2005.

R. F. Betzel, L. Byrge, Y. He, J. Goñi, X.-N. Zuo, and O. Sporns. Changes in structural and functional connectivity among resting-state networks across the human lifespan. *NeuroImage*, 102, Part 2:345 – 357, 2014. ISSN 1053-8119. doi: http://dx.doi.org/10.1016/j.neuroimage.2014.07.067.

R. M. Birn, E. K. Molloy, R. Patriat, T. Parker, T. B. Meier, G. R. Kirk, V. A. Nair, M. E. Meyerand, and V. Prabhakaran. The effect of scan length on the reliability of resting-state fMRI connectivity estimates. *NeuroImage*, 83: 550–558, Dec. 2013. ISSN 1053-8119. doi: 10.1016/j.neuroimage.2013.05.099.

B. Biswal, F. Zerrin Yetkin, V. M. Haughton, and J. S. Hyde. Functional connectivity in the motor cortex of resting human brain using echo-planar mri. *Magnetic Resonance in Medicine*, 34(4):537–541, 1995. ISSN 1522-2594. doi: 10.1002/mrm.1910340409.

J. M. Bland and D. G. Altman. Statistical methods for assessing agreement between two methods of clinical measurement. *Lancet*, 1(8476):307–310, Feb. 1986. ISSN 0140-6736.

H. Blumenfeld. *Neuroanatomy Through Clinical Cases*. Blumenfeld, Neuroanatomy Through Clinical Cases. Sinauer Associates, 2010. ISBN 9780878930586.

T. J. Boardman. Confidence intervals for variance components–a comparative monte carlo study. *Biometrics*, 30(2):251–262, 1974.

S. Boccaletti, V. Latora, Y. Moreno, M. Chavez, and D. Hwang. Complex networks: Structure and dynamics. *Physics Reports*, 424(4–5):175–308, Feb 2006. ISSN 0370-1573. doi: 10.1016/j.physrep.2005.10.009.

Boundless. *Boundless Anatomy and Physiology*. 06 2016.

L. V. Bradnam, C. M. Stinear, P. A. Barber, and W. D. Byblow. Contralesional hemisphere control of the proximal paretic upper limb following stroke. *Cereb. Cortex*, 22(11):2662–2671, 2012.

U. Brandes. A faster algorithm for betweenness centrality. *Journal of Mathematical Sociology*, 25:163–177, 2001.

M. Brant-Zawadzki, D. Atkinson, M. Detrick, W. G. Bradley, and G. Scidmore. Fluid-attenuated inversion recovery (flair) for assessment of cerebral infarction: Initial clinical experience in 50 patients. *Stroke*, 27(7):1187–1191, 1996. doi: 10.1161/01.STR.27.7.1187.

U. Braun, M. M. Plichta, C. Esslinger, C. Sauer, L. Haddad, O. Grimm, D. Mier, S. Mohnke, A. Heinz, S. Erk, H. Walter, N. Seiferth, P. Kirsch, and A. Meyer-Lindenberg. Test-retest reliability of resting-state connectivity network characteristics using fMRI and graph theoretical measures. *NeuroImage*, 59(2): 1404–1412, Jan. 2012. ISSN 1053-8119. doi: 10.1016/j.neuroimage.2011.08.044.

T. Brott, H. P. Adams, C. P. Olinger, J. R. Marler, W. G. Barsan, J. Biller, J. Spilker, R. Holleran, R. Eberle, and V. Hertzberg. Measurements of acute cerebral infarction: a clinical examination scale. *Stroke*, 20(7):864–870, 1989.

R. L. Buckner, J. R. Andrews-Hanna, and D. L. Schacter. The brain's default network. *Annals of the New York Academy of Sciences*, 1124(1):1–38, 2008. ISSN 1749-6632. doi: 10.1196/annals.1440.011.

R. L. Buckner, J. Sepulcre, T. Talukdar, F. M. Krienen, H. Liu, T. Hedden, J. R. Andrews-Hanna, R. A. Sperling, and K. A. Johnson. Cortical Hubs Revealed by Intrinsic Functional Connectivity: Mapping, Assessment of Stability, and Relation to Alzheimer's Disease. *The Journal of Neuroscience*, 29(6):1860–1873, Feb. 2009. ISSN 0270-6474, 1529-2401. doi: 10.1523/JNEUROSCI.5062-08.2009.

E. Bullmore and O. Sporns. Complex brain networks: graph theoretical analysis of structural and functional systems. *Nature Reviews Neuroscience*, 10(3): 186–198, Mar. 2009. ISSN 1471-003X. doi: 10.1038/nrn2575. 01680.

E. Bullmore and O. Sporns. The economy of brain network organization. *Nat Rev Neurosci*, 13(5):336–349, May 2012. ISSN 1471-003X. doi: 10.1038/nrn3214.

E. Bullmore, J. Fadili, V. Maxim, L. Şendur, B. Whitcher, J. Suckling, M. Brammer, , and M. Breakspear. Wavelets and functional magnetic resonance imaging of the human brain. *NeuroImage*, 23, Supplement 1:S234 – S249, 2004. ISSN 1053-8119. doi: http://dx.doi.org/10.1016/j.neuroimage.2004.07.012. Mathematics in Brain Imaging.

K. S. Button, J. P. A. Ioannidis, C. Mokrysz, B. A. Nosek, J. Flint, E. S. J. Robinson, and M. R. Munafò. Power failure: why small sample size undermines the reliability of neuroscience. *Nat Rev Neurosci*, 14(5):365–376, May 2013. doi: 10.1038/nrn3475.

J. Cabral, M. L. Kringelbach, and G. Deco. Exploring the network dynamics underlying brain activity during rest. *Progress in Neurobiology*, 114:102 – 131, 2014. ISSN 0301-0082. doi: http://dx.doi.org/10.1016/j.pneurobio.2013.12.005.

C. Calautti, M. Naccarato, P. S. Jones, N. Sharma, D. D. Day, A. T. Carpenter, E. T. Bullmore, E. A. Warburton, and J. C. Baron. The relationship between motor deficit and hemisphere activation balance after stroke: A 3T fMRI study. *Neuroimage*, 34(1):322–331, 2007.

H. Cao, M. M. Plichta, A. Schäfer, L. Haddad, O. Grimm, M. Schneider, C. Esslinger, P. Kirsch, A. Meyer-Lindenberg, and H. Tost. Test-retest reliability of fMRI-based graph theoretical properties during working memory, emotion processing, and resting state. *NeuroImage*, 84:888–900, Jan. 2014. ISSN 1095-9572. doi: 10.1016/j.neuroimage.2013.09.013. PMID: 24055506.

A. R. Carter, S. V. Astafiev, C. E. Lang, L. T. Connor, J. Rengachary, M. J. Strube, D. L. Pope, G. L. Shulman, and M. Corbetta. Resting interhemispheric functional magnetic resonance imaging connectivity predicts performance after stroke. *Ann. Neurol.*, 67(3):365–375, Mar 2010.

A. R. Carter, K. R. Patel, S. V. Astafiev, A. Z. Snyder, J. Rengachary, M. J. Strube, A. Pope, J. S. Shimony, C. E. Lang, G. L. Shulman, and M. Corbetta. Upstream dysfunction of somatomotor functional connectivity after corticospinal damage in stroke. *Neurorehabil Neural Repair*, 26(1):7–19, Jan 2012a.

A. R. Carter, G. L. Shulman, and M. Corbetta. Why use a connectivity-based approach to study stroke and recovery of function? *NeuroImage*, 62(4):2271 – 2280, 2012b. ISSN 1053-8119. doi: http://dx.doi.org/10.1016/j.neuroimage.2012.02.070. ConnectivityConnectivity.

J. Chen and G. Schlaug. Resting state interhemispheric motor connectivity and white matter integrity correlate with motor impairment in chronic stroke. *Frontiers in Neurology*, 4:178, 2013. ISSN 1664-2295. doi: 10.3389/fneur.2013.00178.

M. Chopp and Y. Li. Treatment of neural injury with marrow stromal cells. *The Lancet Neurology*, 1(2):92–100, 2002. ISSN 1474-4422. doi: 10.1016/S1474-4422(02)00040-6.

D. V. Cicchetti. Guidelines, criteria, and rules of thumb for evaluating normed and standardized assessment instruments in psychology. *Psychological assessment*, 6(4):284, 1994.

R. C. Craddock, G. A. James, P. E. Holtzheimer, X. P. Hu, and H. S. Mayberg. A whole brain fmri atlas generated via spatially constrained spectral clustering. *Human brain mapping*, 33(8):1914–1928, August 2012. ISSN 1065-9471. doi: 10.1002/hbm.21333.

N. A. Crossley, A. Mechelli, J. Scott, F. Carletti, P. T. Fox, P. McGuire, and E. T. Bullmore. The hubs of the human connectome are generally implicated in the anatomy of brain disorders. *Brain: a journal of neurology*, 137(Pt 8):2382–2395, August 2014. ISSN 0006-8950. doi: 10.1093/brain/awu132.

R. Dacosta-Aguayo, M. Graña, A. Savio, M. Fernández-Andújar, M. Millán, E. López-Cancio, C. Cáceres, N. Bargalló, C. Garrido, M. Barrios, I. C. Clemente, M. Hernández, J. Munuera, A. Dávalos, T. Auer, and M. Mataró. Prognostic value of changes in resting-state functional connectivity patterns in

cognitive recovery after stroke: A 3t fmri pilot study. *Human Brain Mapping*, 35(8):3819–3831, 2014. ISSN 1097-0193. doi: 10.1002/hbm.22439.

R. Dacosta-Aguayo, M. Graña, Y. Iturria-Medina, M. Fernández-Andújar, E. López-Cancio, C. Cáceres, N. Bargalló, M. Barrios, I. Clemente, P. Toran, R. Forés, A. Dávalos, T. Auer, and M. Mataró. Impairment of functional integration of the default mode network correlates with cognitive outcome at three months after stroke. *Human Brain Mapping*, 36(2):577–590, 2015. ISSN 1097-0193. doi: 10.1002/hbm.22648.

E. Damaraju, J. Phillips, J. R. Lowe, R. Ohls, V. D. Calhoun, and A. Caprihan. Resting-state functional connectivity differences in premature children. *Frontiers in Systems Neuroscience*, 4(23), 2010. ISSN 1662-5137. doi: 10.3389/fnsys.2010.00023.

E. Dammekens, S. Vanneste, J. Ost, and D. De Ridder. Neural correlates of high frequency repetitive transcranial magnetic stimulation improvement in post-stroke non-fluent aphasia: a case study. *Neurocase*, 20(1):1–9, 2014.

I. Daubechies. *Ten Lectures on Wavelets*. Society for Industrial and Applied Mathematics, 1992. doi: 10.1137/1.9781611970104.

F. De Vico Fallani, J. Richiardi, M. Chavez, and S. Achard. Graph analysis of functional brain networks: practical issues in translational neuroscience. *Philosophical Transactions of the Royal Society B: Biological Sciences*, 369 (1653):20130521, Oct. 2014. doi: 10.1098/rstb.2013.0521.

R. S. Desikan, F. Ségonne, B. Fischl, B. T. Quinn, B. C. Dickerson, D. Blacker, R. L. Buckner, A. M. Dale, R. P. Maguire, B. T. Hyman, M. S. Albert, and R. J. Killiany. An automated labeling system for subdividing the human cerebral cortex on {MRI} scans into gyral based regions of interest. *NeuroImage*, 31(3):968 – 980, 2006. ISSN 1053-8119. doi: http://dx.doi.org/10.1016/j.neuroimage.2006.01.021.

I. Despotović, B. Goossens, and W. Philips. Mri segmentation of the human brain: Challenges, methods, and applications. *Computational and Mathematical Methods in Medicine*, 2015, 2015.

O. Detante, A. Jaillard, A. Moisan, M. Barbieux, I. Favre, K. Garambois, M. Hommel, and C. Remy. Biotherapies in stroke. *Revue Neurologique*, 4350 (12):721–853, 2014. ISSN 0035-3787. doi: http://dx.doi.org/10.1016/j.neurol.2014.10.005.

J. Diedrichsen, J. H. Balsters, J. Flavell, E. Cussans, and N. Ramnani. A probabilistic {MR} atlas of the human cerebellum. *NeuroImage*, 46(1):39 – 46, 2009. ISSN 1053-8119. doi: http://dx.doi.org/10.1016/j.neuroimage.2009.01.045.

X. Ding, C.-Y. Li, Q.-S. Wang, F.-Z. Du, Z.-W. Ke, F. Peng, J. Wang, and L. Chen. Patterns in default-mode network connectivity for determining outcomes in cognitive function in acute stroke patients. *Neuroscience*, 277:637 – 646, 2014. ISSN 0306-4522. doi: http://dx.doi.org/10.1016/j.neuroscience.2014.07.060.

A. Donner. A review of inference procedures for the intraclass correlation coefficient in the one-way random effects model. *International Statistical Review/Revue Internationale de Statistique*, 54(1):67–82, 1986.

A. Donner and G. Wells. A comparison of confidence interval methods for the intraclass correlation coefficient. *Biometrics*, 42(2):401–412, 1986.

L. Douw, J. C. Baayen, M. Klein, D. Velis, W. C. Alpherts, J. Bot, J. J. Heimans, J. C. Reijneveld, and C. J. Stam. Functional connectivity in the brain before and during intra-arterial amobarbital injection (wada test). *NeuroImage*, 46(3):584 – 588, 2009. ISSN 1053-8119. doi: http://dx.doi.org/10.1016/j.neuroimage.2009.02.034.

H.-X. Du, X.-H. Liao, Q.-X. Lin, G.-S. Li, Y.-Z. Chi, X. Liu, H.-Z. Yang, Y. Wang, and M.-R. Xia. Test-retest reliability of graph metrics in high-resolution functional connectomics: A resting-state functional mri study. *CNS Neurosci Ther*, Jul 2015. doi: 10.1111/cns.12431.

S. B. Eickhoff, D. Bzdok, A. R. Laird, C. Roski, S. Caspers, K. Zilles, and P. T. Fox. Co-activation patterns distinguish cortical modules, their connectivity and functional differentiation. *Neuroimage*, 57(3):938–949, Aug 2011.

I. Favre, T. A. Zeffiro, O. Detante, A. Krainik, M. Hommel, and A. Jaillard. Upper limb recovery after stroke is associated with ipsilesional primary motor cortical activity: A meta-analysis. *Stroke*, 45(4):1077–1083, 2014. doi: 10.1161/STROKEAHA.113.003168.

D. A. Feinberg, S. Moeller, S. M. Smith, E. Auerbach, S. Ramanna, M. F. Glasser, K. L. Miller, K. Uğurbil, and E. Yacoub. Multiplexed echo planar imaging for sub-second whole brain fmri and fast diffusion imaging. *PLoS ONE*, 5(12):e15710, 12 2010. doi: 10.1371/journal.pone.0015710.

L. K. Ferreira and G. F. Busatto. Resting-state functional connectivity in normal brain aging. *Neuroscience and Biobehavioral Reviews*, 37(3):384–400, Mar. 2013. ISSN 1873-7528. doi: 10.1016/j.neubiorev.2013.01.017. 00037 PMID: 23333262.

M. Fiecas, H. Ombao, D. van Lunen, R. Baumgartner, A. Coimbra, and D. Feng. Quantifying temporal correlations: A test-retest evaluation of functional connectivity in resting-state fMRI. *NeuroImage*, 65:231–241, Jan. 2013. ISSN 1053-8119. doi: 10.1016/j.neuroimage.2012.09.052. 00008.

N. Filippini, B. J. MacIntosh, M. G. Hough, G. M. Goodwin, G. B. Frisoni, S. M. Smith, P. M. Matthews, C. F. Beckmann, and C. E. Mackay. Distinct patterns of brain activity in young carriers of the apoe-epsilon4 allele. *Proceedings of the National Academy of Sciences of the United States of America*, 106(17): 7209–7214, April 2009. ISSN 0027-8424. doi: 10.1073/pnas.0811879106.

E. J. Fine, C. C. Ionita, and L. Lohr. The history of the development of the cerebellar examination. *Semin Neurol*, 22(4):375–384, Dec 2002.

R. A. Fisher. Theory of Statistical Estimation. *Mathematical Proceedings of the Cambridge Philosophical Society*, 22(05):700–725, July 1925. ISSN 1469-8064. doi: 10.1017/S0305004100009580.

M. F. Folstein, S. E. Folstein, and P. R. McHugh. "Mini-mental state". A practical method for grading the cognitive state of patients for the clinician. *J Psychiatr Res*, 12(3):189–198, 1975.

V. Fonov, A. Evans, R. McKinstry, C. Almli, and D. Collins. Unbiased nonlinear average age-appropriate brain templates from birth to adulthood. *NeuroImage*, 47, Supplement 1:S102 –, 2009. ISSN 1053-8119. doi: http://dx.doi.org/10.1016/S1053-8119(09)70884-5. Organization for Human Brain Mapping 2009 Annual Meeting.

M. D. Fox and M. E. Raichle. Spontaneous fluctuations in brain activity observed with functional magnetic resonance imaging. *Nat Rev Neurosci*, 8(9): 700–711, Sep 2007. ISSN 1471-003X. doi: 10.1038/nrn2201.

M. D. Fox, A. Z. Snyder, J. L. Vincent, M. Corbetta, D. C. Van Essen, and M. E. Raichle. The human brain is intrinsically organized into dynamic, anticorrelated functional networks. *Proceedings of the National Academy of Sciences of the United States of America*, 102(27):9673–9678, 2005. doi: 10.1073/pnas.0504136102.

L. C. Freeman. A set of measures of centrality based on betweenness. *Sociometry*, 40(1):35–41, 1977. ISSN 00380431.

A. Gandy. Sequential implementation of monte carlo tests with uniformly bounded resampling risk. *Journal of the American Statistical Association*, 104(488):1504–1511, Dec. 2009. ISSN 0162-1459. doi: 10.1198/jasa.2009.tm08368.

A. Gandy and G. Hahn. A Safe Algorithm for Implementing Multiple Monte Carlo Tests. *Scandinavian Journal of Statistics*, 41(4):1083–1101, 2014. ISSN 1467-9469. doi: 10.1111/sjos.12085.

W. Gao, W. Lin, K. Grewen, and J. H. Gilmore. Functional Connectivity of the Infant Human Brain: Plastic and Modifiable. *Neuroscientist*, Feb 2016.

C. Gerloff, K. Bushara, A. Sailer, E. M. Wassermann, R. Chen, T. Matsuoka, D. Waldvogel, G. F. Wittenberg, K. Ishii, L. G. Cohen, and M. Hallett. Multimodal imaging of brain reorganization in motor areas of the contralesional hemisphere of well recovered patients after capsular stroke. *Brain*, 129(3): 791–808, 2006. ISSN 0006-8950. doi: 10.1093/brain/awh713.

M. F. Glasser, S. N. Sotiropoulos, J. A. Wilson, T. S. Coalson, B. Fischl, J. L. Andersson, J. Xu, S. Jbabdi, M. Webster, J. R. Polimeni, D. C. Van Essen, and M. Jenkinson. The minimal preprocessing pipelines for the human connectome project. *NeuroImage*, 80:105–124, Oct. 2013. ISSN 1053-8119. doi: 10.1016/j.neuroimage.2013.04.127.

M. F. Glasser, T. S. Coalson, E. C. Robinson, C. D. Hacker, J. Harwell, E. Yacoub, K. Ugurbil, J. Andersson, C. F. Beckmann, M. Jenkinson, S. M. Smith, and D. C. Van Essen. A multi-modal parcellation of human cerebral cortex. *Nature*, 536(7615):171–178, Aug 2016.

A. M. Golestani, S. Tymchuk, A. Demchuk, B. G. Goodyear, A. Y. Poppe, S. Tymchuk, C. O'Reilly, T. Green, S. Idris, E. Stewart, C. Stephenson, C. Kenney, P. N. Sylaja, M. D. Hill, S. B. Coutts, A. M. Demchuk, P. Sharma, M. Eesa, and M. Goyal. Longitudinal evaluation of resting-state FMRI after acute stroke with hemiparesis. *Neurorehabil Neural Repair*, 27(2):153–163, 2013.

P. Golland, Y. Golland, and R. Malach. Detection of spatial activation patterns as unsupervised segmentation of fMRI data. *Med Image Comput Comput Assist Interv*, 10(Pt 1):110–118, 2007.

J. C. Gore. Principles and practice of functional mri of the human brain. *The Journal of clinical investigation*, 112(1):4–9, July 2003. ISSN 0021-9738. doi: 10.1172/jci200319010.

J. A. Grahn, J. A. Parkinson, and A. M. Owen. The role of the basal ganglia in learning and memory: Neuropsychological studies. *Behavioural Brain Research*, 199(1):53 – 60, 2009. ISSN 0166-4328. doi: http://dx.doi.org/10.1016/j.bbr.2008.11.020. Special issue on the role of the basal ganglia in learning and memory.

C. Gratton, E. M. Nomura, F. Pérez, and M. D'Esposito. Focal brain lesions to critical locations cause widespread disruption of the modular organization of the brain. *Journal of Cognitive Neuroscience*, 24(6):1275–1285, Mar 2012. ISSN 0898-929X. doi: 10.1162/jocn_a_00222.

C. Grefkes and G. R. Fink. Connectivity-based approaches in stroke and recovery of function. *The Lancet Neurology*, 13(2):206 – 216, 2014. ISSN 1474-4422. doi: http://dx.doi.org/10.1016/S1474-4422(13)70264-3.

J. L. Gross, J. Yellen, and P. Zhang. *Handbook of Graph Theory, Second Edition.* Chapman & Hall/CRC, 2nd edition, 2013. ISBN 1439880182, 9781439880180.

C. C. Guo, F. Kurth, J. Zhou, E. A. Mayer, S. B. Eickhoff, J. H. Kramer, and W. W. Seeley. One-year test-retest reliability of intrinsic connectivity network fMRI in older adults. *NeuroImage*, 61(4):1471–1483, July 2012. ISSN 1053-8119. doi: 10.1016/j.neuroimage.2012.03.027. 00034.

A. Gustavsson, M. Svensson, F. Jacobi, C. Allgulander, J. Alonso, E. Beghi, R. Dodel, M. Ekman, C. Faravelli, L. Fratiglioni, B. Gannon, D. H. Jones, P. Jennum, A. Jordanova, L. Jönsson, K. Karampampa, M. Knapp, G. Kobelt, T. Kurth, R. Lieb, M. Linde, C. Ljungcrantz, A. Maercker, B. Melin, M. Moscarelli, A. Musayev, F. Norwood, M. Preisig, M. Pugliatti, J. Rehm, L. Salvador-Carulla, B. Schlehofer, R. Simon, H.-C. Steinhausen, L. J. Stovner, J.-M. Vallat, P. V. den Bergh, J. van Os, P. Vos, W. Xu, H.-U. Wittchen, B. Jönsson, and J. Olesen. Cost of disorders of the brain in europe 2010. *European Neuropsychopharmacology*, 21(10):718–779, July 2010. doi: 10.1016/j.euroneuro.2011.08.008.

M. Gutiérrez-Fernández, B. Rodríguez-Frutos, J. Ramos-Cejudo, M. Teresa Vallejo-Cremades, B. Fuentes, S. Cerdán, and E. Díez-Tejedor. Effects of intravenous administration of allogenic bone marrow- and adipose tissue-derived mesenchymal stem cells on functional recovery and brain repair markers in experimental ischemic stroke. *Stem Cell Research & Therapy*, 4(1):1–12, 2013.

E. M. Haacke, N. Y. Cheng, M. J. House, Q. Liu, J. Neelavalli, R. J. Ogg, A. Khan, M. Ayaz, W. Kirsch, and A. Obenaus. Imaging iron stores in the brain using magnetic resonance imaging. *Magnetic Resonance Imaging*, 23 (1):1 – 25, 2005. ISSN 0730-725X. doi: http://dx.doi.org/10.1016/j.mri.2004.10.001.

A. Hahamy, V. Calhoun, G. Pearlson, M. Harel, N. Stern, F. Attar, R. Malach, and R. Salomon. Save the global: global signal connectivity as a tool for studying clinical populations with functional magnetic resonance imaging. *Brain connectivity*, 4(6):395–403, August 2014. ISSN 2158-0014. doi: 10.1089/brain.2014.0244.

J. Hall. *Guyton and Hall Textbook of Medical Physiology*. Guyton Physiology. Elsevier Health Sciences, 2010. ISBN 9781437726749.

S. J. Hanson, R. Rebecchi, C. Hanson, and Y. O. Halchenko. Dense mode clustering in brain maps. *Magn Reson Imaging*, 25(9):1249–1262, Nov 2007.

G. Helms, B. Draganski, R. Frackowiak, J. Ashburner, and N. Weiskopf. Improved segmentation of deep brain grey matter structures using magnetization transfer (mt) parameter maps. *NeuroImage*, 47(1):194 – 198, 2009. ISSN 1053-8119. doi: http://dx.doi.org/10.1016/j.neuroimage.2009.03.053.

C. Hemmert, S. Achard, F. Renard, C. Delon-Martin, J. Dietmann, J.-P. Armspach, J. De Sèze, and S. Kremer. Resting-state functional MRI demonstrates brain network reorganisation in neuromyelitis optica. *MULTIPLE SCLEROSIS JOURNAL*, 19(11):167–167, Oct 2013.

S. Holm. A simple sequentially rejective multiple test procedure. *Scandinavian Journal of Statistics*, 6:65–70, 1979.

M. Hommel, S. T. Miguel, B. Naegele, N. Gonnet, and A. Jaillard. Cognitive determinants of social functioning after a first ever mild to moderate stroke at vocational age. *J. Neurol. Neurosurg. Psychiatr.*, 80(8):876–880, Aug 2009.

M. Hommel, L. Carey, and A. Jaillard. Depression: cognition relations after stroke. *Int J Stroke*, 10(6):893–896, Aug 2015.

M. Hommel, O. Detante, I. Favre, E. Touzé, and A. Jaillard. How to measure recovery? revisiting concepts and methods for stroke studies. *Translational Stroke Research*, 7(5):388–394, 2016. ISSN 1868-601X. doi: 10.1007/s12975-016-0488-0.

E. H. Hoyer and P. A. Celnik. Understanding and enhancing motor recovery after stroke using transcranial magnetic stimulation. *Restor. Neurol. Neurosci.*, 29(6):395–409, 2011.

S. A. Huettel, A. W. Song, and G. McCarthy. *Functional Magnetic Resonance Imaging, Third Edition*. Sinauer Associates, Inc., Sunderland, Massachusetts, U.S.A, 3rd edition edition, Aug. 2014. ISBN 978-0-87893-627-4.

C. S. Inman, G. A. James, S. Hamann, J. K. Rajendra, G. Pagnoni, and A. J. Butler. Altered resting-state effective connectivity of fronto-parietal motor control systems on the primary motor network following stroke. *NeuroImage*, 59(1):227–237, Jan. 2012. ISSN 1053-8119. doi: 10.1016/j.neuroimage.2011.07.083.

J. P. A. Ioannidis. How to make more published research true. *PLoS Med*, 11 (10):e1001747, Oct 2014. doi: 10.1371/journal.pmed.1001747.

A. C. Ionan, M.-Y. C. Polley, L. M. McShane, and K. K. Dobbin. Comparison of confidence interval methods for an intra-class correlation coefficient (icc). *BMC medical research methodology*, 14:121, 2014. ISSN 1471-2288. doi: 10.1186/1471-2288-14-121.

A. Jaillard, C. D. Martin, K. Garambois, J. F. Lebas, and M. Hommel. Vicarious function within the human primary motor cortex? *Brain*, 128(5):1122–1138, 2005. ISSN 0006-8950. doi: 10.1093/brain/awh456.

A. Jaillard, B. Naegele, S. Trabucco-Miguel, J. F. LeBas, and M. Hommel. Hidden dysfunctioning in subacute stroke. *Stroke*, 40(7):2473–2479, Jul 2009.

A. Jaillard, S. Grand, J. F. Le Bas, and M. Hommel. Predicting cognitive dysfunctioning in nondemented patients early after stroke. *Cerebrovasc. Dis.*, 29(5):415–423, 2010.

S. C. Johnston, S. Mendis, and C. D. Mathers. Global variation in stroke burden and mortality: estimates from monitoring, surveillance, and modelling. *The Lancet Neurology*, 8(4):345–354, 2009. ISSN 1474-4422. doi: 10.1016/S1474-4422(09)70023-7.

T. D. Jung, J. Y. Kim, J. H. Seo, S. U. Jin, H. J. Lee, S. H. Lee, Y. S. Lee, and Y. Chang. Combined information from resting-state functional connectivity and passive movements with functional magnetic resonance imaging differentiates fast late-onset motor recovery from progressive recovery in hemiplegic stroke patients: a pilot study. *J Rehabil Med*, 45(6):546–552, 2013.

T. Kahnt, L. J. Chang, S. Q. Park, J. Heinzle, and J. D. Haynes. Connectivity-based parcellation of the human orbitofrontal cortex. *J. Neurosci.*, 32(18): 6240–6250, May 2012.

S. Lassalle-Lagadec, I. Sibon, B. Dilharreguy, P. Renou, O. Fleury, and M. Allard. Subacute default mode network dysfunction in the prediction of post-stroke depression severity. *Radiology*, 264(1):218–224, 2012.

V. Latora and M. Marchiori. Efficient behavior of small-world networks. *Phys. Rev. Lett.*, 87:198701, Oct 2001. doi: 10.1103/PhysRevLett.87.198701.

M. Leclercq and P. E. Chipp. [A test battery of simple reaction times: value of the evaluation of oculomotor reaction rate in degenerative processes]. *Acta Neurol Belg*, 89(3-4):315, 1989.

J. S. Lees, E. S. Sena, K. J. Egan, A. Antonic, S. A. Koblar, D. W. Howells, and M. R. Macleod. Stem cell-based therapy for experimental stroke: A systematic review and meta-analysis. *International Journal of Stroke*, 7(7): 582–588, 2012. doi: 10.1111/j.1747-4949.2012.00797.x.

X. Liang, J. Wang, C. Yan, N. Shu, K. Xu, G. Gong, and Y. He. Effects of different correlation metrics and preprocessing factors on small-world brain functional networks: A resting-state functional MRI study. *PLoS ONE*, 7(3): e32766, Mar. 2012. doi: 10.1371/journal.pone.0032766. 00032.

X.-H. Liao, M.-R. Xia, T. Xu, Z.-J. Dai, X.-Y. Cao, H.-J. Niu, X.-N. Zuo, Y.-F. Zang, and Y. He. Functional brain hubs and their test-retest reliability: a multiband resting-state functional MRI study. *NeuroImage*, 83:969–982, Dec. 2013. ISSN 1053-8119. doi: 10.1016/j.neuroimage.2013.07.058. 00007.

D. E. Linden and D. L. Turner. Real-time functional magnetic resonance imaging neurofeedback in motor neurorehabilitation. *Curr Opin Neurol*, 29(4): 412–418, Aug 2016. ISSN 1350-7540. doi: 10.1097/WCO.0000000000000340. 27213774[pmid].

H. Liu, T. Tian, W. Qin, K. Li, and C. Yu. Contrasting evolutionary patterns of functional connectivity in sensorimotor and cognitive regions after stroke. *Frontiers in Behavioral Neuroscience*, 10:72, 2016. ISSN 1662-5153. doi: 10.3389/fnbeh.2016.00072.

M. Lotze, J. Markert, P. Sauseng, J. Hoppe, C. Plewnia, and C. Gerloff. The role of multiple contralesional motor areas for complex hand movements after internal capsular lesion. *The Journal of Neuroscience*, 26(22):6096–6102, 2006. doi: 10.1523/JNEUROSCI.4564-05.2006.

I. Loubinoux, C. Carel, J. Pariente, S. Dechaumont, J.-F. Albucher, P. Marque, C. Manelfe, and F. Chollet. Correlation between cerebral reorganization and motor recovery after subcortical infarcts. *NeuroImage*, 20(4):2166 – 2180, 2003. ISSN 1053-8119. doi: http://dx.doi.org/10.1016/j.neuroimage.2003.08.017.

M.-E. Lynall, D. S. Bassett, R. Kerwin, P. J. McKenna, M. Kitzbichler, U. Muller, and E. Bullmore. Functional connectivity and brain networks in schizophrenia. *The Journal of Neuroscience*, 30(28):9477–9487, 2010. doi: 10.1523/JNEUROSCI.0333-10.2010.

F. I. Mahoney and D. W. Barthel. FUNCTIONAL EVALUATION: THE BARTHEL INDEX. *Md State Med J*, 14:61–65, 1965.

C. Malherbe, A. Messe, E. Bardinet, M. Pelegrini-Issac, V. Perlbarg, G. Marrelec, Y. Worbe, J. Yelnik, S. Lehericy, and H. Benali. Combining spatial independent component analysis with regression to identify the subcortical components of resting-state FMRI functional networks. *Brain Connect*, 4(3):181–192, Apr 2014.

K. O. McGraw and S. P. Wong. Forming inferences about some intraclass correlation coefficients. *Psychological Methods*, 1(1):30–46, 1996. ISSN 1939-1463(Electronic);1082-989X(Print). doi: 10.1037/1082-989X.1.1.30.

D. McRobbie, E. Moore, M. Graves, and M. Prince. *MRI from Picture to Proton*. Cambridge University Press, 2007. ISBN 9781139457194.

N. Metropolis and S. Ulam. The Monte Carlo Method. *J. Amer. Stat. Assoc.*, 44(247):335–341, Sept. 1949.

F. A. Middleton and P. L. Strick. Basal ganglia output and cognition: Evidence from anatomical, behavioral, and clinical studies. *Brain and Cognition*, 42(2):183 – 200, 2000. ISSN 0278-2626. doi: http://dx.doi.org/10.1006/brcg.1999.1099.

S. L. Minger, A. Ekonomou, E. M. Carta, A. Chinoy, R. H. Perry, and C. G. Ballard. Endogenous neurogenesis in the human brain following cerebral infarction. *Regen Med*, 2(1):69–74, Jan 2007.

E. Moulton, M. Amor-Sahli, V. Perlbarg, C. Pires, S. Crozier, D. Galanaud, R. Valabregue, M. Yger, F. Baronnet-Chauvet, Y. Samson, D. Dormont, and C. Rosso. Axial diffusivity of the corona radiata at 24 hours post-stroke: A new biomarker for motor and global outcome. *PLoS ONE*, 10(11):e0142910, 11 2015. doi: 10.1371/journal.pone.0142910.

R. Müller and P. Büttner. A critical discussion of intraclass correlation coefficients. *Statistics in Medicine*, 13(23-24):2465–2476, 1994. ISSN 1097-0258. doi: 10.1002/sim.4780132310. 00360.

R.-A. Müller, P. Shih, B. Keehn, J. R. Deyoe, K. M. Leyden, and D. K. Shukla. Underconnected, but how? a survey of functional connectivity mri studies in autism spectrum disorders. *Cerebral Cortex*, 21(10):2233–2243, 2011. doi: 10.1093/cercor/bhq296.

K. Murphy, R. M. Birn, D. A. Handwerker, T. B. Jones, and P. A. Bandettini. The impact of global signal regression on resting state correlations: Are anti-correlated networks introduced? *NeuroImage*, 44(3):893–905, Feb 2009. ISSN 1053-8119. doi: 10.1016/j.neuroimage.2008.09.036.

K. Murphy, R. M. Birn, and P. A. Bandettini. Resting-state fmri confounds and cleanup. *NeuroImage*, 80:349 – 359, 2013. ISSN 1053-8119. doi: http://dx.doi.org/10.1016/j.neuroimage.2013.04.001. Mapping the Connectome.

V. A. Nair, B. M. Young, C. La, P. Reiter, T. N. Nadkarni, J. Song, S. Vergun, N. S. Addepally, K. Mylavarapu, J. L. Swartz, M. B. Jensen, M. R. Chacon, J. A. Sattin, and V. Prabhakaran. Functional connectivity changes in the language network during stroke recovery. *Annals of clinical and translational neurology*, 2(2):185–195, February 2015. ISSN 2328-9503. doi: 10.1002/acn3.165.

S. Nakagawa and H. Schielzeth. Repeatability for gaussian and non-gaussian data: a practical guide for biologists. *Biol Rev Camb Philos Soc*, 85(4):935–956, Nov 2010. doi: 10.1111/j.1469-185X.2010.00141.x.

A. B. New, D. A. Robin, A. L. Parkinson, J. R. Duffy, M. R. McNeil, O. Piguet, M. Hornberger, C. J. Price, S. B. Eickhoff, and K. J. Ballard. Altered resting-state network connectivity in stroke patients with and without apraxia of speech. *Neuroimage Clin*, 8:429–439, 2015.

J. A. Nielsen, B. A. Zielinski, M. A. Ferguson, J. E. Lainhart, and J. S. Anderson. An evaluation of the left-brain vs. right-brain hypothesis with resting state functional connectivity magnetic resonance imaging. *PLoS ONE*, 8(8):1–11, 08 2013. doi: 10.1371/journal.pone.0071275.

E. M. Nomura, C. Gratton, R. M. Visser, A. Kayser, F. Perez, and M. D'Esposito. Double dissociation of two cognitive control networks in patients with focal brain lesions. *Proceedings of the National Academy of Sciences*, 107(26):12017–12022, June 2010. ISSN 0027-8424, 1091-6490. doi: 10.1073/pnas.1002431107. PMID: 20547857.

R. J. Nudo. Recovery after brain injury: mechanisms and principles. *Frontiers in human neuroscience*, 7:887, 2013. ISSN 1662-5161. doi: 10.3389/fnhum.2013.00887.

S. Ogawa, T. M. Lee, A. R. Kay, and D. W. Tank. Brain magnetic resonance imaging with contrast dependent on blood oxygenation. *Proc. Natl. Acad. Sci. U.S.A.*, 87(24):9868–9872, Dec 1990.

J. X. O'Reilly, C. F. Beckmann, V. Tomassini, N. Ramnani, and H. Johansen-Berg. Distinct and overlapping functional zones in the cerebellum defined by resting state functional connectivity. *Cerebral cortex (New York, N.Y. : 1991)*, 20(4):953–965, April 2010. ISSN 1047-3211. doi: 10.1093/cercor/bhp157.

S. Ovadia-Caro, K. Villringer, J. Fiebach, G. J. Jungehulsing, E. van der Meer, D. S. Margulies, and A. Villringer. Longitudinal effects of lesions on functional networks after stroke. *Journal of Cerebral Blood Flow & Metabolism*, 33(8): 1279–1285, Aug. 2013. ISSN 0271-678X. doi: 10.1038/jcbfm.2013.80.

C.-h. Park, W. H. Chang, S. H. Ohn, S. T. Kim, O. Y. Bang, A. Pascual-Leone, and Y.-H. Kim. Longitudinal changes of resting-state functional connectivity during motor recovery after stroke. *Stroke; a journal of cerebral circulation*, 42(5):1357–1362, May 2011. ISSN 1524-4628. doi: 10.1161/STROKEAHA.110.596155. PMID: 21441147.

J. Y. Park, Y. H. Kim, W. H. Chang, C. H. Park, Y. I. Shin, S. T. Kim, and A. Pascual-Leone. Significance of longitudinal changes in the default-mode network for cognitive recovery after stroke. *Eur. J. Neurosci.*, 40(4):2715–2722, 2014.

S. Pettie and V. Ramachandran. An optimal minimum spanning tree algorithm. *J. ACM*, 49(1):16–34, Jan. 2002. ISSN 0004-5411. doi: 10.1145/505241.505243.

F. Pizzagalli, G. Auzias, C. Delon-Martin, and M. Dojat. Local landmark alignment for high-resolution fmri group studies: Toward a fine cortical investigation of hand movements in human. *Journal of Neuroscience Methods*, 218(1): 83 – 95, 2013. ISSN 0165-0270. doi: http://dx.doi.org/10.1016/j.jneumeth.2013.05.005.

R. A. Poldrack, J. A. Mumford, and T. E. Nichols. *Handbook of Functional MRI Data Analysis*. Cambridge University Press, 1 edition edition, Aug. 2011. ISBN 978-0-521-51766-9.

J. D. Power, B. L. Schlaggar, and S. E. Petersen. Recent progress and outstanding issues in motion correction in resting state fmri. *NeuroImage*, 105:536 – 551, 2015. ISSN 1053-8119. doi: http://dx.doi.org/10.1016/j.neuroimage.2014.10.044.

R. C. Prim. Shortest connection networks and some generalizations. *Bell System Technical Journal*, 36(6):1389–1401, 1957. ISSN 1538-7305. doi: 10.1002/j.1538-7305.1957.tb01515.x.

P.-F. Qiao, P.-Y. Gao, J.-P. Dai, and G.-M. Niu. Research progress on resting state fmri of epilepsy. *Brain and Development*, 34(1):8 – 12, 2012. ISSN 0387-7604. doi: http://dx.doi.org/10.1016/j.braindev.2011.01.001.

C. Randolph, M. C. Tierney, E. Mohr, and T. N. Chase. The Repeatable Battery for the Assessment of Neuropsychological Status (RBANS): preliminary clinical validity. *J Clin Exp Neuropsychol*, 20(3):310–319, 1998.

J. Rankin. Cerebral vascular accidents in patients over the age of 60. I. General considerations. *Scott Med J*, 2(4):127–136, 1957.

A. K. Rehme, G. R. Fink, D. Y. von Cramon, and C. Grefkes. The role of the contralesional motor cortex for motor recovery in the early days after stroke assessed with longitudinal fmri. *Cerebral Cortex*, 21(4):756–768, 2011. doi: 10.1093/cercor/bhq140.

B. G. Y. Ridley, C. Rousseau, J. Wirsich, A. L. Troter, E. Soulier, S. Confort-Gouny, F. Bartolomei, J.-P. Ranjeva, S. Achard, and M. Guye. Nodal approach reveals differential impact of lateralized focal epilepsies on hub reorganization. *NeuroImage*, 118:39 – 48, 2015. ISSN 1053-8119. doi: http://dx.doi.org/10.1016/j.neuroimage.2015.05.096.

A. Riecker, K. Gröschel, H. Ackermann, S. Schnaudigel, J. Kassubek, and A. Kastrup. The role of the unaffected hemisphere in motor recovery after stroke. *Human Brain Mapping*, 31(7):1017–1029, 2010. ISSN 1097-0193. doi: 10.1002/hbm.20914.

A. Ropper, M. Samuels, and J. Klein. *Adams and Victor's Principles of Neurology 10th Edition*. McGraw-Hill Education, 2014. ISBN 9780071800914.

C. S. Roy and C. S. Sherrington. On the Regulation of the Blood-supply of the Brain. *J. Physiol. (Lond.)*, 11(1-2):85–158, 1890.

M. Rubinov and O. Sporns. Complex network measures of brain connectivity: uses and interpretations. *NeuroImage*, 52(3):1059–1069, Sept. 2010. ISSN 1095-9572. doi: 10.1016/j.neuroimage.2009.10.003.

Z. S. Saad, S. J. Gotts, K. Murphy, G. Chen, H. J. Jo, A. Martin, and R. W. Cox. Trouble at rest: how correlation patterns and group differences become distorted after global signal regression. *Brain connectivity*, 2(1):25–32, 2012. ISSN 2158-0014. doi: 10.1089/brain.2012.0080.

M. P. Sampat, G. J. Whitman, T. W. Stephens, L. D. Broemeling, N. A. Heger, A. C. Bovik, and M. K. Markey. The reliability of measuring physical characteristics of spiculated masses on mammography. *The British Journal of Radiology*, 79 Spec No 2:S134–140, Dec. 2006. ISSN 1748-880X. doi: 10.1259/bjr/96723280.

T. D. Satterthwaite, D. H. Wolf, D. R. Roalf, K. Ruparel, G. Erus, S. Vandekar, E. D. Gennatas, M. A. Elliott, A. Smith, H. Hakonarson, R. Verma, C. Davatzikos, R. E. Gur, and R. C. Gur. Linked sex differences in cognition and functional connectivity in youth. *Cereb Cortex*, 25(9):2383–2394, Sep 2015. doi: 10.1093/cercor/bhu036.

J. L. Saver, K. C. Johnston, D. Homer, R. Wityk, W. Koroshetz, L. L. Truskowski, and E. C. Haley. Infarct volume as a surrogate or auxiliary outcome measure in ischemic stroke clinical trials. *Stroke*, 30(2):293–298, 1999. ISSN 0039-2499. doi: 10.1161/01.STR.30.2.293.

A. J. Schwarz and J. McGonigle. Negative edges and soft thresholding in complex network analysis of resting state functional connectivity data. *NeuroImage*, 55(3):1132–1146, Apr. 2011. ISSN 1053-8119. doi: 10.1016/j.neuroimage.2010.12.047. 00047.

W. R. Shirer, H. Jiang, C. M. Price, B. Ng, and M. D. Greicius. Optimization of rs-fmri pre-processing for enhanced signal-noise separation, test-retest reliability, and group discrimination. *NeuroImage*, 117:67 – 79, 2015. ISSN 1053-8119. doi: http://dx.doi.org/10.1016/j.neuroimage.2015.05.015.

P. E. Shrout and J. L. Fleiss. Intraclass correlations: uses in assessing rater reliability. *Psychological Bulletin*, 86(2):420–428, Mar. 1979. ISSN 0033-2909.

J. G. Sled and G. B. Pike. *Understanding intensity non-uniformity in MRI*, pages 614–622. Springer Berlin Heidelberg, Berlin, Heidelberg, 1998. ISBN 978-3-540-49563-5. doi: 10.1007/BFb0056247.

S. M. Smith, K. L. Miller, G. Salimi-Khorshidi, M. Webster, C. F. Beckmann, T. E. Nichols, J. D. Ramsey, and M. W. Woolrich. Network modelling methods for FMRI. *Neuroimage*, 54(2):875–891, 2011.

S. M. Smith, C. F. Beckmann, J. Andersson, E. J. Auerbach, J. Bijsterbosch, G. Douaud, E. Duff, D. A. Feinberg, L. Griffanti, M. P. Harms, M. Kelly, T. Laumann, K. L. Miller, S. Moeller, S. Petersen, J. Power, G. Salimi-Khorshidi, A. Z. Snyder, A. T. Vu, M. W. Woolrich, J. Xu, E. Yacoub, K. Uğurbil, D. C. Van Essen, and M. F. Glasser. Resting-state fMRI in the human connectome project. *NeuroImage*, 80:144–168, Oct. 2013a. ISSN 1053-8119. doi: 10.1016/j.neuroimage.2013.05.039.

S. M. Smith, D. Vidaurre, C. F. Beckmann, M. F. Glasser, M. Jenkinson, K. L. Miller, T. E. Nichols, E. C. Robinson, G. Salimi-Khorshidi, M. W. Woolrich, D. M. Barch, K. Uğurbil, and D. C. Van Essen. Functional connectomics from resting-state fMRI. *Trends in cognitive sciences*, Nov. 2013b. ISSN 1879-307X. doi: 10.1016/j.tics.2013.09.016. PMID: 24238796.

J. Song, A. S. Desphande, T. B. Meier, D. L. Tudorascu, S. Vergun, V. A. Nair, B. B. Biswal, M. E. Meyerand, R. M. Birn, P. Bellec, and V. Prabhakaran. Age-related differences in test-retest reliability in resting-state

brain functional connectivity. *PLoS ONE*, 7(12):e49847, Dec. 2012. doi: 10.1371/journal.pone.0049847. 00014.

E. W. Steyerberg, F. E. Harrell, G. J. Borsboom, M. J. Eijkemans, Y. Vergouwe, and J. D. Habbema. Internal validation of predictive models: efficiency of some procedures for logistic regression analysis. *J Clin Epidemiol*, 54(8): 774–781, 2001.

C. J. Stoodley and J. D. Schmahmann. Functional topography in the human cerebellum: A meta-analysis of neuroimaging studies. *NeuroImage*, 44(2):489 – 501, 2009. ISSN 1053-8119. doi: http://dx.doi.org/10.1016/j.neuroimage.2008.08.039.

C. J. Stoodley, E. M. Valera, and J. D. Schmahmann. Functional topography of the cerebellum for motor and cognitive tasks: An fmri study. *NeuroImage*, 59(2):1560 – 1570, 2012. ISSN 1053-8119. doi: http://dx.doi.org/10.1016/j.neuroimage.2011.08.065.

R. S. Swenson. *Review of clinical and functional neuroscience*. Educational review manual in neurology. New York: Castle Connolly Graduate Medical Publishing, 2006.

S. Teki, G. R. Barnes, W. D. Penny, P. Iverson, Z. V. J. Woodhead, T. D. Griffiths, and A. P. Leff. The right hemisphere supports but does not replace left hemisphere auditory function in patients with persisting aphasia. *Brain*, 136(6):1901–1912, 2013. ISSN 0006-8950. doi: 10.1093/brain/awt087.

M. Termenon, A. Jaillard, C. Delon-Martin, and S. Achard. Reliability of graph analysis of resting state fmri using test-retest dataset from the human connectome project. *NeuroImage*, pages –, 2016. ISSN 1053-8119. doi: http://dx.doi.org/10.1016/j.neuroimage.2016.05.062.

A. Thiel and S. Vahdat. Structural and resting-state brain connectivity of motor networks after stroke. *Stroke*, 46(1):296–301, 2015. ISSN 0039-2499. doi: 10.1161/STROKEAHA.114.006307.

B. Thirion, G. Flandin, P. Pinel, A. Roche, P. Ciuciu, and J. B. Poline. Dealing with the shortcomings of spatial normalization: multi-subject parcellation of fMRI datasets. *Hum Brain Mapp*, 27(8):678–693, Aug 2006.

B. Thirion, G. Varoquaux, E. Dohmatob, and J. B. Poline. Which fMRI clustering gives good brain parcellations? *Front Neurosci*, 8:167, 2014.

L. Tian, J. Wang, C. Yan, and Y. He. Hemisphere- and gender-related differences in small-world brain networks: A resting-state functional {MRI} study. *NeuroImage*, 54(1):191 – 202, 2011. ISSN 1053-8119. doi: http://dx.doi.org/10.1016/j.neuroimage.2010.07.066.

D. Tomasi and N. D. Volkow. Laterality patterns of brain functional connectivity: gender effects. *Cereb Cortex*, 22(6):1455–1462, Jun 2012. doi: 10.1093/cercor/bhr230.

D. Tomasi, E. Shokri-Kojori, and N. D. Volkow. High-resolution functional connectivity density: Hub locations, sensitivity, specificity, reproducibility, and reliability. *Cerebral Cortex*, 2015. doi: 10.1093/cercor/bhv171.

A. M. Tuladhar, L. Snaphaan, E. Shumskaya, M. Rijpkema, G. Fernandez, D. G. Norris, and F.-E. de Leeuw. Default mode network connectivity in stroke patients. *PLoS ONE*, 8(6):1–9, 06 2013. doi: 10.1371/journal.pone.0066556.

N. Tzourio-Mazoyer, B. Landeau, D. Papathanassiou, F. Crivello, O. Etard, N. Delcroix, B. Mazoyer, and M. Joliot. Automated anatomical labeling of activations in SPM using a macroscopic anatomical parcellation of the MNI MRI single-subject brain. *NeuroImage*, 15(1), Jan. 2002. ISSN 1053-8119. doi: 10.1006/nimg.2001.0978.

K. R. A. Van Dijk, T. Hedden, A. Venkataraman, K. C. Evans, S. W. Lazar, and R. L. Buckner. Intrinsic functional connectivity as a tool for human connectomics: theory, properties, and optimization. *J Neurophysiol*, 103(1): 297–321, Jan 2010. doi: 10.1152/jn.00783.2009.

D. C. Van Essen, H. A. Drury, J. Dickson, J. Harwell, D. Hanlon, and C. H. Anderson. An integrated software suite for surface-based analyses of cerebral cortex. *Journal of American Medical Informatics Association*, 8:443–459, 2001.

L. J. Volz, A.-S. Sarfeld, S. Diekhoff, A. K. Rehme, E.-M. Pool, S. B. Eickhoff, G. R. Fink, and C. Grefkes. Motor cortex excitability and connectivity in chronic stroke: a multimodal model of functional reorganization. *Brain Structure and Function*, 220(2):1093–1107, 2015. ISSN 1863-2661. doi: 10.1007/s00429-013-0702-8.

S. I. Vrieze. Model selection and psychological theory: a discussion of the differences between the Akaike information criterion (AIC) and the Bayesian information criterion (BIC). *Psychol Methods*, 17(2):228–243, 2012.

C. Wang, W. Qin, J. Zhang, T. Tian, Y. Li, L. Meng, X. Zhang, and C. Yu. Altered functional organization within and between resting-state networks in chronic subcortical infarction. *J. Cereb. Blood Flow Metab.*, 34(4):597–605, 2014.

J.-H. Wang, X.-N. Zuo, S. Gohel, M. P. Milham, B. B. Biswal, and Y. He. Graph theoretical analysis of functional brain networks: Test-retest evaluation on short- and long-term resting-state functional MRI data. *PLoS ONE*, 6(7): e21976, July 2011. doi: 10.1371/journal.pone.0021976. 00069.

L. Wang, C. Yu, H. Chen, W. Qin, Y. He, F. Fan, Y. Zhang, M. Wang, K. Li, Y. Zang, T. Woodward, and C. Zhu. Dynamic functional reorganization of the motor execution network after stroke. *Brain: a journal of neurology*, 133 (5):1224–38, 2010. ISSN 1460-2156. doi: 10.1093/brain/awq043.

D. J. Watts and S. H. Strogatz. Collective dynamics of 'small-world'networks. *Nature*, 393(6684):440–442, June 1998. ISSN 0028-0836. doi: 10.1038/30918.20860.

T. Welton, D. Kent, D. Auer, and R. Dineen. Reproducibility of graph-theoretic brain network metrics: A systematic review. *Brain Connectivity*, 5(4):193–202, 2015. doi: 10.1089/brain.2014.0313.

C. T. Whitlow, R. Casanova, and J. A. Maldjian. Effect of resting-state functional MR imaging duration on stability of graph theory metrics of brain network connectivity. *Radiology*, 259(2):516–524, May 2011. ISSN 1527-1315. doi: 10.1148/radiol.11101708. 00020 PMID: 21406628.

R. Wiest, E. Abela, J. Missimer, G. Schroth, C. W. Hess, M. Sturzenegger, D. J. Wang, B. Weder, and A. Federspiel. Interhemispheric cerebral blood flow balance during recovery of motor hand function after ischemic stroke–a longitudinal MRI study using arterial spin labeling perfusion. *PLoS ONE*, 9 (9):e106327, 2014.

A. M. Wood, I. R. White, and P. Royston. How should variable selection be performed with multiply imputed data? *Stat Med*, 27(17):3227–3246, 2008.

T. Wu, X. Long, L. Wang, M. Hallett, Y. Zang, K. Li, and P. Chan. Functional connectivity of cortical motor areas in the resting state in Parkinson's disease. *Human Brain Mapping*, 32(9):1443–1457, 2011. ISSN 1097-0193. doi: 10.1002/hbm.21118.

H. Xu, W. Qin, H. Chen, L. Jiang, K. Li, and C. Yu. Contribution of the resting-state functional connectivity of the contralesional primary sensorimotor cortex to motor recovery after subcortical stroke. *PLoS ONE*, 9(1):1–9, 01 2014a. doi: 10.1371/journal.pone.0084729.

P. Xu, R. Huang, J. Wang, N. T. V. Dam, T. Xie, Z. Dong, C. Chen, R. Gu, Y.-F. Zang, Y. He, J. Fan, and Y. jia Luo. Different topological organization of human brain functional networks with eyes open versus eyes closed. *NeuroImage*, 90:246 – 255, 2014b. ISSN 1053-8119. doi: http://dx.doi.org/10.1016/j.neuroimage.2013.12.060.

D. Yin, F. Song, D. Xu, L. Sun, W. Men, L. Zang, X. Yan, and M. Fan. Altered topological properties of the cortical motor-related network in patients with subcortical stroke revealed by graph theoretical analysis. *Human brain mapping*, Nov. 2013. ISSN 1097-0193. doi: 10.1002/hbm.22406. PMID: 24222337.

H. Yong, C. Zhang, G. Gaolang, and A. Evans. Neuronal networks in Alzheimer's disease. *The Neuroscientist*, 15(4):333–350, 2009. doi: 10.1177/1073858409334423.

P. Zhang, Q. Xu, J. Dai, J. Wang, N. Zhang, and Y. Luo. Dysfunction of affective network in post ischemic stroke depression: a resting-state functional magnetic resonance imaging study. *Biomed Res Int*, 2014:846830, 2014.

D. Zhu, J. Chang, S. Freeman, Z. Tan, J. Xiao, Y. Gao, and J. Kong. Changes of functional connectivity in the left frontoparietal network following aphasic stroke. *Front Behav Neurosci*, 8:167, 2014.

X.-N. Zuo and X.-X. Xing. Test-retest reliabilities of resting-state fmri measurements in human brain functional connectomics: a systems neuroscience perspective. *Neuroscience and biobehavioral reviews*, 45:100–118, Sep 2014. ISSN 1873-7528. doi: 10.1016/j.neubiorev.2014.05.009.